Heinrich Heine
Universität
Düsseldorf

Dynamics of Andreev bound states in Josephson junctions

Inaugural-Dissertation

zur Erlangung des Doktorgrades
der Mathematisch-Naturwissenschaftlichen Fakultät
der Heinrich-Heine-Universität Düsseldorf

vorgelegt von

Kateryna Zatsarynna
aus Noyabrsk (Russland)

Düsseldorf, Dezember 2025

aus dem Institut für Theoretische Physik, Lehrstuhl IV
der Heinrich-Heine Universität Düsseldorf

Gedruckt mit der Genehmigung der
Mathematisch-Naturwissenschaftlichen Fakultät der
Heinrich-Heine Universität Düsseldorf

Berichterstatter:

1. Prof. Dr. Reinhold Egger

2. Apl. Prof. Dr. Hermann Kampermann

Tag der mündlichen Prüfung:

List of publications

The publications that constitute the basis of this thesis are listed below. An explanation of the author's role and contributions to each work is provided.

Many-body quantum dynamics of spin-orbit coupled Andreev states in a Zeeman field

Contribution: Main author, responsible for the principal scientific work, including extending the previous theoretical model to the case with spin-symmetry breaking, designing and implementing the code, comparing numerical results with preceding work, generating all data used in the research, producing the figures, and contributing to the writing of the manuscript.

Zenodo data repository containing the datasets used for figure generation: https://zenodo.org/records/11444594.
The code for the project can be found on GitHub:
https://github.com/KatyaZats/Dynamical-Parity-Stabilization-code-examples.

Reference: Kateryna Zatsarynna, Andrea Nava, Alex Zazunov, Reinhold Egger, *Many-body quantum dynamics of spin-orbit coupled Andreev states in a Zeeman field*, Phys.Rev.B 109 (2024) 21, 214505.

Green's Function Approach to Josephson Dot Dynamics and Application to Quantum Mpemba Effects

Contribution: Main author, conducted the preliminary scientific work and was responsible for applying the theoretical framework to the specific cases discussed in the paper. Designed and implemented the code, generated the data used in the numerical studies, produced the figures, and contributed to the writing of the manuscript.

Zenodo data repository containing the datasets used for figure generation: https://zenodo.org/records/14937796.
The code for the project can be found on GitHub:
https://github.com/KatyaZats/QME-code-examples.

Reference: Kateryna Zatsarynna, Andrea Nava, Alex Zazunov, Reinhold Egger, *Green's Function Approach to Josephson Dot Dynamics and Application to Quantum Mpemba Effects*, Phys.Rev.B 111 (2025) 10, 104506.

Summary

In recent years, hybrid devices hosting Andreev bound states have become increasingly widespread in quantum information processing, superconducting electronics, and mesoscopic quantum transport. Both experimental and theoretical studies of Andreev state physics are extremely versatile, encompassing a wide range of phenomena from superconducting transport and spin dynamics to quantum coherence and topological effects. The interplay of Andreev bound states with external driving, continuum quasiparticles, and spin-dependent interactions provides a rich landscape for investigating quantum coherent phenomena, non-equilibrium dynamics, and phase transitions.

In this work, first, we explore the many-body dynamics and dynamical parity stabilization in Josephson junctions with spin-symmetry breaking. Interactions between the ABSs and continuum states cause parity switches in the Andreev sector. Stabilizing the parity of the Andreev sector is therefore important for the coherent Andreev qubit dynamics. We develop a theoretical approach to describe the many-body dynamics of the Andreev bound states in a Josephson junction embedded in a superconducting loop and inductively coupled to a microwave resonator that induces transitions between the single-particle states of the junction, both Andreev and continuum states. Here, we include the Zeeman magnetic field and Rashba spin-orbit interactions on the quantum dot that cause the spin splitting of the Andreev levels. In this case, it is convenient to use the doubled Nambu spinor for the states description; however, one encounters the double-counting problem. By deriving the Lindblad equation in the excitation picture, we obtain a consistent description of the Andreev many-body dynamics without doubled degrees of freedom. We apply the obtained approach to observe dynamical parity stabilization and investigate the influence of the spin breaking on the parity stabilization effect.

Further, we discuss the quantum Mpemba effect in Josephson junctions. Here, the quantum dot coupled to a fermionic bath in the presence of an electromagnetic environment is described with the help of the Green's functions. Green's functions formalism is simpler than the Keldysh contour integration, however, it still can be used to describe nonequilibrium situations. Additionally, this approach allows one to potentially include Coulomb interactions on the quantum dot, apart from the spin-orbit interaction and external Zeeman field that we take into account. Combining this single-particle description with the previously derived Lindblad equation for the many-body dynamics of the Andreev bound states, we study the relaxation dynamics of the system after a superconducting phase difference quench and observe the presence of the quantum Mpemba effect. We study this effect for short and intermediate wire lengths as well as for different junction transparencies. Quantum Mpemba effect, apart from being conceptually interesting as an anomalous relaxation phenomenon resulting from the interplay between the quantum coherence, dissipation, and thermalization, is also useful from a practical point of view. Possible applications include faster cooling of quantum devices, faster state preparation, and shorter qubit reset times.

Zusammenfassung

In den letzten Jahren haben sich hybride Systeme, die Andreev-Gebundene Zustände (Andreev Bound States, ABSs) beherbergen, in Bereichen wie der Quanteninformationsverarbeitung, der supraleitenden Elektronik und dem mesoskopischen Quantentransport stark verbreitet. Sowohl experimentelle als auch theoretische Untersuchungen der Andreev-Physik sind äußerst vielseitig und umfassen ein breites Spektrum an Phänomenen – von supraleitendem Transport und Spindynamik bis hin zu Quantenkohärenz und topologischen Effekten.

Das Zusammenspiel der Andreev-Zustände mit äußerer Anregung, Kontinuumsquasiteilchen und spinabhängigen Wechselwirkungen eröffnet eine reiche Landschaft zur Untersuchung von kohärenten Quanteneffekten, Nichtgleichgewichtsdynamik und Phasenübergängen.

In dieser Arbeit untersuchen wir zunächst die Viele-Körper-Dynamik und die dynamische Paritätsstabilisierung in Josephson-Kontakten mit gebrochener Spinsymmetrie. Wechselwirkungen zwischen den Andreev-Zuständen und den Kontinuumszuständen führen zu Paritätswechseln im Andreev-Sektor. Die Stabilisierung der Parität dieses Sektors ist daher entscheidend für eine kohärente Dynamik des Andreev-Qubits. Wir entwickeln einen theoretischen Ansatz, um die Viele-Körper-Dynamik der Andreev-Zustände in einem Josephson-Kontakt zu beschreiben, der in einer supraleitenden Verbindung eingebettet und induktiv an einen Mikrowellenresonator gekoppelt ist. Dieser Resonator induziert Übergänge zwischen den Einteilchenzuständen der Struktur – sowohl den Andreev- als auch den Kontinuumszuständen. Wir berücksichtigen dabei ein Zeeman-Feld sowie Rashba-Spin-Bahn-Wechselwirkungen auf dem Quantendot, die eine Spinaufspaltung der Andreev-Niveaus verursachen. In diesem Fall ist es zweckmäßig, den verdoppelten Nambu-Spinor zur Zustandsbeschreibung zu verwenden; allerdings tritt hierbei das Problem der Doppelzählung auf. Durch die Herleitung der Lindblad-Gleichung im Anregungsbild erhalten wir eine konsistente Beschreibung der Andreev-Viele-Körper-Dynamik ohne doppelte Freiheitsgrade. Den so gewonnenen Ansatz wenden wir an, um die dynamische Paritätsstabilisierung zu untersuchen und den Einfluss der Spinsymmetriebrechung auf diesen Effekt zu analysieren.

Im weiteren Verlauf diskutieren wir den quantum Mpemba-Effekt in Josephson-Kontakten. Hier wird der Quantendot, der an ein fermionisches Bad in Gegenwart einer elektromagnetischen Umgebung gekoppelt ist, mit Hilfe des Green'schen-Funktionsansatzes beschrieben. Dieser Ansatz ist einfacher als die Keldysh-Konturintegration, erlaubt aber dennoch die Beschreibung von Nichtgleichgewichtszuständen. Zudem bietet er die Möglichkeit, Coulomb-Wechselwirkungen auf dem Quantendot einzubeziehen – zusätzlich zu den Spin-Bahn-Wechselwirkungen und dem externen Zeeman-Feld, die wir bereits berücksichtigen. Durch die Kombination dieser Einteilchenbeschreibung mit der zuvor hergeleiteten Lindblad-Gleichung für die Viele-Körper-Dynamik der Andreev-Zustände untersuchen wir die Relaxationsdynamik des Systems nach einem Quench der supraleitenden Phasendifferenz und beobachten das Auftreten des quantum Mpemba-Effekts. Wir analysieren diesen Effekt für kurze und mittlere Drahtlängen sowie für unterschiedliche Transparenzen des Kontakts. Der quantum Mpemba-Effekt ist nicht nur konzeptionell interessant als anomales Relaxationsphänomen, das Einblicke in das Zusammenspiel von Quantenkohärenz, Dissipation und Thermalisierung bietet, sondern auch praktisch relevant. Zu den möglichen Anwendungen zählen die schnellere Kühlung von Quantengeräten, beschleunigte Zustandsvorbereitung und verkürzte Qubit-Reset-Zeiten.

Contents

1 Introduction

1.1 Preface and outline of the thesis

In 1962, B. Josephson predicted the Josephson effect - the current flowing between two superconductors coupled by a thin non-superconducting barrier by quantum tunnelling of Cooper pairs, without application of external voltage [1]. In Josephson's theory, the junction is described by two central equations - Josephson equations, given by

$$I(t) = I_c \sin(\varphi(t)),$$

$$V(t) = \frac{\Phi_0}{2\pi}\dot{\varphi}(t),$$

where the first equation - the current-phase relation - describes the supercurrent across the junction, with I_c - critical current of the junction and φ - the superconducting phase difference across the junction. The second equation - the superconducting phase evolution relation - gives the voltage across the junction, with $\Phi_0 = h/2e$ - magnetic flux quantum. The experimental confirmation of this prediction followed in 1963 by P. W. Anderson and J. Rowell [2]. Since then, Josephson junctions gained numerous applications across physics, engineering and metrology. One of the most prominent applications of the Josephson junctions, which, however, is beyond the scope of this thesis, the superconducting qubit, was awarded this year's Nobel prize [3].

Given these widespread applications, it is important to understand the microscopic mechanism that is the basis of the Josephson effect. In 1964, A. F. Andreev described the process of Andreev reflection [4]: when there is an electron of energy less than the superconducting gap in a normal state material interfaced with the superconductor (NS-interface), this electron cannot simply enter the superconductor, since there are no available single-particle states of energies less than the superconducting gap. Instead, this electron gets retroreflected into a hole, while a Cooper pair is added to the superconductor. If one now adds a second NS-interface, so that one now has an S-N-S junction, due to the multiple Andreev reflections at the interfaces, the quasiparticles' "standing electronic waves" are formed between the two superconductors. These quasiparticles are called Andreev bound states (ABSs), and their energies, for a short, single-channel junction, can be written as

$$E_A(\varphi) = \pm\Delta\sqrt{1 - \mathcal{T}\sin^2(\varphi/2)}, \tag{1.1}$$

with Δ - the superconducting gap, $\varphi = \varphi_1 - \varphi_2$ - the superconducting phase difference between the two leads, $\mathcal{T}$ - transparency of the junction. It is worth noting that for the formation of ABSs, the superconducting phase difference between two superconductors is required. Each ABS carries a supercurrent,

$$I(\varphi) = \frac{2e}{\hbar}\frac{\partial E_A(\varphi)}{\partial\varphi}.$$

The Josephson current in the junction is the sum of contributions from all occupied Andreev levels.

ABSs reveal the microscopic structure of the Josephson junction, and what is especially interesting today is not only their statics but foremost their dynamics - how these discrete quantum

levels evolve in time when driven, coupled, or perturbed. Specifically, here we consider the situation where the coupling to the bosonic degree of freedom of an LC-resonator causes the variation in time superconducting phase difference. Moreover, ABSs are coupled to the continuum states of the junction. How do the ABSs interact with each other and the continuum states of the junction under the external driving, and how is this reflected in the dynamics and what are the resulting effects of these interactions on the system dynamics? Also note that equation (1.1) describes the energies of the ABSs in the simplest case. These energy levels change in more complex situations — for instance, when introducing a Zeeman field, spin-orbit interactions, Coulomb interactions, or considering a long normal material region. How do these additional ingredients modify the dynamics between the levels and the occupations of the many-body states of the system? These are the central questions that form the foundation of this work and are explored throughout this thesis.

It is worth noting that coupling to an external bosonic field - such as the one present in the LC-resonator or a microwave cavity - is one of the main physical ways to coherently control and manipulate ABSs (and Andreev qubit) by causing fluctuations of the superconducting phase difference across the weak link [5–7]. This setup allows not only to observe the transitions between the Andreev levels but also to coherently control and manipulate the ABSs as a qubit. Additionally, in the last work, the interaction between spin, phase, and microwave photons allows the exploration of the Andreev states to Majorana states transition. In theory [8], interplay between the Rashba spin-orbit interaction, Zeeman field, and proximity-induced s-wave superconductivity in a Josephson weak link induces a topological phase transition for the specifically tuned parameters. During this phase transition, the lowest-energy ABSs evolve continuously into Majorana bound states at the wire ends. Additionally, there are parameter regimes where the so-called partially-separated ABSs emerge - the trivial near-zero-energy ABSs that are not topologically protected. Topological phase transition is of particular interest, since it could provide a tunable route from conventional Andreev qubits to topologically protected Majorana qubits. The interactions between the ABSs and continuum states are explored, e.g. in the following references [9–11]. In realistic Josephson junctions, ABSs can not be perfectly decoupled from the continuum states, so that the quasiparticles can tunnel between the ABSs and continuum states. Not only does the presence of continuum states modify the shape of the supercurrent, but also the tunnelling processes hinder the coherent ABSs dynamics, causing the so-called quasiparticle poisoning - switches of the fermionic parity in the Andreev sector. Such processes are relevant not only for the Andreev qubits, but also for a so much aspired Majorana qubit, since strong continuum coupling can destroy the topological protection.

Outline.— In the following sections of this chapter, we briefly discuss topics that are relevant to Andreev bound states physics and that lie at the basis of the research presented in this thesis. Sec. 1.2 discusses superconductivity and the theoretical frameworks used to describe it. Sec. 1.3 is devoted to the formation of Andreev bound states (ABSs), particularly in Josephson junctions, and their applications. In Sec. 1.4, the main experimental setup used in this work is introduced. Sec. 1.5 provides a brief description of the scattering and transfer matrix methods, while Sec. 1.6 outlines the fundamentals of the Green's functions method. Both of these methods are used later in this thesis to describe ABSs.

In chapter 2, we consider the many-body dynamics and dynamical parity stabilization in Josephson junctions with the spin symmetry breaking. Transfer matrix and Bogoliubov-de-Gennes approaches are employed to describe the single-particle states of the junction (Andreev bound states and continuum states) and derive the transition rates between these states. The transitions between the states are triggered by the external electromagnetic field. We develop a method that allows one to overcome the double-counting problem when constructing the many-body Andreev states, write down the equation describing the dynamics of the Andreev many-body states and apply it to observe the dynamical stabilisation process.

Chapter 3 is devoted to the quantum Mpemba effect in Josephson junctions. Here, instead of describing the junction with the help of the transfer matrix and Bogoliubov-de-Gennes method, we are going to use the Green's functions approach, where the states of the system are encoded as the poles of the single-particle Green's function.

1.2 Superconductivity

Superconductivity is a quantum macroscopic effect observed in some materials - superconductors - when they are cooled below a certain critical temperature. Macroscopically, superconductivity manifests itself by a vanishing electrical resistance and Meissner effect - expulsion of magnetic field [12–15]. Throughout this thesis, we will be encountering superconductors as a crucial component in the generation of the Andreev bound states. Here, only s-wave superconductors will be considered, although Andreev bound states can be formed in other types of superconductors too [16, 17].

1.2.1 Conventional (s-wave) superconductors and BCS theory

A microscopic theory of superconductivity was suggested by Bardeen-Cooper-Schrieffer (BCS theory) in 1957 [12, 13]. It explains the superconductivity by condensation of the Cooper pairs - pairs of electrons - at sufficiently small temperatures. The attractive force between the electrons becomes stronger than the Coulomb repulsion.

S-wave superconductors are characterized by a spherically symmetric (orbital quantum number $l = 0$) Cooper pair wave function, with antisymmetric spin-singlet part $\frac{1}{\sqrt{2}}(|\uparrow_1\downarrow_2\rangle - |\downarrow_1\uparrow_2)$ [14] (here index 1 refers to the first electron in the pair, 2 - to the second). The antisymmetric spin part ensures that the total wave function of the electron pair is antisymmetric. The electrons have opposite momenta $\mathbf{k}$, $-\mathbf{k}$, so that the total energy of the pair is minimal. In this way, the s-wave Cooper pair consists of two electrons with momenta and spins $(\mathbf{k}, \uparrow)$ and $(-\mathbf{k}, \downarrow)$ (note that this type of pairing preserves time-reversal symmetry).

The standard BCS theory assumes the presence of a weak potential generated by the interactions between electrons and vibrations of the crystal lattice (phonons) [14]: one electron of the pair polarises the medium by attracting and displacing the ion, which, in its turn, attracts the second electron of the pair. The net effect is an effective attractive phonon-mediated interaction between two electrons. This interaction is most effective within a shell $\hbar\omega_D$ around the Fermi surface, with ω_D - Debye frequency - the maximum frequency of the phonons. Note that for the stable Cooper pairs, low temperatures are required since the energy of the pairing interaction is weak and, as the temperature increases, thermal energy breaks the pairing.

Cooper problem. — The fundamental result underlying the BCS superconductivity theory is provided by the Cooper problem [18] formulated in the following way: one considers two electrons added on top of a Fermi sea - a system of non-interacting fermions (e.g., electrons in a metal) filling all single-particle states up to the Fermi energy E_F. These electrons interact with each other through a weak attractive interaction, no matter how small. The question is, do these electrons form a bound state? L.N.Cooper showed that, indeed, these two fermions will always form a bound state (a Cooper pair) just above the Fermi surface, regardless of how weak the attraction is. The solution of the problem results in the following equation for the energy of the bound state $E < 2E_F$:

$$-\frac{1}{V} = \int_{E_F}^{E_F+E_R} \frac{D(\epsilon)d\epsilon}{2(\epsilon - E_F) + |E|} \approx \frac{D(E_F)}{2} \ln\left(\frac{2E_F - E + 2E_R}{2E_F - E}\right), \quad \epsilon = \frac{q^2}{2m},$$

with $E_R = \hbar\omega_D$ - the cutoff energy, beyond which the interaction between electrons goes to zero, $D(\epsilon)$ - the density of states at energy ϵ. The key point here is the presence of the Fermi sea, since for free electrons in the 3D space, the density of states $D_{\text{free}}(\epsilon) \propto \sqrt{\epsilon}$, and we would

not get the infrared divergence in the integral, corresponding to any arbitrary weak interaction. In the free case, the bound state would exist only for interactions above a certain threshold. In contrast, in the presence of the Fermi sea, the integration is restricted to the shell E_R above E_F, and in this thin shell, the density of states is effectively constant $D(\epsilon) \approx D(E_F)$, and the integral gets a logarithmic divergence when $2E_F - E \to 0$. This divergence corresponds to the divergence on the left-hand side when the interaction is arbitrarily weak $V \to 0$, so we can always find the solution of this equation, that is, the bound state. Assuming the weak attraction between the electrons, one can obtain for the energy of the bound state

$$E = 2E_F - 2E_R \exp\left(\frac{-2}{D(E_F)|V|}\right).$$

This result demonstrates that for any arbitrarily small attractive potential $V > 0$, a bound state of two electrons does exist, which is the instability of the Fermi sea that underlies the BCS theory.

BCS Hamiltonian. — However, in the Cooper problem, all the fermions of the Fermi sea were dynamically ignored - they are only considered as a static background that sets up the density of states and the phase-space restriction. In BCS theory, the pairing instability extends from two electrons to the entire Fermi sea, leading to a coherent macroscopic quantum state — the superconducting condensate, in which all electrons near the Fermi surface participate. The microscopic BCS Hamiltonian has a form

$$H_{\text{BCS}} = \sum_{\mathbf{k},\text{œ}} \epsilon_{\mathbf{k}} c^{\dagger}_{\mathbf{k}\text{œ}} c_{\mathbf{k}\text{œ}} - \sum_{\mathbf{k},\mathbf{k}'} V_{\mathbf{k},\mathbf{k}'} c^{\dagger}_{\mathbf{k}\uparrow} c^{\dagger}_{-\mathbf{k}\downarrow} c_{-\mathbf{k}'\downarrow} c_{\mathbf{k}'\uparrow} \tag{1.2}$$

$$= H_0 + H_{\text{int}}, \tag{1.3}$$

with $\epsilon_{\mathbf{k}} = (\hbar k)^2/2m - \mu$ - single-particle energy, fermionic operator $c^{\dagger}_{\mathbf{k},\text{œ}}$ creates an electron of momentum $\mathbf{k}$ and spin projection σ, $V_{\mathbf{k},\mathbf{k}'}$ - matrix element of the attractive electron-electron interaction. To diagonalise this Hamiltonian, mean-field decoupling can be applied. Since the pairing happens between the electrons of opposite momenta and spins, the mean-field decoupling is applied around the expectation values

$$b_{\mathbf{k}} = \langle c_{-\mathbf{k}\downarrow} c_{\mathbf{k}\uparrow} \rangle. \tag{1.4}$$

Cooper approximation assumes the attractive pairing potential is nonzero and constant within the shell $\hbar\omega_D$ around the Fermi energy $V_{\mathbf{k},\mathbf{k}'} = -U/\Omega\,\Theta(E - E_F \mp \hbar\omega_D)$, $U > 0$. Defining the energy gap through this mean-field parameter

$$\Delta = -\frac{U}{\Omega} \sum_{\mathbf{k}} b_{\mathbf{k}}, \tag{1.5}$$

the microscopic BCS Hamiltonian can be rewritten in the mean-field form

$$H^{\text{MF}}_{\text{BCS}} = \sum_{\mathbf{k},\text{œ}} \epsilon_{\mathbf{k}} c^{\dagger}_{\mathbf{k}\text{œ}} c_{\mathbf{k}\text{œ}} - \sum_{\mathbf{k}} \left(\Delta c^{\dagger}_{\mathbf{k}\uparrow} c^{\dagger}_{-\mathbf{k}\downarrow} + \Delta^* c_{-\mathbf{k}\downarrow} c_{\mathbf{k}\uparrow} \right) - \frac{|\Delta|^2}{U/\Omega}. \tag{1.6}$$

1.2.2 $U(1)$ symmetry breaking

It is worth noting that the mean-field parameter Δ is a complex number: $\Delta = |\Delta| e^{i\varphi}$, where φ is a superconducting phase - macroscopic quantum phase of the Cooper pair condensate. It determines the macroscopic quantum coherence in the superconductor - all Cooper pairs share the same phase across macroscopic distances, and their wave functions add coherently. This selection of the definite phase indicates the spontaneous breaking of the global $U(1)$ symmetry

that is a characteristic of the original BCS Hamiltonian. The original microscopic Hamiltonian (1.2) is invariant under the phase rotations of the creation/annihilation operators

$$c_{\mathbf{k}\sigma} \to e^{i\theta} c_{\mathbf{k}\sigma}, \qquad c^\dagger_{\mathbf{k}\sigma} \to e^{-i\theta} c^\dagger_{\mathbf{k}\sigma}, \qquad \theta \in \mathbb{R}. \tag{1.7}$$

By Noether's theorem, this invariance implies the conservation of the total particle number

$$[H_{\text{BCS}}, \hat{N}] = 0, \quad \hat{N} = \sum_{\mathbf{k},\sigma} c^\dagger_{\mathbf{k}\sigma} c_{\mathbf{k}\sigma}. \tag{1.8}$$

Whereas, the mean-field BCS Hamiltonian (1.6) is not invariant under the phase rotations, due to the pairing terms (note that Δ is a fixed complex number with a chosen phase φ). This also implies that the total particle number is not conserved

$$[H^{\text{MF}}_{\text{BCS}}, \hat{N}] \neq 0. \tag{1.9}$$

In this way, the emergence of superconductivity in a material necessarily breaks $U(1)$ symmetry, with the superconducting phase φ being a symmetry-breaking parameter.

1.2.3 BCS groundstate

To diagonalize mean-field BCS Hamiltonian (1.6) and determine the mean-field parameter Δ self-consistently one applies the Bogoliubov transformation [19]: the new quasiparticles are defined as

$$\gamma_{\mathbf{k}\uparrow} = u_k c_{\mathbf{k}\uparrow} - v_k c^\dagger_{-\mathbf{k}\downarrow}, \tag{1.10}$$

$$\gamma^\dagger_{-\mathbf{k}\downarrow} = v^*_k c_{\mathbf{k}\uparrow} + u^*_k c^\dagger_{-\mathbf{k}\downarrow}, \tag{1.11}$$

with $|u_k|^2 + |v_k|^2 = 1$. In this way, $\gamma_{\pm\mathbf{k}\sigma}$ are fermionic operators that obey fermionic commutation relations. In the γ-operators representation, the mean field BCS Hamiltonian acquires a diagonal form

$$H^{\text{MF}}_{\text{BCS}} = \sum_{\mathbf{k}} E_k (\gamma^\dagger_{\mathbf{k}\uparrow}\gamma_{\mathbf{k}\uparrow} + \gamma^\dagger_{-\mathbf{k}\downarrow}\gamma_{-\mathbf{k}\downarrow}) + H_F, \tag{1.12}$$

where $E_k = \sqrt{\Delta^2 + \epsilon_k^2}$ is the quasiparticle energy, and H_F - free energy of the pair condensate. The ground state of this Hamiltonian is the quasiparticle vacuum state $|\Psi_{\text{BCS}}\rangle$ defined by

$$\gamma_{\mathbf{k}\uparrow}|\Psi_{\text{BCS}}\rangle = \gamma_{-\mathbf{k}\downarrow}|\Psi_{\text{BCS}}\rangle = 0. \tag{1.13}$$

In terms of the c-operators, this state can be written as

$$|\Psi_{\text{BCS}}\rangle = \prod_{\mathbf{k}} \left(u_k + v_k c^\dagger_{\mathbf{k}\uparrow} c^\dagger_{-\mathbf{k}\downarrow}|0\rangle\right), \tag{1.14}$$

with $|0\rangle$ - particles' vacuum and u_k, v_k - probability amplitudes that a Cooper pair is unoccupied or occupied, respectively. From the diagonalisation procedure of the mean-field Hamiltonian (setting the off-diagonal terms in γ-representation to zero) and the normalisation condition for u_k, v_k amplitudes, one derives

$$u_k^2 = \frac{1}{2}\left(1 + \frac{\epsilon_k}{\Delta}\frac{1}{\sqrt{1+\epsilon_k^2/\Delta^2}}\right), \quad v_k^2 = \frac{1}{2}\left(1 - \frac{\epsilon_k}{\Delta}\frac{1}{\sqrt{1+\epsilon_k^2/\Delta^2}}\right). \tag{1.15}$$

Note that $|\Psi_{\text{BCS}}\rangle$ is not an eigenstate of the number of particle operator $\hat{N} = \sum_{\mathbf{k},\sigma} c^\dagger_{\mathbf{k}\sigma} c_{\mathbf{k}\sigma}$. The BCS ground state is a coherent superposition of states with different (but all even) particle numbers and allows for fluctuations of particle number (electrons are created/annihilated in pairs). However, the BCS ground state is sharply peaked around the average particle number $\langle\hat{N}\rangle = 2\sum_k |v_k|^2$ (twice the number of Cooper pairs) in the thermodynamic limit.

1.2.4 Self-consistency equation for the mean-field parameter

The derivation of the self-consistency equation for the mean-field parameter can be found, for instance, in [14]. Here, the main equations for zero and finite temperatures are summarized.

The self-consistency equation for the mean-field parameter Δ at $T = 0$ is given by

$$\Delta = -\frac{U}{\Omega}\sum_{\mathbf{k}}\langle\Psi_{\mathrm{BCS}}|\, c_{-\mathbf{k}\downarrow}c_{\mathbf{k}\uparrow}\,|\Psi_{\mathrm{BCS}}\rangle = -\frac{U}{2\Omega}\sum_{\mathbf{k}}\frac{\Delta}{\sqrt{\Delta^2+\epsilon_k^2}}. \tag{1.16}$$

The nontrivial solution ($\Delta \neq 0$) can be obtained by solving

$$1 = -\frac{U}{2\Omega}\sum_{k}\frac{1}{\sqrt{\Delta^2+\epsilon_k^2}} = -U\int_0^{E_R} d\epsilon \frac{D(\epsilon)}{\sqrt{\Delta^2+\epsilon^2}} \approx -UD(E_f)\sinh^{-1}\frac{E_R}{\Delta}, \tag{1.17}$$

with $D(\epsilon)$ - density of states at energy ϵ and $E_R = \hbar\omega_D$ - cutoff energy. Inverting this expression, one gets

$$\Delta = \frac{E_R}{\sinh\left(-1/D(E_f)U\right)} \approx 2E_R\exp\left(-\frac{1}{D(E_f)|U|}\right), \tag{1.18}$$

where the weak-coupling approximation $D(E_f)U \ll 1$ is used. This expression is similar to the energy of the bound state of the Cooper problem

$$E = 2E_f - 2E_R\exp\left(-\frac{2}{D(E_f)|U|}\right). \tag{1.19}$$

At finite temperature, one needs to take into account that the probability that a quasiparticle state is excited in thermal equilibrium is given by the Fermi distribution

$$n_f(E_k) = \frac{1}{e^{\beta E_k}+1}, \quad \beta = 1/T. \tag{1.20}$$

With this, one can derive the gap equation at a finite temperature

$$-\frac{1}{U} = \frac{1}{2\Omega}\sum_{k}\frac{\tanh(\beta E_k/2)}{E_k}. \tag{1.21}$$

This equation determines the dependence of the SC gap on temperature $\Delta(T)$ and the critical temperature T_c when the gap disappears:

$$\beta_c^{-1} \approx 1.13E_R\exp\left(-\frac{1}{D(E_f)|U|}\right). \tag{1.22}$$

1.2.5 Nambu space

The Bogoliubov transformation defined by equations (1.10 - 1.11) can be rewritten in matrix form

$$\begin{pmatrix}\gamma_{\mathbf{k}\uparrow}\\ \gamma^\dagger_{-\mathbf{k}\downarrow}\end{pmatrix} = \begin{pmatrix}u_k & -v_k\\ v_k^* & u_k^*\end{pmatrix}\begin{pmatrix}c_{\mathbf{k}\uparrow}\\ c^\dagger_{-\mathbf{k}\downarrow}\end{pmatrix}, \quad \begin{pmatrix}c_{\mathbf{k}\uparrow}\\ c^\dagger_{-\mathbf{k}\downarrow}\end{pmatrix} = \begin{pmatrix}u_k^* & v_k\\ -v_k^* & u_k\end{pmatrix}\begin{pmatrix}\gamma_{\mathbf{k}\uparrow}\\ \gamma^\dagger_{-\mathbf{k}\downarrow}\end{pmatrix}. \tag{1.23}$$

In this notation, the original mean-field Hamiltonian becomes

$$H_{\mathrm{BCS}}^{\mathrm{MF}} = \frac{1}{2}\sum_{\mathbf{k}}\Psi^\dagger_{\mathbf{k}}\begin{pmatrix}\epsilon_k & \Delta\\ -\Delta^* & -\epsilon_k\end{pmatrix}\Psi_{\mathbf{k}} + \mathrm{const}, \quad \Psi_{\mathbf{k}} = \begin{pmatrix}c_{\mathbf{k}\uparrow}\\ c^\dagger_{-\mathbf{k}\downarrow}\end{pmatrix}, \tag{1.24}$$

where a two-component spinor $\Psi_{\mathbf{k}}$ is a so-called Nambu spinor of momentum $\mathbf{k}$ that combines electron and hole operators and allows to treat them symmetrically [20, 21]. The corresponding Nambu matrix (in momentum space) [15, 22]

$$H_{\mathrm{BdG}}(\mathbf{k}) = \begin{pmatrix} \epsilon_k & -\Delta \\ -\Delta^* & -\epsilon_k \end{pmatrix} \tag{1.25}$$

is called the Bogoliubov-de-Gennes (BdG) Hamiltonian. In real space, it can be generalised to an operator matrix acting on the Nambu vector of spatially varying particle and hole wave functions

$$H_{\mathrm{BdG}} = \begin{pmatrix} H_0(\mathbf{r}) & \Delta(\mathbf{r}) \\ \Delta^*(\mathbf{r}) & -H_0(\mathbf{r}) \end{pmatrix}, \quad H_0(\mathbf{r}) = -\frac{\hbar^2}{2m}\frac{\partial^2}{\partial \mathbf{r}^2} - \mu + V(\mathbf{r}), \tag{1.26}$$

with μ - chemical potential and $V(\mathbf{r})$ - scalar potential.

An important consequence of the convenient Nambu matrix notation is the artificial doubling of the Hilbert space [15, 21]. One can notice that the following relation between the Nambu spinors at momenta $\mathbf{k}$ and $-\mathbf{k}$ holds:

$$\Psi_{\mathbf{k}} = \tau_x \Psi^*_{-\mathbf{k}}. \tag{1.27}$$

This equation is called the reality constraint, and it points out the redundancy of the degrees of freedom in the BdG formalism. Indeed, while in the original BCS form there were two operators $c_{\mathbf{k}}, c_{-\mathbf{k}}$ for the momenta $\mathbf{k}, -\mathbf{k}$, while in the BdG formalism the Nambu spinors $\Psi_{\mathbf{k}}, \Psi_{-\mathbf{k}}$ already contain 4 original operators $c_{\mathbf{k}}$, $c_{-\mathbf{k}}$ and their complex conjugated partners $c^\dagger_{\mathbf{k}}$, $c^\dagger_{-\mathbf{k}}$. This doubling of the degrees of freedom is artificial and arises since both particles and holes are treated in a symmetric way. However, the number of physical degrees of freedom remains unchanged. Later in this thesis, we will see a discussion of several ways to overcome the doubling problem and treat the system so that no spurious unphysical states arise.

1.2.6 Particle-hole symmetry

Another important aspect of the BCS theory and the BdG formalism is the particle-hole symmetry [23, 24]. This symmetry arises due to the underlying physical mechanism of the superconductivity: Cooper pairing of the electrons and holes. In the BdG formalism, the particle-hole symmetry is represented by the relation for the BdG Hamiltonian

$$\mathcal{C}\, H_{\mathrm{BdG}}(\mathbf{k})\, \mathcal{C}^{-1} = -H_{\mathrm{BdG}}(-\mathbf{k}), \quad \mathcal{C} = \tau_x \mathcal{K}, \tag{1.28}$$

and for the Nambu spinor

$$\mathcal{C}\Psi_{\mathbf{k}} = \tau_x \Psi^*_{-\mathbf{k}}, \tag{1.29}$$

with $\mathcal{C}$ - charge conjugation operator transforming an electron into a hole, τ_x - Pauli matrix in the Nambu space and $\mathcal{K}$ - complex conjugation operator. The consequences of the particle-hole symmetry are: each state with energy E has a particle-hole symmetric state with energy $-E$. Due to this, the spectrum is symmetric around zero. Indeed, assume that u_E is an eigenstate of the BdG Hamiltonian:

$$H_{\mathrm{BdG}} u_E = E u_E. \tag{1.30}$$

From the symmetry of the Hamiltonian, one can obtain the following

$$H_{\mathrm{BdG}}(\mathcal{C}u_E) = -E(\mathcal{C}u_E), \tag{1.31}$$

so that the state $\mathcal{C}u_E$ is also an eigenstate of the BdG Hamiltonian with energy $-E$. With this, we can conclude

$$\mathcal{C}u_E = u_{-E}. \tag{1.32}$$

On the operator level, the particle-hole symmetry is expressed by the relation

$$\gamma_E = \gamma^\dagger_{-E}, \tag{1.33}$$

where the operator $\gamma^\dagger_E$ annihilates a state with energy E, and operator $\gamma^\dagger_{-E}$ creates a state with energy $-E$. In other words, this relation means that destroying a state with energy E is equivalent to creating a state of negative energy $-E$. These relations again point out the redundancy of the Nambu formalism - the artificial doubling of the states, where each state is accompanied by a particle-hole symmetric partner.

Another interesting consequence of the particle-hole symmetry that follows from the reasoning given above is that if the zero-energy state is present in the system, it becomes its own particle-hole conjugate, up to a phase factor. The creation and annihilation operators of a zero-energy state satisfy the relation

$$\gamma_{E=0} = \gamma^\dagger_{E=0}. \tag{1.34}$$

Such operators are called Majorana operators [17, 25].

If the zero-energy state is localised (e.g. bound to a vortex or an edge) and is topologically protected by a bulk gap, so that it is robust against local perturbations, such a state is called a (topologically-protected) Majorana bound state [26]. However, accidental zero-energy Andreev bound states can also satisfy $E = 0$ condition and be their own particle–hole partner. But if these states lack topological protection, they can be removed by small perturbations [27–29].

1.3 Andreev bound states formation

Andreev bound states (ABSs) are localised fermionic quasiparticle states that arise on the interfaces of the superconducting and normal state materials. They are a coherent superposition of electron- and hole-states and are formed due to the Andreev reflection process [4].

1.3.1 Andreev reflection

Let us consider a normal state material - superconductor interface (NS boundary further). The superconductor has a band gap Δ. An electron with energy $E > \Delta$ from the normal state material can enter the superconductor, where it will be converted into a quasiparticle of the same energy. However, this scattering process does not work for electrons with energy $E < \Delta$, since in the superconductor there are no quasiparticles below the band gap. Therefore, for voltages and temperatures below Δ there is no current flowing between the normal and SC state materials that is sustained by this normal scattering process [30]. However, there is a different type of scattering that appears on the NS boundary - the so-called Andreev reflection or scattering - that results in the charge transfer. During Andreev reflection, an incident electron forms a Cooper pair in the superconductor with retroreflection of a hole [4], [31]. By retroreflection, in comparison to normal (specular reflection) one means that both normal and parallel velocity components are reversed. The process of Andreev scattering is illustrated in Figure 1.1. Another property of Andreev scattering is that the momentum of the reflected hole is almost equal to the momentum of the incoming electron. This process conserves energy, but it does not conserve charge - indeed, a charge $2e$ is transferred from the normal state material to the superconductor.

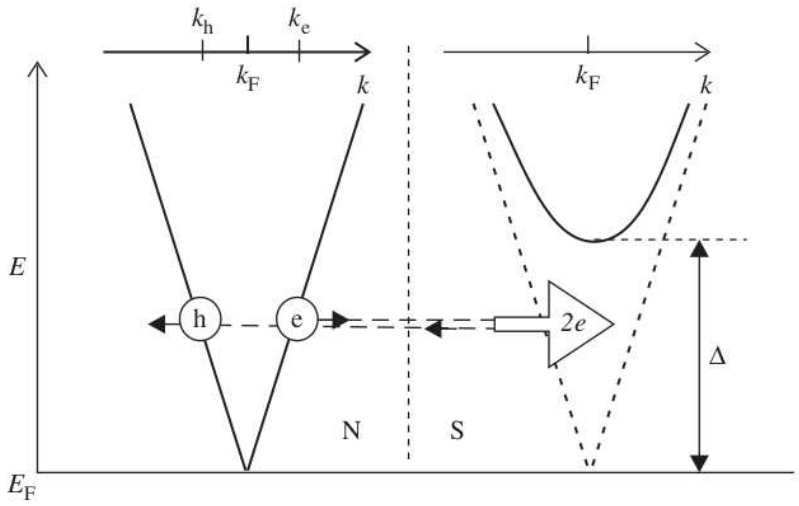

Figure 1.1: Illustration from [30]: Andreev reflection of an electron on NS boundary.

It is worth noting that Andreev reflection is a highly spin-dependent process [32]: since the Cooper pair consists of two electrons of opposite spin, the retroreflected hole has an opposite spin with respect to the incoming electron. Therefore, in the fully spin-polarised case, when the conductance electrons of the normal state material possess a single spin projection, Andreev reflection will be inhibited since it becomes impossible to form a Cooper pair of two opposite-spin electrons. An example of such a case is a ferromagnet (FS boundary) or a material where a strong spin polarisation exists or is induced by an external magnetic field. In these cases, the strength of the Andreev reflection and the conductance of the junction become dependent on the spin polarization of the normal state material.

Let us consider a scattering process between the metal ($x < 0$) and a superconductor ($x > 0$). We look at the wavefunction $\psi(x)$, with the electron and hole component of the form $\psi_{e,h}(x) \propto \tilde{\psi}_{e,h}(x) \exp(ik_F x)$, where the envelope $\tilde{\psi}_{e,h}(x)$ satisfies Bogoliubov-de-Gennes equation [30]

$$\begin{pmatrix} -iv_F\, d/dx & \Delta(x)e^{i\varphi} \\ \Delta(x)e^{-i\varphi} & iv_F\, d/dx \end{pmatrix} \begin{pmatrix} \tilde{\psi}_e(x) \\ \tilde{\psi}_h(x) \end{pmatrix} = E \begin{pmatrix} \tilde{\psi}_e(x) \\ \tilde{\psi}_h(x) \end{pmatrix}. \tag{1.35}$$

In the normal metal, the wavefunction has a form

$$\tilde{\psi}(x < 0) = \begin{pmatrix} e^{ixE/v_F} \\ r_A e^{-ixE/v_F} \end{pmatrix}, \tag{1.36}$$

which describes the incoming electron and the outgoing Andreev reflected hole, with r_A - amplitude of Andreev reflection. In the superconductor, for $E < \Delta$, the solution is exponentially decaying

$$\tilde{\psi}(x > 0) = \frac{1}{\sqrt{2}} \begin{pmatrix} f_e \\ f_h \end{pmatrix} e^{-x\sqrt{\Delta^2 - E^2}/v_F}, \quad \begin{pmatrix} f_e \\ f_h \end{pmatrix} = \begin{pmatrix} 1 \\ e^{-i\varphi}\left(\frac{E}{\Delta} - i\sqrt{1 - \frac{E^2}{\Delta^2}}\right) \end{pmatrix}. \tag{1.37}$$

By matching both solutions at $x = 0$, one can obtain for the Andreev reflection amplitude

$$r_A(E) = e^{i\chi} = e^{-i\varphi}\left(\frac{E}{\Delta} - i\sqrt{1 - \frac{E^2}{\Delta^2}}\right), \quad \chi = -\arccos\left(\frac{E}{\Delta}\right) - \varphi. \tag{1.38}$$

We see that the phase of the outgoing hole is shifted by χ with respect to the incoming electron. For the energy of the incoming electron $E < \Delta$, one finds the probability of the Andreev reflection $|r_A|^2 = 1$, so that the incoming electron is fully Andreev reflected. While in the case $E > \Delta$ for the Andreev reflection amplitude, one finds

$$r_A(E) = e^{-i\varphi}\left(\frac{E}{\Delta} - \sqrt{\frac{E^2}{\Delta^2} - 1}\right), \tag{1.39}$$

and $|r_A|^2 < 1$. In the limit $E \gg \Delta$, the probability of the Andreev reflection vanishes $|r_A| \to 0$: all the incoming electrons get converted into the quasiparticles.

1.3.2 Andreev bound states

We consider now a Josephson junction - a nanostructure placed between two superconductors with the same superconducting gap Δ but different superconducting phases. Consider an electron in the nanostructure with energy less than Δ. It will get Andreev-reflected trying to get to the superconductor; the retroreflected hole will also get Andreev-reflected back to an electron. In this way, an electron/hole performs a finite motion, which gives rise to discrete levels, called Andreev levels, see Fig. 1.2.

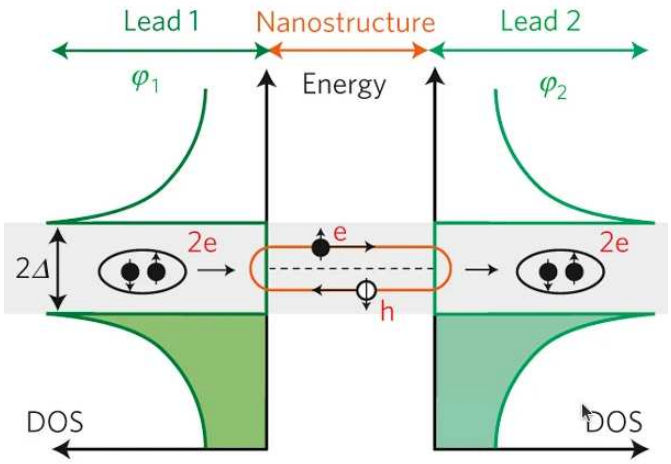

Figure 1.2: Illustration from [31]: general diagram showing the formation of Andreev bound states in SNS junction, where the superconductors have density of states with a gap Δ and superconducting phases $\varphi_{1,2}$. Within the superconducting gap (grey region), ABSs are formed due to the Andreev reflection of electrons and holes. ABSs are equivalent to the standing waves in a Fabry-Perot resonator.

Therefore, Andreev bound states (ABSs) are coherent superpositions of electrons and holes of opposite spins and energies smaller than Delta. One can view ABSs as the electronic analogues of the resonant states in a Fabry-Perot cavity [33]: the cavity here is a nanostructure, interfaces with the superconductors play the role of the mirrors. Furthermore, the "mirrors" behave as optical phase-conjugate mirrors, in which the direction of propagation and the optical phase factor get reversed during the reflection, making it analogous to Andreev reflection. Then ABSs are equivalent of the resonant standing waves. Changing the superconducting phase difference in the leads is analogous to moving the mirrors and changes the energy of the ABSs.

Important for the formation of the ABSs is strong spatial variation of the superconducting order parameter $\Delta(\mathbf{r})$ [31]. Based on this requirement, apart from the NS-interfaces and SNS-

junctions, such as Josephson junctions, Andreev-like bound states can emerge in the following systems:

- Vortex cores of type-II superconductors: inside the vortex core the order parameter vanishes, $\Delta \to 0$, so the quasiparticles get Andreev-reflected from the boundary between the gapped region and the core, forming Caroli–de Gennes–Matricon bound states [15, 34], which are ABSs circulating around the vortex;
- In the junctions or interfaces, where the normal region is replaced with a superconductor with a smaller superconducting gap $\Delta' < \Delta$: the quasiparticles with energy between Δ' and Δ can be trapped between the two gap boundaries, resulting in the subgap states;
- Similar effect, as above, occurs in the local superconducting gap suppression regions, due to e.g. presence of impurities, defects, or strong magnetic fields (see Yu-Shiba-Rusinov states [35–37]);
- Superconducting order parameter sign change in unconventional superconductors ($s+\pm$-superconductors): ABSs emerge at the interface between the regions with opposite-sign order parameters [16, 38];
- Topological superconductors: in the junctions with topological superconductors ABSs at zero energy may evolve into Majorana bound states [17, 39].

1.3.3 Josephson junctions

We consider a short weak link. Here "short" means that the length of the nanostructure L satisfies $L \ll \xi_0$, where $\xi_0 = \hbar v_F/\Delta$ is the superconducting coherence length - the characteristic Cooper pair size, and "weak" meaning that the coupling between the nanostructure and the superconductor is weak compared to the superconducting pairing correlations, so that the junction mediates superconducting transport via proximity effect, not bulk superconductivity. In a short weak link, with several transport channels, particle-hole symmetric energy levels of the ABSs of the n-th channel are given by

$$E_{A,n}(\varphi) = \pm\Delta\sqrt{1 - \mathcal{T}_n \sin^2(\varphi/2)}, \tag{1.40}$$

with $\varphi = \varphi_1 - \varphi_2$ and $\varphi_{1,2}$ - superconducting phases of the left and right superconducting bulks, $\mathcal{T}_n$ - transparency of the n-th channel of the junction. Since the energy of the ABSs is phase-dependent, a supercurrent through the nanostructure emerges. This is known as the DC Josephson effect, and the ABSs are considered to be the main carriers of the Josephson current. The supercurrent at zero temperature is given by

$$I(\varphi) = \frac{2e}{\hbar}\sum_n \frac{\partial E_{A,n}}{\partial \varphi}, \tag{1.41}$$

The supercurrent through a Josephson junction is carried by phase coherence between the superconductors, so that no voltage drop is needed. This means that Cooper pairs move through the junction without energy loss - dissipationless, with effectively zero resistance, unlike normal current, which requires a voltage to move charges. In the case when the phase difference changes in time, a finite voltage across the junction appears. The voltage is related to the phase variation through the Josephson relation

$$\frac{d\varphi}{dt} = \frac{2e}{\hbar}V. \tag{1.42}$$

This leads to an AC Josephson current oscillating at frequency $\frac{2e}{\hbar}V$. In this regime, which includes external energy input to change the phase difference over time, the junction is driven out of the equilibrium and can show a nonzero resistance and energy dissipation, for instance, via quasiparticle excitations or the environment.

At a finite temperature, the supercurrent carried by the ABSs is given by

$$I(\varphi) = \frac{2e}{\hbar}\sum_n \frac{\partial E_{A,n}}{\partial \varphi} n_F\left(E_{A,n}\right), \tag{1.43}$$

where $n_F(\epsilon)$ is Fermi distribution function.

If the length of the junction increases, more Andreev states appear inside the superconducting gap, arising from multiple quantised Andreev reflections. Because of the particle-hole symmetry, new states always appear in pairs. For long junctions, with $L \gg \xi_0$, ABSs levels become more closely spaced in energy, forming a quasicontinuum inside the gap. The ABSs dispersion in the long junction case is analysed in the articles [40, 41].

Another type of states present in Josephson junctions are the continuum states - free excitations of the superconducting condensate, with energies above the superconducting gap $E_c = \sqrt{\Delta^2 + k^2/2m}$ and the density of states given by the superconductor density of states (DOS)

$$D(E) = D(E_f)\frac{|E|}{\sqrt{E^2 - \Delta^2}}, \quad |E| > \Delta. \tag{1.44}$$

These states are not confined to the junction; they can propagate freely. Continuum quasiparticles are intrinsic to the superconducting leads and are present regardless of the junction. Continuum states can carry dissipative current and play a role in the non-equilibrium situations, for instance, the one mentioned above, when there is a time-dependent phase difference, described by equation (1.42).

1.3.4 Applications of Josephson junction

ABSs carry the supercurrent in the Josephson junctions (JJs) and therefore provide a microscopic origin of the Josephson effect. Josephson junctions have a wide range of applications:

- Quantum computing: JJs are the basic building block of superconducting qubits (e.g., transmon [42, 43], flux [44], phase [44, 45], and gatemon qubits [46]); they enable coherent control of quantum states with high fidelity [47]. The idea behind the Josephson qubits is the following: in an LC circuit that has a harmonic, equally spaced energy spectrum, the inductor is replaced by a JJ. This results in an anharmonic energy spectrum, with different spacing between the levels. This anharmonicity allows for the isolation of only two states ($|0\rangle$ and $|1\rangle$), without leakage to higher levels. One can manipulate qubit states with microwave photons, keeping coherence long enough to perform quantum operations. Control, manipulation, and readout of these qubits are provided by coupling to a microwave resonator [48].

- Another type of qubit that is very different from the circuit-level qubits, where the qubit states are represented by the quantised collective mode of the superconducting circuit, is the Andreev qubit. In Andreev cubit, the states are represented by the ABSs of the weak link. The advantages of these qubits are strong coupling to the microwave field, which enables fast manipulation, and a potential link between the ABSs and Majorana states, under the right conditions, that would enable topologically protected computations. However, the Andreev qubit is very susceptible to environment fluctuations (quasilarticles and charge noise), which makes the coherence time much shorter (current coherence time $\approx 100\,\mu$s) than the coherence time of more robust superconducting systems (coherence time ≈ 1 ms [49]).

- High precision measurements of magnetic field with SQUID (superconducting quantum interference device) circuit [50]: the Josephson current depends on the phase difference, and the phase difference is sensitive to magnetic flux.
- RSFQ (Rapid Single Flux Quantum) logic [51, 52] - ultra-fast low-power classical computing logic. In RSFQ, information is stored in the form of magnetic flux quanta ($\Phi_0 = h/(2e)$) and transferred as single flux quantum voltage pulses. In comparison, in semiconductor-based classical computers, the information is stored as voltage/current levels. Advantages of RSFQ logic: extremely fast switching, low power dissipation, robustness to noise. However, because of the superconductors, cryogenic cooling is needed. A very promising use of this technology is as a cryogenic classical computing coprocessor in quantum computers [53–55].
- Superconducting diodes [56–58];
- JJs are also used in light sensors, ultra-sensitive thermometers, neuromorphic devices, and even particle/radiation detectors [14, 59].

1.4 The main setup

In this thesis, we are going to study the dissipative dynamics of Andreev bound states in conventional (s-wave) superconducting junctions. The system in question is a multilevel quantum dot sandwiched between two BCS leads. We focus on a phase-biased regime, that is, the junction is held at a superconducting phase difference $\phi(t) = \phi_0 + \tilde{\phi}(t)$, with a small time-dependent component $|\tilde{\phi}(t)| \ll 1$ due to fluctuations of the electromagnetic environment. This

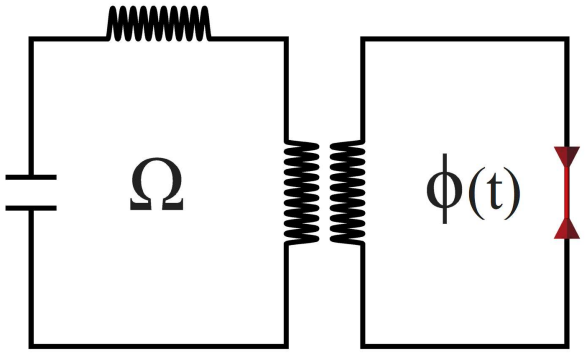

Figure 1.3: Sketch of the setup considered in this thesis: a Josephson junction, with superconducting phase difference $\phi(t)$ across the junction, is embedded in a superconducting loop threaded by a magnetic flux and inductively coupled to a microwave resonator of resonance frequency Ω.

setup can be realised by embedding a nanowire dot in a superconducting loop threaded by a magnetic flux, see Fig. 1.3. The magnetic flux imposes the phase difference across the junction

$$\phi_0 = \phi_L - \phi_R = 2\pi \left(n - \frac{\Phi_{\text{ext}}}{\Phi_0} \right), \quad n \in \mathbb{N} \tag{1.45}$$

where Φ_{ext} is the external magnetic flux and $\Phi_0 = \hbar/(2e)$ is the quantum magnetic flux. By changing the magnetic flux threading the loop, one can vary the phase difference across the weak link. The superconducting loop is inductively coupled to a microwave resonator with

resonance frequency Ω_e. This microwave resonator represents the electromagnetic environment and is responsible for the phase fluctuations $\tilde{\phi}(t)$. In addition, the dot can be subject to microwave irradiation for manipulation and readout of the Andreev states.

The main focus of this thesis is Josephson junctions with broken spin symmetry. The weak link is modelled as a quantum dot with spin-orbit (SO) and Zeeman couplings. Later on, we also include Coulomb interactions on the dot. Note that the same ingredients (s-wave pairing, SO, Zeeman field) are used for Majorana-state engineering with Josephson junction devices.

The presence of SO and a magnetic field in superconducting junctions causes the splitting of the ABSs and the nontrivial dependence of their energies on the superconducting phase difference. This, in turn, contributes to more complex interactions within the ABSs sector and between the ABSs and continuum states, leading to an interesting and rich dynamics. Additionally, in this setup effects such as anomalous Josephson effect and superconducting diode effect may be observed.

1.5 Transfer matrix method

One of the methods to describe the transport of electrons through the junction and derive the energies and wavefunctions of the ABSs is the transfer matrix method.

1.5.1 Scattering matrix

Let us consider a nanostructure with a single transmission channel placed between the right and left banks. Consider the right-moving (+) and left-moving (-) envelopes on the right and left side of a potential barrier: $\Psi_L^{(+)}, \Psi_L^{(-)}, \Psi_R^{(+)}, \Psi_R^{(-)}$. The scattering matrix (S-matrix) relates the incoming (with respect to the barrier) to the outgoing states [30]

$$\Psi_{\text{out}} = \begin{pmatrix} \Psi_L^{(-)} \\ \Psi_R^{(+)} \end{pmatrix} = \begin{pmatrix} r & \tilde{t} \\ t & \tilde{r} \end{pmatrix} \begin{pmatrix} \Psi_L^{(+)} \\ \Psi_R^{(-)} \end{pmatrix} = S\,\Psi_{\text{in}}, \tag{1.46}$$

where r is reflection amplitude ($|r|^2$ - reflection probability), t - transmission amplitude. Due to the conservation of probability in the scattering process $|\Psi_{\text{out}}|^2 = |\Psi_{\text{in}}|^2$, any scattering matrix satisfies the unitarity condition

$$S^\dagger S = \mathbb{1}. \tag{1.47}$$

The unitarity condition implies for the determinant of S that

$$\det S = e^{i\theta} = r\tilde{r} - t\tilde{t}. \tag{1.48}$$

From these conditions for amplitudes $\tilde{r}, \tilde{t}$ one can derive

$$\tilde{r} = r^* e^{i\theta}, \quad \tilde{t} = -t^* e^{i\theta}, \tag{1.49}$$

or

$$|r|^2 + |t|^2 = 1, \quad \tilde{r}/r^* = -\tilde{t}/t^*. \tag{1.50}$$

In the case of several channels or when the states $\Psi_{L/R}^{(+/-)}$ have internal degrees of freedom like spin, the S-matrix consists of block matrices: $r, \tilde{r}$ - reflection matrices, $t, \tilde{t}$ - transition matrices. In this case, the off-diagonal elements in the block matrices signal that the scattering causes, for instance, transitions between different channels or mixing of spins.

1.5.2 Transfer matrix

While the scattering matrix provides the relation between the incoming and outgoing states, the transfer matrix relates the envelopes on the left and right sides of the barrier. Rewriting equation (1.46) for the S-matrix, one derives

$$\begin{pmatrix} \Psi_L^{(+)} \\ \Psi_L^{(-)} \end{pmatrix} = \begin{pmatrix} 1/t & -\tilde{r}/t \\ r/t & \tilde{t} - r\tilde{r}/t \end{pmatrix} \begin{pmatrix} \Psi_R^{(+)} \\ \Psi_R^{(-)} \end{pmatrix} = T \begin{pmatrix} \Psi_R^{(+)} \\ \Psi_R^{(-)} \end{pmatrix}. \tag{1.51}$$

Using relations (1.49, 1.50) for amplitudes $\tilde{r}, \tilde{t}$ we derive for the T-matrix

$$T = \begin{pmatrix} 1/t & -\tilde{r}/t \\ r/t & 1/\tilde{t}^* \end{pmatrix}. \tag{1.52}$$

The transfer matrix can be constructed from the stationary Schrödinger equation in the following way [60]: we consider a stationary eigenvalue problem

$$H(x)\Psi(x) = E\Psi(x), \tag{1.53}$$

where $H(x)$ is a differential operator in x, $\Psi(x)$ - multicomponent spinor. Since here we consider BdG-type equations, $H(x)$ contains only a first-order derivative, and we can rearrange the equation to the form

$$\frac{d}{dx}\Psi(x) = \mathcal{K}(x, E)\Psi(x). \tag{1.54}$$

Formal integration gives

$$\Psi(x_2) = \mathcal{T} \exp\left(\int_{x_1}^{x_2} \mathcal{K}(x', E) dx' \right) \Psi(x_1), \tag{1.55}$$

where $\mathcal{T}$ denotes spatial ordering (analogically to the time ordering). Denoting the spatially ordered integral

$$T(x_2, x_1; E) \equiv \mathcal{T} \exp\left(\int_{x_1}^{x_2} \mathcal{K}(x', E) dx' \right), \tag{1.56}$$

as the transfer matrix, one obtains the relation between the states at different x-points $x_2 > x_1$:

$$\Psi(x_2) = T(x_2, x_1; E)\Psi(x_1). \tag{1.57}$$

1.6 Green's function method

The Green's function (GF) in condensed matter is fundamentally a correlation function. In simple words, it gives a mathematical description of how the presence (or absence) of a particle at one point in space-time is correlated with the presence (or absence) of particles at other points. It captures both quantum and statistical correlations, including the effects of interactions. There are many "species" of the GFs, each of which is better suited to one or another physical situation (equilibrium or non-equilibrium, zero or finite temperature, real or imaginary time formalism), and provides different information about the system. Green's function methods for condensed matter theory are described in sources [61, 62].

1.6.1 Green's functions in Heisenberg picture

The GF method is typically formulated in the Heisenberg or interaction pictures. It can also be formulated in the Schrödinger picture; however, this is inconvenient for calculations, since the Schrödinger picture is primarily used for wavefunction evolution, while the GF describes correlations between operators.

In the Heisenberg picture, the time dependence is carried by the operators. The Heisenberg operators are defined as

$$\hat{\psi}(x,t) = e^{iHt}\hat{\psi}(x)e^{-iHt}, \tag{1.58}$$

where H - the Hamiltonian of the system.

We will encounter the following types of GFs throughout this thesis:

- real-time single-particle GF:

$$G(x,t;x',t') = -i\langle\, \mathcal{T}\hat{\psi}(x,t)\hat{\psi}^\dagger(x',t')\,\rangle, \tag{1.59}$$

  with $\mathcal{T}$ - time ordering operator and $\langle ... \rangle$ denotes the thermal average

$$\langle\hat{O}\rangle = \frac{\mathrm{Tr}[e^{-\beta H}\hat{O}]}{\mathrm{Tr}[e^{-\beta H}]} = \frac{\mathrm{Tr}[e^{-\beta H}\hat{O}]}{Z}, \tag{1.60}$$

  where Z is the partition function. The Fourier transform of the real-time single-particle GF is given by

$$G(x,x';\omega) = \int_{-\infty}^{\infty} dt\, G(x,t-t';x',0)e^{i\omega(t-t')}, \tag{1.61}$$

  if the system is translationally invariant in time (stationary), and therefore $G(x,t;x',t') = G(x,t-t';x',0)$. This is usually the case in equilibrium, for time-independent Hamiltonians.

- retarded GF:

$$G^R(x,t;x',t') = -i\theta(t-t')\langle\{\hat{\psi}(x,t),\hat{\psi}^\dagger(x',t')\}\rangle, \tag{1.62}$$

  where $\{...\}$ denotes the anticommutator of two operators. It should be noted that in the retarded GF, the Heaviside theta function ensures causality: the response of the system at time t depends only on the earlier times. When performing the Fourier transform to the frequency domain, with non-interacting GF $G^R(t) \sim -i\theta(t)e^{-iHt}$, the theta function results in the infinitesimal imaginary shift $i0^+$:

$$G^R(\omega) = \int_{-\infty}^{\infty} dt\, e^{i\omega t}G^R(t) = \frac{1}{\omega - H + i0^+}. \tag{1.63}$$

  This shift ensures the convergence of the integral and ensures causality.

$$G^A(x,t;x',t') = i\theta(t'-t)\langle\{\hat{\psi}(x,t),\hat{\psi}^\dagger(x',t')\}\rangle. \tag{1.64}$$

  Similarly, as for the retarded GF, when performing the Fourier transform, one introduces an infinitesimal imaginary shift $-i0^+$. Then $G^A(\omega) = (G^R(\omega))^*$.

- imaginary-time Matsubara (thermal) GF:

$$G(x,\tau;x',\tau') = -\langle\, \mathcal{T}_\tau\hat{\psi}(x,\tau)\hat{\psi}^\dagger(x',\tau')\,\rangle, \quad \tau = it \in [0,\beta), \tag{1.65}$$

where $\mathcal{T}_\tau$ is time ordering along the imaginary time axis, and the time-dependent operators are defined as

$$\hat{\psi}(x,\tau) = e^{\tau H}\hat{\psi}(x)e^{-\tau H}, \quad \hat{\psi}^\dagger(x,\tau) = e^{\tau H}\hat{\psi}^\dagger(x)e^{-\tau H} \tag{1.66}$$

Note that with this definition $\psi^\dagger(x,\tau) \neq (\hat{\psi}(x,\tau))^\dagger$. The fermionic Matsubara GF satisfies the antiperiodic boundary condition $G(\tau+\beta) = -G(\tau)$. Since the thermal GF is defined on a bounded domain $\tau \in [0,\beta)$, its Fourier transform is defined only on the discrete frequencies. For the fermionic case $\omega_n = (2n+1)\pi T$, ensure the correct boundary condition. The relation between the time-dependent Matsubara GF and the Fourier transformed to the fermionic Matsubara frequencies GF (for the time translationally invariant system) is given by

$$G(x,x';\omega_n) = \int_0^\beta d\tau\, e^{i\omega_n\tau} G(x,\tau;x',0), \tag{1.67}$$

$$G(x,\tau;x',0) = \frac{1}{\beta}\sum_n e^{-i\omega_n\tau} G(x,x';\omega_n) \tag{1.68}$$

There are also other types of GFs, such as greater/lesser and contour GFs; however, they will not be used in this thesis.

1.6.2 Analytical properties

The analytic structure of the Green's function provides a lot of important information about the physical system. The poles of the retarded GF in the frequency representation $G^R(\omega)$ correspond to the single-particle excitation energies $\omega = E_k - i0^+$. While the branch cuts occur for continua of excitations (e.g., Bogoliubov quasiparticle continua $|E| > \Delta$), where the spectrum is continuous instead of discrete.

As one can see from the denominator of the frequency representation of the retarded GF (1.63), it has poles in the lower half-plane of complex ω, and it is analytic in the upper half-plane. The opposite holds for the advanced GF: it has poles in the upper half-plane and is analytical in the lower half-plane. The retarded and advanced GFs in the frequency space can be obtained from the Matsubara GF by the analytic continuation: $i\omega_n \to \omega + i0^+$ gives $G^R(\omega)$, $i\omega_n \to \omega - i0^+$ gives $G^A(\omega)$.

1.6.3 Path integral representation

Expressing the partition function and Green's functions in terms of path integrals is one of the most elegant formulations of many-body quantum theory. One starts with the grand-canonical partition function

$$Z = \mathrm{Tr}\, e^{-\beta(H-\mu N)}. \tag{1.69}$$

Using coherent states (here, fermionic) and Trotter factorization (time slicing), Z can be rewritten as a path integral over Grassmann fields $\psi(\tau), \bar{\psi}(\tau)$:

$$Z = \int \mathcal{D}[\bar{\psi},\psi]\, e^{-S[\bar{\psi},\psi]}, \tag{1.70}$$

with S - Euclidean action in imaginary time, given by

$$S[\bar{\psi},\psi] = \int_0^\beta d\tau \left[\sum_\alpha \bar{\psi}_\alpha(\tau)\partial_\tau\psi_\alpha(\tau) + H(\bar{\psi},\psi) - \mu N(\bar{\psi},\psi)\right], \tag{1.71}$$

where index α labels the single-particle states. In the path-integral representation, the Matsubara GF, defined by equation (1.65), becomes

$$G(x,\tau;x',\tau') = \int \mathcal{D}[\bar{\psi},\psi]\,\psi(x,\tau)\bar{\psi}(x',\tau')\,e^{-S[\bar{\psi},\psi]}. \tag{1.72}$$

In the case of a quadratic non-interacting system, the action is given by

$$S[\bar{\psi},\psi] = \sum_{i,j}\bar{\psi}_i\,G^{-1}_{i,j}\,\psi_j. \tag{1.73}$$

The partition function becomes

$$Z = \int \mathcal{D}[\bar{\psi},\psi]\,e^{-\sum_{i,j}\bar{\psi}_i\,G^{-1}_{i,j}\,\psi_j} = \int \prod_i d\bar{\psi}_i d\psi_i\,e^{-\sum_{i,j}\bar{\psi}_i\,G^{-1}_{i,j}\,\psi_j} = \det G^{-1}. \tag{1.74}$$

1.6.4 Partition function in the interaction picture

In the case when the Hamiltonian of the system consists of the free part and interacting part $H = H_0 + H_{\text{int}}$, it is convenient to go to the interaction picture. The time evolution of the operators is provided by the free part of the Hamiltonian:

$$\mathcal{O}(\tau) = e^{\tau H_0}\mathcal{O}e^{-\tau H_0}, \quad \bar{\mathcal{O}}(\tau) = e^{\tau H_0}\mathcal{O}^\dagger e^{-\tau H_0}. \tag{1.75}$$

In this case the $e^{-\beta H}$ reads

$$e^{-\beta H} = e^{-\beta H_0}\mathcal{T}_\tau \exp\left(-\int_0^\beta d\tau\, H_{\text{int}}(\tau)\right), \quad H_{\text{int}}(\tau) = e^{\tau H_0}H_{\text{int}}e^{-\tau H_0}. \tag{1.76}$$

Then the partition function becomes

$$Z = \text{Tr}\,e^{-\beta H} = \text{Tr}\left[e^{-\beta H_0}\mathcal{T}_\tau \exp\left(-\int_0^\beta d\tau\, H_{\text{int}}(\tau)\right)\right]. \tag{1.77}$$

At this point, if H_{int} is small compared to H_0, and the expansion of $\exp\left(-\int_0^\beta d\tau\, H_{\text{int}}(\tau)\right)$ converges reasonably (each next term - next order in the interaction is smaller than the previous one), perturbation theory can be applied. One performs a formal expansion of the exponent in the partition function:

$$Z = Z_0\sum_{n=0}^{\infty}\frac{(-1)^n}{n!}\int_0^\beta d\tau_1 \ldots \int_0^\beta d\tau_n\,\langle\mathcal{T}_\tau\,H_{\text{int}}(\tau_1)\ldots H_{\text{int}}(\tau_n)\rangle_0, \tag{1.78}$$

with $Z_0 = e^{-\beta H_0}$ and $\langle\mathcal{O}\rangle_0$ - thermal average with respect to the non=interacting Hamiltonian

$$\langle\mathcal{O}\rangle_0 = \frac{1}{Z_0}\text{Tr}\left(e^{-\beta H_0}\mathcal{O}\right). \tag{1.79}$$

Further, one applies Wick's theorem to the many-body correlator, replacing it by a sum over all pairwise contractions - time-ordered thermal average of two operators, which, in different words, is basically a Matsubara Green's function.

1.6.5 Description of ABSs in SNS junction

To illustrate the GF approach, we derive the GF of a spin-degenerate single-level quantum dot, tunnel-coupled to two superconducting leads. The dot has two basis states

$$n = 1 = \uparrow, \tag{1.80}$$

$$n = 2 = \downarrow, \tag{1.81}$$

with energy ε. The dot Hamiltonian is given by

$$H_{\text{dot}} = \varepsilon\, \bar{c}\tau_z c, \quad c = \begin{pmatrix} c_1 \\ \bar{c}_2 \end{pmatrix} = \begin{pmatrix} c_\uparrow \\ \bar{c}_\downarrow \end{pmatrix}. \tag{1.82}$$

The leads are described by the leads Matsubara Green's function

$$g(\tau) = -\langle \mathcal{T}_\tau \psi_j(\tau)\bar{\psi}_j(0)\rangle, \quad \psi_j = \begin{pmatrix} \psi_{j,\uparrow} \\ \bar{\psi}_{j,\downarrow} \end{pmatrix}. \tag{1.83}$$

In the frequency representation, the GF has the form

$$g(\omega) = -\pi\nu_F \frac{i\omega + \Delta\tau_x}{\sqrt{\omega^2 + \Delta^2}}. \tag{1.84}$$

Here ψ_j with $j = L/R$ is the Nambu spinor of the j-th superconducting lead, and c is the Nambu spinor describing the dot.

The tunnelling amplitudes between the quantum dot and the superconducting lead can be written as a 2×2 matrix

$$\hat{t} = \begin{pmatrix} t_{\uparrow\uparrow} & t_{\downarrow\uparrow} \\ t_{\uparrow\downarrow} & t_{\downarrow\downarrow} \end{pmatrix}, \tag{1.85}$$

where $t_{\sigma\sigma}$ is a tunnelling amplitude of a spin-up quasiparticle of the lead into the corresponding spin component of the dot, where no spin mixing happens; $t_{\sigma\sigma'}$ is the tunnelling amplitude with spin mixing. Here, we assume the spin is conserved during tunnelling (no spin-orbit or Zeeman field present) and that the tunnelling is spin-independent, so that the tunnelling matrix of the j-th lead is given by

$$\hat{t}_j = \begin{pmatrix} t_{j\uparrow} & 0 \\ 0 & t_{j\downarrow} \end{pmatrix} = \begin{pmatrix} t_j & 0 \\ 0 & t_j \end{pmatrix}. \tag{1.86}$$

Note that this matrix is in the spin-level space, and, for brevity, can be written as $t_{j,n\sigma} = t_j(\delta_{n1}\delta_{\sigma\uparrow} + \delta_{n2}\delta_{\sigma\downarrow})$.

Tunnelling between the leads and the dot is described by the tunnelling Hamiltonian:

$$H_{\text{tun}} = \sum_{j=L,R} \left(\bar{\psi}_j T_j c + \text{h.c.}\right), \quad T_j = t_j \tau_z e^{i\tau_z \varphi_j/2}, \tag{1.87}$$

with the superconducting phases $\varphi_R = \varphi/2,\ \varphi_L = -\varphi/2$ for right and left leads.

The partition function of this system is given by

$$Z = \int \mathcal{D}[\bar{\psi}_j, \psi_j, \bar{c}, c]\, e^{-S[\bar{\psi}_j,\psi_j,\bar{c},c]}, \tag{1.88}$$

$$S = \int_0^\beta d\tau \int_0^\beta d\tau' \left(\sum_{j=L,R} \bar{\psi}_j(\tau)\, g^{-1}(\tau-\tau')\psi_j(\tau') + \bar{c}(\tau)\, G_0^{-1}(\tau-\tau')c(\tau') \right. \tag{1.89}$$

$$\left. + \sum_{j=L,R} \left(\bar{\psi}_j(\tau)\, T_j\, \delta(\tau-\tau')\, c(\tau') + \text{h.c.}\right) \right). \tag{1.90}$$

The inverse free dot Green's function in the frequency representation is given by

$$G_0^{-1}(\omega) = i\omega - \epsilon\tau_z. \tag{1.91}$$

The Lagrangian equations of motion for the operators $\bar{\psi}_j$, $\bar{c}$ give the following system of equations (in the frequency representation):

$$\begin{cases} g^{-1}\psi_j + T_j c = 0, \\ G_0^{-1} c + \sum_j T_j^\dagger \psi_j = 0. \end{cases} \tag{1.92}$$

From this system of equations, by expressing the lead Nambu spinor ψ_j through the dot Nambu spinor, one derives the Dyson equation for the Green's function of the dot coupled to the superconducting leads

$$G^{-1}(\omega) = G_0^{-1}(\omega) + \sum_j T_j^\dagger g(\omega) T_j. \tag{1.93}$$

After inserting the free Green's functions of the dot and leads, and the tunnelling matrix T_j, one arrives at the equation

$$G^{-1}(\omega) = i\omega - \varepsilon\tau_z + \frac{\Gamma}{\sqrt{\omega^2+\Delta^2}}\left[i\omega - \Delta\left(\cos\frac{\varphi}{2}\tau_x + \lambda\sin\frac{\varphi}{2}\tau_y\right)\right], \tag{1.94}$$

with $\Gamma = \Gamma_L + \Gamma_R$, $\lambda = (\Gamma_L - \Gamma_R)/\Gamma$ and $\Gamma_j = \pi\nu_F t_j^2$. Now, when we integrated out the leads, the partition function of the dot can be written in terms of the full GF of the dot as

$$Z = \int \mathcal{D}[\bar{c}, c]\, e^{-\int d\omega\, \bar{c}(\omega) G^{-1}(\omega) c(\omega)} = \prod_\omega \det G^{-1}(\omega). \tag{1.95}$$

From the expression $Z = e^{-\beta F}$ we can derive the free energy as

$$F = -\frac{1}{\beta}\sum_\omega \ln\det G^{-1}(\omega). \tag{1.96}$$

With this, we can determine the Josephson current through the dot:

$$I(\varphi) = 2\frac{\partial F}{\partial\varphi.} \tag{1.97}$$

We can analyse the dot GF (1.94) in the atomic limit $\Delta \to \infty$, to get the analytical expression for the energies of the ABSs in this limit. The GF becomes

$$G_{\mathrm{AL}}^{-1}(\omega) = i\omega - \varepsilon\tau_z - \Gamma\left(\cos\frac{\varphi}{2}\tau_x + \lambda\sin\frac{\varphi}{2}\tau_y\right). \tag{1.98}$$

From the condition for the single-particle states $\det G_{\mathrm{AL}}^{-1}(\omega) \stackrel{!}{=} 0$ we can find

$$\det G_{\mathrm{AL}}^{-1}(\omega) = (i\omega)^2 - E_A^2, \tag{1.99}$$

with

$$E_A = \sqrt{\varepsilon^2 + \Gamma^2\left(\cos^2\frac{\varphi}{2} + \lambda^2\sin^2\frac{\varphi}{2}\right)} = \tilde{\Delta}\sqrt{1 - \widetilde{\mathcal{T}}\sin^2\frac{\varphi}{2}}, \tag{1.100}$$

$$\tilde{\Delta} = \sqrt{\varepsilon^2+\Gamma^2}, \quad \widetilde{\mathcal{T}} = \frac{(1-\lambda^2)\Gamma^2}{\varepsilon^2+\Gamma^2} \in [0,1], \tag{1.101}$$

where $\tilde{\Delta}$ is the atomic limit gap and $\widetilde{\mathcal{T}}$ is the effective transparency of the junction. In this case, there are no continuum states present in the Green's function, due to the $\Delta \to \infty$ limit.

References

[1] B.D. Josephson. "Possible new effects in superconductive tunnelling". In: *Physics Letters* 1 (1962). URL: https://www.sciencedirect.com/science/article/pii/0031916362913690.

[2] P. W. Anderson and J. M. Rowell. "Probable Observation of the Josephson Superconducting Tunneling Effect". In: *Phys. Rev. Lett.* 10 (Mar. 1963). URL: https://link.aps.org/doi/10.1103/PhysRevLett.10.230.

[3] Michel H. Devoret et al. "Resonant Activation from the Zero-Voltage State of a Current-Biased Josephson Junction". In: *Phys. Rev. Lett.* 53 (Sept. 1984). URL: https://link.aps.org/doi/10.1103/PhysRevLett.53.1260.

[4] A. F. Andreev. "Thermal Conductivity of the Intermediate State in Superconductors". In: *Sov. Phys. JETP, 19, 1228* (1964).

[5] L. Bretheau et al. "Supercurrent Spectroscopy of Andreev States". In: *Phys. Rev. X* 3 (Dec. 2013). URL: https://link.aps.org/doi/10.1103/PhysRevX.3.041034.

[6] C. Janvier et al. "Coherent manipulation of Andreev states in superconducting atomic contacts". In: *Science* 349 (2015). URL: https://www.science.org/doi/abs/10.1126/science.aab2179.

[7] M. Hays et al. "Coherent manipulation of an Andreev spin qubit". In: *Science* 373 (2021). URL: https://www.science.org/doi/abs/10.1126/science.abf0345.

[8] Elsa Prada et al. "From Andreev to Majorana bound states in hybrid superconductor-semiconductor nanowires". In: *Nature Reviews Physics* 2 (Oct. 2020). DOI: 10.1038/s42254-020-0228-y.

[9] R. Seoane Souto, A. Martín-Rodero, and A. Levy Yeyati. "Andreev Bound States Formation and Quasiparticle Trapping in Quench Dynamics Revealed by Time-Dependent Counting Statistics". In: *Phys. Rev. Lett.* 117 (Dec. 2016). URL: https://link.aps.org/doi/10.1103/PhysRevLett.117.267701.

[10] A. Zazunov et al. "Quasiparticle trapping, Andreev level population dynamics, and charge imbalance in superconducting weak links". In: *Phys. Rev. B* 90 (Sept. 2014). URL: https://link.aps.org/doi/10.1103/PhysRevB.90.104508.

[11] A. Higginbotham et al. "Parity lifetime of bound states in a proximitized semiconductor nanowire". In: *Nature Physics* 11 (Jan. 2015). DOI: 10.1038/nphys3461.

[12] L. N. Cooper J. Bardeen and J. R. Schrieffer. "Microscopic Theory of Superconductivity". In: *Phys. Rev. 106.1* (Apr. 1957). ISSN: 1536-6065. DOI: 10.1103/PhysRev.106.162.

[13] L. N. Cooper J. Bardeen and J. R. Schrieffer. "Theory of Superconductivity". In: *Phys. Rev. 108.5* (Dec. 1957). ISSN: 1536-6065. DOI: 10.1103/PhysRev.108.1175.

[14] Michael Tinkham. *Introduction to superconductivity*. 2nd ed. McGraw Hill, 1996.

[15] P.G. De Gennes. *Superconductivity Of Metals And Alloys*. New York, W.A. Benjamin, 1966.

[16] Yukio Tanaka and Satoshi Kashiwaya. "Theory of Tunneling Spectroscopy of *d*-Wave Superconductors". In: *Phys. Rev. Lett.* 74 (Apr. 1995). DOI: 10.1103/PhysRevLett.74.3451.

[17] Sankar Das Sarma, Michael Freedman, and Chetan Nayak. "Majorana Zero Modes and Topological Quantum Computation". In: *npj Quantum Information* 1 (Jan. 2015). DOI: 10.1038/npjqi.2015.1.

[18] Leon N. Cooper. "Bound Electron Pairs in a Degenerate Fermi Gas". In: *Phys. Rev.* 104 (Nov. 1956). DOI: 10.1103/PhysRev.104.1189.

[19] N. N. Bogoliubov. "A New Method in the Theory of Superconductivity". In: *Sov. Phys. JETP* 7 (1958).

[20] Y. Nambu and G. Jona-Lasinio. "Dynamical Model of Elementary Particles Based on an Analogy with Superconductivity. I". In: *Phys. Rev.* 122 (Apr. 1961). DOI: 10.1103/PhysRev.122.345.

[21] Y. Nambu. "Quasi-Particles and Gauge Invariance in the Theory of Superconductivity". In: *Phys. Rev.* 117 (1960). DOI: 10.1103/PhysRev.117.648.

[22] L. P. Gorkov. "On the Energy Spectrum of Superconductors". In: *Soviet Physics JETP* 7 (Sept. 1958).

[23] Martin R. Zirnbauer. "Particle–hole symmetries in condensed matter". In: *Journal of Mathematical Physics* 62 (Feb. 2021). DOI: 10.1063/5.0035358.

[24] Max Geier, Piet W. Brouwer, and L. Trifunovic. "Symmetry-based indicators for topological Bogoliubov-de Gennes Hamiltonians". In: *Phys. Rev. B* 101 (June 2020). DOI: 10.1103/PhysRevB.101.245128.

[25] A. Y. Kitaev. "Unpaired Majorana fermions in quantum wires". In: *Physics-Uspekhi* 44 (Oct. 2001). URL: https://doi.org/10.1070/1063-7869/44/10S/S29.

[26] Pasquale Marra. "Majorana nanowires for topological quantum computation". In: (Nov. 2022). DOI: 10.48550/arXiv.2206.14828.

[27] Tudor Stanescu and S Tewari. "Majorana fermions in semiconductor nanowires: Fundamentals, modeling, and experiment". In: *Journal of physics. Condensed matter : an Institute of Physics journal* 25 (May 2013). DOI: 10.1088/0953-8984/25/23/233201.

[28] Ramon Aguado. "Majorana quasiparticles in condensed matter". In: *Rivista del Nuovo Cimento* 40 (Oct. 2017). DOI: 10.1393/ncr/i2017-10141-9.

[29] Elsa Prada et al. "From Andreev to Majorana bound states in hybrid superconductor–semiconductor nanowires". In: *Nature Reviews Physics* 2 (Sept. 2020). DOI: 10.1038/s42254-020-0228-y.

[30] Yuli V. Nazarov and Yaroslav M. Blanter. In: *Quantum Transport: Introduction to Nanoscience*. Cambridge University Press, 2009.

[31] Sauls J. A. "Andreev bound states and their signatures". In: *Phil. Trans. R. Soc. A.37620180140* (2018). DOI: 10.1098/rsta.2018.0140.

[32] M. J. M. de Jong and C. W. J. Beenakker. "Andreev Reflection in Ferromagnet-Superconductor Junctions". In: *Phys. Rev. Lett.* 74 (Feb. 1995). DOI: 10.1103/PhysRevLett.74.1657.

[33] Jean-Damien Pillet et al. "Andreev bound states in supercurrent-carrying carbon nanotubes revealed". In: *Nature Physics* 6 (May 2010), p. 695. DOI: 10.1038/nphys1811.

[34] C. Caroli, P.G. De Gennes, and J. Matricon. "Bound Fermion states on a vortex line in a type II superconductor". In: *Physics Letters* 9 (1964). DOI: https://doi.org/10.1016/0031-9163(64)90375-0.

[35] Hiroyuki Shiba. "Classical Spins in Superconductors". In: *Progress of Theoretical Physics* 40 (Sept. 1968). URL: https://doi.org/10.1143/PTP.40.435.

[36] L Yu. "Bound state in superconductors with paramagnetic impurities". In: *Acta Phyica Sinica* 21 (Dec. 1964). URL: https://www.osti.gov/biblio/4638963.

[37] A I Rusinov. "Superconductivity near a paramagnetic impurity". In: *JETP Lett.* (Dec. 1968). URL: https://www.osti.gov/biblio/4780988.

[38] Chia-Ren Hu. "Midgap surface states as a novel signature for d^2_{xa}-x^2_b-wave superconductivity". In: *Phys. Rev. Lett.* 72 (Mar. 1994). DOI: 10.1103/PhysRevLett.72.1526.

[39] Liang Fu and C. L. Kane. "Superconducting Proximity Effect and Majorana Fermions at the Surface of a Topological Insulator". In: *Phys. Rev. Lett.* 100 (Mar. 2008). DOI: 10.1103/PhysRevLett.100.096407.

[40] Sarah Pinon, Vardan Kaladzhyan, and Cristina Bena. "Modeling long imperfect SNS junctions and Andreev bound states using two impurities and the T-matrix formalism". In: *Phys. Rev. B* 101 (May 2020). DOI: 10.1103/PhysRevB.101.205136.

[41] Edouard Sonin. "Andreev reflection, Andreev states, and long ballistic SNS junction". In: *Journal of Low Temperature Physics* 217 (June 2024). DOI: 10.1007/s10909-024-03137-7.

[42] Jens Koch et al. "Charge-insensitive qubit design derived from the Cooper pair box". In: *Physical Review A* 76 (2007). URL: https://api.semanticscholar.org/CorpusID:53983107.

[43] J. A. Schreier et al. "Suppressing Charge Noise Decoherence in Superconducting Charge Qubits". In: *Physical Review B* 77 (2007). URL: https://api.semanticscholar.org/CorpusID:119181860.

[44] T. P. Orlando et al. "Superconducting persistent-current qubit". In: *Phys. Rev. B* 60 (Dec. 1999). URL: https://link.aps.org/doi/10.1103/PhysRevB.60.15398.

[45] M. Devoret, Andreas Wallraff, and J.M. Martinis. "Superconducting Qubits: A Short Review". In: (Dec. 2004).

[46] Lucas Casparis et al. "Superconducting Gatemon Qubit based on a Proximitized Two-Dimensional Electron Gas". In: *Nature Nanotechnology* 13 (Oct. 2018). DOI: 10.1038/s41565-018-0207-y.

[47] Hanhee Paik et al. "Observation of High Coherence in Josephson Junction Qubits Measured in a Three-Dimensional Circuit QED Architecture". In: *Phys. Rev. Lett.* 107 (Dec. 2011). URL: https://link.aps.org/doi/10.1103/PhysRevLett.107.240501.

[48] Alexandre Blais et al. "Circuit quantum electrodynamics". In: *Rev. Mod. Phys.* 93 (May 2021). URL: https://link.aps.org/doi/10.1103/RevModPhys.93.025005.

[49] A. Somoroff et al. "Millisecond Coherence in a Superconducting Qubit". In: *Phys. Rev. Lett.* 130 (June 2023). DOI: 10.1103/PhysRevLett.130.267001.

[50] J. Clarke and A.I. Braginski. *The SQUID handbook: Fundamentals and technology of SQUIDs and SQUID systems*. Vol. 1. Wiley VCH, 2004.

[51] K. Likharev, O. Mukhanov, and V Semenov. "Resistive Single Flux Quantum Logic for the Josephson- Junction Digital Technology". In: (Jan. 1985).

[52] K. Nakajima et al. "Experimental analysis of phase-mode Josephson digital circuits". In: *Journal of Applied Physics* 66 (July 1989).

[53] R. McDermott et al. "Quantum–Classical Interface Based on Single Flux Quantum Digital Logic". In: *Quantum Science and Technology* 3 (Jan. 2018). DOI: 10.1088/2058-9565/aaa3a0.

[54] Yosuke Ueno et al. "C3-VQA: Cryogenic Counter-Based Coprocessor for Variational Quantum Algorithms". In: *IEEE Trans. Quantum Eng.* 6 (2025). DOI: 10.1109/TQE.2024.3521442.

[55] Chuanhong Liu et al. "Single Flux Quantum-Based Digital Control of Superconducting Qubits in a Multichip Module". In: *PRX Quantum* 4 (July 2023). DOI: 10.1103/PRXQuantum.4.030310.

[56] Margarita Davydova, Saranesh Prembabu, and Liang Fu. "Universal Josephson diode effect". In: (Jan. 2022). DOI: 10.48550/arXiv.2201.00831.

[57] Noah Yuan and Liang Fu. "Supercurrent diode effect and finite-momentum superconductors". In: *Proceedings of the National Academy of Sciences* 119 (Apr. 2022). DOI: 10.1073/pnas.2119548119.

[58] A. Zazunov et al. "Nonreciprocal charge transport and subharmonic structure in voltage-biased Josephson diodes". In: *Phys. Rev. B* 109 (Jan. 2024). DOI: 10.1103/PhysRevB.109.024504.

[59] In: *Physics and Applications of the Josephson Effect*. John Wiley Sons, Ltd, 1982. ISBN: 9783527602780. DOI: https://doi.org/10.1002/352760278X.

[60] Costas M. Soukoulis Peter Markoš. *Wave Propagation: From Electrons to Photonic Crystals and Left-Handed Materials*. Princeton University Press, 2008.

[61] A. L. Fetter and J. D. Walecka. *Quantum Theory of Many-Particle Systems*. Boston: McGraw-Hill, 1971.

[62] A. A. Abrikosov et al. *Methods of quantum field theory in statistical physics*. New York: Dover, 1975.

2 Dynamical parity stabilization in Josephson junctions with spin symmetry breaking

This chapter is based on the content of the author's publication *Many-body quantum dynamics of spin-orbit coupled Andreev states in a Zeeman field*, Phys.Rev.B 109 (2024) 21, 214505, which is adapted and extended for the purposes of the thesis.

2.1 Introduction

Recently, advances in the fabrication techniques resulted in availability of the high-quality hybrid nanowires that realize Josephson junctions (e.g. semiconducting InAs wires with a superconducting Al shell), with just a few transport channels of high transmission probability [1–20]. As discussed in the previous chapter, the Josephson junction hosts ABSs, localized near the weak link between the superconducting banks, with phase-dependent energy levels below the superconducting gap. ABSs are considered to be the main carriers of the Josephson current [21–28]. One application of ABSs is their potential use as a platform for quantum computing: a qubit can be encoded by the ABSs [29–33] if the fermion number parity of the Andreev sector (referred to as "parity" below) is preserved on sufficiently long time scales below the parity switching time τ_p. The time scale τ_p describes transitions between states of opposite parity and is generated by a variety of microscopic mechanisms [16, 34–36], such as transitions between ABSs and continuum states above the gap. These transitions are one of the main decoherence mechanisms of the Andreev qubit and, therefore, need to be understood and controlled to achieve longer coherence times. Recent experiments have shown that coherent Andreev qubit manipulations are feasible on time scales of up to $\sim 100\mu$s [3, 7, 9, 11, 16–19].

Dynamical parity stabilization is a technique that allows one to actively suppress or control parity switching so that the qubit remains in a well-defined parity sector [19]. The procedure is the following: initial microwave pulse triggers a transition to a many-body Andreev state of odd or even parity. After the pulse, the system is found to be almost perfectly polarized in the opposite parity sector for times $t \leq \tau_p$.

Currently, the Josephson junctions studied experimentally include nanowires based on materials with strong spin-orbit interactions (SOI), e.g., InAs or InSb. Therefore, Andreev qubits with broken spin symmetry are of particular interest in the context of quantum information processing applications [16–19, 32, 37, 38]. The Andreev spin qubit manipulations are possible through electrostatic gate modulations of the SOI [8, 12, 18, 39], by magnetic flux variations [9, 11], and/or by Zeeman field changes. The combined influence of SOI and weak Zeeman fields is central to the dynamics of ABSs and consequently to the behavior of ABS-based qubits.

Here, we consider weak links of intermediate length $L \approx \xi_0$, with ξ_0 - superconducting coherence length. In this case there are typically four spin-split positive-energy ABSs and nontrivial consequences of the SOI can arise. (In the short-junction limit $L \ll \xi_0$ [40–44], there are only two levels and SOI only result into an energy shift. For the complementary long-junction limit, see, e.g., Refs. [45–47].) Here we consider Josephson junctions with relatively high transparency, where Coulomb interaction effects are strongly suppressed; we therefore neglect interaction effects, but see Refs. [39, 48, 49].

In the articles [38, 39, 50–54] the ABSs dispersion relation and the corresponding wave functions in Josephson junctions with SOI and Zeeman fields were analyzed. Here we study the

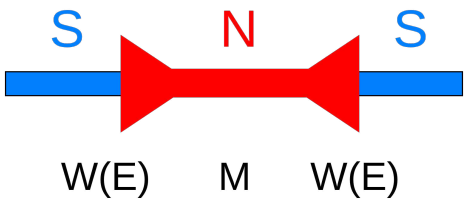

Figure 2.1: The Josephson junction is formed by a ballistic spinful single-channel nanowire of length L between two superconducting banks. At the left and right ends of the wire, boundary states in the respective superconductor and in the wire are coupled by spin- and energy-independent tunneling amplitudes which we assume to be equal. These are encoded by the matrix M. We also include spin-orbit coupling and a constant magnetic Zeeman field in the nanowire, encoded by the matrix $W(E)$. For details, see main text.

nonequilibrium many-body population dynamics in the Andreev sector in the presence of both SOI and Zeeman field. To do this, we derive the master equation governing the population dynamics of the many-body ABSs. We then apply this equation to investigate the effect of SOI and magnetic field on the Andreev population dynamics after an initial microwave pulse. Such a pulse has been shown experimentally [16] and theoretically [34, 35] to allow for dynamical parity polarization over long but finite time scales. In this chapter, we examine how the dynamical parity stabilization is affected by the SOI and the Zeeman field. The analogous case without SOI and magnetic field has been studied in Ref. [34].

The structure of this chapter is as follows. In Sec. 2.2, the model is described. The details on the eigenstates are given in the Appendix. In Sec. 2.3, we derive a Lindblad master equation governing the dynamics of the Andreev sector (under certain assumptions specified below). The diagonal elements of the time-dependent reduced density matrix describing the Andreev sector, which are associated with the population probabilities of many-body Andreev states, obey a matrix rate equation. In Sec. 2.4, we then use this matrix rate equation to study the population dynamics after an initial strong microwave pulse. We compare our results to those of Ref. [34], obtained in the absence of the SOI and the Zeeman field. Here we do not aim for a quantitative comparison to the experiments of Ref. [16]. Instead, our main goal is to provide a conceptual framework for describing the many-body population dynamics in the Andreev sector if both the SOI and a Zeeman field are present. Since in this case it is convenient to work in an augmented spin-right/left movers-Nambu space, one encounters a double-counting problem: the physical degrees of freedom are doubled by the mathematical description. We here show how to overcome the double-counting problem and consistently formulate the Lindblad equation. This formalism is generally applicable for this type of problem, well beyond the specific example discussed in this work. Finally, we conclude with a summary and an outlook in Sec. 2.5.

2.2 Model

In this section, we describe the model used in our study. Particularly, in Sec. 2.2.1, where a spin-orbit coupled Josephson junction is embedded in a superconducting loop coupled to an electromagnetic environment (see the setup discussed in Chapter 1 Fig. 1.3), the Josephson junction is described in terms of the spinors in spin-right/left movers-Nambu space, satisfying the Bogoliubov-de-Gennes equation and coupled by the transfer matrix across the nanowire region. In Sec. 2.2.3, we perform an expansion to the lowest order in the coupling to the bosonic

environment and arrive at the model formulation that allows us to apply Lindblad equation further. Note that throughout this thesis we use units convention with

$$\hbar = e = k_B = 1,$$

unless specified differently.

2.2.1 Description of the Josephson junction with spin-orbit coupling and Zeeman field

Setup description.— The setup is schematically shown in Fig. 1.3 of Chapter 1. We consider a single-channel Josephson junction between two superconductors of conventional s-wave BCS type with the same pairing gap Δ and the same Fermi velocity v_F (the coherence length is then given by $\xi_0 = v_F/\Delta$). The respective order parameter phases are denoted by ϕ_1 and ϕ_2. The weak link of the junction is represented by a ballistic nanowire, with SOI and Zeeman field. The nanowire is tunnel-coupled to the respective ends of the superconducting bulks. The Josephson junction is embedded in the superconducting loop that is threaded by a magnetic flux, imposing the average phase difference $\phi_0 = \phi_1 - \phi_2$ across the Josephson junction. Additionally, the superconducting loop is inductively coupled to a microwave resonator with resonance frequency Ω, that represents the electromagnetic environment.

Superconducting banks.— Within the low-energy quasi-classical approach [27], one describes the superconductors in terms of field envelopes $\Psi_{\alpha,\sigma}(x,t)$ for right- and left-moving ($\alpha = \pm$) electrons with spin $\sigma \in \{\uparrow,\downarrow\}$. The coordinate $x < 0$ ($x > 0$) correspond to the left (right) superconducting lead. We consider only the 1D channel propagating through the junction and perform a low-energy expansion around the Fermi momenta $\pm k_F$. To take into account the SOI and the Zeeman field in the normal region, for right- and left-moving fields, with spin-up and spin-down projection, are collected into a single four-spinor field,

$$\Psi(x,t) = \begin{pmatrix} \Psi_{+,\uparrow} \\ \Psi_{+,\downarrow} \\ \Psi_{-,\uparrow} \\ \Psi_{-,\downarrow} \end{pmatrix}. \tag{2.1}$$

We define an eight-spinor field $\Phi(x,t)$ by employing particle-hole (Nambu) space [55],

$$\Phi(x,t) = \frac{1}{\sqrt{2}} \begin{pmatrix} \Psi(x,t) \\ \tilde{\Psi}^*(x,t) \end{pmatrix}, \tag{2.2}$$

with

$$\tilde{\Psi}(x,t) = \rho_x i\sigma_y \Psi(x,t) = \begin{pmatrix} \Psi_{-,\downarrow} \\ -\Psi_{-,\uparrow} \\ \Psi_{+,\downarrow} \\ -\Psi_{+,\uparrow} \end{pmatrix}. \tag{2.3}$$

We use Pauli matrices $\tau_{x,y,z}$ in Nambu space, $\rho_{x,y,z}$ in right-left mover space, and $\sigma_{x,y,z}$ in spin space. The corresponding identity matrices $(\tau_0, \rho_0, \sigma_0)$ are often kept implicit. The Nambu spinor field in Eq. (2.2) satisfies the reality constraint

$$\rho_x \sigma_y \tau_y \Phi(x,t) = \Phi^*(x,t), \tag{2.4}$$

which implies redundancy of the degrees of freedom. Hence, one needs to be careful to avoid double counting problems [55].

With the above definitions, within the low-energy quasi-classical approximation, the superconducting banks are described by a Bogoliubov-de Gennes (BdG) Hamiltonian [27, 34],

$$H(t) = \sum_{j=1,2} \int_{s_j x<0} dx\, \Phi^\dagger(x,t) \Big[\big(-iv_F \rho_z \partial_x + V_j(t)\big)\, \tau_z + \Delta \tau_x e^{i\tau_z \phi_j(t)} \Big] \Phi(x,t), \tag{2.5}$$

$$V_j(t) = \dot{\phi}_j(t)/2$$

where we define

$$s_j = \begin{cases} +1, & \text{for } j = 1 \\ -1, & \text{for } j = 2 \end{cases} .$$

Note that the left superconductor ($j = 1$) corresponds to $x < 0$ and the right one ($j = 2$) to $x > 0$. The boundary Nambu spinor states $\Phi(0^-, t)$ and $\Phi(0^+, t)$ are then tunnel-coupled to the respective ends of the normal wire forming the weak link. We next show that those couplings generate a time- (or energy-)dependent transfer matrix connecting these boundary spinors.

Nanowire.— The weak link representing the junction region is assumed to be a normal-conducting impurity-free one-dimensional (1D) nanowire of length L. This single-channel wire is connected by tunnel couplings at its ends ($x = \mp L/2$) to the respective superconducting bank, see Fig. 2.1.

The single-particle Hamiltonian for the uncoupled and ballistic normal-conducting nanowire, with new coordinates $|x| < L/2$ pertaining to the nanowire, is taken in the form

$$h_N = \frac{\hat{p}^2}{2m} + \gamma_{\rm SO}\, \hat{p}\, \sigma_z + \mathbf{b} \cdot \boldsymbol{\sigma}, \tag{2.6}$$

with an effective mass m and the 1D momentum operator $\hat{p}$. The SOI strength and the Zeeman field are encoded by $\gamma_{\rm SO}$ and the vector $\mathbf{b}$, respectively, where $\boldsymbol{\sigma} = (\sigma_x, \sigma_y, \sigma_z)$. Estimates for $\gamma_{\rm SO}$ for realistic geometries can be found, e.g., in Refs. [8, 54]. We now linearize Eq. (2.6) around the Fermi points in the wire, which are denoted by $\pm k_0$. Using

$$\hat{p} \to \alpha k_0 - i\partial_x,$$

we introduce field operators $\psi_{\alpha,\sigma}(x, E)$ for right- and left-movers ($\alpha = \pm$) in the nanowire with spin $\sigma \in \{\uparrow, \downarrow\}$ and energy E. The second-quantized low-energy Hamiltonian for the nanowire is then given by

$$H_N = \sum_{\alpha=\pm} \int_{-L/2}^{L/2} dx\, \psi_\alpha^\dagger(x) \Big\{ \left[\alpha v_0 + \gamma_{\rm SO} \sigma_z\right] (-i\partial_x) + \alpha \gamma_{\rm SO}\, k_0 \sigma_z + \mathbf{b} \cdot \boldsymbol{\sigma} \Big\} \psi_\alpha(x), \tag{2.7}$$

$$\psi_\alpha = (\psi_{\alpha,\uparrow}, \psi_{\alpha,\downarrow})^T,$$

where $v_0 = k_0/m$ is the Fermi velocity in the wire. Since there is no backscattering inside the nanowire described by Eq. (2.7), the right-left-mover index $\alpha = \pm$ is conserved.

2.2.2 Integrating out the nanowire region: construction of the transfer matrix

In this section we construct the transfer matrix that couples the boundary superconducting leads Nambu spinors across the nanowire with SOI and Zeeman effects. This method allows us to effectively integrate out the nanowire region, and include all the information about the nanowire in the boundary condition of the BdG problem that will be formulated further.

Transfer matrix in spin space, across the nanowire.— First, we connect the boundary spinors $\psi_\alpha(-L/2, E)$ and $\psi_\alpha(+L/2, E)$ by a transfer matrix $W_\alpha(E)$ in spin space across the nanwire

region. From the Hamiltonian, we derive the system of equations for spinor $\psi_\alpha(x,E)$ of the form

$$\partial_x \begin{pmatrix} \psi_{\alpha,\uparrow} \\ \psi_{\alpha,\downarrow} \end{pmatrix} = i\alpha \begin{pmatrix} \frac{E-(b_z+\alpha\gamma_{SO}k_0)}{v_0+\alpha\gamma_{SO}} & -\frac{b_x-ib_y}{v_0+\alpha\gamma_{SO}} \\ -\frac{b_x+ib_y}{v_0-\alpha\gamma_{SO}} & \frac{E+(b_z+\alpha\gamma_{SO}k_F)}{v_0-\alpha\gamma_{SO}} \end{pmatrix} \begin{pmatrix} \psi_{\alpha,\uparrow} \\ \psi_{\alpha,\downarrow} \end{pmatrix}. \tag{2.8}$$

Explicitly, we find

$$\psi_\alpha(-L/2,E) = W_\alpha(E)\,\psi_\alpha(L/2,E), \tag{2.9}$$

$$W_\alpha(E) = B_\alpha \begin{pmatrix} e^{i\lambda_{\alpha,\uparrow}L} & 0 \\ 0 & e^{i\lambda_{\alpha,\downarrow}L} \end{pmatrix} B_\alpha^{-1},$$

where the matrix $B_\alpha(E)$ and the numbers $\lambda_{\alpha,\sigma}(E)$ are found by diagonalizing a matrix resulting from Eq. (2.1),

$$\begin{pmatrix} \frac{b_z+\alpha\gamma_{SO}k_0-E}{\alpha v_0+\gamma_{SO}} & \frac{b_x-ib_y}{\alpha v_0+\gamma_{SO}} \\ \frac{b_x+ib_y}{\alpha v_0-\gamma_{SO}} & \frac{b_z+\alpha\gamma_{SO}k_0+E}{\alpha v_0-\gamma_{SO}} \end{pmatrix} = B_\alpha \begin{pmatrix} \lambda_{\alpha,\uparrow} & 0 \\ 0 & \lambda_{\alpha,\downarrow} \end{pmatrix} B_\alpha^{-1}. \tag{2.10}$$

Below we use the four-spinor field $\psi(x) = (\psi_+,\psi_-)^T$, in analogy to the corresponding definition in the superconducting banks, see Eq. (2.1). Furthermore, we use a 4×4 transfer matrix $W(E)$ which is diagonal in left-right-mover space, $W(E) = \mathrm{diag}[W_+(E), W_-(E)]$.

Transfer matrix in spin-right/left-mover space.— Next we take into account spin-independent tunneling amplitudes connecting the nanowire ends to the corresponding left and right superconducting banks. We assume that the respective contacts have the energy-independent transmission probabilities $\mathcal{T}_1$ and $\mathcal{T}_2$. For simplicity, in what follows, we assume equal transmission probabilities, $\mathcal{T}_1 = \mathcal{T}_2 = \mathcal{T}$. However, the generalization to asymmetric cases poses no conceptual challenge. The corresponding reflection amplitude at each junction is then defined by $r = \sqrt{1-\mathcal{T}}$. At the left contact ($j=1$), the state at the right boundary of the left superconductor, $\Psi(0^-,E)$, and the state at the left end of the nanowire, $\psi(-L/2,E)$, are then matched according to the transfer matrix condition [27, 31, 41]

$$\Psi(0^-,E) = M\psi(-L/2,E), \quad M = \frac{1}{\sqrt{\mathcal{T}}}(\rho_0 + r\rho_x)\sigma_0. \tag{2.11}$$

In our convention the left (right) superconductor has spatial coordinates with $x<0$ ($x>0$), while we use different coordinates with $-L/2 < x < L/2$ for the nanowire. Similarly, at the right contact ($j=2$), we have the condition

$$\psi(L/2,E) = M\Psi(0^+,E). \tag{2.12}$$

Combining Eqs. (2.11) and (2.12) with the transfer matrix $W(E)$ across the normal-conducting nanowire region, we arrive at a matching condition connecting the two superconducting boundary states,

$$\Psi(0^-,E) = T(E)\Psi(0^+,E), \quad T(E) = MW(E)M, \tag{2.13}$$

where $T(E)$ is the full transfer matrix, see Fig. 2.1. In this way, we have effectively integrated out the normal-conducting region.

Transfer matrix in spin-right/left-mover-Nambu space.— The corresponding matching condition for the Nambu spinor states (2.2) is given by

$$\Phi(0^-,E) = \hat{T}(E)\,\Phi(0^+,E), \tag{2.14}$$

$$\hat{T}(E) = \begin{pmatrix} T(E) & 0 \\ 0 & \rho_x\sigma_y T^*(-E)\sigma_y\rho_x \end{pmatrix},$$

where the explicit 2×2 structure of $\hat{T}(E)$ refers to Nambu space. In the time domain, the matching condition (2.14) is equivalently written as

$$\Phi(0^-, t) = \hat{T}(t)\, \Phi(0^+, t). \tag{2.15}$$

Since we focus on the symmetric case $\mathcal{T}_1 = \mathcal{T}_2$, we are free to choose a gauge where the voltage in the normal-conducting region vanishes and the superconducting phases can be written as

$$\phi_j(t) = s_j \phi(t)/2,$$

with $\phi(t)$ - the phase difference across the junction. One then obtains $\hat{T}(t)$ from $\hat{T}(E)$ through the replacement $E \to i\partial_t$ (we assume that the voltage drops at the contacts, so that inside the wire $V = 0$. With this the covariant time-derivative is given by a simple time derivative $E = i\partial_t - V(t)\tau_z = i\partial_t$). Finally, the Nambu spinors obey the normalization condition

$$\int_{-\infty}^{\infty} dx\ |\Phi(x, E)|^2 = 1 - \xi_w(E), \tag{2.16}$$
$$\xi_w(E) = \frac{L}{2} \left(|\Phi(0^-, E)|^2 + |\Phi(0^+, E)|^2 \right).$$

The $\xi_w(E)$ term here arises due to the wave function weight in the normal-conducting region [34].

2.2.3 Expansion of the BdG Hamiltonian in small phase fluctuation

Here we expand the BdG Hamiltonian given by Eq. (2.5) that describes the superconducting leads in the small system-environment coupling.

The phase difference can be written as

$$\phi(t) = \phi_0 + \tilde{\phi}(t), \quad |\tilde{\phi}(t)| \ll 1$$

where the fluctuating phase $\delta\varphi(t)$ due to the microwave resonator is assumed to be a small perturbation. Using the second Josephson relation for the voltage, we perform the Taylor expansion of the BdG Hamiltonian (2.5) to the leading order in the perturbation $\delta\varphi(t)$:

$$V_j(t)\tau_z + \Delta\tau_x e^{i\tau_z s_j \phi_j(t)} = e^{-i\tau_z s_j \phi_0/4} \left[s_j \left(\frac{\dot{\tilde{\phi}}}{4}\tau_z + \Delta\frac{\tilde{\phi}}{2}\tau_y \right) + \Delta\tau_x \right] e^{i\tau_z s_j \phi_0/4} + O(\tilde{\phi}^2).$$

After a global canonical transformation,

$$\Phi(x, t)|_{s_j x < 0} \to e^{-i\tau_z s_j \phi_0/4}\, \Phi(x, t), \tag{2.17}$$

we obtain the Hamiltonian

$$H(t) = H_0 + H_I(t) + H_{\text{env}} + \mathcal{O}(\tilde{\phi}^2), \tag{2.18}$$

where H_{env} describes the electromagnetic environment which is equivalent to a set of harmonic oscillators [27]. The noninteracting ($\delta\varphi = 0$) BdG Hamiltonian is given by

$$H_0 = \sum_{j=1,2} \int_{s_j x < 0} dx\, \Phi^\dagger(x, t) \left[-i v_F \rho_z \tau_z \partial_x + \Delta\tau_x \right] \Phi(x, t), \tag{2.19}$$

and the leading-order interaction term follows as

$$H_I(t) = \sum_j \int_{s_j x < 0} dx\, \Phi^\dagger(x, t)\, \mathrm{sgn}(-x) \left[\frac{\dot{\tilde{\phi}}}{4}\tau_z + \Delta\frac{\tilde{\phi}}{2}\tau_y \right] \Phi(x, t). \tag{2.20}$$

Due to the gauge transformation (2.17), the transfer matrix acquires an additional phase factor. As a result, the final matching condition reads

$$\Phi(0^-, t) = e^{i\tau_z \phi_0/2}\, \hat{T}(E \to i\partial_t)\, \Phi(0^+, t). \tag{2.21}$$

2.2.4 Formulation of the Bogoliubov - de Gennes problem

We consider the above problem, stated by the full system Hamiltonian (2.18), in the interaction picture. The leads Nambu field operator can be written in the form

$$\Phi(x,t) = \sum_{\nu} \Phi_\nu(x)\gamma_\nu(t), \tag{2.22}$$

where $\gamma_\nu(t) = e^{-iE_\nu t}\gamma_\nu$, $\{\gamma_\mu, \gamma_\nu^\dagger\} = \delta_{\mu,\nu}$ are fermionic operators and $\Phi_\nu(x)$ with energy E_ν are the stationary solutions of the BdG problem posed by H_0 in Eq. (2.19) and the matching condition (2.21). Explicitly, with Eq. (2.14), this BdG problem is given by

$$\left[-iv_F\rho_z\tau_z\partial_x + \Delta\tau_x\right]\Phi_\nu(x) = E_\nu\Phi_\nu(x), \tag{2.23}$$

$$\Phi_\nu(0^-) = e^{i\tau_z\phi_0/2}\,\hat{T}(E_\nu)\,\Phi_\nu(0^+). \tag{2.24}$$

As a result, we find

$$H_0 = \sum_{\nu} E_\nu\gamma_\nu^\dagger\gamma_\nu, \tag{2.25}$$

where the index ν includes subgap ABS solutions with $|E_\nu| < \Delta$ as well as quasiparticle continuum states with quantum numbers $\nu = p \equiv (E, s, \sigma)$ where $|E| > \Delta$. The index $s \in \{1,2,3,4\}$ specifies the incoming scattering state type (electron- or hole-type right-/left-mover states), and σ refers to the spin state. Due to the particle-hole symmetry of the BdG Hamiltonian,

$$\mathcal{C}H_0\mathcal{C}^{-1} = -H_0, \quad \mathcal{C} = \sigma_y\tau_y K, \tag{2.26}$$

where K denotes complex conjugation, for every solution with $E_\nu > 0$, we must have a corresponding solution at the opposite energy

$$E_{\bar{\nu}} = -E_\nu, \quad \gamma_{\bar{\nu}} = \gamma_\nu^\dagger, \tag{2.27}$$

with $\gamma_{\bar{\nu}}$ being the corresponding quasiparticle operator. This can be shown by combining Eqs. (2.4) and (2.24), see also Ref. [50]. Using in addition Eq. (2.22), one can derive the operators relation.

Current operator.— In the interaction picture, up to an irrelevant time-derivative term [34], the interaction term (2.20) can be written as

$$H_I(t) = \frac{\tilde{\phi}(t)}{2}\mathcal{I}(t), \tag{2.28}$$

with the Josephson current operator

$$\mathcal{I}(t) = \sum_{\mu\neq\nu} \mathcal{I}_{\mu,\nu}\gamma_\mu^\dagger(t)\gamma_\nu(t), \tag{2.29}$$

$$\mathcal{I}_{\mu,\nu} = \int dx\,\Phi_\mu^\dagger(x)\,\mathrm{sgn}(-x)\left[\frac{E_\mu - E_\nu}{2i}\tau_z + \Delta\tau_y\right]\Phi_\nu(x) = \mathcal{I}_{\nu,\mu}^*.$$

We provide a concise discussion of the BdG eigenstates resulting from Eq. (2.24) and of the current matrix elements (2.29) in the Appendix.

Derivation of ABSs energies and wavefunctions.— In what follows, we denote ABSs solutions with the quantum number $\nu = \lambda$. Using the matrix $T(E)$ in Eq. (2.13) and the function

$$\gamma(E) = \arccos\left(\frac{E}{\Delta}\right),$$

we show in the Appendix that the matching equation has nontrivial solutions only for energies satisfying the condition

$$\det[A_p(E) - A_h(E)] = 0 \tag{2.30}$$

with the particle and hole matrices

$$\begin{aligned} A_p(E) &= e^{i\phi_0/2} e^{i\rho_z \gamma(E)/2}\, T(E)\, e^{i\rho_z \gamma(E)/2}, \\ A_h(E) &= \rho_x \sigma_y A_p^*(-E) \sigma_y \rho_x. \end{aligned} \tag{2.31}$$

We obtain $E_\lambda(\varphi_0)$ and the corresponding ABS wave function, see Eq. (.52) in the Appendix, by numerically solving Eq. (2.30) and determining the corresponding eigenvectors. In practice, we study cases with $L \approx \xi_0 = v_F/\Delta$, where one typically encounters four spin-split positive-energy ABS solutions.

2.3 Many-body Andreev-state population dynamics

In this section, we derive the dynamical equations governing the time evolution of the many-body Andreev states for the above model. First, in Sec. 2.3.1, we introduce the so-called excitation picture and compare it with the alternative semiconductor picture [34, 41]. We show that the excitation picture offers a particularly convenient representation for superconducting problems with SOI and Zeeman fields, since double-counting issues are more difficult to handle in the semiconductor picture. In Sec. 2.3.2, we then derive a Lindblad master equation for the dynamics of the reduced density operator $\rho_A(t)$ describing the Andreev-state sector. In Sec. 2.3.3, we discuss the many-body population dynamics in the Andreev subspace by considering the diagonal elements of $\rho_A(t)$. For $\gamma_{\rm SO} = 0$ and $\mathbf{b} = 0$, our approach recovers the results of Ref. [34]. Applications of the formalism to cases with finite SOI and/or magnetic Zeeman field are presented in Sec. 2.4.

2.3.1 Excitation picture vs semiconductor picture

The Nambu representation introduced in Eq. (2.2) is very convenient to theoretically describe the combined effects of superconductivity, SOI, and Zeeman fields in a unified framework [55]. However, due to the reality constraint (2.4), this representation also comes at a cost since it implies an artificial doubling of the number of single-particle states. In order to avoid spurious non-physical many-body states one needs to carefully choose half of the single particle states. Below the possible choices of the single-particle states are described.

Short junction case.— Let us first consider the case of a short junction without SOI and Zeeman field at fixed phase difference ϕ_0 and fixed other parameters, see Fig. 2.2. In this example, we have a single spin-degenerate ABS with positive energy $E_\uparrow = E_\downarrow = E$, plus the particle-hole partner states at energy $-E$. In order to avoid the double-counting problem, one may employ the *semiconductor picture* [34, 41], where one retains only the single-particle ABSs with, e.g., energy $E_\uparrow$ and $-E_\downarrow$, as shown in Fig. 2.2(a). The corresponding four many-body states are shown in the left part of Fig. 2.2(b). An alternative choice of single-particle states is given by the *excitation picture*, where we instead retain the two positive energy levels $(E_\uparrow, E_\downarrow)$. The corresponding many-body states are shown in the right part of Fig. 2.2(b).

Let us summarize the many-body Andreev states for this example, as shown in Fig. 2.2(b):

- *Ground state:* in the semiconductor picture, the ground state $|g\rangle$ is obtained by filling the energy level $-E$ and leaving the energy level $+E$ empty. In the excitation picture, both energy levels $E_{\sigma=\uparrow,\downarrow}$ are empty. We denote the ground state as $|00\rangle$ in the excitation picture. This state has (by convention [34]) even parity.

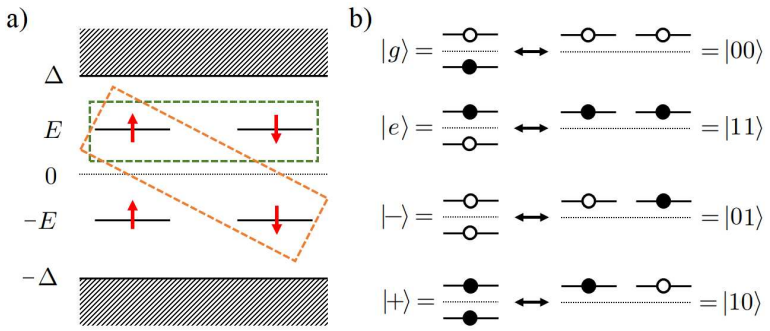

Figure 2.2: Schematic BdG spectrum of a short ($L \ll \xi_0$) junction without SOI and Zeeman field, taken at fixed phase difference φ_0. In this case, one obtains a single spin-degenerate ABS with energies $E_\uparrow = E_\downarrow = E > 0$ and $E < \Delta$, plus the corresponding states at energy $-E$ obtained from particle-hole symmetry. (a) Double counting can be removed in the semiconductor picture by retaining only the single-particle states $(E_\uparrow, -E_\downarrow)$ inside the tilted orange-dashed box. Alternatively, in the excitation picture, double counting is removed by retaining only the positive-energy single-particle states $(E_\uparrow, E_\downarrow)$ inside the horizontal green-dashed box. Continuum states with $|E| > \Delta$ correspond to the shaded regions. (b) The four possible many-body Andreev states $\{|g\rangle, |e\rangle, |-\rangle, |+\rangle\}$ in the semiconductor picture (left side), where filled (empty) dots indicate occupied (empty) single-particle ABS levels. In the equivalent excitation picture (right side), these four states are represented by $\{|00\rangle, |11\rangle, |01\rangle, |10\rangle\}$, respectively.

- *Even parity:* in the even parity sector, there is one excited state with excitation energy $2E$ above the ground state. In the semiconductor picture, the lower level is empty but now the upper level is occupied. This state has been labeled $|e\rangle$ in Ref. [34]. In the excitation picture, both levels E_σ are occupied, and the state is thus denoted as $|11\rangle$.

- *Odd parity:* in the odd parity sector, there are two degenerate states with energy E above the ground state. In the semiconductor picture, the state $|-\rangle$ has both levels $\pm E$ empty, while the state $|+\rangle$ has both levels occupied [34]. In the excitation picture, one occupies only one of the two states. Here the two corresponding odd-parity states are called $|01\rangle$ and $|10\rangle$, respectively.

It is worth noting that the semiconductor and excitation pictures are related by the particle-hole symmetry, see Eq. (2.27). In words, thes relation can be read as: a particle of negative energy corresponds to a whole of positive energy or a hole of negative energy corresponds to the partucle of the positive energy.

Junction of intermediate length.— Turning back to our problem, we consider a junction in the presence of the SOI and the Zeeman field. (In the absence of the Zeeman field, the Kramers degeneracy takes over the role of spin degeneracy.) In a weak link of intermediate length $L \approx \xi_0 = v_F/\Delta$, one typically finds four single-particle ABSs at positive energies, where two spin-degenerate levels split into four levels if both SOI and a Zeeman term are present. An example is shown in Fig. 2.3(a). In this case, we find that the *semiconductor picture is not useful* for constructing a many-body formulation of the theory since, *due to the broken spin degeneracy, it is ambiguous how to select pairs of positive and negative energy states*. From now on, we therefore *use the excitation picture to construct the many-body states and the Lindblad equation for the population dynamics of these states*. This picture allows us to directly circumvent double-counting problems in the many-body theory by construction.

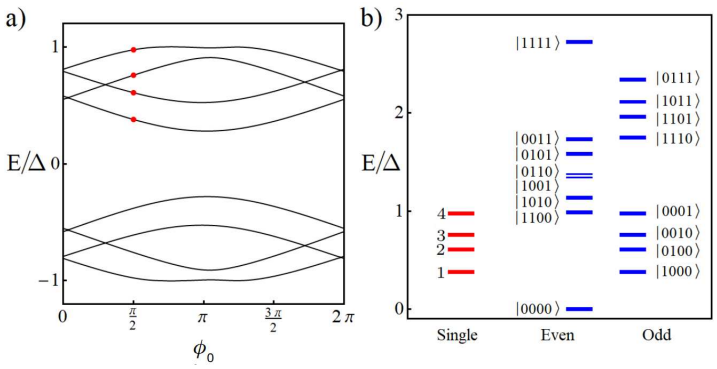

Figure 2.3: Andreev state dispersion and many-body Andreev states for a junction with SOI and Zeeman field. (a) ABS dispersion E_λ vs phase difference φ_0 obtained numerically from Eq. (2.30). The red dots indicate the four positive-energy states for $\phi_0 = \pi/2$. We here consider $L = 1.5\xi_0, k_0\xi_0 = 0.1, \mathcal{T} = 0.75, \gamma_{SO} = 0.14, v_0 = v_F$, and $|\mathbf{b}| = 0.2\Delta$ with $b_x/b_z = 3$ and $b_y = 0$. (b) The red levels show the positive-energy single-particle ABS levels for $\phi_0 = \pi/2$, cf. the red dots in panel (a). The sixteen possible many-body states are shown in the excitation picture as blue levels. We distinguish the even and odd fermion parity sectors. The notation $|n_1n_2n_3n_4\rangle$ with $n_\lambda \in \{0,1\}$ means that the energy level E_λ is either empty or occupied.

For the case $L \approx \xi_0$, with fixed phase difference φ_0, we order the positive ABS energies by increasing energy, $0 \leq E_1 \leq E_2 \leq E_3 \leq E_4 < \Delta$, see Fig. 2.3(b). The resulting 16 many-body Andreev states are written as $|n_1n_2n_3n_4\rangle$ with $n_\lambda \in \{0,1\}$, where $n_\lambda = 0$ ($n_\lambda = 1$) means that the energy level E_λ is unoccupied (occupied). The ground state is then given by $|0000\rangle$. One can group those states into even- and odd-parity states, see Fig. 2.3(b).

Current operator in the excitation picture.— In the Schrödinger picture, the current operator (2.29) then takes the form

$$\mathcal{I} = \sum_{\mu\neq\nu} \left(2\mathcal{I}_{\mu,\nu}\gamma_\mu^\dagger\gamma_\nu + \mathcal{I}_{\bar{\mu},\nu}\gamma_\mu\gamma_\nu + \mathcal{I}_{\mu,\bar{\nu}}\gamma_\mu^\dagger\gamma_\nu^\dagger \right), \tag{2.32}$$

where summations are taken over non-negative BdG energy solutions only. We here used the particle-hole relations $\gamma_{\bar{\nu}} = \gamma_\nu^\dagger$ and $E_{\bar{\nu}} = -E_\nu$, which imply $\mathcal{I}_{\mu,\nu} = -\mathcal{I}_{\bar{\nu},\bar{\mu}}$. The term with $\mu = \nu$ has been excluded in Eq. (2.32) since it does not contribute to the dynamical equations

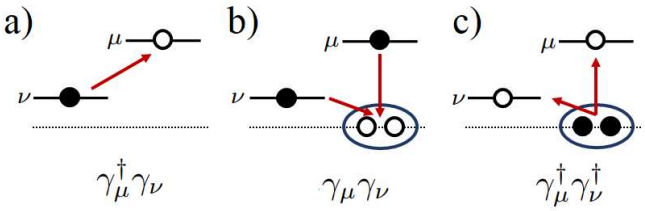

Figure 2.4: Illustration of the three contributions to the current matrix element (2.32) in the excitation picture. (a) Transition between positive-energy BdG single-particle states $\nu \to \mu$, where the filled (empty) dot implies that the state $|\nu\rangle$ ($|\mu\rangle$) is initially filled (empty). The diagram in panel (b) [panel (c)] involves fermionic pair annihilation [creation] processes, along with the creation [annihilation] of a zero-energy Cooper pair. Such processes emerge in the excitation picture due to negative-energy BdG states.

below (no zero energy photons). The possible transitions contributing to the current matrix elements (2.32) are illustrated in Fig. 2.4. The first term in Eq. (2.32) describes transitions between BdG single-particle eigenstates with quantum numbers $\nu \to \mu$, see Fig. 2.4(a). The other two terms, shown on Fig. 2.4(b,c), describe fermionic pair annihilation or creation processes, which involves creation or annihilation of a zero energy Cooper pair, respectively. Such processes effectively arise from terms mixing ABSs with positive and negative energies in the excitation picture, see also Ref. [50].

2.3.2 Lindblad equation in the excitation picture

In this section we construct the Lindblad master equation for the Andreev many-body states in the excitation picture. Although our focus is on this specific problem, the resulting equation has a broader range of applicability. Its construction requires only the current matrix elements between the ABSs and ABSs and contiuum states given in Eq. (2.29). These current matrix elements determine the transition rates between the states of the system, and, as we will see, fully determine the dynamics of the system. The derived Lindblad equation for the Andreev sector will also be used in the next Chapter, devoted to the Mpemba effect in Josephson junctions.

Lindblad master equation for the fermionic density matrix.— We start by constructing the dynamical equation for the density matrix $\rho(t)$ for the fermionic part of the system. We assume that the fermionic system does not influence the bosonic environment, so that the harmonic oscillator bath representing H_{env} in Eq. (2.18) remains in thermal equilibrium at temperature T_{env} at all times. This is reflected in the factorization of the total density operator into the fermionic and bosonic parts,

$$\rho_{\text{tot}}(t) \approx \rho(t) \otimes \rho_{\text{env}},$$

in the interaction picture. Further, we make the standard Born-Markov assumptions of weak system-bath coupling and short bath memory time, which for our system are met for $T_{\text{env}} \gtrsim 10^{-2}\Delta$ and dimensionless system-bath coupling strength $\kappa_0 \ll 1$ [34]. After tracing over the environmental modes, we obtain

$$\partial_t \rho = \int_0^\infty d\tau\, \mathfrak{D}(\tau)\Big[\mathcal{I}(t-\tau)\rho(t)\mathcal{I}(t) - \mathcal{I}(t)\mathcal{I}(t-\tau)\rho(t)\Big] + \text{h.c.}, \tag{2.33}$$

with a bath correlation function $\mathfrak{D}(\tau)$. Introducing real and imaginary parts in the frequency domain,

$$\int_0^\infty d\tau\, \mathfrak{D}(\tau) e^{i\omega\tau} = X(\omega) + iY(\omega), \tag{2.34}$$

the imaginary part $Y(\omega)$ is neglected below since it only weakly renormalizes the BdG quasiparticle energies. This causes the so-called Lamb shifts. For the population dynamics studied in Sec. 2.3.3 below within the Born approximation, such Lamb shifts are irrelevant. However, in order to study quantum coherences encoded by the off-diagonal elements of the density operator, $Y(\omega)$ may have to be included [56].

The real part of the integral can be represented in terms of the spectral density of a microwave-circuit environment as

$$X(\omega) = \pi J(\omega)[n_B(\omega) + 1], \tag{2.35}$$

with the bath states following the Bose-Planck distribution,

$$n_B(\omega) = (e^{\omega/T_{\text{env}}} - 1)^{-1}. \tag{2.36}$$

The bosonic environment spectral density, describing the intensity of the system-bath interaction, is given by ([27])

$$J(\omega) = \frac{\kappa_0^2 \eta_d}{\pi}\left(\frac{1}{(\omega-\Omega)^2 + \frac{\eta_d^2}{2}} - \frac{1}{(\omega+\Omega)^2 + \frac{\eta_d^2}{2}}\right), \tag{2.37}$$

where Ω is the resonance frequency of the photons, κ_0 - dimensionless coupling strength, and η_d - and damping constant Additionally, we include a background Ohmic spectral density in $J(\omega)$,

$$J_{\text{ohm}} = 2\alpha_0 \omega e^{-|\omega|/\omega_c},$$

with a dimensionless coupling $\alpha_0 \ll 1$ and the ultraviolet cutoff frequency ω_c. Note that, in any case, the spectral density is defined to be asymmetric, $J(-\omega) = -J(\omega)$.

For a given jump operator c, we employ the standard dissipator superoperator $\mathcal{L}[c]$ defined as [56]

$$\mathcal{L}[c]\rho = c\rho c^\dagger - \frac{1}{2}\{c^\dagger c, \rho\}, \tag{2.38}$$

where $\{\cdot,\cdot\}$ is the anticommutator. Inserting $\mathcal{I}(t)$ obtained from Eq. (2.32) into Eq. (2.33), and using H_0 in Eq. (2.25), we then obtain a *Lindblad master equation* [56, 57] for the time evolution of the fermionic density operator,

$$\begin{aligned} \partial_t \rho &= -i\sum_\nu E_\nu [\gamma_\nu^\dagger \gamma_\nu, \rho(t)] + \sum_{\mu,\nu}\Big(\Gamma_{\mu,\nu}\,\mathcal{L}\left[\gamma_\mu^\dagger \gamma_\nu\right]\rho(t) + \\ &+ \frac{1}{2}\left(\Gamma_{\bar\mu,\nu}\,\mathcal{L}\left[\gamma_\mu \gamma_\nu\right]\rho(t) + \Gamma_{\mu,\bar\nu}\,\mathcal{L}\left[\gamma_\mu^\dagger \gamma_\nu^\dagger\right]\rho(t)\right)\Big). \end{aligned} \tag{2.39}$$

Since we work in the excitation picture, all summations over indices ν or μ involve only non-negative (ABS and continuum) quasiparticle energies E_ν and E_μ. Using Eq. (2.35), the corresponding transition rates, see also Fig. 2.4, are given by

$$\Gamma_{a,b} = 2X(E_b - E_a)\,|\mathcal{I}_{a,b}|^2, \tag{2.40}$$

with the indices $a \in \{\mu, \bar\mu\}$ and $b \in \{\nu, \bar\nu\}$, including both positive and negative BdG energy levels. For $a = \bar\mu$, we define $\bar a = \mu$. (We recall our notation $\bar\nu$ for the particle-hole partner state with negative energy $E_{\bar\nu} = -E_\nu$ and quasiparticle operator $\gamma_{\bar\nu} = \gamma_\nu^\dagger$.)

The transition rates in Eq. (2.40) satisfy certain *symmetry relations*:

1. detailed balance equation since the environment is in thermal equilibrium

$$\Gamma_{a,b} = e^{(E_b - E_a)/T_{\text{env}}}\,\Gamma_{b,a}; \tag{2.41}$$

2. from the particle-hole symmetry in Eq. (2.26), we infer the relation

$$\Gamma_{a,b} = \Gamma_{\bar b,\bar a}. \tag{2.42}$$

Lindblad master equation for the ABSs.— Since our aim is to study the time evolution of the many-body Andreev states, we next trace over the quasiparticle continuum states. In general, this is a difficult task, and we here follow Ref. [34] by making two assumptions:

1. We assume that entanglement between the Andreev sector and the continuum sector can be neglected at all times such that the fermionic density operator factorizes,

$$\rho(t) \approx \rho_A(t) \otimes \rho_c(t).$$

Here, $\rho_A(t)$ denotes the reduced density operator of the Andreev sector while $\rho_c(t)$ describes the continuum quasiparticle sector;

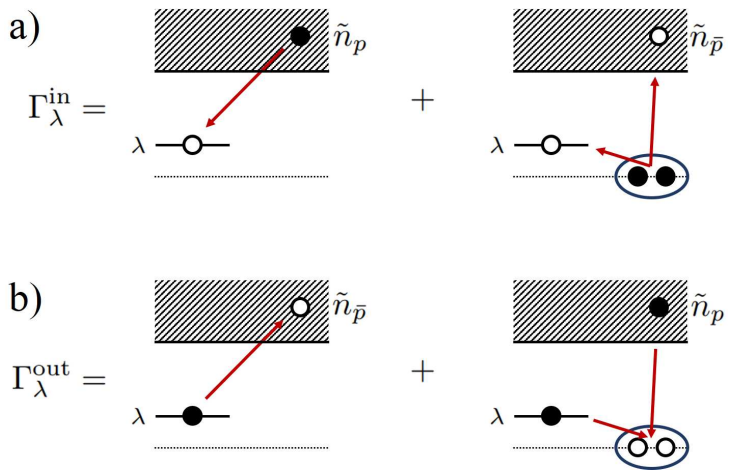

Figure 2.5: Illustration of the transition rates $\Gamma_\lambda^{\rm in}$ [panel (a)] and $\Gamma_\lambda^{\rm out}$ [panel (b)] connecting the ABS level λ to the quasiparticle continuum, see Eq. (2.40). The distribution function $\tilde{n}_p$ of the continuum particles is defined in Eq. (2.44). Note that in the excitation picture, "anomalous" processes involving a Cooper pair have to be taken into account.

2. We also assume that $\rho_c(t)$ can be written in terms of an equilibrium distribution function, $\tilde{n}_p$, which depends only on the continuum-state quantum numbers $p = (E, s, \sigma)$,

$$\rho_{\rm c}(t) = \prod_p \left(\tilde{n}_p |1_p\rangle\langle 1_p| + (1-\tilde{n}_p)|0_p\rangle\langle 0_p|\right), \tag{2.43}$$

where $|1_p\rangle = \gamma_p^\dagger|0_p\rangle$ and $|0_p\rangle$ are the eigenstates of $\gamma_p^\dagger\gamma_p$ with eigenvalue 1 and 0, respectively. Note that the product extends only over $E > \Delta$ solutions since we work in the excitation picture. For the distribution function, we choose a Fermi-Dirac distribution parametrized by a "quasiparticle temperature" $T_{\rm qp}$,

$$\tilde{n}_p = (e^{E/T_{\rm qp}} + 1)^{-1}. \tag{2.44}$$

For the corresponding negative-energy state $\tilde{n}_{\bar{p}} = 1 - \tilde{n}_p$ holds.

The temperature of the continuum $T_{\rm qp}$ may differ from the temperature $T_{\rm env}$ of the electromagnetic environment. For instance, in order to describe quasiparticle poisoning effects due to the presence of excess above-gap quasiparticles, at least in a qualitative manner, we consider $T_{\rm qp} > T_{\rm env}$.

Using the symmetry relation (2.42) and performing the trace over the continuum sector in Eq. (2.39), we finally arrive at a Lindblad equation describing only the Andreev sector,

$$\begin{aligned}\partial_t \rho_A &= -i\sum_\lambda E_\lambda[\gamma_\lambda^\dagger\gamma_\lambda, \rho_A] + \sum_{\lambda,\lambda'}\Bigg(\Gamma_{\lambda,\lambda'}\,\mathcal{L}\left[\gamma_\lambda^\dagger\gamma_{\lambda'}\right]\rho_A + \\ &+ \frac{1}{2}\left(\Gamma_{\bar{\lambda},\lambda'}\,\mathcal{L}\left[\gamma_\lambda\gamma_{\lambda'}\right]\rho_A + \Gamma_{\lambda,\bar{\lambda}'}\,\mathcal{L}\left[\gamma_\lambda^\dagger\gamma_{\lambda'}^\dagger\right]\rho_A\right)\Bigg) \\ &+ \sum_\lambda\left(\Gamma_\lambda^{\rm in}\,\mathcal{L}[\gamma_\lambda^\dagger]\rho_A + \Gamma_\lambda^{\rm out}\,\mathcal{L}[\gamma_\lambda]\rho_A\right).\end{aligned}$$

Apart from the transition rates (2.40) between ABSs, Eq. (2.45) also involves transition rates

connecting the sub-gap Andreev and the above-gap continuum sector,

$$\Gamma_{\lambda}^{\text{in}} = \sum_{p} \left(\Gamma_{\lambda,p} \tilde{n}_{p} + \Gamma_{\lambda,\bar{p}} \tilde{n}_{\bar{p}} \right), \tag{2.45}$$

$$\Gamma_{\lambda}^{\text{out}} = \sum_{p} \left(\Gamma_{p,\lambda} \tilde{n}_{\bar{p}} + \Gamma_{\bar{p},\lambda} \tilde{n}_{p} \right) = \Gamma_{\bar{\lambda}}^{\text{in}}. \tag{2.46}$$

Summations over ABS indices λ and over continuum indices p involve only non-negative energy levels. The corresponding processes are schematically illustrated in Fig. 2.5. Transition rate $\Gamma_{\lambda}^{\text{in}}$ describes the processes that populate the λ-th ABS involving continuum states. These processes include a hopping from the continuum state and ABS, and an additional "anomalous process", the annihilation of a zero energy Cooper pair with the subsequent population of a continuum state and ABS. Similarly, transition rate $\Gamma_{\lambda}^{\text{out}}$ that describes the depopulation of the λ-th ABS involving continuum states, includes two processes: the usual hopping between two states and an "anomalous" process of annihilation of ABS and continuum state with the subsequent creation of a zero energy Cooper pair. Note that the "anomalous" processes that include zero energy Cooper pairs arise due to the description of the many-body system in the excitation picture. In the semiconductor picture the anomalous processes would be the hopping between the ABS λ and negative continuum.

	$\lvert 0000\rangle$	$\lvert 1000\rangle$	$\lvert 0010\rangle$	$\lvert 1010\rangle$	$\lvert 0101\rangle$	$\lvert 1111\rangle$	$\lvert 1100\rangle$	$\lvert 0011\rangle$	$\lvert 1001\rangle$	$\lvert 0110\rangle$	$\lvert 0100\rangle$	$\lvert 0001\rangle$	$\lvert 1110\rangle$	$\lvert 1011\rangle$	$\lvert 1101\rangle$	$\lvert 0111\rangle$
$\langle 0000\rvert$		$\Gamma^{\mathrm{in}}_{\bar{1}}$	$\Gamma^{\mathrm{in}}_{\bar{3}}$	$\Gamma_{\bar{1},3}$	$\Gamma_{\bar{2},4}$	0	$\Gamma_{\bar{1},2}$	$\Gamma_{\bar{3},4}$	$\Gamma_{\bar{1},4}$	$\Gamma_{\bar{2},3}$	$\Gamma^{\mathrm{in}}_{\bar{2}}$	$\Gamma^{\mathrm{in}}_{\bar{4}}$	0	0	0	0
$\langle 1000\rvert$	Γ^{in}_{1}		$\Gamma_{1,3}$	$\Gamma^{\mathrm{in}}_{\bar{3}}$	0	0	$\Gamma^{\mathrm{in}}_{\bar{2}}$	0	$\Gamma^{\mathrm{in}}_{\bar{4}}$	0	$\Gamma_{1,2}$	$\Gamma_{1,4}$	$\Gamma_{\bar{2},3}$	$\Gamma_{\bar{3},4}$	$\Gamma_{\bar{2},4}$	0
$\langle 0010\rvert$	Γ^{in}_{3}	$\Gamma_{3,1}$		$\Gamma^{\mathrm{in}}_{\bar{1}}$	0	0	0	$\Gamma^{\mathrm{in}}_{\bar{4}}$	0	$\Gamma^{\mathrm{in}}_{\bar{2}}$	$\Gamma_{3,2}$	$\Gamma_{3,4}$	$\Gamma_{\bar{1},2}$	$\Gamma_{\bar{1},4}$	0	$\Gamma_{\bar{2},4}$
$\langle 1010\rvert$	$\Gamma_{1,\bar{3}}$	Γ^{in}_{3}	Γ^{in}_{1}		0	$\Gamma_{\bar{2},4}$	$\Gamma_{3,2}$	$\Gamma_{1,4}$	$\Gamma_{3,4}$	$\Gamma_{1,2}$	0	0	$\Gamma^{\mathrm{in}}_{\bar{2}}$	$\Gamma^{\mathrm{in}}_{\bar{4}}$	0	0
$\langle 0101\rvert$	$\Gamma_{2,\bar{4}}$	0	0	0		$\Gamma_{\bar{1},3}$	$\Gamma_{4,1}$	$\Gamma_{2,3}$	$\Gamma_{2,1}$	$\Gamma_{4,3}$	Γ^{in}_{4}	Γ^{in}_{2}	0	0	$\Gamma^{\mathrm{in}}_{\bar{1}}$	$\Gamma^{\mathrm{in}}_{\bar{3}}$
$\langle 1111\rvert$	0	0	0	$\Gamma_{2,\bar{4}}$	$\Gamma_{1,\bar{3}}$		$\Gamma_{3,\bar{4}}$	$\Gamma_{1,\bar{2}}$	$\Gamma_{2,\bar{3}}$	$\Gamma_{1,\bar{4}}$	0	0	Γ^{in}_{4}	Γ^{in}_{2}	Γ^{in}_{3}	Γ^{in}_{1}
$\langle 1100\rvert$	$\Gamma_{1,\bar{2}}$	Γ^{in}_{2}	0	$\Gamma_{2,3}$	$\Gamma_{1,4}$	$\Gamma_{\bar{3},4}$		0	$\Gamma_{2,4}$	$\Gamma_{1,3}$	Γ^{in}_{1}	0	$\Gamma^{\mathrm{in}}_{\bar{3}}$	0	$\Gamma^{\mathrm{in}}_{\bar{4}}$	0
$\langle 0011\rvert$	$\Gamma_{3,\bar{4}}$	0	Γ^{in}_{4}	$\Gamma_{4,1}$	$\Gamma_{3,2}$	$\Gamma_{\bar{1},2}$	0		$\Gamma_{3,1}$	$\Gamma_{4,2}$	0	Γ^{in}_{3}	0	$\Gamma^{\mathrm{in}}_{\bar{1}}$	0	$\Gamma^{\mathrm{in}}_{\bar{2}}$
$\langle 1001\rvert$	$\Gamma_{1,\bar{4}}$	Γ^{in}_{4}	0	$\Gamma_{4,3}$	$\Gamma_{1,2}$	$\Gamma_{\bar{2},3}$	$\Gamma_{4,2}$	$\Gamma_{1,3}$		0	0	Γ^{in}_{1}	0	$\Gamma^{\mathrm{in}}_{\bar{3}}$	$\Gamma^{\mathrm{in}}_{\bar{2}}$	0
$\langle 0110\rvert$	$\Gamma_{2,\bar{3}}$	0	Γ^{in}_{2}	$\Gamma_{2,1}$	$\Gamma_{3,4}$	$\Gamma_{\bar{1},4}$	$\Gamma_{3,1}$	$\Gamma_{2,4}$	0		Γ^{in}_{3}	0	$\Gamma^{\mathrm{in}}_{\bar{1}}$	0	0	$\Gamma^{\mathrm{in}}_{\bar{4}}$
$\langle 0100\rvert$	Γ^{in}_{2}	$\Gamma_{2,1}$	$\Gamma_{2,3}$	0	$\Gamma^{\mathrm{in}}_{\bar{4}}$	0	$\Gamma^{\mathrm{in}}_{\bar{1}}$	0	0	$\Gamma^{\mathrm{in}}_{\bar{3}}$		$\Gamma_{2,4}$	$\Gamma_{\bar{1},3}$	0	$\Gamma_{\bar{1},4}$	$\Gamma_{\bar{3},4}$
$\langle 0001\rvert$	Γ^{in}_{4}	$\Gamma_{4,1}$	$\Gamma_{3,4}$	0	$\Gamma^{\mathrm{in}}_{\bar{2}}$	0	0	$\Gamma^{\mathrm{in}}_{\bar{3}}$	$\Gamma^{\mathrm{in}}_{\bar{1}}$	0	$\Gamma_{4,2}$		0	$\Gamma_{\bar{1},3}$	$\Gamma_{\bar{1},2}$	$\Gamma_{\bar{2},3}$
$\langle 1110\rvert$	0	$\Gamma_{2,\bar{3}}$	$\Gamma_{1,\bar{2}}$	Γ^{in}_{2}	0	$\Gamma^{\mathrm{in}}_{\bar{4}}$	Γ^{in}_{3}	0	0	Γ^{in}_{1}	$\Gamma_{1,\bar{3}}$	0		$\Gamma_{2,4}$	$\Gamma_{3,4}$	$\Gamma_{1,4}$
$\langle 1011\rvert$	0	$\Gamma_{3,\bar{4}}$	$\Gamma_{1,\bar{4}}$	Γ^{in}_{4}	0	$\Gamma^{\mathrm{in}}_{\bar{3}}$	0	Γ^{in}_{1}	Γ^{in}_{3}	0	0	$\Gamma_{1,\bar{3}}$	$\Gamma_{4,2}$		$\Gamma_{3,2}$	$\Gamma_{1,2}$
$\langle 1101\rvert$	0	$\Gamma_{2,\bar{4}}$	0	0	Γ^{in}_{1}	$\Gamma^{\mathrm{in}}_{\bar{3}}$	Γ^{in}_{4}	0	Γ^{in}_{2}	0	$\Gamma_{1,\bar{4}}$	$\Gamma_{1,\bar{2}}$	$\Gamma_{4,3}$	$\Gamma_{2,3}$		$\Gamma_{1,3}$
$\langle 0111\rvert$	0	0	$\Gamma_{2,\bar{4}}$	0	Γ^{in}_{3}	$\Gamma^{\mathrm{in}}_{\bar{1}}$	0	Γ^{in}_{2}	0	Γ^{in}_{4}	$\Gamma_{3,\bar{4}}$	$\Gamma_{2,\bar{3}}$	$\Gamma_{4,1}$	$\Gamma_{2,1}$	$\Gamma_{3,1}$	

Table 2.1: Off-diagonal matrix elements $M_{\mathbf{n},\mathbf{n}'}$ for the matrix $\mathbf{M}$ in Eq. (2.49), expressed in terms of the transition rates (2.40) and (2.45). Here $|\mathbf{n}\rangle = |n_1 n_2 n_3 n_4\rangle$ with $n_\lambda \in \{0,1\}$ labels the 16 possible many-body Andreev states. The indices $\lambda \in \{1,2,3,4\}$ refer to the four single-particle ABS states, see, e.g., Fig. 2.3, where $\bar{\lambda}$ corresponds to the negative-partner state. Diagonal matrix elements $M_{\mathbf{n},\mathbf{n}}$ are given in Table 2.2.

$\lvert\mathbf{n}\rangle$	$-M_{\mathbf{n},\mathbf{n}}$
$\lvert 0000\rangle$	$\Gamma_{1,\bar{2}}+\Gamma_{1,\bar{3}}+\Gamma_{2,\bar{3}}+\Gamma_{1,\bar{4}}+\Gamma_{2,\bar{4}}+\Gamma_{3,\bar{4}}+\Gamma_{1}^{\mathrm{in}}+\Gamma_{2}^{\mathrm{in}}+\Gamma_{3}^{\mathrm{in}}+\Gamma_{4}^{\mathrm{in}}$
$\lvert 1000\rangle$	$\Gamma_{2,1}+\Gamma_{3,1}+\Gamma_{4,1}+\Gamma_{2,\bar{3}}+\Gamma_{2,\bar{4}}+\Gamma_{3,\bar{4}}+\Gamma_{2}^{\mathrm{in}}+\Gamma_{3}^{\mathrm{in}}+\Gamma_{4}^{\mathrm{in}}+\Gamma_{\bar{1}}^{\mathrm{in}}$
$\lvert 0010\rangle$	$\Gamma_{1,3}+\Gamma_{2,3}+\Gamma_{4,3}+\Gamma_{1,\bar{2}}+\Gamma_{1,\bar{4}}+\Gamma_{2,\bar{4}}+\Gamma_{1}^{\mathrm{in}}+\Gamma_{2}^{\mathrm{in}}+\Gamma_{4}^{\mathrm{in}}+\Gamma_{\bar{3}}^{\mathrm{in}}$
$\lvert 1010\rangle$	$\Gamma_{2,1}+\Gamma_{4,1}+\Gamma_{2,3}+\Gamma_{4,3}+\Gamma_{2,\bar{4}}+\Gamma_{\bar{1},3}+\Gamma_{2}^{\mathrm{in}}+\Gamma_{4}^{\mathrm{in}}+\Gamma_{\bar{1}}^{\mathrm{in}}+\Gamma_{\bar{3}}^{\mathrm{in}}$
$\lvert 0101\rangle$	$\Gamma_{1,2}+\Gamma_{3,2}+\Gamma_{1,4}+\Gamma_{3,4}+\Gamma_{1,\bar{3}}+\Gamma_{\bar{2},4}+\Gamma_{1}^{\mathrm{in}}+\Gamma_{3}^{\mathrm{in}}+\Gamma_{\bar{2}}^{\mathrm{in}}+\Gamma_{4}^{\mathrm{in}}$
$\lvert 1111\rangle$	$\Gamma_{\bar{1},2}+\Gamma_{\bar{1},3}+\Gamma_{\bar{2},3}+\Gamma_{\bar{1},4}+\Gamma_{\bar{2},4}+\Gamma_{\bar{3},4}+\Gamma_{\bar{1}}^{\mathrm{in}}+\Gamma_{\bar{2}}^{\mathrm{in}}+\Gamma_{\bar{3}}^{\mathrm{in}}+\Gamma_{4}^{\mathrm{in}}$
$\lvert 1100\rangle$	$\Gamma_{3,1}+\Gamma_{4,1}+\Gamma_{3,2}+\Gamma_{4,2}+\Gamma_{3,\bar{4}}+\Gamma_{\bar{1},2}+\Gamma_{3}^{\mathrm{in}}+\Gamma_{4}^{\mathrm{in}}+\Gamma_{\bar{1}}^{\mathrm{in}}+\Gamma_{\bar{2}}^{\mathrm{in}}$
$\lvert 0011\rangle$	$\Gamma_{1,3}+\Gamma_{1,4}+\Gamma_{2,3}+\Gamma_{2,4}+\Gamma_{1,\bar{2}}+\Gamma_{\bar{3},4}+\Gamma_{1}^{\mathrm{in}}+\Gamma_{2}^{\mathrm{in}}+\Gamma_{\bar{3}}^{\mathrm{in}}+\Gamma_{4}^{\mathrm{in}}$
$\lvert 1001\rangle$	$\Gamma_{2,1}+\Gamma_{3,1}+\Gamma_{2,4}+\Gamma_{3,4}+\Gamma_{2,\bar{3}}+\Gamma_{\bar{1},4}+\Gamma_{2}^{\mathrm{in}}+\Gamma_{3}^{\mathrm{in}}+\Gamma_{\bar{1}}^{\mathrm{in}}+\Gamma_{4}^{\mathrm{in}}$
$\lvert 0110\rangle$	$\Gamma_{1,2}+\Gamma_{4,2}+\Gamma_{1,3}+\Gamma_{4,3}+\Gamma_{1,\bar{4}}+\Gamma_{\bar{2},3}+\Gamma_{1}^{\mathrm{in}}+\Gamma_{4}^{\mathrm{in}}+\Gamma_{\bar{2}}^{\mathrm{in}}+\Gamma_{\bar{3}}^{\mathrm{in}}$
$\lvert 0100\rangle$	$\Gamma_{1,2}+\Gamma_{3,2}+\Gamma_{4,2}+\Gamma_{1,\bar{3}}+\Gamma_{1,\bar{4}}+\Gamma_{3,\bar{4}}+\Gamma_{1}^{\mathrm{in}}+\Gamma_{3}^{\mathrm{in}}+\Gamma_{4}^{\mathrm{in}}+\Gamma_{\bar{2}}^{\mathrm{in}}$
$\lvert 0001\rangle$	$\Gamma_{1,4}+\Gamma_{2,4}+\Gamma_{3,4}+\Gamma_{1,\bar{2}}+\Gamma_{1,\bar{3}}+\Gamma_{2,\bar{3}}+\Gamma_{1}^{\mathrm{in}}+\Gamma_{2}^{\mathrm{in}}+\Gamma_{3}^{\mathrm{in}}+\Gamma_{4}^{\mathrm{in}}$
$\lvert 1110\rangle$	$\Gamma_{4,1}+\Gamma_{4,2}+\Gamma_{4,3}+\Gamma_{\bar{1},2}+\Gamma_{\bar{1},3}+\Gamma_{\bar{2},3}+\Gamma_{4}^{\mathrm{in}}+\Gamma_{\bar{1}}^{\mathrm{in}}+\Gamma_{\bar{2}}^{\mathrm{in}}+\Gamma_{\bar{3}}^{\mathrm{in}}$
$\lvert 1011\rangle$	$\Gamma_{2,1}+\Gamma_{2,3}+\Gamma_{2,4}+\Gamma_{\bar{1},3}+\Gamma_{\bar{1},4}+\Gamma_{\bar{3},4}+\Gamma_{2}^{\mathrm{in}}+\Gamma_{\bar{1}}^{\mathrm{in}}+\Gamma_{\bar{3}}^{\mathrm{in}}+\Gamma_{4}^{\mathrm{in}}$
$\lvert 1101\rangle$	$\Gamma_{3,1}+\Gamma_{3,2}+\Gamma_{3,4}+\Gamma_{\bar{1},2}+\Gamma_{\bar{1},4}+\Gamma_{\bar{2},4}+\Gamma_{3}^{\mathrm{in}}+\Gamma_{\bar{1}}^{\mathrm{in}}+\Gamma_{\bar{2}}^{\mathrm{in}}+\Gamma_{4}^{\mathrm{in}}$
$\lvert 0111\rangle$	$\Gamma_{1,2}+\Gamma_{1,3}+\Gamma_{1,4}+\Gamma_{\bar{2},3}+\Gamma_{\bar{2},4}+\Gamma_{\bar{3},4}+\Gamma_{1}^{\mathrm{in}}+\Gamma_{\bar{2}}^{\mathrm{in}}+\Gamma_{\bar{3}}^{\mathrm{in}}+\Gamma_{\bar{4}}^{\mathrm{in}}$

Table 2.2: Diagonal matrix elements $M_{\mathbf{n},\mathbf{n}}$ in Eq. (2.49) expressed in terms of the transition rates (2.40) and (2.45), where $\lvert\mathbf{n}\rangle = \lvert n_1 n_2 n_3 n_4\rangle$ labels the many-body Andreev states. Note that we specify $-M_{\mathbf{n},\mathbf{n}}$. Off-diagonal matrix elements are specified in Table 2.1.

2.3.3 Matrix rate equation for the many-body ABSs populations

As final step, we project the Lindblad equation (2.45) for the density operator $\rho_A(t)$ into the many-body Andreev states $\lvert\mathbf{n}\rangle$. In our case, we focus on intermediate-length junctions with $L \approx \xi_0$, so that there are four spin-split positive-energy ABS solutions. Then, the Andreev many-body state $\lvert\mathbf{n}\rangle$ can be written in terms of the lenvels occupations as

$$\lvert\mathbf{n}\rangle = \lvert n_1 n_2 n_3 n_4\rangle, \quad n_\lambda \in \{0,1\}, \tag{2.47}$$

where n_λ specifies whether the (non-negative) ABS level E_λ is unoccupied or occupied. The diagonal elements of ρ_A represent the occupation probabilities of the respective 16 Andreev many-body states,

$$P_{\mathbf{n}}(t) = \langle\mathbf{n}|\rho_A(t)|\mathbf{n}\rangle, \quad \sum_{\mathbf{n}} P_{\mathbf{n}}(t) = 1. \tag{2.48}$$

We combine these probabilities into a 16-dimensional vector $\mathbf{P}(t)$. Since the dynamics of $\mathbf{P}(t)$ decouples from the off-diagonal part of $\rho_A(t)$, the occupation probabilities evolve independently from quantum coherences. In this case, the coherences decay exponentially, and therefore, we focus on the time evolution of $\mathbf{P}(t)$.

From Eq. (2.45), by taking the appropriate matrix elements, we obtain a matrix rate equation of the form

$$\dot{\mathbf{P}}(t) = \mathbf{M}\,\mathbf{P}(t), \tag{2.49}$$

where the 16×16 matrix $\mathbf{M}$ consisting of transition rates between the states is specified in Tables 2.1 (off-diagonal elements) and 2.2 (diagonal elements).

Stationary state. — For the stationary state reached at asymptotically long times,

$$\dot{\mathbf{P}}_{\text{stat}} = 0,$$

the steady-state occupation probabilities $\mathbf{P}_{\text{stat}}$ follow by determining the kernel of the matrix $\mathbf{M}$. In general, given the (real-valued and non-positive) eigenvalues λ_k and the corresponding right eigenvectors $\mathbf{P}_k$ of $\mathbf{M}$, the general solution of Eq. (2.49) follows as

$$\mathbf{P}(t) = \sum_{k=1}^{16} c_k \mathbf{P}_k e^{\lambda_k t}. \tag{2.50}$$

The coefficients c_k are determined by matching Eq. (2.50) to the initial configuration $\mathbf{P}(0)$ at time $t = 0$. By collecting the contributions from the odd- and even-parity states only, we can define the probabilities $P_{\text{odd}}(t)$ and $P_{\text{even}}(t) = 1 - P_{\text{odd}}(t)$ for occupying the respective parity sector.

2.4 Results for the population dynamics and parity stabilization

In this section we focus on the results obtained by solving matrix rate equation for the populations of the Andreev many-body states Eq. (2.49). For concreteness, we consider a weak link of intermediate length, $L = 1.5\xi_0$, with contact transparencies $\mathcal{T}_1 = \mathcal{T}_2 = \mathcal{T} = 0.75$. One then generically finds four positive-energy single-particle ABS solutions for given phase difference ϕ_0. For the SOI parameter, we assume $\gamma_{\text{SO}} = 0.14$ following the estimates in Ref. [8], but we also contrast our results to the case without SOI. Similarly, if the Zeeman field is switched on, we assume $|\mathbf{b}| = 0.2\Delta$. For instance, taking Nb as superconductor and InAs as nanowire material, accounting for the rather large g-factors in such nanowires [58], $|\mathbf{b}| = 0.2\Delta$ translates into a field strength ≈ 0.2 Tesla at low temperatures. We then consider arbitrary directions of the field with respect to the polar axis defined by the SOI (which is the z-axis).

2.4.1 ABSs dispersion

First we derive the energies and the wavefunctions of the ABSs. We construct these states as the stationary eigenstates of the noninteracting BdG Hamiltonian (2.23) satisfying the boundary condition given by Eq. (2.24), with energies smaller than the superconducting gap. The matching equation has nontrivial solution only for the energies that satisfy the relation (2.30). The (numerical) solutions of this equation give the energies of the ABSs, while the corresponding eigenvectors determine the wavefunctions of the ABSs.

One example for the single-particle ABSs dispersion of such a junction has already been shown in Fig. 2.3(a). In Fig. 2.6, four additional examples for different combinations of SOI and Zeeman field are shown.

a) In Fig. 2.6(a), only the SOI interaction is present and the time-reversal symmetry is preserved.At $\phi_0 = 0, \pi$ the Kramer's degeneracy takes over the role of the usual spin degeneracy (in these points the states are their own time-reversal partners). Moreover, the dispersion is symmetric, $E_\lambda(2\pi - \phi_0) = E_\lambda(\phi_0)$;

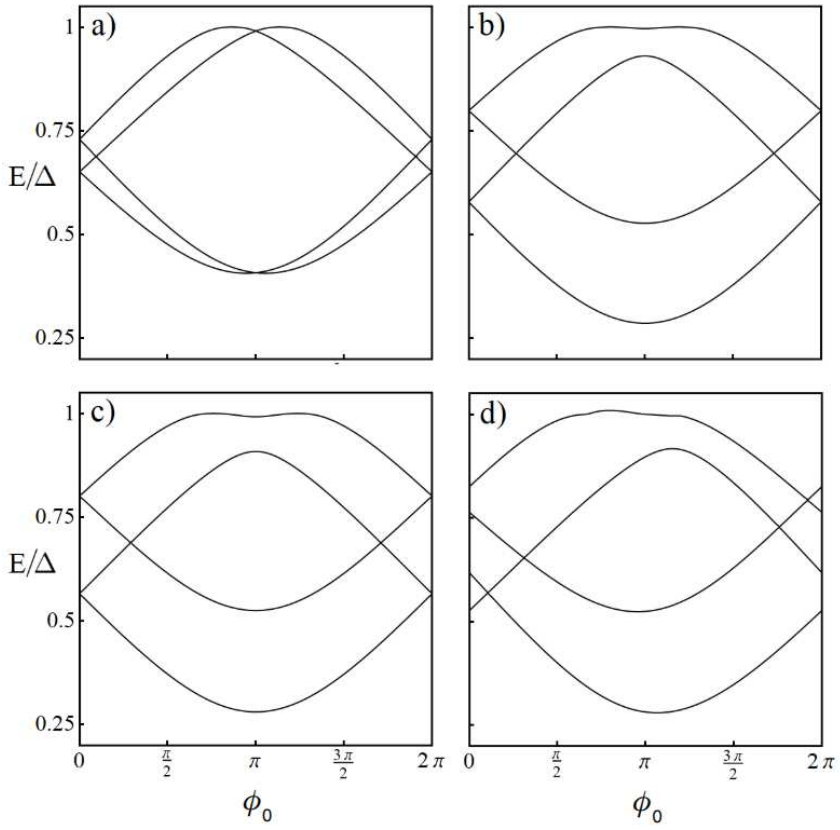

Figure 2.6: ABS dispersion E_λ (with $E_\lambda > 0$) vs ϕ_0 for a weak link with parameters $L = 1.5\xi_0$, $k_0\xi_0 = 0.1$, $\mathcal{T} = 0.75$, and $v_0 = v_F$. (a) Finite SOI strength $\gamma_{\rm SO} = 0.14$ but vanishing Zeeman field, $\mathbf{b} = 0$. (b) Vanishing SOI strength, $\gamma_{\rm SO} = 0$, with $\mathbf{b}$ along an arbitrary direction for $|\mathbf{b}| = 0.2\Delta$. (c) Case $\gamma_{\rm SO} = 0.14$ and Zeeman field $\mathbf{b}$ along the x-direction with $|\mathbf{b}| = 0.2\Delta$. (d) Same as in panel (c) but with the Zeeman field along the z-direction.

b) As seen in Fig. 2.6(b), this symmetry of the dispersion is also found when we switch off the SOI but switch on the magnetic field. However, the time-reversal symmetry is broken by the magnetic fields and there are no time-reversal-invariant points anymore.

c) In Fig. 2.6(c), we consider the case where both SOI and Zeeman field are present, with the Zeeman field along the nanowire axis. Now all degeneracies are broken but the above symmetry still remains intact. While the spectrum looks very similar to the one in panel (b), there are small differences. We note that the level crossings are not avoided crossings.

d) However, if the magnetic field is oriented along the polar axis of the SOI, we find $E_\lambda(2\pi - \phi_0) \neq E_\lambda(\phi_0)$, as shown in Fig. 2.6(d). Incidentally, in such cases, the anomalous Josephson effect and the superconducting diode effect will arise, see, e.g., Refs. [37, 59, 60].

2.4.2 Protocol

In order to study the population dynamics $P_{\mathbf{n}}(t)$ of the respective many-body Andreev states $|\mathbf{n}\rangle$, the following protocol is applied:

1. At times $t < 0$, for a given parameter set, the system has been prepared in its steady state with probabilities $\mathbf{P}_{\text{stat}}$, see Sec. 2.3.3;

2. At time $t = 0$, one applies a short and strong microwave pulse of frequency Ω_d. We assume that Ω_d is resonant with a transition from the ground state $|\mathbf{n}_0\rangle = |0000\rangle$ to an excited many-body Andreev state $|\mathbf{n}\rangle = |n_1 n_2 n_3 n_4\rangle$ of the same fermion parity, i.e., $(-1)^{n_1+n_2+n_3+n_4} = +1$. (The microwave drive cannot change the fermion parity.) If the respective transition rate $M_{\mathbf{n},\mathbf{n}_0}$ in Table 2.1 is finite (this condition imposes a *selection rule*), population inversion between $|\mathbf{n}_0\rangle$ and $|\mathbf{n}\rangle$ can be induced by the microwave pulse, as explained in Ref. [34]. In this way, one can effectively study the effect of the microwave drive through a nonequilibrium initial condition in Eq. (2.49), where the occupation probabilities for the two levels $|\mathbf{n}_0\rangle$ and $|\mathbf{n}\rangle$ are exchanged with respect to their steady-state values.

3. After applying the pulse, the respective initial ($t = 0$) population probabilities are then given by $P_{\mathbf{n}_0}(0) = P_{\mathbf{n};\text{stat}}$ and $P_{\mathbf{n}}(0) = P_{\mathbf{n}_0;\text{stat}}$, while for all other states we have $P_{\mathbf{n}'}(0) = P_{\mathbf{n}';\text{stat}}$. We then solve Eq. (2.49) subject to this initial condition.

Selection rules for the microwave drive.— In the absence of the SOI and the Zeeman field, selection rules can be inferred by analyzing the orbital and spin angular momenta of each ABS. When spin degeneracy is broken, however, the transition rates exhibit a non-trivial dependence on both ϑ, and on the phase difference ϕ_0. In Fig. 2.7(a), we plot the transition rates $M_{\mathbf{n},\mathbf{n}_0}$ from the ground state $|\mathbf{n}_0\rangle$ to the six two-quasiparticle states ($n_1 + n_2 + n_3 + n_4 = 2$) as a function of the angle ϑ between the Zeeman field and the polar SOI axis (for simplicity, $b_y = 0$). We observe that, while the transition rates to the states $|0110\rangle$, $|0101\rangle$, and $|1100\rangle$ are different from zero for all ϑ, the transition rates to the states $|1010\rangle$, $|1001\rangle$, and $|0011\rangle$ vanish for $\vartheta \to 0$ (i.e., for $\mathbf{b}$ along the z-direction). Therefore, for angle $\vartheta = 0$, the microwave drive can not induce the transitions from the ground state to the two-particle states $|1010\rangle$, $|1001\rangle$, and $|0011\rangle$ (see also Fig. 2.7(b, c)). This is a signature for the onset of a selection rule.

In Fig. 2.8, we show the ϕ_0-dependence of the transition rates $M_{\mathbf{n},\mathbf{n}_0}$ from the ground state $|\mathbf{n}_0\rangle$ to each of the six possible two-quasiparticle states $|\mathbf{n}\rangle$, for the magnetic field orientations $\vartheta = 0$ and for $\vartheta = \pi/2$. Similarly to panels (c) and (d) of Fig. 2.6, the transition rates for $\vartheta = \pi/2$ are symmetric around $\phi_0 = \pi$, while for $\vartheta = 0$, a strong asymmetry is present. Furthermore, the transition rates quickly drop to zero for some values of the phase difference, pointing out the onset of a selection rule for the corresponding target states. Compared to the

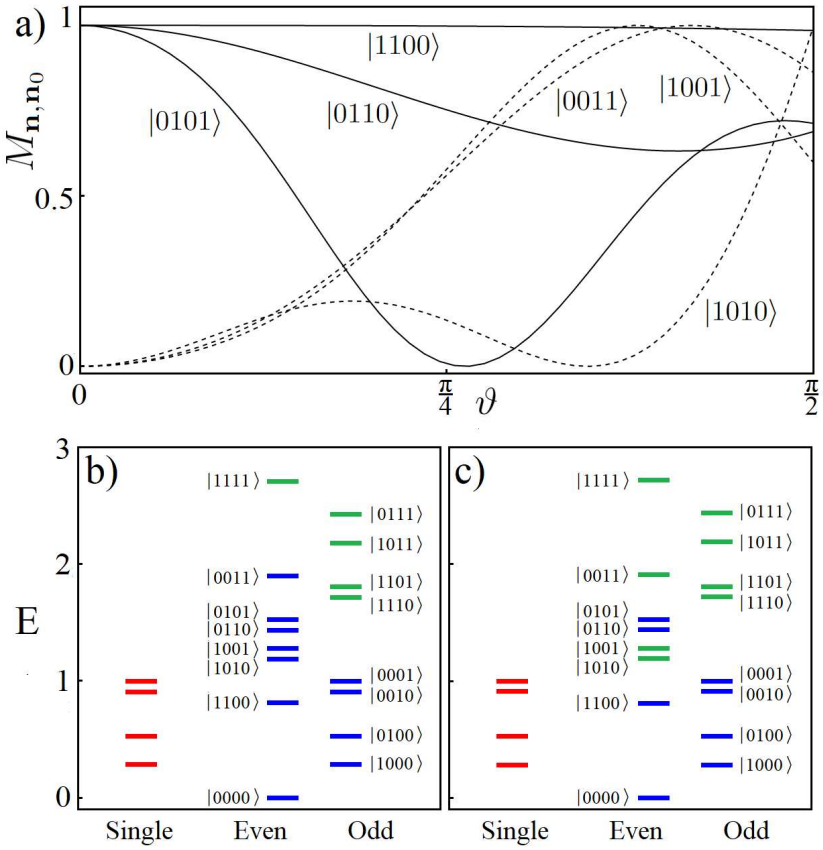

Figure 2.7: Transition rates as well as single- and many-body Andreev states for a Josephson junction with the parameters in Fig. 2.6 and finite SOI and Zeeman field. (a) Transition rates $M_{\mathbf{n},\mathbf{n}_0}$ from the ground state $|\mathbf{n}_0\rangle = |0000\rangle$ to each of the six two-quasiparticle states (cf. the first row of Table 2.1) vs the angle ϑ between the SOI axis and the Zeeman field. We only show non-zero transition rates within the same parity sector, where each rate is normalized to its maximum value in order to allow for a comparison of their ϑ-dependence. The target state $|\mathbf{n}\rangle$ is specified near each curve. Solid (dashed) lines correspond to transitions which are allowed (forbidden) by selection rules for $\vartheta \to 0$. (b) Single and many-body states for $\mathbf{b}$ in the x-direction, i.e., for $\vartheta = \pi/2$, cf. Fig. 2.6(c), with phase difference $\phi_0 = 1.08\pi$. The red levels show the positive-energy single-particle ABS levels. The many-body states with zero (non-zero) transition rate $M_{\mathbf{n},\mathbf{n}_0}$ from the ground state are shown as green (blue) levels. (c) Same as panel (b) but with the Zeeman field along the z-direction, i.e., for $\vartheta = 0$, cf. Fig. 2.6(d).

case without SOI and Zeeman field, by properly tuning φ_0, one can thus select which states can be accessed by an external perturbation.

Further we will be studying dynamical parity stabilization for the phase difference value $\phi_0 = 1.08\pi$, with $\vartheta = \pi/2$ and $\vartheta = 0$. From Fig. 2.8 we see that for $\vartheta = \pi/2$ all six transitions rates are different from zero, while three of them vanish for $\vartheta \to 0$.

2.4.3 Observing dynamical parity stabilization

No SOI and magnetic field.— First, we consider the case with $\gamma_{SO} = 0$ and $\mathbf{b} = 0$, and using the transfer matrix from Ref. [34], and compare the obtained results to those from the Ref. [34].

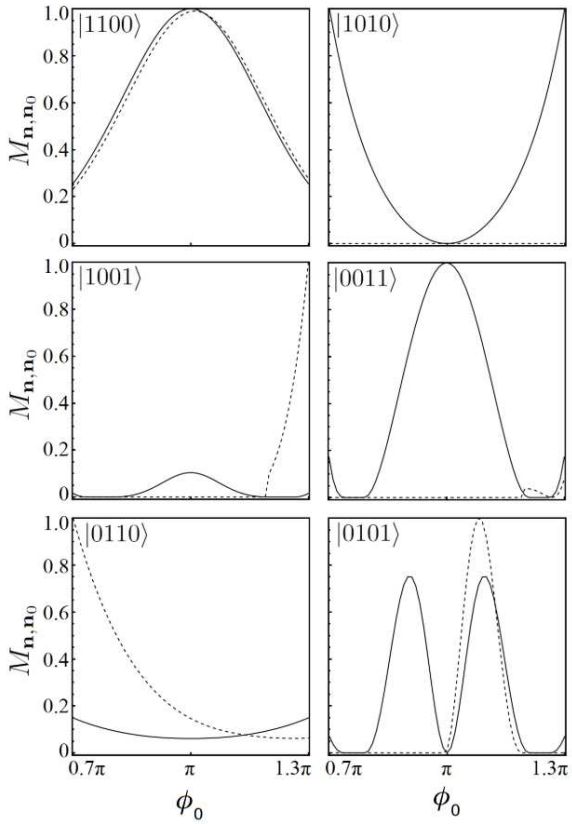

Figure 2.8: Transition rates $M_{\mathbf{n},\mathbf{n}_0}$ from the ground state $|\mathbf{n}_0\rangle$ to each of the six possible two-quasiparticle states $|\mathbf{n}\rangle$ vs phase difference ϕ_0 for a Josephson junction with the parameters in Fig. 2.6. The target states $|\mathbf{n}\rangle$ are shown in each panel. Solid (dashed) lines correspond to the angle $\vartheta = \pi/2$ ($\vartheta = 0$) between $\mathbf{b}$ and the SOI polar axis. In each panel, transition rates are normalized to their maximum value in the shown interval.

As expected, our scheme precisely reproduces the results of Ref. [34] on dynamical parity stabilization after a microwave pulse. Further, we study how the interplay of SOI and Zeeman field influences this phenomenon. For clarity, we focus on the system parameters corresponding to panels (c) (SOI and magnetic field perpendicular to the SOI direction) and (d) (SOI and magnetic field parallel to the SOI direction) in Fig. 2.6.

Magnetic field perpendicular to the SOI direction. — We procede with the case shown in Fig. 2.6(c), where the Zeeman field is oriented along the nanowire direction, and perpendicular to the SOI orientation (this configuration is typically considered for the generation of Majorana bound states at the nanowire ends [61]). Applying a resonant microwave drive, one can then drive six different transitions out of the ground state $|\mathbf{n}_0\rangle$. In Fig. 2.7(b), the corresponding single-particle and many-body Andreev states are shown. Starting from the ground state, all transitions to states with one or two quasiparticles have a non-zero transition rate $M_{\mathbf{n},\mathbf{n}_0}$. However, as discussed earlier, only transitions to states with the same parity can be induced by the microwave pulse. In Fig. 2.9, we show the population dynamics after three of these microwave-induced transitions:

a) In Fig. 2.9(a), we consider a resonant transition $|0000\rangle \to |1001\rangle$, (driving the transition $|0000\rangle \to |1010\rangle$ instead gives very similar results).

b) In Fig. 2.9(b), we consider the resonant microwave-induced transition $|0000\rangle \to |0110\rangle$,

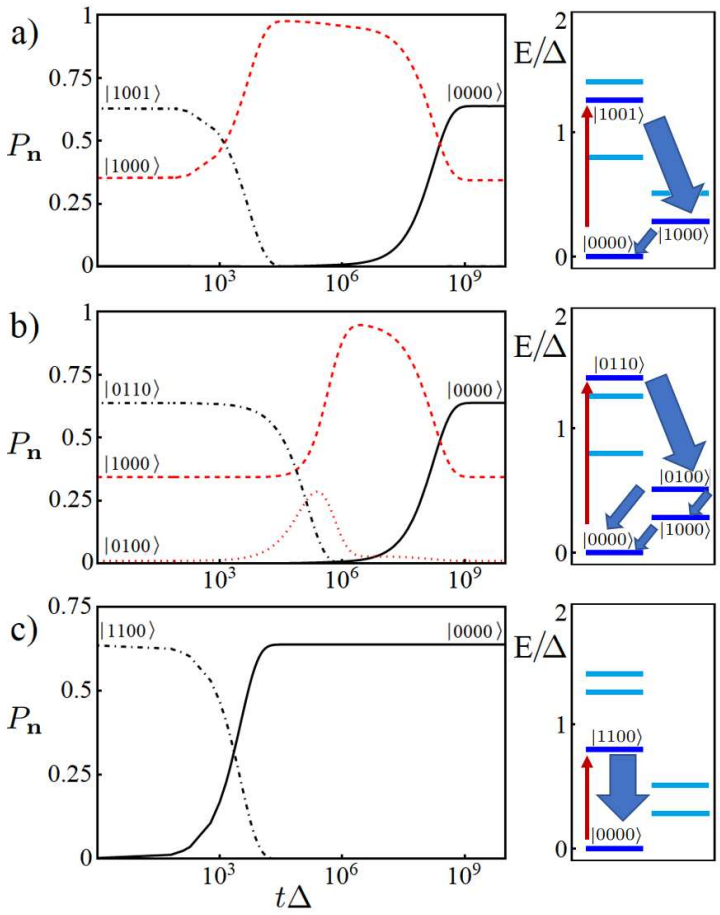

Figure 2.9: Many-body Andreev state population dynamics $P_{\mathbf{n}}(t)$ vs time (in units of Δ^{-1}) for a Josephson junction with the parameters in Fig. 2.6(c), with **b** in the x-direction and phase difference $\phi_0 = 1.08\pi$. We use $\kappa_0 = 0.1$, $\Omega = 10^{-3}\Delta$, and $\eta_d = 0.01\Delta$ in the spectral density (2.37), with the background Ohmic part determined by $\alpha_0 = 10^{-4}$ and $\omega_c = \Delta$. We use the temperature scales $T_{\rm qp} = 0.15\Delta$ and $T_{\rm env} = 0.07\Delta$. Note the logarithmic time scales. We show only the curves for many-body levels with time-dependent probability weights. (There is some time-independent probability weight in other levels.) Red curves correspond to odd-parity states, black curves to even-parity states. Three different transitions are shown in panels (a), (b), and (c), respectively, which can be induced by a microwave drive from the ground state $|0000\rangle$. These transitions are shown as red arrows in the corresponding right column panels, where selected many-body Andreev energy levels are depicted; we again distinguish even- and odd-parity states, cf. the right panel of Fig. 2.3. Thick (thin) arrows indicate large (small) transition rates connecting many-body Andreev states, cf. Table 2.1.

where we obtain similar results for the population dynamics after the transition $|0000\rangle \rightarrow |0101\rangle$.

c) Finally, in Fig. 2.9(c), we show the population dynamics after the transition $|0000\rangle \rightarrow |1100\rangle$, where the transition $|0000\rangle \rightarrow |0011\rangle$ gives similar results.

We observe that for the cases shown in Fig. 2.9(a,b), an *odd-parity* state (either $|1000\rangle$ or $|0100\rangle$) is occupied with large probability for a long intermediate time interval. These observations correspond to the *dynamical parity stabilization* discovered in Ref. [16]: *By driving a transition in the even-parity sector, one stabilizes the odd-parity polarization.*

It is worth noting that in Fig. 2.9(b), there is a transition between both odd-parity states, with state $|0100\rangle$ acting as an intermediate state towards $|1000\rangle$. This behavior is a consequence of the level splitting induced by both SOI and Zeeman field. Such effects can play a crucial role in further increasing the lifetime of the odd-parity polarization effect. Indeed, the energy difference between the states $|0110\rangle$ and $|0100\rangle$ (which belong to different parity sectors) is much bigger compared to the one between $|0100\rangle$ and $|1000\rangle$ (within the same parity sector). By suitably designing the electromagnetic environment such that the spectral density $J(\omega)$ exhibits a sub- or super-Ohmic behavior [62] could allow one to modify the ratio $M_{|0100\rangle,|0110\rangle}/M_{|1000\rangle,|0100\rangle}$. In that way, one may be able to further stabilize the lifetime of transient states as discussed, for example, in Ref. [63].

It is also possible to drive the system by a microwave pulse connecting two states in the odd-parity sector, and to thereby polarize the even-parity sector, but we do not discuss this case here.

Reason for dynamical parity stabilization.— In our model, the reason for the dynamical stabilization is the existence of a large many-body transition rate into the respective odd-parity many-body state, cf. Table 2.1. The largeness of the rate can be understood from the closeness of some ABSs to the quasiparticle continuum. Note that all the parity-changing transitions between the many-body Andreev states proceed through the continuum. Thus, if the even-parity state excited by the microwave pulse is energetically close to the continuum states, there is a high probability for this state to decay into an odd-parity state. At the same time, the transition rate from the odd-parity state into the even-parity ground state $|0000\rangle$ is very small since the ground state and the relevant odd-parity ABSs are far away from the quasiparticle continuum. This mechanism can explain the stabilization of the odd-parity polarization at intermediate time scales [34]. However, for the transition in Fig. 2.9(c), since the state $|1100\rangle$ is energetically far away from the continuum, the vanishing rate from the excited even-parity state into the intermediate odd-parity state excludes this phenomenon.

Additionally, from Fig. 2.9 we can conclude that the combined effects of SOI and Zeeman field may result in qualitative changes in the many-body population dynamics in the Andreev sector. Indeed, the energy splitting induced by the SOI and the Zeeman field allows one to have a non-zero spectral density (2.37), and thus a non-zero transition rate between states which are otherwise disconnected. At the same time, selection rules are less restrictive due to the fact that orbital and spin angular momenta are no longer conserved. As a consequence, a wider set of initial conditions can be explored, exhibiting different parity polarization behavior depending on precisely which transition is driven.

Magnetic field parallel to the SOI direction. — Next we turn to the parameter choice corresponding to Fig. 2.6(d), where the Zeeman field is oriented along the z-direction. We then obtain the population dynamics shown in the left column of Fig. 2.10, where the three panels (a), (b), and (c) correspond to the three possible transitions from the ground state $|\mathbf{n}_0\rangle$ which can be induced by a resonant microwave field and which are allowed by selection rules. In Fig. 2.7(c), we show the single-particle and many-body Andreev states for $\vartheta = 0$, where the Zeeman field is aligned along the z-direction. As in Fig. 2.7(b), we have highlighted all states that exhibit a non-zero transition rate $M_{\mathbf{n},\mathbf{n}_0}$ with the ground state. This is in contrast to the

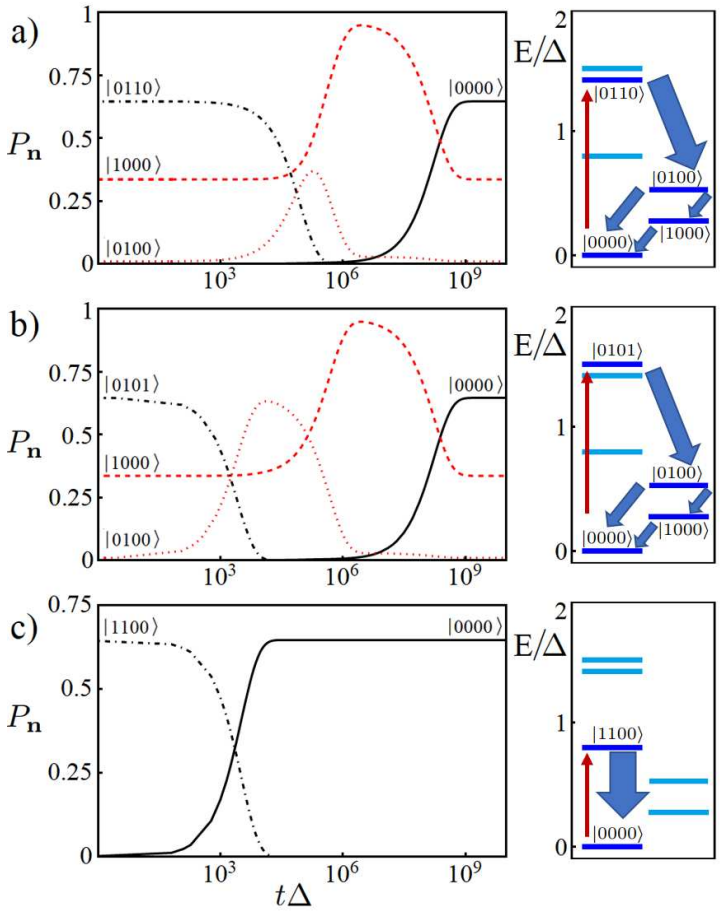

Figure 2.10: Many-body Andreev state population dynamics $P_{\mathbf{n}}(t)$ vs time (in units of Δ^{-1}) for the parameters in Fig. 2.6(d), with $\mathbf{b}$ in the z-direction and the phase difference $\phi_0 = 1.08\pi$. The spectral density of the environment was taken as in Fig. 2.9. Note the logarithmic time scales. We show only the curves for many-body levels with time-dependent probability weights. (There is some time-independent probability weight in other levels.) Red curves correspond to odd-parity states, black curves to even-parity states. In contrast to the case in Fig. 2.6, here only three transitions, corresponding to panels (a), (b), and (c), can be induced by a microwave drive starting from the ground state $|\mathbf{n}_0\rangle$ because of selection rules. These transitions are shown as red arrows in the corresponding right column panels, where selected many-body Andreev energy levels are depicted. Thick (thin) arrows indicate large (small) many-body transition rates.

case shown in Fig. 2.9 with a Zeeman field in the x-direction ($\vartheta = \pi/2$), where six transitions are allowed by selection rules but we show only three of those. For the microwave-induced transitions shown in panels (a) and (b) of Fig. 2.10, we again observe a dynamical polarization of the odd-parity sector at intermediate times, where two odd-parity states are relevant. For the transition shown in panel (c), we once more encounter a case where a vanishing transition rate into the odd-parity state excludes dynamical parity polarization. The qualitative impact of SOI and Zeeman field on this phenomenon is therefore of similar importance as for the case shown in Fig. 2.9.

Dependence of dynamical parity stabilization on the magnetic field orientation.— In Fig. 2.11, we study how the dynamical parity polarization effect depends on the angle ϑ. We examine all six transitions $|\mathbf{n}_0\rangle \rightarrow |\mathbf{n}\rangle$ that can in principle be excited by a resonant microwave driving

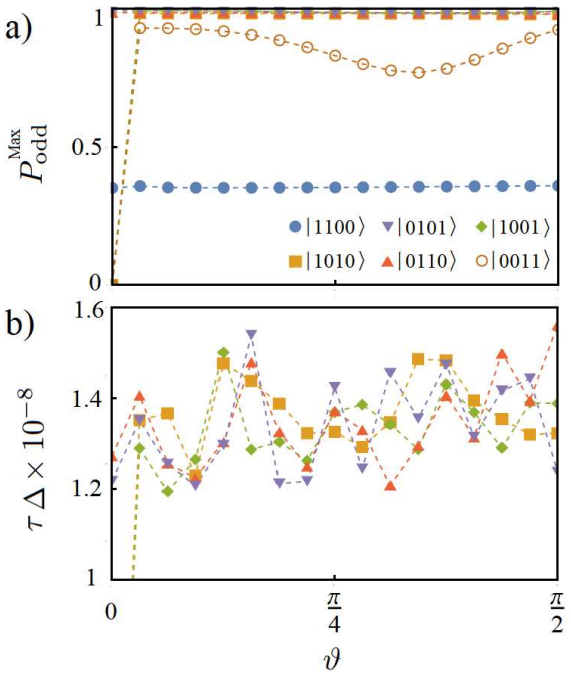

Figure 2.11: Dynamical parity polarization as a function of the angle ϑ between the Zeeman field and the polar SOI axis. The spectral density of the environment was taken as in Fig. 2.9. (a) Maximally achievable odd-parity polarization $P_{\rm odd}^{\rm Max}$ vs ϑ after each of the six possible microwave-induced transitions $|\mathbf{n_0}\rangle \to |\mathbf{n}\rangle$. We use the system parameters corresponding to Fig. 2.9 (where $\vartheta = \pi/2$) and Fig. 2.10 (where $\vartheta = 0$). Dashed lines are guides to the eye only. Different symbols correspond to the excited initial states $|\mathbf{n}\rangle$, as explained in the legend. (b) Odd-parity lifetime τ (in units of $10^8\Delta^{-1}$) vs ϑ for the six transitions in panel (a). For two of these transitions, the lifetime is very short and does not appear on the scale of the figure. Dashed lines are guides to the eye only. The symbols are used as in panel (a).

pulse. For each $|\mathbf{n}\rangle$, we determine the maximal probability for occupying the odd-parity sector during the time evolution, $P_{\rm odd}^{\rm Max}$, and the lifetime of the corresponding odd-parity states, τ. We define the latter time scale as the half-width of the corresponding broad peak in $P_{\rm odd}(t)$, see Figs. 2.9 and 2.10. We observe from Fig. 2.11(a) that the achievable odd-parity polarization depends significantly on which transition is driven, while there is only a weak dependence on the angle ϑ (except near $\vartheta = 0$). Importantly, almost full odd-parity polarization is possible for several resonant drive frequencies while for other drive frequencies, the system does not get polarized at all, see Fig. 2.9(c) and Fig. 2.10(c). As shown in Fig. 2.11(b), the lifetime τ of the odd-parity polarization state is rather insensitive of the angle ϑ as long as one chooses one of the drive frequencies corresponding to large $P_{\rm odd}^{\rm Max}$. The variations in Fig. 2.11(b) come from changes in the transition rates $\Gamma_{\mu,\nu}$ with ϑ. We conclude that the combined effect of SOI and Zeeman fields can influence the dynamical polarization effect, both concerning the degree of polarization and (to a lesser degree) the achievable lifetimes.

2.5 Summary

In this chapter, we have constructed a theoretical approach for describing the many-body quantum dynamics of superconducting systems with spin-orbit coupling and magnetic fields. Such systems can be efficiently described in terms of a doubled Nambu spinor approach,

where one keeps the electron and hole spinors with both spin projections. This doubling of the actual number of degrees of freedom is referred to as double-counting problem and can give rise to spurious many-body effects if the theory is constructed in a cavalier manner. We resolve this general problem by working in the so-called excitation picture, where only the positive single-particle solutions of the BdG equation are employed to construct the many-body theory. This is possible since the negative-energy solutions are related to the corresponding positive-energy solutions by particle-hole symmetry, and we systematically exploit this relation in our approach.

We apply our general formalism to a Josephson junction formed by a clean 1D nanowire with spin-orbit coupling in a Zeeman field, which is tunnel-coupled at its end to superconducting banks. The junction is embedded in a loop and inductively coupled to a microwave resonator, see Fig. 2.1. In the absence of the electromagnetic environment defined by the resonator, the BdG single-particle problem can be solved exactly. This solution provides a convenient basis for the construction of many-body states. From the diagonal elements of the reduced density operator of the many-body Andreev bound states, the Lindblad equation derived in Sec. 2.3 then yields a matrix rate equation for the population dynamics of the corresponding many-body Andreev states. We here study how the corresponding populations evolve in time after a strong initial microwave pulse driving a specific transition. This question is related to the dynamical parity stabilization phenomenon discovered experimentally in Ref. [16]. Previous results [34] for the simpler case without spin-orbit coupling and without Zeeman field are recovered by our results. We find that, depending on the microwave driving frequency, the maximally reachable parity polarization $P_{\rm odd}^{\rm Max}$ and, to a lesser degree, the time scale over which the odd-parity sector becomes dynamically stabilized, show a dependence on the angle ϑ between the spin-orbit polar axis and the Zeeman field. Our results suggest that one can optimize the parity stabilization mechanism by proper field alignment.

To conclude, we have introduced a systematic theoretical framework for studying the quantum many-body dynamics of superconducting systems where a doubling of the fermionic space is indicated, e.g., due to the presence of spin-orbit interactions and Zeeman fields. The presence of particle-hole symmetry then implies that the excitation picture allows for the construction of a many-body theory free from the double-counting problem. The approach to the dynamics of many-body systems with double-counting proposed here could be useful also for other theoretical many-body studies.

Appendix: BdG solutions

In this Appendix, we summarize the solution of the BdG problem defined by Eq. (2.24) and the supercurrent matrix elements in Eq. (2.29). For simplicity, we set $\Delta = v_F = 1$ below.

A Andreev bound states

We begin with ABS solutions ($\mu = \lambda$) with dispersion $E = E_\lambda(\varphi_0)$. For $|E| < \Delta$, with the Heaviside step function $\Theta(x)$ and the Nambu spinor form in Eq. (2.2), ABS solutions of the BdG equation are given by

$$\begin{aligned}\Phi_{E,\lambda}(x) = \Theta(-x)e^{\kappa_\lambda x}\big(&a_{\lambda,\uparrow}\psi_{\lambda,h,+,\uparrow} + a_{\lambda,\downarrow}\psi_{\lambda,h,+,\downarrow} + b_{\lambda,\uparrow}\psi_{\lambda,e,-,\uparrow} + b_{\lambda,\downarrow}\psi_{\lambda,e,-,\downarrow}\big)\\ &+ \Theta(x)e^{-\kappa_\lambda x}\big(c_{\lambda,\uparrow}\psi_{\lambda,e,+,\uparrow} + c_{\lambda,\downarrow}\psi_{\lambda,e,+,\downarrow} + d_{\lambda,\uparrow}\psi_{\lambda,h,-,\uparrow} + d_{\lambda,\downarrow}\psi_{\lambda,h,-,\downarrow}\big),\end{aligned}$$

where $\psi_{\lambda,e/h,\pm,\uparrow/\downarrow}$ are electron/hole, right-/left-movers, spin-up-/spin-down 8 component Nambu spinors of the λth ABS solution.

The logic behind the (a, b, c, d) coefficients is the following: for an electron falling on the contact there are 4 possible scattering processes: it can get Andreev reflected into a hole (process

a), it can get reflected back into an electron (process b), it can get converted into an electron on the other side of the contact (process c), or lastly it can get converted into a hole on the other side of the contact (process d). These scattering processes are schematically shown on Fig. (12). Since BdG equation does not involve spin, its solution is identical for both spin

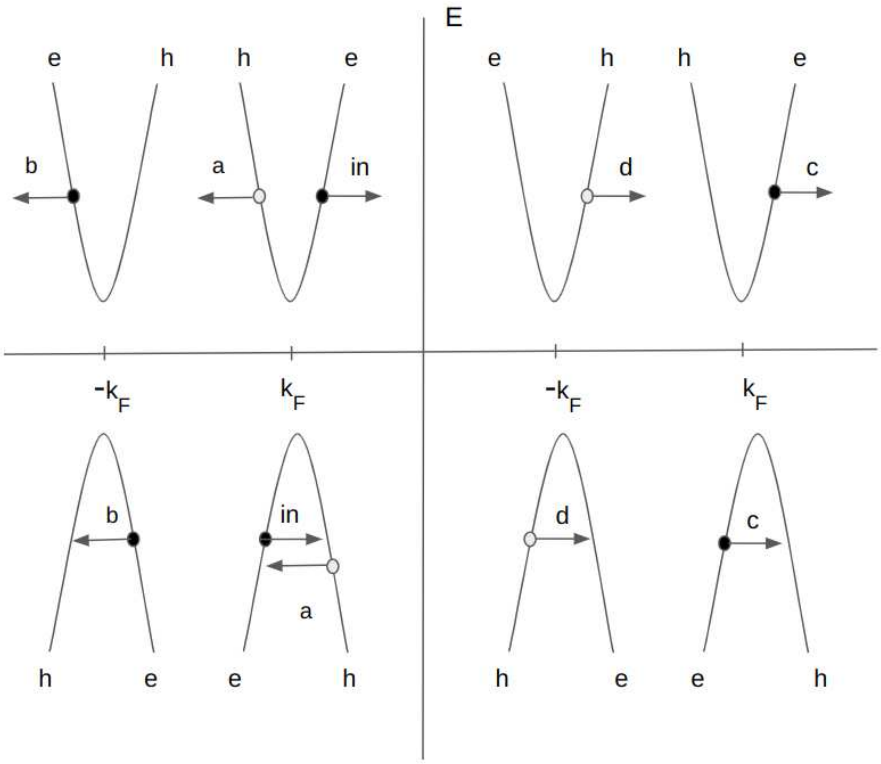

Figure 12: Schematic illustration of scattering of an incoming electron from the junction: 4 type of scattering processes, of types a, b, c and d are shown.

projections. Therefore, as in the case without spin, from Eq. (2.23) we find

$$(E_\lambda \mp i\kappa_\lambda \tau_z - \tau_x)\psi_{\lambda,e/h} = 0. \tag{.51}$$

Inserting the Pauli matrices, one finds

$$E_\lambda^2 + \kappa_\lambda^2 = 1.$$

Therefore, we define $E_\lambda = \cos(\gamma_\lambda)$, $\kappa_\lambda = \sin(\gamma_\lambda)$ and choose $\gamma_\lambda \in (0, \pi)$. For the electron and hole solutions of the BdG Eq. (.51) one derives

$$\psi_{\lambda,e} = \frac{1}{\sqrt{2}}\begin{pmatrix} e^{i\gamma_\lambda/2} \\ e^{-i\gamma_\lambda/2} \end{pmatrix} = \frac{e^{i\tau_z\gamma_\lambda/2}}{\sqrt{2}}\begin{pmatrix} 1 \\ 1 \end{pmatrix}, \quad \psi_{\lambda,h} = \frac{e^{-i\tau_z\gamma_\lambda/2}}{\sqrt{2}}\begin{pmatrix} 1 \\ 1 \end{pmatrix}.$$

Form this, for the electron branch we obtain

$$\psi_{\lambda,e,+,\uparrow} = \frac{1}{\sqrt{2}}\left(e^{i\gamma_\lambda/2} \quad 0 \quad 0 \quad 0 \quad e^{-i\gamma_\lambda/2} \quad 0 \quad 0 \quad 0\right)^T,$$

$$\psi_{\lambda,e,+,\downarrow} = \frac{1}{\sqrt{2}}\left(0 \quad e^{i\gamma_\lambda/2} \quad 0 \quad 0 \quad 0 \quad e^{-i\gamma_\lambda/2} \quad 0 \quad 0\right)^T,$$

$$\psi_{\lambda,e,-,\uparrow} = \frac{1}{\sqrt{2}}\left(0 \quad 0 \quad e^{i\gamma_\lambda/2} \quad 0 \quad 0 \quad 0 \quad e^{-i\gamma_\lambda/2} \quad 0\right)^T,$$

$$\psi_{\lambda,e,-,\uparrow} = \frac{1}{\sqrt{2}}\left(0 \quad 0 \quad 0 \quad e^{i\gamma_\lambda/2} \quad 0 \quad 0 \quad 0 \quad e^{-i\gamma_\lambda/2}\right)^T.$$

Similarly, for the hole branch we find

$$\psi_{\lambda,h,+,\uparrow} = \frac{1}{\sqrt{2}}\left(e^{-i\gamma_\lambda/2} \quad 0 \quad 0 \quad 0 \quad e^{i\gamma_\lambda/2} \quad 0 \quad 0 \quad 0\right)^T,$$

$$\psi_{\lambda,h,+,\downarrow} = \frac{1}{\sqrt{2}}\left(0 \quad e^{-i\gamma_\lambda/2} \quad 0 \quad 0 \quad 0 \quad e^{i\gamma_\lambda/2} \quad 0 \quad 0\right)^T,$$

$$\psi_{\lambda,h,-,\uparrow} = \frac{1}{\sqrt{2}}\left(0 \quad 0 \quad e^{-i\gamma_\lambda/2} \quad 0 \quad 0 \quad 0 \quad e^{i\gamma_\lambda/2} \quad 0\right)^T,$$

$$\psi_{\lambda,h,-,\uparrow} = \frac{1}{\sqrt{2}}\left(0 \quad 0 \quad 0 \quad e^{-i\gamma_\lambda/2} \quad 0 \quad 0 \quad 0 \quad e^{i\gamma_\lambda/2}\right)^T.$$

Combining the spin projections into a single vector $a_\lambda = (a_{\lambda,\uparrow}, a_{\lambda,\downarrow})^T$, and similarly for b_λ, c_λ, and d_λ, we obtain the wavefunction of the ABS,

$$\Phi_{E,\lambda}(x) = \frac{\Theta(-x)e^{\kappa_\lambda x}}{\sqrt{2}}\begin{pmatrix} a_\lambda e^{-i\gamma_\lambda/2} \\ b_\lambda e^{i\gamma_\lambda/2} \\ a_\lambda e^{i\gamma_\lambda/2} \\ b_\lambda e^{-i\gamma_\lambda/2}\end{pmatrix} + \frac{\Theta(x)e^{-\kappa_\lambda x}}{\sqrt{2}}\begin{pmatrix} c_\lambda e^{i\gamma_\lambda/2} \\ d_\lambda e^{-i\gamma_\lambda/2} \\ c_\lambda e^{-i\gamma_\lambda/2} \\ d_\lambda e^{i\gamma_\lambda/2}\end{pmatrix}, \tag{.52}$$

where $E_\lambda = \cos\gamma_\lambda$ and $\kappa_\lambda = \sin\gamma_\lambda$. The normalization condition for the amplitudes in Eq. (.52) is

$$\sum_\sigma \left(|a_{\lambda,\sigma}|^2 + |b_{\lambda,\sigma}|^2 + |c_{\lambda,\sigma}|^2 + |d_{\lambda,\sigma}|^2\right) = \frac{2\kappa_\lambda}{1+\kappa_\lambda L}. \tag{.53}$$

The ABS dispersion relation follows by inserting Eq. (.52) into the matching condition (2.21). Nontrivial solutions require the vanishing of a corresponding determinant, explicitly,

$$\det\left[e^{i\phi_0/2}\begin{pmatrix} e^{i\gamma_\lambda}(W_+ + r_1r_2W_-) & r_2W_+ + r_1W_- \\ r_1W_+ + r_2W_- & e^{-i\gamma_\lambda}(W_- + r_1r_2W_+)\end{pmatrix}\right.$$

$$\left. - e^{-i\phi_0/2}\begin{pmatrix} e^{-i\gamma_\lambda}\sigma_y(W_-^*(-E) + r_1r_2W_+^*(-E))\sigma_y & \sigma_y(r_2W_-^*(-E) + r_1W_+^*(-E))\sigma_y \\ \sigma_y(r_1W_-^*(-E) + r_2W_+^*(-E))\sigma_y & e^{i\gamma_\lambda}\sigma_y(W_+^*(-E) + r_1r_2W_-^*(-E))\sigma_y\end{pmatrix}\right] = 0,$$

which leads to Eq. (2.30). The corresponding eigenvectors then determine the ABS wave functions.

B Continuum states

Quasiparticle continuum states with energy $|E| > \Delta$ are labeled by the multi-index $p = (E, s, \sigma)$, with the scattering channel index $s \in \{1,2,3,4\}$ [34] which labels electron-/hole-type states coming from the left or right side and the spin index σ. The corresponding Nambu states are given by a sum of an incoming and a scattered outgoing state,

$$\Phi_p(x) = \Phi_p^{(\text{in})}(x) + \Phi_p^{(\text{out})}(x),$$

The incoming state is given by

$$\Phi_p^{(\text{in})}(x) = \Theta(-x)\frac{e^{ikx}}{\sqrt{\mathcal{L}}}\left[\delta_{s=1,\sigma}\tilde{\psi}_{e,+,\sigma} + \delta_{s=2,\sigma}\tilde{\psi}_{h,-,\sigma}\right] \tag{.54}$$

$$+ \Theta(x)\frac{e^{-ikx}}{\sqrt{\mathcal{L}}}\left[\delta_{s=3,\sigma}\tilde{\psi}_{h,+,\sigma} + \delta_{s=4,\sigma}\tilde{\psi}_{e,-,\sigma}\right],$$

where $\tilde{\psi}_{e/h,\pm,\sigma}$ are electron/hole branch, right-/left-mover, spin-up/-down type Nambu spinors for continuum states and $\mathcal{L}$ is the length of the leads. Note that in this case we have 8 scattering channels: $s = \{1,2,3,4\}$ with $\sigma = \uparrow, \downarrow$. The outgoing states are of the form

$$\Phi_p^{(\text{out})}(x) = \Theta(-x)\frac{e^{-ikx}}{\sqrt{\mathcal{L}}}\left[a_{p,\sigma'}\tilde{\psi}_{h,+,\sigma'} + b_{p,\sigma'}\tilde{\psi}_{e,-,\sigma'}\right]$$

$$+ \Theta(x)\frac{e^{ikx}}{\sqrt{\mathcal{L}}}\left[c_{p,\sigma'}\tilde{\psi}_{e,+,\sigma'} + d_{p,\sigma'}\tilde{\psi}_{h,-,\sigma'}\right].$$

Here the first index p labels the scattering channel, while each scattered wave has still upper and lower spin components, labeled by σ' index. The electron/hole Nambu spinors satisfy the following equation, derived the BdG eigenvalue problem:

$$\left(E \mp k\tau_z - \tau_x\right)\tilde{\psi}_{e/h} = 0.$$

Writing the electron spinor as $\tilde{\psi}_e = (x \;\; y)^T$ we find the following system of equations for the electron branch

$$\begin{cases} (E-k)x = y, \\ (E+k)y = x. \end{cases}$$

Solving this system we obtain the relation

$$E^2 - k^2 = 1.$$

Introducing $\tilde{\gamma} = \operatorname{arsinh}\sqrt{E^2-1} \in [0,\infty)$, we find

$$|E| = \cosh\tilde{\gamma}, \quad k = \sigma_E \sinh\tilde{\gamma}, \tag{.55}$$

where $\sigma_E = \operatorname{sgn}(E)$. The choice of the sign, similar for both E and k, is dictated by the following argument: let us consider the first term in the continuum incoming state (.54). It is given by a right-moving electron, of positive or negative energy (see also Fig. (12)). Since the electron is moving to the right side (towards the contact), its velocity $v_k = dE/dk$ has to be positive. For $\tilde{\gamma} \in (0,\infty]$, both $\cosh\tilde{\gamma}$ and $\sinh\tilde{\gamma}$ are increasing functions, which means that both $d\cosh\tilde{\gamma}$ and $d\sinh\tilde{\gamma}$ are positive increments. Therefore, to obtain a positive derivative dE/dk we need both

E and k from the above equation to have the same sign. Additionally, the following relation describing connection between Andreev and continuum states, suggests the similar result

$$\sqrt{1-(E+i0^+)^2} = \begin{cases} \sqrt{1-E^2} = \kappa(E), & \text{for } |E|<1 \\ -i\sigma_E\sqrt{E^2-1} = -ik(E), & \text{for } |E|>1 \end{cases}.$$

Following this argument we obtain

$$E-k = \sigma_E(\cosh\tilde{\gamma} - \sinh\tilde{\gamma}) = \sigma_E e^{-\tilde{\gamma}}.$$

Setting $x = e^{\tilde{\gamma}/2}$ for the electron spinor we get

$$\tilde{\psi}_e = \frac{1}{\sqrt{2\cosh\tilde{\gamma}}}\begin{pmatrix} e^{\tilde{\gamma}/2} \\ \sigma_E\, e^{-\tilde{\gamma}/2} \end{pmatrix}.$$

Taking into account the structure of the full Nambu spinor for the electron branch right-/left-mover spin-up/-down Nambu spinors we obtain

$$\tilde{\psi}_{e,+,\uparrow} = \frac{1}{\sqrt{2\cosh\tilde{\gamma}}}\begin{pmatrix} e^{\tilde{\gamma}/2} & 0 & 0 & 0 & \sigma_E\, e^{-\tilde{\gamma}/2} & 0 & 0 & 0 \end{pmatrix}^T,$$

$$\tilde{\psi}_{e,+,\downarrow} = \frac{1}{\sqrt{2\cosh\tilde{\gamma}}}\begin{pmatrix} 0 & e^{\tilde{\gamma}/2} & 0 & 0 & 0 & \sigma_E\, e^{-\tilde{\gamma}/2} & 0 & 0 \end{pmatrix}^T,$$

$$\tilde{\psi}_{e,-,\uparrow} = \frac{1}{\sqrt{2\cosh\tilde{\gamma}}}\begin{pmatrix} 0 & 0 & e^{\tilde{\gamma}/2} & 0 & 0 & 0 & \sigma_E\, e^{-\tilde{\gamma}/2} & 0 \end{pmatrix}^T,$$

$$\tilde{\psi}_{e,-,\downarrow} = \frac{1}{\sqrt{2\cosh\tilde{\gamma}}}\begin{pmatrix} 0 & 0 & 0 & e^{\tilde{\gamma}/2} & 0 & 0 & 0 & \sigma_E\, e^{-\tilde{\gamma}/2} \end{pmatrix}^T.$$

Similarly, for the hole spinor we find

$$\tilde{\psi}_h = \frac{1}{\sqrt{2\cosh\tilde{\gamma}}}\begin{pmatrix} e^{-\tilde{\gamma}/2} \\ \sigma_E\, e^{\tilde{\gamma}/2} \end{pmatrix}.$$

The hole branch right-/left-mover spin-up/-down Nambu spinors are given by

$$\tilde{\psi}_{h,+,\uparrow} = \frac{1}{\sqrt{2\cosh\tilde{\gamma}}}\begin{pmatrix} e^{-\tilde{\gamma}/2} & 0 & 0 & 0 & \sigma_E\, e^{\tilde{\gamma}/2} & 0 & 0 & 0 \end{pmatrix}^T,$$

$$\tilde{\psi}_{h,+,\downarrow} = \frac{1}{\sqrt{2\cosh\tilde{\gamma}}}\begin{pmatrix} 0 & e^{-\tilde{\gamma}/2} & 0 & 0 & 0 & \sigma_E\, e^{\tilde{\gamma}/2} & 0 & 0 \end{pmatrix}^T,$$

$$\tilde{\psi}_{h,-,\uparrow} = \frac{1}{\sqrt{2\cosh\tilde{\gamma}}}\begin{pmatrix} 0 & 0 & e^{-\tilde{\gamma}/2} & 0 & 0 & 0 & \sigma_E\, e^{\tilde{\gamma}/2} & 0 \end{pmatrix}^T,$$

$$\tilde{\psi}_{h,-,\downarrow} = \frac{1}{\sqrt{2\cosh\tilde{\gamma}}}\begin{pmatrix} 0 & 0 & 0 & e^{-\tilde{\gamma}/2} & 0 & 0 & 0 & \sigma_E\, e^{\tilde{\gamma}/2} \end{pmatrix}^T.$$

Summarizing the above calculations, an incoming state of type s can be written as

$$\Phi_p^{(\mathrm{in})}(x) = \frac{\Theta(-x)}{\sqrt{2\cosh\tilde{\gamma}}}\frac{e^{ikx}}{\sqrt{\mathcal{L}}}\begin{pmatrix} \delta_{s,1}\delta_{\sigma,\uparrow}\, e^{\tilde{\gamma}/2} \\ \delta_{s,1}\delta_{\sigma,\downarrow}\, e^{\tilde{\gamma}/2} \\ \delta_{s,2}\delta_{\sigma,\uparrow}\, e^{-\tilde{\gamma}/2} \\ \delta_{s,2}\delta_{\sigma,\downarrow}\, e^{-\tilde{\gamma}/2} \\ \delta_{s,1}\delta_{\sigma,\uparrow}\,\sigma_E e^{-\tilde{\gamma}/2} \\ \delta_{s,1}\delta_{\sigma,\downarrow}\,\sigma_E e^{-\tilde{\gamma}/2} \\ \delta_{s,2}\delta_{\sigma,\uparrow}\,\sigma_E e^{\tilde{\gamma}/2} \\ \delta_{s,2}\delta_{\sigma,\downarrow}\,\sigma_E e^{\tilde{\gamma}/2} \end{pmatrix} + \frac{\Theta(x)}{\sqrt{2\cosh\tilde{\gamma}}}\frac{e^{-ikx}}{\sqrt{\mathcal{L}}}\begin{pmatrix} \delta_{s,3}\delta_{\sigma,\uparrow}\, e^{-\tilde{\gamma}/2} \\ \delta_{s,3}\delta_{\sigma,\downarrow}\, e^{-\tilde{\gamma}/2} \\ \delta_{s,4}\delta_{\sigma,\uparrow}\, e^{\tilde{\gamma}/2} \\ \delta_{s,4}\delta_{\sigma,\downarrow}\, e^{\tilde{\gamma}/2} \\ \delta_{s,3}\delta_{\sigma,\uparrow}\,\sigma_E e^{\tilde{\gamma}/2} \\ \delta_{s,3}\delta_{\sigma,\downarrow}\,\sigma_E e^{\tilde{\gamma}/2} \\ \delta_{s,4}\delta_{\sigma,\uparrow}\,\sigma_E e^{-\tilde{\gamma}/2} \\ \delta_{s,4}\delta_{\sigma,\downarrow}\,\sigma_E e^{-\tilde{\gamma}/2} \end{pmatrix}, \tag{.56}$$

where $|E|$ and $k(E)$, with $\tilde{\gamma}(E) \in [0,\infty)$, are defined in Eq. (.55). Similarly, for a given incident (incoming) state with quantum numbers p, the scattered (outgoing) state is written as

$$\Phi_p^{(\mathrm{out})}(x) = \frac{\Theta(-x)}{\sqrt{2\cosh\tilde{\gamma}}}\frac{e^{ikx}}{\sqrt{\mathcal{L}}}\begin{pmatrix} a_{p,\uparrow}\, e^{-\tilde{\gamma}/2} \\ a_{p,\downarrow}\, e^{-\tilde{\gamma}/2} \\ b_{p,\uparrow}\, e^{\tilde{\gamma}/2} \\ b_{p,\downarrow}\, e^{\tilde{\gamma}/2} \\ a_{p,\uparrow}\,\sigma_E e^{\tilde{\gamma}/2} \\ a_{p,\downarrow}\,\sigma_E e^{\tilde{\gamma}/2} \\ b_{p,\uparrow}\,\sigma_E e^{-\tilde{\gamma}/2} \\ b_{p,\downarrow}\,\sigma_E e^{-\tilde{\gamma}/2} \end{pmatrix} + \frac{\Theta(x)}{\sqrt{2\cosh\tilde{\gamma}}}\frac{e^{-ikx}}{\sqrt{\mathcal{L}}}\begin{pmatrix} c_{p,\uparrow}\, e^{\tilde{\gamma}/2} \\ c_{p,\downarrow}\, e^{\tilde{\gamma}/2} \\ d_{p,\uparrow}\, e^{-\tilde{\gamma}/2} \\ d_{p,\downarrow}\, e^{-\tilde{\gamma}/2} \\ c_{p,\uparrow}\,\sigma_E e^{-\tilde{\gamma}/2} \\ c_{p,\downarrow}\,\sigma_E e^{-\tilde{\gamma}/2} \\ d_{p,\uparrow}\,\sigma_E e^{\tilde{\gamma}/2} \\ d_{p,\downarrow}\,\sigma_E e^{\tilde{\gamma}/2} \end{pmatrix}. \tag{.57}$$

One can then determine the scattering amplitudes, and thereby the quasiparticle wave functions, by inserting the above Ansatz into the matching condition (2.21). This implies a linear algebra problem that can easily be solved numerically. Explicitly, we obtain the equations

$$\begin{pmatrix} a_{p,\uparrow}e^{-\tilde{\gamma}/2} + \delta_{s=1,\sigma=\uparrow}e^{\tilde{\gamma}/2} \\ a_{p,\downarrow}e^{-\tilde{\gamma}/2} + \delta_{s=1,\sigma=\downarrow}e^{\tilde{\gamma}/2} \\ b_{p,\uparrow}e^{\tilde{\gamma}/2} + \delta_{s=2,\uparrow}e^{-\tilde{\gamma}/2} \\ b_{p,\downarrow}e^{\tilde{\gamma}/2} + \delta_{s=2,\downarrow}e^{-\tilde{\gamma}/2} \end{pmatrix} = e^{i\phi_0/2}\, T(\theta) \begin{pmatrix} c_{p,\uparrow}e^{\tilde{\gamma}/2} + \delta_{s=3,\sigma=\uparrow}e^{-\tilde{\gamma}/2} \\ c_{p,\downarrow}e^{\tilde{\gamma}/2} + \delta_{s=3,\sigma=\downarrow}e^{-\tilde{\gamma}/2} \\ d_{p,\uparrow}e^{-\tilde{\gamma}/2} + \delta_{s=4,\sigma=\uparrow}e^{\tilde{\gamma}/2} \\ d_{p,\downarrow}e^{-\tilde{\gamma}/2} + \delta_{s=4,\sigma=\downarrow}e^{\tilde{\gamma}/2} \end{pmatrix},$$

$$\begin{pmatrix} a_{p,\uparrow}e^{\tilde{\gamma}/2} + \delta_{s=1,\sigma=\uparrow}e^{-\tilde{\gamma}/2} \\ a_{p,\downarrow}e^{\tilde{\gamma}/2} + \delta_{s=1,\sigma=\downarrow}e^{-\tilde{\gamma}/2} \\ b_{p,\uparrow}e^{-\tilde{\gamma}/2} + \delta_{s=2,\sigma=\uparrow}e^{\tilde{\gamma}/2} \\ b_{p,\downarrow}e^{-\tilde{\gamma}/2} + \delta_{s=2,\sigma=\downarrow}e^{\tilde{\gamma}/2} \end{pmatrix} = e^{-i\phi_0/2}\,\sigma_y T(-\theta)^*_{-\alpha}\sigma_y \begin{pmatrix} c_{p,\uparrow}e^{-\tilde{\gamma}/2} + \delta_{s=3,\sigma=\uparrow}e^{\tilde{\gamma}/2} \\ c_{p,\downarrow}e^{-\tilde{\gamma}/2} + \delta_{s=3,\sigma=\downarrow}e^{\tilde{\gamma}/2} \\ d_{p,\uparrow}e^{\tilde{\gamma}/2} + \delta_{s=4,\sigma=\uparrow}e^{-\tilde{\gamma}/2} \\ d_{p,\downarrow}e^{\tilde{\gamma}/2} + \delta_{s=4,\sigma=\downarrow}e^{-\tilde{\gamma}/2} \end{pmatrix}.$$

The normalization condition for the complex-valued scattering amplitudes $(a_{p,\sigma}, b_{p,\sigma}, c_{p,\sigma}, d_{p,\sigma})$ is given by

$$\sum_\sigma \left(|a_{p,\sigma}|^2 + |b_{p,\sigma}|^2 + |c_{p,\sigma}|^2 + |d_{p,\sigma}|^2\right) = 1. \tag{.58}$$

C Current matrix elements

Useful integrals for current matrix elements.— Here we list the integrals used for the calculation of the supercurrent matrix elements:

$$\int_{x<0} dx \left[\Theta(-x)e^{\kappa_\lambda x} + \Theta(x)e^{-\kappa_\lambda x}\right] = \int_{-\infty}^{0} dx e^{\kappa_\lambda x} = \frac{1}{\kappa_\lambda},$$
$$-\int_{x>0} dx \left[\Theta(-x)e^{\kappa_\lambda x} + \Theta(x)e^{-\kappa_\lambda x}\right] = -\int_{0}^{\infty} dx e^{-\kappa_\lambda x} = -\frac{1}{\kappa_\lambda}.$$

Next we discuss the current matrix elements $\mathcal{I}_{\mu,\nu}$ in Eq. (2.29).

ABS to ABS current.— First, if both indices $(\mu,\nu) = (\lambda,\lambda')$ correspond to ABSs, we obtain

$$\bar{\psi}^{(\lambda)}_{e/h}\,\tau_z\,\psi^{(\lambda')}_{e/h} = \frac{1}{2}\begin{pmatrix} e^{\mp i\gamma_\lambda/2} & e^{\pm i\gamma_\lambda/2}\end{pmatrix}\begin{pmatrix}1 & \\ & -1\end{pmatrix}\begin{pmatrix} e^{\pm i\gamma_{\lambda'}/2} \\ e^{\mp i\gamma_{\lambda'}/2}\end{pmatrix} = \mp i\sin\left(\frac{\gamma_\lambda - \gamma_{\lambda'}}{2}\right),$$
$$\bar{\psi}^{(\lambda)}_{e/h}\,\tau_y\,\psi^{(\lambda')}_{e/h} = \mp\sin\left(\frac{\gamma_\lambda + \gamma_{\lambda'}}{2}\right),$$

so that the current matrix element bewteen two ABSs is given by

$$\mathcal{I}_{\lambda,\lambda'} = \frac{\frac{E_\lambda - E_{\lambda'}}{2}\sin\left(\frac{\gamma_\lambda-\gamma_{\lambda'}}{2}\right) + \sin\left(\frac{\gamma_\lambda+\gamma_{\lambda'}}{2}\right)}{\kappa_\lambda + \kappa_{\lambda'}} \times \sum_\sigma \left(a^*_{\lambda,\sigma}a_{\lambda',\sigma} - b^*_{\lambda,\sigma}b_{\lambda',\sigma} + c^*_{\lambda,\sigma}c_{\lambda',\sigma} - d^*_{\lambda,\sigma}d_{\lambda',\sigma}\right). \tag{.59}$$

Continuum to continuum current.— Following similar arguments as in Ref. [34], we find that in the limit $\mathcal{L}\to\infty$ the only nonvanishing current matrix elements are those between continuum states Φ_p and $\Phi_{p'}$ with the same energy $\epsilon = \epsilon'$, so that the matrix element is given by

$$\mathcal{I}_{pp'} \equiv \delta(\epsilon - \epsilon')\int dx\ \bar{\Phi}_p(x)\mathrm{sgn(-x)}\tau_y\Phi_{p'}(x).$$

However, since

$$\bar{\tilde{\psi}}_{e/h}\,\tau_y\,\tilde{\psi}_{e/h} = 0,$$

all matrix elements between the continuum states vanish $\mathcal{I}_{pp'} = 0$. One can conclude that the superconducting phase fluctuations do not induce the transition between continuum states.

Current between ABSs and continuum.— Finally, for transitions between an ABS with energy E_λ and a continuum state with quantum numbers $p = (E, s, \sigma)$, we obtain

$$\begin{aligned}
\bar{\psi}^{(\lambda)}_e\,\tau_z\,\tilde{\psi}_e &= \frac{1}{2}\frac{1}{\sqrt{\cosh\tilde{\gamma}}}\begin{pmatrix} e^{-i\gamma_\lambda/2} & -e^{i\gamma_\lambda/2}\end{pmatrix}\begin{pmatrix} e^{\tilde{\gamma}/2} \\ \sigma_\epsilon e^{-\tilde{\gamma}/2}\end{pmatrix} \\
&= \frac{1}{2}\frac{1}{\sqrt{\cosh\tilde{\gamma}}}\left(e^{-i\gamma_\lambda/2+\tilde{\gamma}/2} - \sigma_\epsilon e^{i\gamma_\lambda/2-\tilde{\gamma}/2}\right) \\
&= \frac{1}{2}\frac{1}{\sqrt{\cosh\tilde{\gamma}}}\left(\Theta(\epsilon)\left[e^{-i\gamma_\lambda/2+\tilde{\gamma}/2} - e^{i\gamma_\lambda/2-\tilde{\gamma}/2}\right] + \Theta(-\epsilon)\left[e^{-i\gamma_\lambda/2+\tilde{\gamma}/2} + e^{i\gamma_\lambda/2-\tilde{\gamma}/2}\right]\right) \\
&= \frac{1}{\sqrt{\cosh\tilde{\gamma}}}\left(\Theta(\epsilon)\frac{e^{z^*} - e^{-z^*}}{2} + \Theta(-\epsilon)\frac{e^{z^*} + e^{-z^*}}{2}\right) \\
&= \frac{1}{\sqrt{\cosh\tilde{\gamma}}}\left(\Theta(\epsilon)\sinh z^* + \Theta(-\epsilon)\cosh z^*\right),
\end{aligned}$$

where we denote $z = (\tilde{\gamma} + i\gamma_\lambda)/2$. Introducing

$$w(z) = \Theta(\epsilon)\sinh z + \Theta(-\epsilon)\cosh z,$$

we can rewrite the above equation in a brevier form,

$$\bar{\psi}_e^{(\lambda)}\,\tau_z\,\tilde{\psi}_e = \frac{w(z^*)}{\sqrt{\cosh\tilde{\gamma}}}. \tag{.60}$$

Similarly, for other spinors we find

$$\begin{aligned}
\bar{\psi}_h^{(\lambda)}\,\tau_z\,\tilde{\psi}_h = \frac{w(-z^*)}{\sqrt{\cosh\tilde{\gamma}}}, \quad \bar{\psi}_{e/h}^{(\lambda)}\,\tau_z\,\tilde{\psi}_{h/e} = \frac{w(\mp z)}{\sqrt{\cosh\tilde{\gamma}}}, \\
\bar{\psi}_{e/h}^{(\lambda)}\,\tau_y\,\tilde{\psi}_{e/h} = \frac{iw(\pm z)}{\sqrt{\cosh\tilde{\gamma}}}, \quad \bar{\psi}_{e/h}^{(\lambda)}\,\tau_y\,\tilde{\psi}_{h/e} = \frac{iw(\mp z^*)}{\sqrt{\cosh\tilde{\gamma}}}.
\end{aligned} \tag{.61}$$

Now we can calculate the current matrix element between continuum and ABS,

$$\begin{aligned}
&\mathcal{I}_{\lambda,(\epsilon,s,\sigma)} = \\
&\int dx\,\Theta(-x)e^{\kappa_\lambda x}\sum_{\sigma_1}\left(a^*_{\lambda,\sigma_1}\bar{\psi}_{h,+,\sigma_1} + b^*_{\lambda,\sigma_1}\bar{\psi}_{e,-,\sigma_1}\right)\mathrm{sgn}(-x)\left[\frac{E_\lambda-\epsilon}{2i}\tau_z + \tau_y\right] \\
&\times\left(\frac{e^{ikx}}{\sqrt{\mathcal{L}}}\left[\delta_{s=1,\sigma}\tilde{\psi}_{e,+,\sigma} + \delta_{s=2,\sigma}\tilde{\psi}_{h,-,\sigma}\right] + \frac{e^{-ikx}}{\sqrt{\mathcal{L}}}\sum_{\sigma_2}\left[a_{(s,\sigma),\sigma_2}\tilde{\psi}_{h,+,\sigma_2} + b_{(s,\sigma),\sigma_2}\tilde{\psi}_{e,-,\sigma_2}\right]\right) \\
&+\int dx\,\Theta(x)e^{-\kappa_\lambda x}\sum_{\sigma_1}\left(c^*_{\lambda,\sigma_1}\bar{\psi}_{e,+,\sigma_1} + d^*_{\lambda,\sigma_1}\bar{\psi}_{h,-,\sigma_1}\right)\mathrm{sgn}(-x)\left[\frac{E_\lambda-\epsilon}{2i}\tau_z + \tau_y\right] \\
&\times\left(\frac{e^{-ikx}}{\sqrt{\mathcal{L}}}\left[\delta_{s=3,\sigma}\tilde{\psi}_{h,+,\sigma} + \delta_{s=4,\sigma}\tilde{\psi}_{e,-,\sigma}\right] + \frac{e^{ikx}}{\sqrt{\mathcal{L}}}\sum_{\sigma_2}\left[c_{(s,\sigma),\sigma_2}\tilde{\psi}_{e,+,\sigma_2} + d_{(s,\sigma),\sigma_2}\tilde{\psi}_{h,-,\sigma_2}\right]\right).
\end{aligned}$$

Performing the integration of theta-functions,

$$\begin{aligned}
\int dx\,\Theta(-x)\mathrm{sgn}(-x)e^{x(\kappa_\lambda\pm ik)} = \int_{-\infty}^{0} dx\,e^{x(\kappa_\lambda\pm ik)} = \frac{1}{\kappa_\lambda\pm ik}, \\
\int dx\,\Theta(x)\mathrm{sgn}(-x)e^{-x(\kappa_\lambda\pm ik)} = \int_{+\infty}^{0} dx\,e^{-x(\kappa_\lambda\pm ik)} = \frac{-1}{\kappa_\lambda\pm ik},
\end{aligned}$$

we derive

$$
\begin{aligned}
&\mathcal{I}_{\lambda,(\epsilon,s,\sigma)} = \\
&\frac{1}{\sqrt{\mathcal{L}}(\kappa_\lambda + ik)}\Bigg(\sum_{\sigma_1}\left(a^*_{\lambda,\sigma_1}\bar{\psi}_{h,+,\sigma_1} + b^*_{\lambda,\sigma_1}\bar{\psi}_{e,-,\sigma_1}\right)\left[\frac{E_\lambda-\epsilon}{2i}\tau_z + \tau_y\right] \\
&\times\left[\delta_{s=1,\sigma}\tilde{\psi}_{e,+,\sigma} + \delta_{s=2,\sigma}\tilde{\psi}_{h,-,\sigma}\right] - \sum_{\sigma_1}\left(c^*_{\lambda,\sigma_1}\bar{\psi}_{e,+,\sigma_1} + d^*_{\lambda,\sigma_1}\bar{\psi}_{h,-,\sigma_1}\right) \\
&\times\left[\frac{E_\lambda-\epsilon}{2i}\tau_z + \tau_y\right]\left[\delta_{s=3,\sigma}\tilde{\psi}_{h,+,\sigma} + \delta_{s=4,\sigma}\tilde{\psi}_{e,-,\sigma}\right]\Bigg) \\
&+\frac{1}{\sqrt{\mathcal{L}}(\kappa_\lambda - ik)}\Bigg(\sum_{\sigma_1}\left(a^*_{\lambda,\sigma_1}\bar{\psi}_{h,+,\sigma_1} + b^*_{\lambda,\sigma_1}\bar{\psi}_{e,-,\sigma_1}\right)\left[\frac{E_\lambda-\epsilon}{2i}\tau_z + \tau_y\right] \\
&\times\sum_{\sigma_2}\left[a_{(s,\sigma),\sigma_2}\tilde{\psi}_{h,+,\sigma_2} + b_{(s,\sigma),\sigma_2}\tilde{\psi}_{e,-,\sigma_2}\right] - \sum_{\sigma_1}\left(c^*_{\lambda,\sigma_1}\bar{\psi}_{e,+,\sigma_1} + d^*_{\lambda,\sigma_1}\bar{\psi}_{h,-,\sigma_1}\right) \\
&\times\left[\frac{E_\lambda-\epsilon}{2i}\tau_z + \tau_y\right]\sum_{\sigma_2}\left[c_{(s,\sigma),\sigma_2}\tilde{\psi}_{e,+,\sigma_2} + d_{(s,\sigma),\sigma_2}\tilde{\psi}_{h,-,\sigma_2}\right]\Bigg).
\end{aligned}
$$

With equations (.60)-(.61), we find

$$
\begin{aligned}
\mathcal{I}_{\lambda,p} &= \frac{i}{\sqrt{\mathcal{L}\cosh\tilde{\gamma}}}\sum_{\sigma'}\Bigg[\frac{1}{\kappa_\lambda - ik}\left\{\left(a^*_{\lambda,\sigma'}a_{p,\sigma'} - d^*_{\lambda,\sigma'}d_{p,\sigma'}\right)W(-z) + \left(b^*_{\lambda,\sigma'}b_{p,\sigma'} - c^*_{\lambda,\sigma'}c_{p,\sigma'}\right)W(z)\right\} \\
&+ \frac{\delta_{\sigma',\sigma}}{\kappa_\lambda + ik}\left\{\left(a^*_{\lambda,\sigma}\delta_{s,1} - d^*_{\lambda,\sigma}\delta_{s,4}\right)W(z^*)\left(b^*_{\lambda,\sigma}\delta_{s,2} - c^*_{\lambda,\sigma}\delta_{s,3}\right)W(-z^*)\right\}\Bigg], \qquad (.62)
\end{aligned}
$$

where we use

$$
\begin{aligned}
W(z) &= w(z) + \frac{E-E_\lambda}{2}w^*(z), \quad W(z^*) = W^*(z) \\
w(z) &= \Theta(E)\sinh(z) + \Theta(-E)\cosh(z), \qquad (.63) \\
z &= (\tilde{\gamma}(E) + i\gamma_\lambda)/2.
\end{aligned}
$$

We note that for $\mathcal{L}\to\infty$, summations over $p=(E,s,\sigma)$ can be performed by using

$$
\frac{1}{\mathcal{L}}\sum_p(\cdots) = \int dE\,\nu(E)\sum_{s=1}^{4}\sum_\sigma(\cdots), \qquad (.64)
$$

where $\nu(E)$ is the BCS density of states (per unit length, and recalling our convention $\Delta = v_F = 1$),

$$
\nu(E) = \frac{1}{2\pi}\frac{|E|}{\sqrt{E^2-1}}\Theta(|E|-1). \qquad (.65)
$$

References

[1] M. Zgirski et al. "Evidence for Long-Lived Quasiparticles Trapped in Superconducting Point Contacts". In: *Phys. Rev. Lett.* 106 (25 June 2011), p. 257003. DOI: 10.1103/PhysRevLett.106.257003. URL: https://link.aps.org/doi/10.1103/PhysRevLett.106.257003.

[2] L. Bretheau et al. "Supercurrent Spectroscopy of Andreev States". In: *Phys. Rev. X* 3 (4 Dec. 2013), p. 041034. DOI: 10.1103/PhysRevX.3.041034. URL: https://link.aps.org/doi/10.1103/PhysRevX.3.041034.

[3] C. Janvier et al. "Coherent manipulation of Andreev states in superconducting atomic contacts". In: *Science* 349.6253 (2015), pp. 1199–1202. DOI: 10.1126/science.aab2179. URL: https://www.science.org/doi/abs/10.1126/science.aab2179.

[4] T. W. Larsen et al. "Semiconductor-Nanowire-Based Superconducting Qubit". In: *Phys. Rev. Lett.* 115 (12 Sept. 2015), p. 127001. DOI: 10.1103/PhysRevLett.115.127001. URL: https://link.aps.org/doi/10.1103/PhysRevLett.115.127001.

[5] G. de Lange et al. "Realization of Microwave Quantum Circuits Using Hybrid Superconducting-Semiconducting Nanowire Josephson Elements". In: *Phys. Rev. Lett.* 115 (12 Sept. 2015), p. 127002. DOI: 10.1103/PhysRevLett.115.127002. URL: https://link.aps.org/doi/10.1103/PhysRevLett.115.127002.

[6] D. J. van Woerkom et al. "Microwave spectroscopy of spinful Andreev bound states in ballistic semiconductor Josephson junctions". In: *Nature Physics* 13 (2017), p. 876. DOI: 10.1038/nphys4150. URL: https://doi.org/10.1038/nphys4150.

[7] M. Hays et al. "Direct Microwave Measurement of Andreev-Bound-State Dynamics in a Semiconductor-Nanowire Josephson Junction". In: *Phys. Rev. Lett.* 121 (4 July 2018), p. 047001. DOI: 10.1103/PhysRevLett.121.047001. URL: https://link.aps.org/doi/10.1103/PhysRevLett.121.047001.

[8] L. Tosi et al. "Spin-Orbit Splitting of Andreev States Revealed by Microwave Spectroscopy". In: *Phys. Rev. X* 9 (1 Jan. 2019), p. 011010. DOI: 10.1103/PhysRevX.9.011010. URL: https://link.aps.org/doi/10.1103/PhysRevX.9.011010.

[9] M. Hays et al. "Continuous monitoring of a trapped superconducting spin". In: *Nature Physics* 16 (2020), p. 1103. DOI: 10.1038/s41567-020-0952-3. URL: https://doi.org/10.1038/s41567-020-0952-3.

[10] A. M. Whiticar et al. "Zeeman-driven parity transitions in an Andreev quantum dot". In: *Phys. Rev. B* 103 (24 June 2021), p. 245308. DOI: 10.1103/PhysRevB.103.245308. URL: https://link.aps.org/doi/10.1103/PhysRevB.103.245308.

[11] M. Hays and V. Fatemi and D. Bouman and J. Cerrillo and S. Diamond and K. Serniak and T. Connolly and P. Krogstrup and J. Nygård and A. Levy Yeyati and A. Geresdi and M. H. Devoret. "Coherent manipulation of an Andreev spin qubit". In: *Science* 373.6553 (2021), pp. 430–433. DOI: 10.1126/science.abf0345. URL: https://www.science.org/doi/abs/10.1126/science.abf0345.

[12] C. Metzger et al. "Circuit-QED with phase-biased Josephson weak links". In: *Phys. Rev. Res.* 3 (1 Jan. 2021), p. 013036. DOI: 10.1103/PhysRevResearch.3.013036. URL: https://link.aps.org/doi/10.1103/PhysRevResearch.3.013036.

[13] V. Fatemi et al. “Microwave Susceptibility Observation of Interacting Many-Body Andreev States”. In: *Phys. Rev. Lett.* 129 (22 Nov. 2022), p. 227701. DOI: 10.1103/PhysRevLett.129.227701. URL: https://link.aps.org/doi/10.1103/PhysRevLett.129.227701.

[14] Andreas Pöschl et al. “Nonlocal conductance spectroscopy of Andreev bound states in gate-defined InAs/Al nanowires”. In: *Phys. Rev. B* 106 (24 Dec. 2022), p. L241301. DOI: 10.1103/PhysRevB.106.L241301. URL: https://link.aps.org/doi/10.1103/PhysRevB.106.L241301.

[15] Alisa Danilenko et al. “Spin spectroscopy of a hybrid superconducting nanowire using side-coupled quantum dots”. In: *Phys. Rev. B* 108 (5 Aug. 2023), p. 054514. DOI: 10.1103/PhysRevB.108.054514. URL: https://link.aps.org/doi/10.1103/PhysRevB.108.054514.

[16] J. J. Wesdorp et al. “Dynamical Polarization of the Fermion Parity in a Nanowire Josephson Junction”. In: *Phys. Rev. Lett.* 131 (11 Sept. 2023), p. 117001. DOI: 10.1103/PhysRevLett.131.117001. URL: https://link.aps.org/doi/10.1103/PhysRevLett.131.117001.

[17] Arno Bargerbos et al. “Spectroscopy of Spin-Split Andreev Levels in a Quantum Dot with Superconducting Leads”. In: *Phys. Rev. Lett.* 131 (9 Aug. 2023), p. 097001. DOI: 10.1103/PhysRevLett.131.097001. URL: https://link.aps.org/doi/10.1103/PhysRevLett.131.097001.

[18] Marta Pita-Vidal et al. “Direct manipulation of a superconducting spin qubit strongly coupled to a transmon qubit”. In: *Nature Physics* 19 (2023), p. 1110. DOI: 10.1038/s41567-023-02071-x. URL: https://doi.org/10.1038/s41567-023-02071-x.

[19] J. J. Wesdorp et al. “Microwave spectroscopy of interacting Andreev spins”. In: *Phys. Rev. B* 109 (4 Jan. 2024), p. 045302. DOI: 10.1103/PhysRevB.109.045302. URL: https://link.aps.org/doi/10.1103/PhysRevB.109.045302.

[20] David van Driel et al. “Charge Sensing the Parity of an Andreev Molecule”. In: *PRX Quantum* 5 (2 Apr. 2024), p. 020301. DOI: 10.1103/PRXQuantum.5.020301. URL: https://link.aps.org/doi/10.1103/PRXQuantum.5.020301.

[21] Mikhail S. Kalenkov, Artem V. Galaktionov, and Andrei D. Zaikin. “Josephson current in ballistic heterostructures with spin-active interfaces”. In: *Phys. Rev. B* 79 (1 Jan. 2009), p. 014521. DOI: 10.1103/PhysRevB.79.014521. URL: https://link.aps.org/doi/10.1103/PhysRevB.79.014521.

[22] A. Martín-Rodero and A. Levy Yeyati. “Josephson and Andreev transport through quantum dots”. In: *Advances in Physics* 60.6 (2011), pp. 899–958. DOI: 10.1080/00018732.2011.624266. URL: https://doi.org/10.1080/00018732.2011.624266.

[23] C. W. J. Beenakker and H. van Houten. “Josephson current through a superconducting quantum point contact shorter than the coherence length”. In: *Phys. Rev. Lett.* 66 (23 June 1991), pp. 3056–3059. DOI: 10.1103/PhysRevLett.66.3056. URL: https://link.aps.org/doi/10.1103/PhysRevLett.66.3056.

[24] Akira Furusaki and Masaru Tsukada. “Current-carrying states in Josephson junctions”. In: *Phys. Rev. B* 43 (13 May 1991), pp. 10164–10169. DOI: 10.1103/PhysRevB.43.10164. URL: https://link.aps.org/doi/10.1103/PhysRevB.43.10164.

[25] Philip F. Bagwell. “Suppression of the Josephson current through a narrow, mesoscopic, semiconductor channel by a single impurity”. In: *Phys. Rev. B* 46 (19 Nov. 1992), pp. 12573–12586. DOI: 10.1103/PhysRevB.46.12573. URL: https://link.aps.org/doi/10.1103/PhysRevB.46.12573.

[26] M. A. Despósito and A. Levy Yeyati. "Controlled dephasing of Andreev states in superconducting quantum point contacts". In: *Phys. Rev. B* 64 (14 Sept. 2001), p. 140511. DOI: 10.1103/PhysRevB.64.140511. URL: https://link.aps.org/doi/10.1103/PhysRevB.64.140511.

[27] Yu. V. Nazarov and Ya. M. Blanter. *Quantum transport: Introduction to Nanoscience*. Cambridge University Press, Cambridge, 2009. URL: https://doi.org/10.1017/CBO9780511626906.

[28] Pavel D. Kurilovich et al. "Microwave response of an Andreev bound state". In: *Phys. Rev. B* 104 (17 Nov. 2021), p. 174517. DOI: 10.1103/PhysRevB.104.174517. URL: https://link.aps.org/doi/10.1103/PhysRevB.104.174517.

[29] A. Zazunov et al. "Andreev Level Qubit". In: *Phys. Rev. Lett.* 90 (8 Feb. 2003), p. 087003. DOI: 10.1103/PhysRevLett.90.087003. URL: https://link.aps.org/doi/10.1103/PhysRevLett.90.087003.

[30] Nikolai M. Chtchelkatchev and Yu. V. Nazarov. "Andreev Quantum Dots for Spin Manipulation". In: *Phys. Rev. Lett.* 90 (22 June 2003), p. 226806. DOI: 10.1103/PhysRevLett.90.226806. URL: https://link.aps.org/doi/10.1103/PhysRevLett.90.226806.

[31] A. Zazunov et al. "Dynamics and phonon-induced decoherence of Andreev level qubit". In: *Phys. Rev. B* 71 (21 June 2005), p. 214505. DOI: 10.1103/PhysRevB.71.214505. URL: https://link.aps.org/doi/10.1103/PhysRevB.71.214505.

[32] C. Padurariu and Yu. V. Nazarov. "Theoretical proposal for superconducting spin qubits". In: *Phys. Rev. B* 81 (14 Apr. 2010), p. 144519. DOI: 10.1103/PhysRevB.81.144519. URL: https://link.aps.org/doi/10.1103/PhysRevB.81.144519.

[33] C. Padurariu and Yu. V. Nazarov. "Spin blockade qubit in a superconducting junction". In: *EPL (Europhysics Letters)* 100.5 (Dec. 2012), p. 57006. DOI: 10.1209/0295-5075/100/57006. URL: https://doi.org/10.1209/0295-5075/100/57006.

[34] Nico Ackermann et al. "Dynamical parity selection in superconducting weak links". In: *Phys. Rev. B* 107 (21 June 2023), p. 214515. DOI: 10.1103/PhysRevB.107.214515. URL: https://link.aps.org/doi/10.1103/PhysRevB.107.214515.

[35] Pavel D. Kurilovich et al. *On-demand population of Andreev levels by their ionization in the presence of Coulomb blockade*. 2023. arXiv: 2312.07512 [cond-mat.mes-hall].

[36] M. R. Sahu et al. "Ground-state phase diagram and parity-flipping microwave transitions in a gate-tunable Josephson junction". In: *Phys. Rev. B* 109 (13 Apr. 2024), p. 134506. DOI: 10.1103/PhysRevB.109.134506. URL: https://link.aps.org/doi/10.1103/PhysRevB.109.134506.

[37] Aldo Brunetti et al. "Anomalous Josephson current, incipient time-reversal symmetry breaking, and Majorana bound states in interacting multilevel dots". In: *Phys. Rev. B* 88 (14 Oct. 2013), p. 144515. DOI: 10.1103/PhysRevB.88.144515. URL: https://link.aps.org/doi/10.1103/PhysRevB.88.144515.

[38] B. van Heck, J. I. Väyrynen, and L. I. Glazman. "Zeeman and spin-orbit effects in the Andreev spectra of nanowire junctions". In: *Phys. Rev. B* 96 (7 Aug. 2017), p. 075404. DOI: 10.1103/PhysRevB.96.075404. URL: https://link.aps.org/doi/10.1103/PhysRevB.96.075404.

[39] F. J. Matute-Cañadas et al. "Signatures of Interactions in the Andreev Spectrum of Nanowire Josephson Junctions". In: *Phys. Rev. Lett.* 128 (19 May 2022), p. 197702. DOI: 10.1103/PhysRevLett.128.197702. URL: https://link.aps.org/doi/10.1103/PhysRevLett.128.197702.

[40] F. Kos, S. E. Nigg, and L. I. Glazman. "Frequency-dependent admittance of a short superconducting weak link". In: *Phys. Rev. B* 87 (17 May 2013), p. 174521. DOI: 10.1103/PhysRevB.87.174521. URL: https://link.aps.org/doi/10.1103/PhysRevB.87.174521.

[41] A. Zazunov et al. "Quasiparticle trapping, Andreev level population dynamics, and charge imbalance in superconducting weak links". In: *Phys. Rev. B* 90 (10 Sept. 2014), p. 104508. DOI: 10.1103/PhysRevB.90.104508. URL: https://link.aps.org/doi/10.1103/PhysRevB.90.104508.

[42] D. G. Olivares et al. "Dynamics of quasiparticle trapping in Andreev levels". In: *Phys. Rev. B* 89 (10 Mar. 2014), p. 104504. DOI: 10.1103/PhysRevB.89.104504. URL: https://link.aps.org/doi/10.1103/PhysRevB.89.104504.

[43] Roman-Pascal Riwar et al. "Strong effects of weak ac driving in short superconducting junctions". In: *Phys. Rev. B* 91 (10 Mar. 2015), p. 104522. DOI: 10.1103/PhysRevB.91.104522. URL: https://link.aps.org/doi/10.1103/PhysRevB.91.104522.

[44] Sunghun Park et al. "From Adiabatic to Dispersive Readout of Quantum Circuits". In: *Phys. Rev. Lett.* 125 (7 Aug. 2020), p. 077701. DOI: 10.1103/PhysRevLett.125.077701. URL: https://link.aps.org/doi/10.1103/PhysRevLett.125.077701.

[45] Domenico Giuliano and Ian Affleck. "The Josephson current through a long quantum wire". In: *Journal of Statistical Mechanics: Theory and Experiment* 2013.02 (Feb. 2013), P02034. DOI: 10.1088/1742-5468/2013/02/P02034. URL: https://dx.doi.org/10.1088/1742-5468/2013/02/P02034.

[46] Domenico Giuliano and Ian Affleck. "dc Josephson current in a long multichannel quantum wire". In: *Phys. Rev. B* 90 (4 July 2014), p. 045133. DOI: 10.1103/PhysRevB.90.045133. URL: https://link.aps.org/doi/10.1103/PhysRevB.90.045133.

[47] Andrea Nava et al. "Transfer matrix approach to the persistent current in quantum rings: Application to hybrid normal-superconducting rings". In: *Phys. Rev. B* 94 (20 Nov. 2016), p. 205125. DOI: 10.1103/PhysRevB.94.205125. URL: https://link.aps.org/doi/10.1103/PhysRevB.94.205125.

[48] Francesco Buccheri et al. "Violation of the Wiedemann-Franz law in the topological Kondo model". In: *Phys. Rev. B* 105 (8 Feb. 2022), p. L081403. DOI: 10.1103/PhysRevB.105.L081403. URL: https://link.aps.org/doi/10.1103/PhysRevB.105.L081403.

[49] Domenico Giuliano et al. "Multiparticle scattering and breakdown of the Wiedemann-Franz law at a junction of N interacting quantum wires". In: *Phys. Rev. B* 105 (3 Jan. 2022), p. 035419. DOI: 10.1103/PhysRevB.105.035419. URL: https://link.aps.org/doi/10.1103/PhysRevB.105.035419.

[50] Sunghun Park and A. Levy Yeyati. "Andreev spin qubits in multichannel Rashba nanowires". In: *Phys. Rev. B* 96 (12 Sept. 2017), p. 125416. DOI: 10.1103/PhysRevB.96.125416. URL: https://link.aps.org/doi/10.1103/PhysRevB.96.125416.

[51] G Campagnano et al. "Spin-orbit coupling and anomalous Josephson effect in nanowires". In: *Journal of Physics: Condensed Matter* 27 (2015), p. 205301. DOI: 10.1088/0953-8984/27/20/205301. URL: https://iopscience.iop.org/article/10.1088/0953-8984/27/20/205301.

[52] M. Minutillo et al. "Anomalous Josephson effect in S/SO/F/S heterostructures". In: *Phys. Rev. B* 98 (14 Oct. 2018), p. 144510. DOI: 10.1103/PhysRevB.98.144510. URL: https://link.aps.org/doi/10.1103/PhysRevB.98.144510.

[53] Yoan Fauvel, Julia S. Meyer, and Manuel Houzet. "Opportunities for the direct manipulation of a phase-driven Andreev spin qubit". In: *Phys. Rev. B* 109 (18 May 2024), p. 184515. DOI: 10.1103/PhysRevB.109.184515. URL: https://link.aps.org/doi/10.1103/PhysRevB.109.184515.

[54] Jonas Lidal and Jeroen Danon. *Andreev bound states and supercurrent in disordered spin-orbit-coupled nanowire SNS-junctions*. 2023. arXiv: 2312.13833 [cond-mat.mes-hall].

[55] M. Z. Hasan and C. L. Kane. "Colloquium: Topological insulators". In: *Rev. Mod. Phys.* 82 (4 Nov. 2010), pp. 3045–3067. DOI: 10.1103/RevModPhys.82.3045. URL: https://link.aps.org/doi/10.1103/RevModPhys.82.3045.

[56] Heinz-Peter Breuer and Francesco Petruccione. *The Theory of Open Quantum Systems*. Oxford: Oxford University Press, 2007, p. 656. DOI: 10.1093/acprof:oso/9780199213900.001.0001.

[57] Andrea Nava, Marco Rossi, and Domenico Giuliano. "Lindblad equation approach to the determination of the optimal working point in nonequilibrium stationary states of an interacting electronic one-dimensional system: Application to the spinless Hubbard chain in the clean and in the weakly disordered limit". In: *Phys. Rev. B* 103 (11 Mar. 2021), p. 115139. DOI: 10.1103/PhysRevB.103.115139. URL: https://link.aps.org/doi/10.1103/PhysRevB.103.115139.

[58] M. T. Björk et al. "Tunable effective g factor in InAs nanowire quantum dots". In: *Phys. Rev. B* 72 (20 Nov. 2005), p. 201307. DOI: 10.1103/PhysRevB.72.201307. URL: https://link.aps.org/doi/10.1103/PhysRevB.72.201307.

[59] A. Zazunov et al. "Anomalous Josephson Current through a Spin-Orbit Coupled Quantum Dot". In: *Phys. Rev. Lett.* 103 (14 Oct. 2009), p. 147004. DOI: 10.1103/PhysRevLett.103.147004. URL: https://link.aps.org/doi/10.1103/PhysRevLett.103.147004.

[60] A. Zazunov et al. "Nonreciprocal charge transport and subharmonic structure in voltage-biased Josephson diodes". In: *Phys. Rev. B* 109 (2 Jan. 2024), p. 024504. DOI: 10.1103/PhysRevB.109.024504. URL: https://link.aps.org/doi/10.1103/PhysRevB.109.024504.

[61] Jason Alicea. "New directions in the pursuit of Majorana fermions in solid state systems". In: *Reports on Progress in Physics* 75.7 (June 2012), p. 076501. DOI: 10.1088/0034-4885/75/7/076501. URL: https://dx.doi.org/10.1088/0034-4885/75/7/076501.

[62] Ulrich Weiss. *Quantum Dissipative Systems*. 4th. World Scientific, Singapore, 2012. DOI: 10.1142/8334. eprint: https://www.worldscientific.com/doi/pdf/10.1142/8334. URL: https://www.worldscientific.com/doi/abs/10.1142/8334.

[63] Andrea Nava and Michele Fabrizio. "Dissipative cooling induced by pulse perturbations". In: *SciPost Phys.* 12 (2022), p. 014. DOI: 10.21468/SciPostPhys.12.1.014. URL: https://scipost.org/10.21468/SciPostPhys.12.1.014.

3 Quantum Mpemba Effect in Josephson Junctions

This chapter is based on the content of the author's publication *Green's Function Approach to Josephson Dot Dynamics and Application to Quantum Mpemba Effects*, Phys.Rev.B 111 (2025) 10, 104506, which is adapted and extended for the purposes of the thesis.

3.1 Introduction

Quantum Mpemba effect.— In the last years, quantum generalizations of the classical thermal Mpemba effect [1–10] have gained a lot of attention [11–29]. The classical Mpemba effect occurs when two system copies are prepared in equilibrium states at different temperatures T_h ("hot") and T_c ("cold"), respectively. For each copy of the system, one performs a sudden temperature quench at time $t = 0$ to the final temperature $T_{\rm eq}$ with $T_{\rm eq} < T_c < T_h$. Further, one measures the corresponding relaxation times of the systems $\tau(T_{h/c})$ towards the final equilibrium state with temperature $T_{\rm eq}$ reached for $t \to \infty$. The classical thermal Mpemba effect occurs if there exist shortcut pathways in the effective energy landscape, for which $\tau(T_h) < \tau(T_c)$ holds [30, 31]. In simpler words, Mpemba effect takes place if the hotter system T_h cools faster than the colder system T_c, see Fig. 3.1 for a symbolic illustration. This poses a contradiction with the logic that if the cooler system T_c is thermally closer than the hotter copy T_h to the final state $T_{\rm eq}$, the path in the energy landscape that it needs to undergo to reach the final state, and therefore, the relaxation time $\tau(T_c)$, is shorter than the path and time $\tau(T_h)$ of the hotter version of the system. In many cases, τ can be estimated as the time the system needs to undergo a phase transition [1, 32–34]. For systems without phase transitions, τ instead has to be extracted from a properly chosen monitoring function [3].

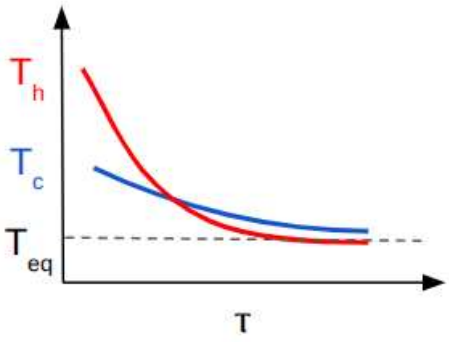

Figure 3.1: Symbolic illustration of thermal Mpemba effect for two copies of the system, $T_h > T_c$ undergoing a relaxation to the final state with $T_{\rm eq}$.

The classical Mpemba effect has been generalized to the quantum version for different quantum platforms, with first experiments already performed for trapped ions [13, 14]. The theory of the QME in *closed* quantum systems was addressed, e.g., in Refs. [11, 12, 20]. For *open nonequilibrium* quantum systems coupled to multiple reservoirs ("baths") [35, 36], as in our case, where the ABSs are considered as the system coupled to a fermionic bath represented by continuum states of the Josephson junction, and bosonic bath represented by the microwave resonator, the situation is more complex. The competition between stochastic relaxation processes and quantum effects may drive the system towards a (nonequilibrium or equilibrium) stationary state, denoted by (N)ESS below. Moreover, under such circumstances, one can encounter a QME which is characterized and sometimes even dominated by quantum correlations, entanglement, and quantum coherence. The significance and uses of QME are:

- Conceptually, QME provides insights into the interplay between quantum coherence,

dissipation, and thermalization;

- Practically, QME can be useful to accelerate certain processes and transitions, for e.g. faster cooling of quantum devices, shorter qubit reset times, or accelerated relaxation in quantum annealers and simulators.

In this chapter, the general protocol for identifying the QME proposed in [24], is adapted to the Josephson dot problem. This protocol can unambiguously identify the QME in open nonequilibrium systems with Markovian dynamics, where two types of QME are possible in general, see Sec. 3.3 for details. We consider a quench of the average phase difference ϕ_0 across the Josephson junction. Experimentally, this can be achieved, e.g., by quenching a magnetic flux [37]. We compare two copies of the system corresponding to pre-quench values $\phi_0^{(c)}$ and $\phi_0^{(f)}$, which are respectively quenched at time $t = 0$ to the same post-quench value $\phi_0^{(\mathrm{eq})}$ describing the final configuration. The superscripts (c) and (f) refer to "close" vs "far" with respect to the final phase difference, corresponding to the "cold" vs "hot" case in the classical Mpemba effect, i.e., we require

$$\left|\phi_0^{(c)} - \phi_0^{(\mathrm{eq})}\right| < \left|\phi_0^{(f)} - \phi_0^{(\mathrm{eq})}\right| .$$

Following Ref. [24], in order to monitor the distance of the post-quench quantum state $\rho_A(t)$, which describes the ABS sector, from the final stationary state $\rho_{A,\mathrm{stat}}$ reached for $t \to \infty$, we employ the trace distance [38],

$$\mathcal{D}_T(\rho_A(t)) = \frac{1}{2}\mathrm{Tr}\,|\rho_A(t) - \rho_{A,\mathrm{stat}}|\,, \tag{3.1}$$

As discussed in Refs. [3, 24], one may equivalently choose a different distance function as long as $\mathcal{D}_T(\rho_A(t))$ is a monotonically non-increasing, continuous, and convex function of time. The trace distance satisfies these consistency relations under Markovian dynamics [38, 39]. In addition, for the case studied here, it could be measured experimentally in terms of microwave spectroscopy, see Sec. 3.3.

Green's functions approach to Josephson junctions.— In many-body quantum systems, identifying low-energy excitations — especially those of fermionic nature — can be challenging if one is solving the eigenvalue problem for the full microscopic Hamiltonian. A more practical approach often involves integrating out the high-energy degrees of freedom to focus on the relevant low-energy sector. As was shown in the first chapter, within the Green's function (GF) framework, quasiparticles are determined by the poles of the single-particle GF [37]. Alternatively, one can construct a low-energy description through an effective action, which typically leads to a time-nonlocal Lagrangian. When external fields or dissipative effects are present, the nonequilibrium behavior of quasiparticles can be modeled using the Lindblad master equation [36]. This formalism depends on the knowledge of quasiparticle transition rates corresponding to all scattering processes triggered by external perturbations or environmental dissipation. However, computing these rates becomes difficult when the quasiparticle dynamics follows a time-nonlocal equation of motion that falls outside the standard Hamiltonian framework. In such situations, Fermi's golden rule is not directly applicable.

Quantum dot Josephson junctions are a typican example for such systems. However, the approach developed in Sec. 3.2 is generally applicable to arbitrary quantum systems coupled to several reservoirs. Andreev bound states, with phase-dependent energies below the BCS superconducting pairing gap Δ in the leads (assumed to be identical in all leads for simplicity), represent the low-energy fermionic modes of a Josephson dot in the phase-biased regime. Localized near the junction, which in our model contains a quantum dot, ABSs are the main carriers of the supercurrent. They are thus inherently linked to the phase dynamics. To calculate transition rates pertaining to ABSs in the presence of phase fluctuations induced by

environmental fluctuations, a standard but somewhat cumbersome method shown in the previous chapter (also see [37, 40–49]) is to solve the Bogoliubov-de Gennes equations in order to find the full wave functions for all quasiparticle states, including those for continuum fermions with energy above Δ.

Here, a more straightforward method using a Green's functions (GF) framework to solving the Heisenberg equations of motion for fermionic fields is introduced and, later, applied to observe quantum Mpemba effect in Josephson junctions. By averaging over the lead fermions, we demonstrate how to address the time-nonlocal and generally non-unitary dynamics of Andreev states, allowing us to compute all inter-level transition rates, including those involving the continuum states. The quantum nanowire region incorporates spin-orbit interaction (SOI), a Zeeman field, and electron-electron interactions. There are several advantages of the GF method when compared to other possible techniques, such as solving BdG problem or using Keldysh contour integration:

1. Unlike solving the BdG equations, this method does not require explicit calculation of BdG eigenstates to determine the transition rates in the Lindblad equation describing the dynamics of ABSs.

2. GF framework allows for a simpler inclusion of Coulomb interactions, compared to the BdG method. However, in the example presented in Sec. 3.3 we consider a noninteracting quantum dot.

3. GF method avoids the complexity of a full-fledged Keldysh approach [35, 37], yet allows to treat nonequilibrium problems;

4. The double-counting problem that occurs for superconducting models in the presence of SOI and magnetic field [50] are avoided by construction;

In Sec. 3.3, the GF-based formalism is applied to a study of the quantum Mpemba effect (QME) for a spin-orbit coupled Josephson dot subject to a magnetic Zeeman field in the presence of an electromagnetic environment.

The remainder of this chapter is structured as follows. In Sec. 3.2, the GF formalism applied to the Josephson dot problem is described. In Sec. 3.3, the emergence of the QME in this system is studied, and the concrete predictions for parameter regimes where QMEs are expected are made. Finally, we briefly conclude in Sec. 3.4. The appendix contains technical details on the calculation of wave functions for the central quantum dot defining the junction. As before, we use units with $\hbar = e = k_B = 1$.

3.2 Description in terms of Green's function formalism

In this section, we outline our general GF approach to the calculation of the transition rates entering the Lindblad master equation governing the dynamics of low-energy quasiparticles of a many-body quantum system. As concrete application, we focus on the Josephson dot model introduced in Sec. 3.2.1. Our EOM approach is then outlined in Sec. 3.2.2, followed by a calculation of all transition rates involving ABSs in Sec. 3.2.3. Finally, we specify the Lindblad equation governing the dynamics in the Andreev subspace of the Hilbert space in Sec. 3.2.4.

3.2.1 Josephson junction model

As in the previous chapter, here we model the setup from Fig. 1.3. The quantum dot forming the Josephson junction as a ballistic one-dimensional (1D) single-mode nanowire of length L tunnel-coupled to two ($j = 1, 2$) conventional s-wave BCS superconducting leads.

Dot, leads and tunneling Hamiltonians.— The total Hamiltonian of the junction consists of the dot, superconducting leads and the tunnel coupling between them,

$$H = H_{\text{dot}} + H_{\text{leads}} + H_{\text{tun}}.$$

The isolated dot is described by

$$H_{\text{dot}} = \int dx\, d^\dagger(x)\hat{h}(x)d(x) + H_{\text{int}}, \quad d = \begin{pmatrix} d_\uparrow \\ d_\downarrow \end{pmatrix}, \tag{3.2}$$

with fermionic annihilation operators $d_\sigma(x)$ for spin projection $\sigma \in \{\uparrow,\downarrow\}$ and the single-particle Hamiltonian

$$\hat{h}(x) = \frac{\hat{p}^2}{2m} - \mu + \alpha\sigma_z\hat{p} + \boldsymbol{b}\cdot\boldsymbol{\sigma} + V(x), \quad \hat{p} = -i\partial_x. \tag{3.3}$$

Here m is the effective electron mass in the wire, μ the chemical potential, the Pauli matrices $\boldsymbol{\sigma} = (\sigma_x, \sigma_y, \sigma_z)$ act in spin space, and the spin quantization axis is chosen along the spin-orbit direction. The SOI coupling strength is denoted by $\alpha \geq 0$, and $\boldsymbol{b} = (b_x, 0, b_z)$ is a Zeeman field including gyromagnetic and Bohr magneton factors. Due to axial symmetry, we set $b_y = 0$ without loss of generality. Furthermore, $V(x)$ is a confinement potential along the transport direction. In the calculations presented in Sec. 3.3, we assume a hard-wall potential for $V(x)$ but one can also employ other choices. The repulsive Coulomb interaction is described by a standard charging energy (E_C) term [37],

$$H_{\text{int}} = E_C\left(\mathcal{N} - n_g\right)^2, \quad \mathcal{N} = \int dx\, d^\dagger(x)d(x), \tag{3.4}$$

where n_g is a dimensionless parameter proportional to a backgate voltage. The superconducting leads are described by conventional s-wave BCS Hamiltonians [37] (for simplicity, we assume identical parameters for both superconductors),

$$H_{\text{leads}} = \sum_{j=1,2}\sum_{\psi}{}_j^\dagger\left(\xi_{\tau z} + \Delta\tau_x\right)\psi_j, \quad \psi_j = \begin{pmatrix} \psi_{j,\uparrow} \\ \psi^\dagger_{j(-),\downarrow} \end{pmatrix}. \tag{3.5}$$

Here, Nabu spinor $\psi^\dagger_{j,\sigma}$ creates an electron in lead j with momentum and spin projection σ. The electron dispersion in the normal-state leads is given by

$$\xi_= k^2/(2m) - \mu,$$

Δ is the homogeneous BCS gap, and the Pauli matrices $\tau_{x,y,z}$ act in Nambu (particle-hole) space. Finally, with the sum over momentum indices

$$\psi_{j\sigma} = \sum_{\mathbf{k}} \psi_{j\mathbf{k},\text{œ}}, \tag{3.6}$$

the tunnel couplings connecting the superconducting leads to the quantum dot at the wire end points, $x = x_1$ and $x = x_2 = x_1 + L$, respectively, are described by

$$H_{\text{tun}} = \sum_{j=1,2} t_j e^{i\phi_j/2} \sum_{\sigma=\uparrow,\downarrow} \psi^\dagger_{j\sigma} d_\sigma(x_j) + \text{h.c.}, \tag{3.7}$$

with t_j - hopping parameters and ϕ_j - superconducting phases of the respective superconductor. For simplicity, we here assume that the tunnel couplings t_j are real-valued, positive,

and spin-independent parameters. However, a complex-valued spin dependence of scattering amplitudes will arise through the SOI. Note that we have chosen a gauge where the order parameter phase appears only in the tunneling Hamiltonian.

Diagonalizing the free dot Hamiltonian. — The noninteracting dot Hamiltonian in Eq. (3.2) can be diagonalized by a canonical transformation,

$$d_\sigma(x) = \sum_\nu \chi_{\nu\sigma}(x) c_\nu,$$

where the single-particle eigenstates $\chi_{\nu\sigma}(x)$ with eigenenergy ϵ_ν describe the low-energy transport properties,

$$\hat{h}(x)\chi_\nu(x) = \epsilon_\nu \chi_\nu(x), \quad \chi_\nu = \begin{pmatrix} \chi_{\nu\uparrow} \\ \chi_{\nu\downarrow} \end{pmatrix}. \tag{3.8}$$

Note that the quantum number ν encapsulates both orbital and spin quantum numbers which cannot be disentangled in the presence of the SOI and the Zeeman field. We apply Neumann boundary conditions,

$$\partial_x \chi_\nu(x_1) = \partial_x \chi_\nu(x_2) = 0,$$

such that no current flows through the wire ends, and choose an orthonormal basis,

$$\int dx\, \chi_\nu^\dagger(x)\chi_{\nu'}(x) = \delta_{\nu\nu'}.$$

In practice, the Hamiltonian matrix appearing in Eq. (3.8) is truncated to the subspace of low-energy eigenstates below an energy cutoff comparable to Δ, and then diagonalized numerically. For notational simplicity and convenience, we assume an even number 2ℓ (with integer $\ell \geq 1$) of relevant dot levels, $\nu \in \{1, \ldots, 2\ell\}$, in what follows. For the spin-degenerate case corresponding to the absence of a Zeeman field, this situation is directly realized. Moreover, the equations below are easily adapted for an odd number of states.

Hamiltonians in the diagonal dot basis.— In the new basis, the dot is represented by normal-mode fermion operators,

$$c_\nu = \sum_\sigma \int dx\, \chi_{\nu\sigma}^*(x) d_\sigma(x).$$

We then arrive at the c-fermion representation of the dot Hamiltonian,

$$H_{\text{dot}} = \sum_{\nu=1}^{2\ell} \epsilon_\nu c_\nu^\dagger c_\nu + E_C \left(\mathcal{N} - n_g\right)^2, \quad \mathcal{N} = \sum_\nu c_\nu^\dagger c_\nu. \tag{3.9}$$

Similarly, Eq. (3.7) takes the form

$$H_{\text{tun}} = \sum_{j,\sigma,\nu} e^{i\phi_j/2} t_{j\sigma,\nu} \psi_{j\sigma}^\dagger c_\nu + \text{h.c.}, \quad t_{j\sigma,\nu} = t_j \chi_{\nu\sigma}(x_j), \tag{3.10}$$

where the hopping parameters $t_{j\sigma,\nu}$ depend on the spin index σ and on the dot level energies ϵ_ν. Defining Nambu spinors for the boundary lead fermions $\psi_{j\sigma}$ and for the dot fermions c_ν,

$$\psi_j = \begin{pmatrix} \psi_{j\uparrow} \\ \psi_{j\downarrow}^\dagger \end{pmatrix}, \quad \gamma_\nu = \begin{pmatrix} c_\nu \\ c_\nu^\dagger \end{pmatrix} = \tau_x \gamma_\nu^*, \tag{3.11}$$

one obtains the equivalent form

$$H_{\text{tun}} = \sum_{j,\nu} \psi_j^\dagger \mathcal{T}_{j\nu} \gamma_\nu + \text{h.c.}, \quad \mathcal{T}_{j\nu} = \begin{pmatrix} t_{j\uparrow,\nu} e^{i\phi_j/2} & 0 \\ 0 & -t_{j\downarrow,\nu}^* e^{-i\phi_j/2} \end{pmatrix}, \tag{3.12}$$

where the matrix structure of $\mathcal{T}_{j\nu}$ is in Nambu space. Note that γ_ν obeys a reality constraint, described by Eq. (3.11), which implies double counting. (In the absence of SOI and Zeeman field, double counting is not required and the formalism allows for some simplifications. Below we consider the general case.) Correspondingly, Eq. (3.12) can be written as

$$H_{\rm tun} = \sum_{j,\nu} \gamma_\nu^\dagger \left(\mathcal{T}_{j\nu}^* \psi_j - \tau_x \mathcal{T}_{j\nu} \psi_j^* \right). \tag{3.13}$$

For the application in Sec. 3.3, we assume $E_C = 0$ (no Coulomb effects) but we discuss interacting Josephson dots using this formalism elsewhere. In Nambu notation, up to an irrelevant constant term, the dot Hamiltonian (3.9) is then given by

$$H_{\rm dot} = \frac{1}{2} \sum_{\nu=1}^{2\ell} \epsilon_\nu \gamma_\nu^\dagger \tau_z \gamma_\nu. \tag{3.14}$$

Fluctuating phase - bosonic bath.— We assume below that the nanowire is embedded in a superconducting loop threaded by a magnetic flux, see Fig. 1.3 from Chapter 1. As in the previous chapter, the superconducting phase difference across the nanowire,

$$\phi = \phi_1 - \phi_2,$$

is treated as dynamical variable,

$$\phi = \phi_0 + \tilde{\phi},$$

where ϕ_0 is the average phase difference induced by the magnetic flux and $\tilde{\phi}$ is a bosonic operator. This operator is time-independent in the Schrödinger picture and represents the fluctuating phase caused by the electromagnetic environment, e.g., a circuit resistance or the inductive coupling to a microwave resonator. Without loss of generality, we write

$$\phi_j = s_j \phi/2, \quad s_1 = 2 + s_2 \in (0,2). \tag{3.15}$$

As previously, we work in a gauge with vanishing vector potential in the nanowire region, see Eq. (3.3). In addition, for nanowires of intermediate length $L \gtrsim \xi_0$, where $\xi_0 = v_{\rm F}/\Delta$ is the superconducting coherence length ($v_{\rm F}$ is the Fermi velocity in the leads), Josephson transport is in general sensitive to the phase shift asymmetry s_1/s_2. In the symmetric case, one has $s_1 = -s_2 = 1$. An asymmetry of the phase shift can be associated with the capacitive asymmetry of the tunnel contacts at $x_{1,2}$.

Modeling the electromagnetic environment by a continuum of harmonic oscillators (boson modes) in thermal equilibrium at temperature T_b, in the Heisenberg picture, phase fluctuations $\tilde{\phi}(t)$ are characterized by the bath correlation function

$$\mathcal{D}(t,t') = \left\langle \frac{\tilde{\phi}(t)}{2} \frac{\tilde{\phi}(t')}{2} \right\rangle_b = \int_{-\infty}^{\infty} \frac{d\omega}{2\pi} e^{-i\omega(t-t')} \mathcal{D}(\omega). \tag{3.16}$$

With $\langle \tilde{\phi}(t) \rangle_b = 0$, where $\langle \cdots \rangle_b$ denotes a thermal average using the Bose-Einstein function $n_B(\omega) = 1/(e^{\omega/T_b} - 1)$, one can write [35]

$$\mathcal{D}(\omega) = 2\pi J(\omega) \left[n_B(\omega) + 1 \right], \tag{3.17}$$

where $J(\omega) = -J(-\omega)$ denotes the spectral density of the environment, with $J(\omega > 0) \geq 0$. We give examples for $J(\omega)$ in the setup of Fig. 2.1 later on, see Eqs. (3.97) and (3.98).

3.2.2 Equation of motion approach

Integrating out the leads - derivation of the closed EOMs for the dot operators. — We next formulate an EOM approach to the dynamics of the system described in Sec. 3.2.1. The Heisenberg EOMs for the Nambu fermion field operators $\psi_{j\mathbf{k}}(t)$ and $\gamma_\nu(t)$ can be derived as Euler-Lagrange equations from the full system Lagrangian, see Eqs. (3.5) and (3.13)–(3.14), and are given by

$$(i\partial_t - h_\mathbf{k})\,\psi_{j\mathbf{k}}(t) = \sum_{\nu=1}^{2\ell} \mathcal{T}_{j\nu}(t)\gamma_\nu(t), \quad h_\mathbf{k} = \xi_\mathbf{k}\tau_z + \Delta\tau_x \tag{3.18}$$

and

$$(i\partial_t - \epsilon_\nu\tau_z)\,\gamma_\nu(t) = \sum_{j=1,2}\left[\mathcal{T}^*_{j\nu}(t)\psi_j(t) - \tau_x\mathcal{T}_{j\nu}(t)\psi^*_j(t)\right], \quad \psi_j(t) = \sum_\mathbf{k}\psi_{j\mathbf{k}}(t). \tag{3.19}$$

Here, $\mathcal{T}_{j\nu}(t)$ following from the corresponding expression in Eq. (3.12), acquires a time-dependence by letting

$$\phi_j \to \phi_j(t) = s_j\phi(t)/2.$$

For time-independent average phase bias ϕ_0, we have

$$\phi(t) = \phi_0 + \tilde{\phi}(t)$$

in the Heisenberg picture.

By inverting Eq. (3.18) for the lead operator, we infer that the retarded response of the boundary fermions $\psi_j(t)$ to the dot dynamics and to the phase fluctuations is given by

$$\psi_j(t) = \int dt'\, g^R(t,t')\sum_\nu \mathcal{T}_{j\nu}(t')\gamma_\nu(t'), \tag{3.20}$$

where $g^R(t,t')$ is the retarded boundary GF of the leads,

$$g^R(t,t') = \int \frac{d\omega}{2\pi}\, e^{-i\omega(t-t')}g^R(\omega), \tag{3.21}$$

$$g^R(\omega) = \sum_\mathbf{k}\frac{1}{\omega - h_\mathbf{k} + i0^+} = -\pi\nu_F\frac{\omega\tau_0 + \Delta\tau_x}{\zeta(\omega)},$$

with the Nambu-space identity matrix τ_0, the normal-state ($\Delta = 0$) lead density of states

$$\nu_F = \sum_\mathbf{k}\delta(\xi_\mathbf{k}),$$

and the auxiliary function

$$\begin{aligned}\zeta(\omega) &= \sqrt{\Delta^2 - (\omega + i0^+)^2} \\ &= \begin{cases} \sqrt{\Delta^2 - \omega^2}, & |\omega| \le \Delta, \\ -i\,\mathrm{sgn}(\omega)\sqrt{\omega^2 - \Delta^2}, & |\omega| > \Delta. \end{cases}\end{aligned} \tag{3.22}$$

Note that function $\zeta(\omega)$ entering the retarded leads GF, consists of two parts: energy range $|\omega| \le \Delta$ which refers to the udergap states, i.e. Andreev bound states, and energy range $|\omega| > \Delta$ which corresponds to the continuum states, above the superconducting gap. We often keep τ_0 implicit in what follows.

We next insert Eq. (3.20) into the EOM for the dot operator $\gamma_\nu(t)$, Eq. (3.19). As a result, with a time-nonlocal matrix kernel acting in level-Nambu space,

$$\tilde{\Lambda}_{\nu\nu'}(t,t') = \sum_{j=1,2}\left(\tilde{W}_{j,\nu\nu'}(t,t') - \tau_x \tilde{W}^*_{j,\nu\nu'}(t,t')\tau_x\right),$$

$$\tilde{W}_{j,\nu\nu'}(t,t') = \mathcal{T}^*_{j\nu}(t) g^R(t,t')\mathcal{T}_{j\nu'}(t'), \tag{3.23}$$

we arrive at a closed set of EOMs for the dot fermions,

$$(i\partial_t - \epsilon_\nu\tau_z)\,\gamma_\nu(t) = \sum_{\nu'=1}^{2\ell}\int dt'\,\tilde{\Lambda}_{\nu\nu'}(t,t')\gamma_{\nu'}(t'), \tag{3.24}$$

which are nonlocal in time. The above steps are equivalent to integrating out the lead fermions on the retarded branch of the Keldysh contour [35]. The tilde notation emphasizes that $\tilde{W}_j$ and $\tilde{\Lambda}$ depend on the phase fluctuations $\tilde{\phi}$ due to the boson modes.

Expansion in the small phase fluctuation.— Below we assume the weak-coupling limit for the electromagnetic environment. Treating the time-dependent $\tilde{\phi}(t)$ as small perturbation,

$$\langle\tilde{\phi}^2\rangle_b \ll 1$$

we expand the tunneling matrix $\mathcal{T}_{j\nu}(t)$ to first order in $\tilde{\phi}(t)$ using, see Eqs. (3.12) and (3.15),

$$e^{\pm i\phi_j(t)/2} = e^{\pm i s_j\phi_0/4}\left(1 \pm \frac{i}{4}s_j\tilde{\phi}(t) + o(\tilde{\phi})\right). \tag{3.25}$$

It is now convenient to introduce a 4ℓ-component multispinor field

$$\gamma = (\gamma_1,\ldots,\gamma_{2\ell})^T,$$

combining Nambu bispinors γ_ν for all dot level numbers ν, such that Eq. (3.24) takes the form

$$(i\partial_t - \epsilon\tau_z)\,\gamma(t) = \int dt'\,\tilde{\Lambda}(t,t')\gamma(t'), \tag{3.26}$$

where $\tilde{\Lambda}(t,t')$ and $\tilde{W}_j(t,t')$ are $4\ell\times 4\ell$ matrices in level-Nambu space, see Eq. (3.23). Similarly, we also define the 2ℓ-dimensional diagonal matrix

$$\epsilon = \mathrm{diag}\,(\epsilon_1,\ldots,\epsilon_{2\ell}),$$

and $2\ell\times 2\ell$ hybridization matrices ($j=1,2$) in level space,

$$\Gamma_{j,\nu'\nu} = \pi\nu_F\sum_\sigma t^*_{j\sigma,\nu'}t_{j\sigma,\nu}, \tag{3.27}$$
$$F_{j,\nu'\nu} = \pi\nu_F\sum_\sigma \sigma t_{j\sigma,\nu'}t_{j(-\sigma),\nu},$$

with $t_{j\sigma,\nu}$ in Eq. (3.10) and $\sigma = \uparrow\,/\,\downarrow = +/-$.

We note that the matrices Γ_j are Hermitian, while the F_j are antisymmetric,

$$\Gamma_j = \Gamma_j^\dagger, \quad F_j = -F_j^T.$$

In the appendix, we provide technical details on the calculation of the wave functions $\chi_\nu(x)$ for the present model. These wave function are used in Sec. 3.3, in particular, to compute the hopping parameters $t_{j\sigma,\nu}$ entering the hybridization matrices in Eq. (3.27).

After some algebra, to the leading order in $\tilde{\phi}(t)$, Eq. (3.26) can be written as

$$\int dt' \mathcal{L}(t,t')\gamma(t') = \int dt' \tilde{V}(t,t')\gamma(t'), \tag{3.28}$$

where the Lagrangian kernel $\mathcal{L}(t,t')$ describes the noninteracting dynamics of the junction, both for ABSs and above-gap continuum excitations, in the absence of phase fluctuations,

$$\mathcal{L}(t,t') = \int \frac{d\omega}{2\pi} e^{-i\omega(t-t')}\mathcal{L}(\omega), \quad \mathcal{L}(\omega) = \omega - \epsilon\tau_z - \Lambda(\omega), \tag{3.29}$$

with $\Lambda(\omega) = \sum_j \Lambda_j(\omega)$. Using Eq. (3.22), we obtain the Nambu matrix structure (the dot level structure is encoded in ϵ, Γ_j and F_j)

$$\Lambda_j(\omega) = -\frac{1}{\zeta(\omega)} \begin{pmatrix} \omega\Gamma_j & \Delta e^{-is_j\phi_0/2}F_j^\dagger \\ \Delta e^{is_j\phi_0/2}F_j & \omega\Gamma_j^* \end{pmatrix}. \tag{3.30}$$

The kernel $\tilde{V}(t,t')$ in Eq. (3.28) describes the linear-in-$\tilde{\phi}$ coupling to the electromagnetic environment,

$$\tilde{V}(t,t') = \frac{\tilde{\phi}(t)}{2}\tau_z\mathcal{I}(t,t') - \mathcal{I}(t,t')\tau_z\frac{\tilde{\phi}(t')}{2}, \tag{3.31}$$

with the time-nonlocal current operator

$$\mathcal{I}(t,t') = \int \frac{d\omega}{2\pi} e^{-i\omega(t-t')}\mathcal{I}(\omega), \quad \mathcal{I}(\omega) = \frac{1}{2i}\sum_j s_j\Lambda_j(\omega). \tag{3.32}$$

Case without the phase fluctuations.— In the absence of phase fluctuations, $\tilde{\phi} = 0$, the above equations simplify to

$$[i\partial_t - h(i\partial_t)]\,\gamma(t) = 0, \quad h(\omega) = \epsilon\tau_z + \Lambda(\omega), \tag{3.33}$$

where $h(i\partial_t)$ plays the role of an effective single-particle Hamiltonian. However, this operator is nonlocal in time since it can be expanded into an infinite series in ∂_t. In particular, we observe from Eqs. (3.22) and (3.30) that $h(\omega)$ is Hermitian,

$$h(\omega) = h^\dagger(\omega),$$

only for energies within the subgap region $|\omega| < \Delta$.

In the *atomic limit*, which is described by a very large pairing gap (formally, $\Delta \to \infty$, such that continuum states can be disregarded [51]), one obtains the frequency-independent Hermitian Hamiltonian

$$h_A = \epsilon\tau_z - \sum_{j=1,2} \begin{pmatrix} 0 & F_j^\dagger e^{-is_j\phi_0/2} \\ F_j e^{is_j\phi_0/2} & 0 \end{pmatrix}. \tag{3.34}$$

Clearly, we then have only ABS solutions.

For finite Δ, the solution of Eq. (3.33) can be written as a series expansion in terms of quasiparticle field operators involving either ABSs or above-gap continuum states,

$$\begin{aligned} \gamma(t) &= \tau_x\gamma^*(t) = \sum_{\nu=1}^{2\ell}\left(a_\nu\eta_\nu e^{-iE_\nu t} + a_\nu^\dagger\tau_x\eta_\nu^* e^{iE_\nu t}\right) \\ &+ \int_{|\omega|>\Delta}\frac{d\omega}{2\pi}e^{-i\omega t}\tilde{\gamma}_\omega, \quad \tilde{\gamma}_{-\omega} = \tau_x\tilde{\gamma}_\omega^*, \end{aligned} \tag{3.35}$$

where the a_ν are fermion annihilation operators for ABSs with energy E_ν with $|E_\nu| < \Delta$ and eigenspinor η_ν in level-Nambu space,

$$h(E_\nu)\eta_\nu = E_\nu \eta_\nu. \tag{3.36}$$

As to the number of subgap solutions, or localized states in a more general context, we assume that it is 2ℓ (without double counting) based on the continuity of the "root flow" in Γ-Δ parameter space. In fact, the number of roots is 2ℓ in two limits, namely $\Gamma = 0$ or $\Delta \to \infty$. We expect that this number remains 2ℓ when increasing (decreasing) Γ (Δ). The only exception is the point $\Delta = 0$, where a phase transition occurs. As a consequence, the dot level energies ϵ_ν do not need to lie below Δ. For high-energy dot states, the corresponding Andreev levels are expected to merge with the BCS gap edges.

The field operator $\tilde{\gamma}_\omega$ represents continuum states at energy ω, where a particle-hole symmetry relation is imposed by double counting,

$$h(\omega) = -\tau_x h^*(-\omega)\tau_x. \tag{3.37}$$

A few remarks are now in order:

1. In contrast to the ABS modes $\propto e^{\pm iE_\nu t}$, the continuum harmonics $\tilde{\gamma}_\omega e^{-i\omega t}$ cannot be defined as eigenstate solutions of Eq. (3.33), since $h(\omega)$ is non-Hermitian for $|\omega| > \Delta$;

2. The Andreev eigenspinors η_ν can always be normalized, $\eta_\nu^\dagger \eta_\nu = 1$. However, in general, they are not necessarily orthogonal for different ABSs, i.e., $\eta_\nu^\dagger \eta_{\nu'} \neq 0$ for $\nu \neq \nu'$, since $[h(E_\nu), h(E_{\nu'})] \neq 0$ except in the atomic limit

Case with the phase fluctuation effects.— We now return to the full EOM (3.28) in the presence of phase fluctuations $\tilde{\phi}$. Since Eq. (3.28) is linear in the field operator $\gamma(t)$, it is convenient to switch to a *first-quantized framework* for the fermionic part. In first quantization, ABS and continuum quasiparticles are represented by a 4ℓ-component wave function $\Psi(t)$, which obeys a time-nonlocal Schrödinger equation,

$$\mathcal{L}(i\partial_t)\Psi(t) = \int dt' \tilde{V}(t,t')\Psi(t'), \quad \mathcal{L}(i\partial_t) = i\partial_t - h(i\partial_t). \tag{3.38}$$

The perturbation $\tilde{V}(t,t')$ is linear in the bosonic operator $\tilde{\phi}(t)$, see Eq. (3.31). The latter plays the role of an external fluctuating force and has the correlation function $\mathcal{D}(t,t')$ in Eq. (3.16). We note that $[\tilde{\phi}(t), \tilde{\phi}(t')] \neq 0$ for $t \neq t'$, and hence $\mathcal{D}(\omega) \neq \mathcal{D}(-\omega)$, cf. Eq. (3.17), except in the classical oscillator limit corresponding to high temperature $T_b \gg \omega$. However, beyond this limit, any solution $\Psi(t)$ of Eq. (3.38) is still an operator with respect to the bosonic bath.

Similar to Eq. (3.35), the expansion of $\Psi(t)$ in the quasiparticle basis can be written as

$$\Psi(t) = \tau_x \Psi^*(t) = \sum_{\nu=1}^{2\ell} \left[a_\nu(t)\eta_\nu e^{-iE_\nu t} + a_\nu^*(t)\tau_x \eta_\nu^* e^{iE_\nu t} \right] + \tilde{\Psi}(t), \tag{3.39}$$

where in the first-quantized framework, the $a_\nu(t)$ are now complex-valued probability amplitudes for ABSs, see Eq. (3.36). Their time dependence comes from $\tilde{\phi}(t)$. Likewise, $\tilde{\Psi}(t)$ represents the continuum harmonics with $|\omega| > \Delta$. In what follows, without loss of generality, we assume $E_\nu > 0$ for all $\nu \in \{1, \ldots, 2\ell\}$, where double-counting partners with negative energy (related by particle-hole symmetry) are labeled by $\bar{\nu}$, i.e.,

$$E_{\bar{\nu}} = -E_\nu, \quad \eta_{\bar{\nu}} = \tau_x \eta_\nu^*.$$

We emphasize that no redefinition of ℓ is required. With double counting, we thus have 4ℓ states. For simplicity, we here assume that no zero modes with $E_\nu = 0$ are present. The

corresponding modifications necessary to describe such situations are straightforward to implement.

To compute transition rates for quasiparticle states in the presence of $\tilde{\phi}(t)$, our strategy is to solve Eq. (3.38) iteratively to first order in $\tilde{V}$. We then calculate the transition probability to a given state by averaging over the phase fluctuations. To do so, several assumptions need to be made:

1. First, we assume that the bath remains in thermal equilibrium at temperature T_b at all times;

2. Besides, we assume that ABSs (with energies $\pm E_\nu$) are not entangled with continuum states ($|\omega| > \Delta$) [42], i.e., continuum states play the role of a fermionic bath for the ABS sector.

We model the continuum state distribution by a thermal quasi-equilibrium Fermi function with an effective "quasiparticle temperature" $T_{\rm qp}$. This temperature is set by the temperature of the BCS superconducting leads, and can in general be different from the environmental temperature T_b. In Sec. 3.3, we consider the regime $T_{\rm qp} \geq T_b$.

Let us now consider the time evolution of the Andreev state η_λ in the presence of phase fluctuations. To first order in $\tilde{V}$, the solution of the Schrödinger equation (3.38) is given by

$$\Psi(t) = \eta_\lambda e^{-iE_\lambda t} + \Psi_\lambda^{(1)}(t),$$

with

$$\Psi_\lambda^{(1)}(t) = \int dt_1 dt_2\, G^R(t,t_1)\tilde{V}(t_1,t_2)\eta_\lambda e^{-iE_\lambda t_2}, \tag{3.40}$$

where $G^R(t,t')$ is the retarded GF of the junction in the absence of phase fluctuations,

$$\begin{aligned} G^R(t,t') &= \int \frac{d\omega}{2\pi}\, e^{-i\omega(t-t')} G^R(\omega), \\ G^R(\omega) &= \frac{1}{\omega - h(\omega) + i\delta_+}. \end{aligned} \tag{3.41}$$

We put $\delta_+ \to 0^+$ at the end of the calculation but allow for a finite phenomenological quasiparticle decay rate δ_+ in intermediate steps. Using Eq. (3.31) with

$$\tilde{\phi}(t) = \int \frac{d\omega}{2\pi}\, e^{-i\omega t}\phi_\omega, \quad \phi_\omega^\dagger = \phi_{-\omega},$$

we obtain

$$\Psi_\lambda^{(1)}(t) = \int \frac{d\omega}{2\pi}\, e^{-i(E_\lambda+\omega)t} G^R(E_\lambda+\omega)\left[\tau_z \mathcal{I}(E_\lambda) - \mathcal{I}(E_\lambda+\omega)\tau_z\right]\eta_\lambda \frac{\phi_\omega}{2}. \tag{3.42}$$

In the next section, this result will be used to compute transition rates involving ABSs. Those transition rates in turn appear in the Lindblad equation governing the dynamics of the ABS sector, see Sec. 3.2.4.

Electron-phonon interactions.— It is worth noting that it is possible to additionally include include thermal phonons in the effective EOM (3.28). This can be achieved by adding the electron-phonon interaction term $H_{\rm e-ph}$ to the full Hamiltonian H. For instance, $H_{\rm e-ph}$ can describe the lead electrons $\psi_j(\mathbf{r})$ coupled to longitudinal acoustic phonons within the deformation potential approximation,

$$H_{\rm e-ph} \sim \int d\mathbf{r}\, \psi_j^\dagger(\mathbf{r})\tau_z\psi_j(\mathbf{r})\nabla\cdot\mathbf{u}(\mathbf{r}),$$

where $\mathbf{u}(\mathbf{r})$ is the phonon displacement field operator. Following the steps in Sec. 3.2.2 then leads to Eq. (3.28), with the right-hand-side containing two types of kernels:

1. The phase-fluctuation kernel $\tilde{V} \propto \tilde{\phi}$, representing an external bosonic environment for the dot fermions. This environment equilibrates at temperature T_b. The coupling to the $\tilde{\phi}$ fluctuations is mainly restricted to the dot region;

2. A similar (non-local in time) phonon interaction kernel $V_{\rm ph} \propto \xi$, which, similarly as the phase-fluctuation term, is linear in a dimensionless bosonic variable ξ encapsulating the phonon modes. This term represents an intrinsic bosonic environment of the dot fermions, which equilibrates at temperature $T_{\rm qp}$. Phonon modes interact with lead electrons throughout the whole junction (for short nanowires, the direct electron-phonon interaction in the dot region can be neglected due to the small size of the corresponding spatial region).

As shown in Sec. 3.3, the condition $T_{\rm qp} > T_b$ is an important ingredient for observing QMEs in our setup. This temperature condition implies local cooling of the dot region, which can be realized if the coupling of the dot to phase fluctuations is stronger than its coupling to phonons. As a consequence, in the nanowire dot region, local equilibration to a thermal state at temperature $\approx T_b$ is then expected.

For superconducting leads, the relaxation rate (inverse lifetime) $\tau_{\rm ph}^{-1}$ of bulk quasiparticles due to electron-phonon interactions can be estimated as the relaxation rate of a normal-state electron with energy Δ above the Fermi level. One finds $\tau_{\rm ph}^{-1} \sim \Delta^3/\Theta_D^2$ [52], where Θ_D is the Debye temperature. This estimate gives an upper bound on the phonon-induced relaxation rate for ABSs. In short junctions, this rate is even smaller by a (generally geometry-dependent) factor L/ξ_0, as shown in Ref. [53] for an adiabatic constriction model. The relaxation rate due to phase fluctuations can be estimated as $\tau_\phi^{-1} \sim \Delta^2 \omega_\phi$, where $\omega_\phi \sim J(\Delta)$ is the characteristic energy scale of the spectral density $J(\omega)$ at relevant transition energies. In particular, for the Lorentzian shape (3.97), we estimate $\omega_\phi \sim \eta/\Delta^2$ in the regime $\Omega_e, \eta \ll \Delta$, where η is the damping strength. As a result, electromagnetic phase fluctuations strongly dominate over phonon relaxation processes, $\tau_\phi^{-1} \gg \tau_{\rm ph}^{-1}$, for sufficiently strong damping of the LC oscillator,

$$\eta/\Delta \gg (L/\xi_0)(\Delta/\Theta_D)^2. \tag{3.43}$$

For instance, for a short junction with Al leads and $L/\xi_0 \sim 10^{-1}$, taking the Lorentzian spectral density (3.97) of an LC circuit, we estimate $\eta \gg 10^{-5}\Delta$. Assuming that this condition is met, phonon-induced processes are henceforth considered as subleading and will not be taken into account.

3.2.3 Transition rates

In this subsection, we compute the rates for transitions, induced by the electromagnetic environment, connecting different ABSs as well as ABS and above-gap continuum states.

Atomic limit

Before tackling the full expression (3.42), it is instructive to first study the atomic limit, where substantial simplifications are possible. Taking $\Delta \to \infty$, see Eq. (3.34), we find

$$G^R(\omega) = \sum_{\nu=1}^{2\ell} \left[\frac{\eta_\nu \eta_\nu^\dagger}{\omega - E_\nu + i\delta_+} + \frac{\eta_{\bar{\nu}} \eta_{\bar{\nu}}^\dagger}{\omega + E_\nu + i\delta_+} \right], \tag{3.44}$$

where we used the completeness of the ABS *orthonormal* basis. In this limit, the perturbation term (3.31) reduces to

$$\tilde{V}(t,t') = \frac{\tilde{\phi}(t)}{2} I_A \delta(t-t'),$$

with the time-independent supercurrent operator $I_A = [\tau_z, \mathcal{I}]$. Using Eq. (3.32), we find

$$I_A = \sum_j s_j \begin{pmatrix} 0 & iF_j^\dagger e^{-is_j\phi_0/2} \\ -iF_j e^{is_j\phi_0/2} & 0 \end{pmatrix} = 2\frac{\partial h_A}{\partial \phi_0}. \tag{3.45}$$

In general, $[I_A, h_A] \neq 0$. One exception is the ballistic limit of perfect transparency, which corresponds to $\epsilon = 0$, symmetric hopping amplitudes $t_1 = t_2$, and $s_1 = -s_2 = 1$ in Eq. (3.15). In this case, with $F_1 = F_2 = F/2$, one finds

$$h_A = -\begin{pmatrix} 0 & F^\dagger \\ F & 0 \end{pmatrix} \cos\frac{\phi_0}{2}, \quad I_A = \begin{pmatrix} 0 & F^\dagger \\ F & 0 \end{pmatrix} \sin\frac{\phi_0}{2}, \tag{3.46}$$

and therefore $[I_A, h_A] = 0$. Phase fluctuations thus cannot induce transitions between ballistic ABSs.

Applying the atomic limit to Eq. (3.42) for general junction parameters, we obtain

$$\begin{aligned} \Psi_\lambda^{(1)}(t) &= \int \frac{d\omega}{2\pi} e^{-i(E_\lambda+\omega)t} G^R(E_\lambda+\omega) I_A \eta_\lambda \frac{\phi_\omega}{2} \\ &= \sum_{\nu=1}^{2\ell} \left[a_\nu(t)\eta_\nu e^{-iE_\nu t} + a_{\bar\nu}(t)\eta_{\bar\nu} e^{iE_{\bar\nu}t} \right]. \end{aligned} \tag{3.47}$$

Note that here $a_\nu(t)$ and $a_{\bar\nu}(t)$ are independent probability amplitudes, in contrast to Eq. (3.39), where $a_{\bar\nu}(t) = a_\nu^*(t)$ due to the imposed reality constraint $\Psi(t) = \tau_x \Psi^*(t)$. The point is that in Eq. (3.40) we consider a scattering problem with an incoming state

$$\Psi_{\rm in}(t) = \eta_\lambda e^{-iE_\lambda t},$$

which breaks particle-hole symmetry,

$$\Psi_{\rm in}(t) \neq \tau_x \Psi_{\rm in}^*(t).$$

Accordingly, the outgoing solution $\Psi_\lambda^{(1)}(t)$ is not required to obey the reality constraint. In Eq. (3.47), the amplitude $a_n(t)$ with $n \in \{\nu, \bar\nu\}$ is given by

$$a_n(t) = e^{iE_n t} \eta_n^\dagger \Psi_\lambda^{(1)}(t).$$

Consequently, the probability for an inter-level transition $\lambda \to n \neq \lambda$, averaged over phase fluctuations, is given by

$$\begin{aligned} w_{\lambda\to n}(t) = \langle a_n^*(t) a_n(t)\rangle_b = \int \frac{d\omega d\omega'}{(2\pi)^2} e^{-i(\omega-\omega')t} \left\langle \frac{\phi_{\omega'}^\dagger}{2} \frac{\phi_\omega}{2} \right\rangle_b \\ \times \left[\eta_\lambda^\dagger I_A G^A(E_\lambda+\omega')\eta_n\right] \left[\eta_n^\dagger G^R(E_\lambda+\omega) I_A \eta_\lambda\right], \end{aligned} \tag{3.48}$$

where

is the advanced GF. Using Eqs. (3.16), (3.17), and (3.44), we obtain

$$w_{\lambda\to n} = \int d\omega\, J(\omega) n_B(\omega) \frac{|I_{n\lambda}|^2}{|E_\lambda + \omega - E_n + i\delta_+|^2}, \quad I_{n\lambda} = \eta_n^\dagger I_A \eta_\lambda. \tag{3.49}$$

For $\delta_+ \to 0^+$, we have

$$\frac{1}{|x+i\delta_+|^2} \to 2\pi\tau_+\delta(x)$$

with the time scale

$$\tau_+ = \frac{1}{2\delta_+} \to \infty.$$

This time scale corresponds to the decay time of the transition probability,

$$w_{\lambda\to n}(t) \propto e^{-t/\tau_+},$$

as follows from

$$G^R(t,0) \propto \Theta(t)e^{-\delta_+ t},$$

before averaging over the bath (where $\Theta(t)$ is the Heaviside step function). For infinitely long observation time, we expect $\tau_+ \to \infty$ if no intrinsic sources of dissipation are present in the junction ($\delta_+ \to 0^+$). Hence the transition probability per unit time, i.e., the transition rate, is given by

$$\Gamma_{\lambda\to n} = \frac{w_{\lambda\to n}}{\tau_+} = 2\pi|I_{n\lambda}|^2 J(\omega) n_B(\omega)\Big|_{\omega=E_n-E_\lambda}. \tag{3.50}$$

Equation (3.50) reproduces the Fermi golden rule result obtained in the atomic limit along the BdG route, e.g., in Refs. [42, 46, 47]. Here, this result has instead been derived from the GF approach by solving the Schrödinger equation (3.38), without explicit construction of BdG eigenstates. The cases $E_n - E_\lambda > 0$ and $E_n - E_\lambda < 0$ describe transitions $\lambda \to n$ induced by the absorption and emission of a boson, respectively.

We next extend the calculation of transition rates beyond the atomic limit. We recall that for finite Δ, the Schrödinger equation (3.38) is nonlocal in time. We first compute all transition rates within the ABS sector, and then those connecting ABSs and continuum states.

Transition rates between Andreev states

We return to the scattering problem (3.40) with $\Psi_\lambda^{(1)}(t)$ in Eq. (3.42), where we may write

$$\Psi_\lambda^{(1)}(t) = \sum_{n\in\{\nu,\bar\nu\}} a_n(t)\eta_n e^{-iE_n t} + \tilde\Psi(t), \quad \eta_{\bar\nu} = \tau_x\eta_\nu^*, \tag{3.51}$$

with $\nu \in \{1,\dots,2\ell\}$. We recall that $\tilde\Psi(t)$ represents above-gap continuum states and that, in general, $\eta_n^\dagger\eta_{n'} \neq 0$ for $n \neq n'$. For very long times $t = T$, $a_n(t)$ approaches the constant value

$$a_n = \frac{1}{T}\int_0^T dt\, e^{iE_n t}\eta_n^\dagger\Psi_\lambda^{(1)}(t),$$

resulting in

$$\begin{aligned} a_n &= \int \frac{d\omega}{2\pi}\frac{\phi_\omega}{2} Q_T^*(E_\lambda+\omega-E_n) \\ &\times \eta_n^\dagger G^R(E_\lambda+\omega)\,[\tau_z\mathcal{I}(E_\lambda) - \mathcal{I}(E_\lambda+\omega)\tau_z]\,\eta_\lambda, \end{aligned} \tag{3.52}$$

with the quantity

$$Q_T(E) \equiv \frac{1}{T}\int_0^T dt\, e^{iEt} = \frac{e^{iET}-1}{iET}. \tag{3.53}$$

This function, for finite but large time T, can be regarded as a *continuous version of the Kronecker symbol* $\delta_{E,0}$, i.e., it is not a singular function of E. Note that $Q_T(E=0)=1$ but $Q_T(E\neq 0)\to 0$ for $T\to\infty$.

For $E_\lambda+\omega\simeq E_n$, which is realized to good accuracy because of the Q_T-factor in Eq. (3.52), one finds, see Eqs. (3.36) and (3.41),

$$\eta_n^\dagger G^R(E_\lambda+\omega)\simeq \eta_n^\dagger\frac{1}{E_\lambda+\omega-h(E_n)+i\delta_+}=\frac{1}{E_\lambda+\omega-E_n+i\delta_+}\eta_n^\dagger.$$

As a result, we find

$$a_n=\int\frac{d\omega}{2\pi}\frac{\phi_\omega}{2}\,Q_T^*(E_\lambda+\omega-E_n)\,\frac{I_{n\lambda}}{E_\lambda+\omega-E_n+i\delta_+}, \tag{3.54}$$

with the current matrix element

$$I_{n\lambda}=\eta_n^\dagger\left[\tau_z\mathcal{I}(E_\lambda)-\mathcal{I}(E_n)\tau_z\right]\eta_\lambda. \tag{3.55}$$

Proceeding now along the same steps as in the atomic limit, the probability for the transition $\lambda\to n$ averaged over phase fluctuations is given by

$$w_{\lambda\to n}=\langle a_n^* a_n\rangle_b=\int d\omega\, J(\omega)n_B(\omega)\,|Q_T(E_\lambda+\omega-E_n)|^2 \times\frac{|I_{n\lambda}|^2}{|E_\lambda+\omega-E_n+i\delta_+|^2}. \tag{3.56}$$

For $\delta_+\to 0$, using

$$|Q_T(E)|^2|E+i\delta_+|^{-2}\to 2\pi\tau_+\delta(E),$$

the transition rate between Andreev states $\lambda\to n$ follows as

$$\Gamma_{\lambda\to n}=\frac{w_{\lambda\to n}}{\tau_+}=2\pi|I_{n\lambda}|^2J(\omega)n_B(\omega)\Big|_{\omega=E_n-E_\lambda}. \tag{3.57}$$

As one may have expected, Eq. (3.57) differs from the atomic-limit result (3.50) only in the current matrix elements. For $\Delta\to\infty$, Eq. (3.55) recovers the current matrix element for the atomic limit specified after Eq. (3.49). Moreover, Eq. (3.57) also agrees with previous derivations based on the BdG formalism [42, 46, 47]. One easily checks that the transition rate (3.57) satisfies a detailed balance relation,

$$\Gamma_{n\to\lambda}=e^{-(E_\lambda-E_n)/T_b}\Gamma_{\lambda\to n}, \tag{3.58}$$

which connects the rates for forward and backward transitions as required for equilibrium fluctuations. In addition, particle-hole symmetry (in particular, $I_{n\lambda}=-I^*_{\bar n\bar\lambda}$) implies the symmetry relation

$$\Gamma_{n\to\lambda}=\Gamma_{\bar\lambda\to\bar n}.$$

Transition rates between ABSs and continuum states

Before calculating the transition rates between ABSs and continuum states, let us briefly discuss the spectral function

$$S(\omega)=i[G^R(\omega)-G^A(\omega)]$$

of the junction in the absence of phase fluctuations. Due to the particle-hole symmetry relation (3.37), the GFs satisfy the relations

$$G^{R/A}(\omega)=-\tau_x\left[G^{R/A}(-\omega)\right]^*\tau_x, \tag{3.59}$$

and hence the spectral function obeys the constraint

$$S(-\omega) = \tau_x S^T(\omega)\tau_x. \tag{3.60}$$

Note that $S(\omega)$ is Hermitian for all ω and thus can be diagonalized,

$$S(\omega) \to \text{diag}\left[\begin{pmatrix} \rho_1(\omega) & 0 \\ 0 & \rho_{\bar{1}}(\omega) \end{pmatrix}, \cdots, \begin{pmatrix} \rho_{2\ell}(\omega) & 0 \\ 0 & \rho_{\bar{2\ell}}(\omega) \end{pmatrix}\right], \tag{3.61}$$

where the 2×2 matrices act in Nambu space. The spectral eigenvalues $\rho_n(\omega) \geq 0$ with $n \in \{\nu, \bar{\nu}\}$ correspond to the density of states for quasiparticles with energy ω. They are related by particle-hole symmetry, see Eq. (3.60), according to

$$\rho_\nu(\omega) = \rho_{\bar{\nu}}(-\omega).$$

In particular, in the subgap region, $h(\omega)$ is Hermitian and $S(\omega)$ corresponds to a set of δ-function peaks located at the ABS energies,

$$S(\omega)\Big|_{|\omega|<\Delta} = 2\pi \sum_{\nu=1}^{2\ell} \left[\eta_\nu \eta_\nu^\dagger \delta(\omega - E_\nu) + \eta_{\bar{\nu}} \eta_{\bar{\nu}}^\dagger \delta(\omega + E_\nu)\right]. \tag{3.62}$$

To compute transition rates connecting ABSs to the continuum sector, we first recall that after integrating out the superconducting leads, the continuum quasiparticles are encoded in the Green's function $G^{R/A}(\omega)$. However, they cannot be described by eigenstates of the Hamiltonian

$$h(\omega) \neq h^\dagger(\omega) \text{ for } |\omega| > \Delta.$$

In order to calculate the transition rates, we identify the continuum modes via the eigenstates of the spectral function $S(\omega)$. Based on Eq. (3.61),

$$S(\omega)\xi_n(\omega) = 2\pi\rho_n(\omega)\xi_n(\omega), \quad \xi_n^\dagger(\omega)\xi_{n'}(\omega) = \delta_{nn'}, \tag{3.63}$$

where the $\xi_n(\omega)$ are 4ℓ-dimensional multispinors in level-Nambu space with $n \in \{\nu, \bar{\nu}\}$ and $\nu \in \{1, \ldots, 2\ell\}$. Using the completeness of the basis $\{\xi_n(\omega)\}$ for given ω, we write

$$S(\omega) = 2\pi \sum_{n\in\{\nu,\bar{\nu}\}} \rho_n(\omega)\xi_n(\omega)\xi_n^\dagger(\omega), \tag{3.64}$$

which generalizes Eq. (3.62) to arbitrary ω, including continuum states with $|\omega| > \Delta$.

To proceed, we expand the continuum wave function $\tilde{\Psi}(t)$, see Eq. (3.51), in the spectral function $S(\omega)$ eigenstate basis (3.63),

$$\tilde{\Psi}(t) = \int_{|E|>\Delta} dE \sum_{n\in\{\nu,\bar{\nu}\}} \tilde{a}_n(E)\rho_n(E)\xi_n(E)e^{-iEt}, \tag{3.65}$$

where $\tilde{a}_n(E)$ are the corresponding probability amplitudes for continuum modes at long times $t = T$. From Eq. (3.51), we now find

$$\begin{aligned} \tilde{a}_n(E) &= \frac{1}{\pi\rho_n(E)} \int_0^T dt e^{iEt} \xi_n^\dagger(E)\Psi_\lambda^{(1)}(t) \\ &= \frac{1}{\pi\rho_n(E)} \int \frac{d\omega}{2\pi} \frac{\phi_\omega}{2} \mathcal{Q}_T^*(E_\lambda + \omega - E) \\ &\times \xi_n^\dagger(E) G^R(E_\lambda + \omega) \left[\tau_z \mathcal{I}(E_\lambda) - \mathcal{I}(E_\lambda + \omega)\tau_z\right] \eta_\lambda, \end{aligned} \tag{3.66}$$

with $T \to \infty$ and $\mathcal{Q}_T(E) = TQ_T(E)$, see Eq. (3.53). Using the basis completeness identity

$$\sum_{k\in\{\nu,\bar{\nu}\}} \xi_k(E)\xi_k^\dagger(E) = 1,$$

and the Lehmann representation for the Green's function $G^R(\omega)$,

$$G^R(\omega) = \int \frac{dz}{2\pi} \frac{S(z)}{\omega - z + i0^+}, \tag{3.67}$$

we obtain

$$\tilde{a}_n(E) = \frac{1}{\pi\rho_n(E)} \int \frac{d\omega}{2\pi} \frac{\phi_\omega}{2} \mathcal{Q}_T^*(E_\lambda + \omega - E) \sum_{k\in\{\nu,\bar{\nu}\}} G^R_{nk}(E)\tilde{I}_{k\lambda}(E),$$

where

$$\tilde{I}_{k\lambda}(E) = \xi_k^\dagger(E)\left[\tau_z \mathcal{I}(E_\lambda) - \mathcal{I}(E_\lambda + \omega)\tau_z\right]\eta_\lambda, \tag{3.68}$$

and

$$G^R_{nk}(E) = \xi_n^\dagger(E) G^R(E_\lambda + \omega)\xi_k(E) \tag{3.69}$$

$$= \sum_{m\in\{\nu,\bar{\nu}\}} \int \frac{dz\,\rho_m(z)}{E_\lambda + \omega - z + i0^+} \left(\xi_n^\dagger(E)\xi_m(z)\right)\left(\xi_m^\dagger(z)\xi_k(E)\right).$$

Following the same procedure as before, the probability for the transition $\lambda \to (E, n)$ between the ABS with index λ and the continuum mode with index n at energy E, averaged over phase fluctuations, is given by

$$w_{\lambda\to(E,n)} = \langle \tilde{a}_n^*(E)\tilde{a}_n(E)\rangle_b$$

$$= \frac{1}{\pi^2\rho_n^2(E)} \int d\omega\, J(\omega) n_B(\omega) \left|\mathcal{Q}_T(E_\lambda + \omega - E)\right|^2 \left| \sum_{k\in\{\nu,\bar{\nu}\}} G^R_{nk}(E)\tilde{I}_{k\lambda}(E)\right|^2.$$

Taking into account that

$$\lim_{T\to\infty} \frac{d}{dT} \left|\mathcal{Q}_T(E)\right|^2 = \lim_{T\to\infty} \frac{\sin(ET)}{E/2} = 2\pi\delta(E), \tag{3.70}$$

the transition rate follows as

$$\Gamma_{\lambda\to(E,n)} = \lim_{T\to\infty} \frac{d}{dT} w_{\lambda\to(E,n)}$$

$$= \frac{2}{\pi\rho_n^2(E)} \int d\omega\, J(\omega) n_B(\omega) \delta(E_\lambda + \omega - E) \left| \sum_{k\in\{\nu,\bar{\nu}\}} G^R_{nk}(E)\tilde{I}_{k\lambda}(E)\right|^2,$$

with the current matrix elements, see Eqs. (3.68) and (3.69) with $E_\lambda + \omega = E$,

$$\tilde{I}_{k\lambda}(E) = \xi_k^\dagger(E)\left[\tau_z \mathcal{I}(E_\lambda) - \mathcal{I}(E)\tau_z\right]\eta_\lambda, \tag{3.71}$$

and using Eq. (3.69). Assuming that $\rho_m(z)$ is a smooth function of z for all m, one can discard the principal value integrals in Eq. (3.69), which yields

$$G^R_{nk}(E) = -i\pi\delta_{nk}\rho_n(E), \tag{3.72}$$

and hence, see Eq. (3.57),

$$\Gamma_{\lambda\to(E,n)} = 2\pi \int d\omega\, J(\omega) n_B(\omega) \delta(E_\lambda + \omega - E) \left|\tilde{I}_{n\lambda}(E)\right|^2. \tag{3.73}$$

The total quasiparticle escape rate out of the ABS sector is obtained by summing over all partial rates (3.73),

$$\Gamma_\lambda^{\rm out} = \int_{|E|>\Delta} dE \sum_{n\in\{\nu,\bar{\nu}\}} \rho_n(E)\left[1 - n_F(E)\right] \Gamma_{\lambda\to(E,n)}, \tag{3.74}$$

where $n_F(E)$ is the Fermi-Dirac function with temperature $T_{\rm qp}$. We arrive at

$$\Gamma_\lambda^{\rm out} = 2\pi \int d\omega\, J(\omega) n_B(\omega) \sum_{n\in\{\nu,\bar{\nu}\}} \Theta(|E|-\Delta)\rho_n(E)\left[1 - n_F(E)\right] \left|\tilde{I}_{n\lambda}(E)\right|^2 \Big|_{E=E_\lambda+\omega}. \tag{3.75}$$

The reverse rate follows from the detailed balance relation (3.58),

$$\Gamma_{(E,n)\to\lambda} = 2\pi \int d\omega\, J(\omega)\left[n_B(\omega)+1\right] \delta(E_\lambda + \omega - E) \left|\tilde{I}_{n\lambda}(E)\right|^2,$$

such that the total transition rate from the continuum band to the ABS with index λ is

$$\Gamma_\lambda^{\rm in} = 2\pi \int d\omega\, J(\omega)\left[n_B(\omega)+1\right] \sum_{n\in\{\nu,\bar{\nu}\}} \Theta(|E|-\Delta)\rho_n(E) n_F(E) \left|\tilde{I}_{n\lambda}(E)\right|^2 \Big|_{E=E_\lambda+\omega}. \tag{3.76}$$

The above expressions are consistent with those derived by the BdG approach in the previous chapter, but allow one to treat the case of a Josephson dot without solving the full BdG scattering problem. Let us emphasize that Eqs. (3.36) and (3.63) contain just matrices in dot-level space whereas the solution of the full BdG equation requires, in addition, the matching of spatially dependent wave functions of the leads. In our approach, the spatially dependent structure of the wave functions is efficiently encapsulated by the boundary GFs in Eq. (3.21), thereby circumventing an explicit construction of the BdG solution.

3.2.4 Lindblad master equation

Next, the obtained transition rates within the ABSs sector and ABSs and continuum are inserted in the Lindblad master equation (2.45) describing the dynamics of the ABS sector within the above approximations

$$\begin{aligned}
\partial_t \rho_A &= -i\sum_\lambda E_\lambda [a_\lambda^\dagger a_\lambda, \rho_A] + \sum_{\lambda,\lambda'} \Bigg(\Gamma_{\lambda'\to\lambda}\, \mathcal{L}\left[a_\lambda^\dagger a_{\lambda'}\right]\rho_A + \\
&+ \frac{1}{2}\left(\Gamma_{\lambda'\to\bar{\lambda}}\, \mathcal{L}\left[a_\lambda a_{\lambda'}\right]\rho_A + \Gamma_{\bar{\lambda}'\to\lambda}\, \mathcal{L}\left[a_\lambda^\dagger a_{\lambda'}^\dagger\right]\rho_A\right)\Bigg) \\
&+ \sum_\lambda \left(\Gamma_\lambda^{\rm in}\, \mathcal{L}[a_\lambda^\dagger]\rho_A + \Gamma_\lambda^{\rm out}\, \mathcal{L}[a_\lambda]\rho_A\right).
\end{aligned} \tag{3.77}$$

Here $\rho_A(t)$ is the reduced density matrix describing the state dynamics in the ABS sector. The fermion annihilation operator a_λ refers to the ABS with energy $E_\lambda > 0$. Also in this case, in order to avoid double counting, summations over λ variables extend only over positive-energy states. Negative-energy states are described by the particle-hole symmetry relations $E_{\bar{\lambda}} = -E_\lambda$ and $a_{\bar{\lambda}} = a_\lambda^\dagger$. The transition rates $\Gamma_{n\to n'}$ between ABSs (with energies of either sign) are specified in Eq. (3.57), and the rates $\Gamma_\lambda^{\rm out/in}$ connecting ABSs to the continuum sector are given by Eqs. (3.75) and (3.76), respectively.

3.3 Quantum Mpemba Effect

In this section, we apply the formalism developed in the previous section to study the QME in the Josephson junctions embedded in the setup of Fig. 1.3. In Sec. 3.3.1, we will see that already the simplest case of a phase-quenched short single-channel junction without SOI and/or Zeeman field gives rise to different types of QMEs. The short-junction case can be also described analytically in the limit $\Gamma \gg \Delta$, where Γ is the hybridization between the dot level and the BCS leads. In Sec. 3.3.2, we consider an intermediate-length junction with SOI and Zeeman field, where we present numerical results on the QME. For simplicity, we always put the chemical potential $\mu = 0$ in the quantum dot region.

As discussed in Sec. 3.2.2, we assume that the transition rates induced by the electromagnetic environment (bosonic bath) dominate over phonon-induced rates, and neglect phonon-related effects in what follows. Many-body states in the Andreev sector then equilibrate according to transition rates determined by the bosonic temperature T_b characterizing the electromagnetic environment. In addition, Andreev states are also coupled to the fermionic bath corresponding to BCS quasiparticles in the superconducting leads, and thus these transition rates also depend on the temperature $T_{\rm qp}$ of the fermionic bath. We assume that quasiparticles are in thermal equilibrium and focus on the case $T_{\rm qp} \geq T_b$.

3.3.1 Short-junction case

We begin with short Josephson junctions without SOI and Zeeman field. We assume that $V(x)$ in Eq. (3.3) is a hard-wall potential of short length $L \ll v_{\rm F}/\Delta$. Below,

$$\epsilon = \pi^2/(2m_x L^2),$$

is the bare dot level energy and, assuming spin-independent tunnel junctions, the hybridizations to the left and right leads are given by $\Gamma_j = 2t_j^2/L$, see Eq. (3.27). Assuming symmetric tunnel couplings in Eq. (3.7), $t_1 = t_2 = t_0$, we obtain

$$\Gamma_L = \Gamma_R \equiv \Gamma/2 = 2t_0^2/L.$$

The junction then allows only for a single (positive energy) spin-degenerate ABS with energy $0 < E_1(\phi_0) < \Delta$. As a consequence, there are four many-body Andreev states,

$$|n\rangle \in \{|0\rangle, |\uparrow\rangle, |\downarrow\rangle, |\uparrow\downarrow\rangle\},$$

which correspond to an empty, singly occupied (with either spin up or down, $\sigma \in \{\uparrow, \downarrow\}$), or doubly occupied ABS level, respectively.

As first step, we then project the Lindblad equation (3.77) for the Andreev quantum state $\rho_A(t)$ into the many-body basis $\{|n\rangle\}$. The diagonal elements of $\rho_A(t)$ define the respective occupation probabilities,

$$P_{|n\rangle}(t) = \langle n|\,\rho_A(t)\,|n\rangle \quad \text{with} \quad \sum_n P_{|n\rangle}(t) = 1,$$

which are summarized in the vector

$$\mathbf{P}(t) = \left(P_{|0\rangle}(t), P_{|\uparrow\rangle}(t), P_{|\downarrow\rangle}(t), P_{|\uparrow\downarrow\rangle}(t)\right)^T. \tag{3.78}$$

For our model, off-diagonal elements of $\rho_A(t)$ ("coherences") decouple from $\mathbf{P}(t)$ which in turn obeys a Pauli master equation,

$$\dot{\mathbf{P}}(t) = \mathbf{M}\,\mathbf{P}(t), \tag{3.79}$$

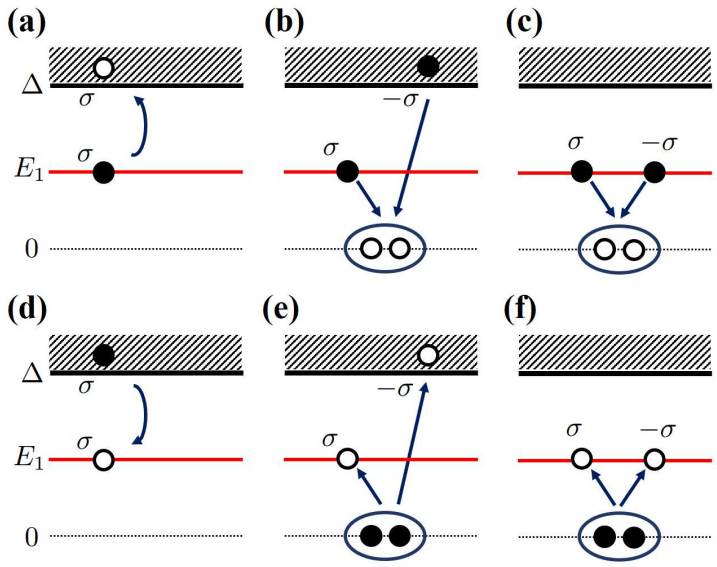

Figure 3.2: Schematic illustration of the six transition rates contributing to the off-diagonal matrix elements in Eq. (3.80). In all panels, black (open) dots refer to the initial (final) population. Encircled double dots indicate Cooper pairs. Panel (a) shows the transition of a quasiparticle of spin $\sigma \in \{\uparrow,\downarrow\}$ from the ABS energy $E_1(\phi_0)$ to a continuum level with energy $E \geq \Delta$. Panel (d) shows the reverse process. Panels (b) and (c) show processes involving fermion pair annihilation, with and without the contribution of a continuum quasiparticle, respectively. Panels (e) and (f) show the reverse processes, where fermion pairs are created. In panels (b,c) and (e,f), the quasiparticle spins must be anti-aligned.

with the matrix

$$\mathbf{M} = \begin{pmatrix} -M_{|0\rangle} & \Gamma_a^- + \Gamma_b^- & \Gamma_a^- + \Gamma_b^- & \Gamma_c^- \\ \Gamma_a^+ + \Gamma_b^+ & -M_{|\uparrow\rangle} & 0 & \Gamma_a^- + \Gamma_b^- \\ \Gamma_a^+ + \Gamma_b^+ & 0 & -M_{|\downarrow\rangle} & \Gamma_a^- + \Gamma_b^- \\ \Gamma_c^+ & \Gamma_a^+ + \Gamma_b^+ & \Gamma_a^+ + \Gamma_b^+ & -M_{|\uparrow\downarrow\rangle} \end{pmatrix}. \tag{3.80}$$

The off-diagonal matrix elements of $\mathbf{M}$ contain transition rates for the physical processes illustrated in Fig. 3.2. These rates follow from Sec. 3.2.3 and are explained in detail below. Probability conservation implies that the quantities $M_{|n\rangle}$ in Eq. (3.80) are equal to the sum of the off-diagonal elements in the corresponding columns.

Case $\Gamma \gg \Delta$

We first describe an analytical approach for identifying the QME for a single-level dot with large hybridization to the superconducting leads, $\Gamma \gg \Delta$. We go beyond this restriction in Sec. 3.3.1 by performing numerical calculations. For $\Gamma \gg \Delta$, the quantum dot model in Sec. 3.2.1 implies the well-known ABS dispersion relation [37, 54, 55]

$$E_1(\phi_0) \simeq \Delta\sqrt{1 - \mathcal{T}\sin^2(\phi_0/2)}, \tag{3.81}$$

where the normal-state transmission probability of the transport channel is given by

$$\mathcal{T} = \frac{1}{1 + (\epsilon/\Gamma)^2}. \tag{3.82}$$

In Fig. 3.2 the possible processes contributing to the off-diagonal elements of Eq. (3.80) are shown:

a, d) The rate Γ_a^- shown in Fig. 3.2(a) describes the transition of a quasiparticle with spin σ (the rate is independent of σ) from the ABS to the quasiparticle continuum. Here and in what follows, we label rates associated with processes that decrease (increase) the number of ABS quasiparticles by Γ^- (Γ^+). The rate Γ_a^- decreases this number by one unit and requires the absorption of a photon with energy

$$\delta E_a = E - E_1(\phi_0), \quad E \geq \Delta, \tag{3.83}$$

where E is the energy of the continuum quasiparticle, together with the possibility to allocate the quasiparticle in the continuum. Integrating over the allowed continuum energies, the transition rate follows from Eq. (3.74) by limiting the integral to $E > \Delta$,

$$\Gamma_a^- = \int_{E>\Delta} dE\, \gamma_a(E, \phi_0)\, J\left(\delta E_a\right) n_B\left(\delta E_a\right)\left[1 - n_F\left(E\right)\right]. \tag{3.84}$$

We recall that n_B is the Bose-Einstein function for the temperature T_b, while n_F is the Fermi-Dirac function for the temperature T_{qp}. Applying the formalism detailed in Sec. 3.2.3 in the limit $\Gamma \gg \Delta$, we find

$$\gamma_a(E, \phi_0) = \frac{\Gamma\nu(E)}{2}\left(1 + \frac{\Delta^2\cos^2\left(\phi_0/2\right)}{EE_1(\phi_0)}\right), \tag{3.85}$$

where the superconducting density of states is encoded by the function

$$\nu(E) = \Theta(|E| - \Delta)\frac{|E|}{\sqrt{E^2 - \Delta^2}}. \tag{3.86}$$

The complementary process to Eq. (3.84) is a transition from the continuum to the ABS, see Fig. 3.2(d). The corresponding rate is proportional to the probability to encounter a continuum quasiparticle times the amplitude for spontaneous or stimulated photon emission,

$$\Gamma_a^+ = \int_{E>\Delta} dE\, \gamma_a(E,\phi_0)\, J\left(\delta E_a\right) \left[1 + n_B\left(\delta E_a\right)\right] n_F\left(E\right), \tag{3.87}$$

with δE_a given by Eq. 3.83.

b, e) The rates $\Gamma_b^{\mp}$ encode the creation or annihilation of a Cooper pair by means of an ABS quasiparticle with spin σ and a continuum quasiparticle with spin $-\sigma$, see Figs. 3.2(b) and Fig. 3.2(e), respectively. (Again, the result is independent of σ.) Cooper pair annihilation comes with the energy cost

$$\delta E_b = E + E_1(\phi_0),$$

and the respective transition rates are encoded in Eq. (3.74), but limiting the integral to $E < -\Delta$. Using the formalism in Sec. 3.2.3 for $\Gamma \gg \Delta$, we can express the rates as

$$\begin{aligned}
\Gamma_b^- &= \int_{E>\Delta} dE\, \gamma_b(E,\phi_0)\, J(\delta E_b)\, [1 + n_B(\delta E_b)]\, n_F(E), \\
\Gamma_b^+ &= \int_{E>\Delta} dE\, \gamma_b(E,\phi_0)\, J(\delta E_b) n_B(\delta E_b)\, [1 - n_F(E)]\,,
\end{aligned}$$

with

$$\gamma_b(E,\phi_0) = \frac{\Gamma\nu(E)}{2}\left(1 - \frac{\Delta^2\cos^2\left(\phi_0/2\right)}{E E_1(\phi_0)}\right). \tag{3.88}$$

c, f) In Fig. 3.2(c,f), Cooper pair creation and annihilation processes involving two ABS quasiparticles with opposite spin are illustrated. Such processes have an energy cost

$$\delta E_c = 2E_1(\phi_0),$$

and change the population of the ABS sector by two units. The corresponding transition rates can be obtained from Eq. (3.57) with $E_n = -E_\lambda = E_1$. They are given by

$$\begin{aligned}
\Gamma_c^- &= \gamma_c(\phi_0)\, J\left(\delta E_c\right)\, \left[1 + n_B\left(\delta E_c\right)\right], \\
\Gamma_c^+ &= \gamma_c(\phi_0)\, J\left(\delta E_c\right)\, n_B\left(\delta E_c\right),
\end{aligned} \tag{3.89}$$

with

$$\gamma_c(\phi_0) = 2\pi\left(\frac{\epsilon\Delta\sin\left(\phi_0/2\right)}{E_1(\phi_0)}\right)^2. \tag{3.90}$$

For each pair of processes above, standard detailed balance conditions [35, 37] hold since both the bosonic environment and the fermionic continuum quasiparticles are separately assumed to be in thermal equilibrium. We note that by multiplying $\gamma_{a,b,c}$ by an overall factor, only the total relaxation time is affected, without changing the stationary state $\mathbf{P}_{\text{stat}}$ reached at asymptotically long times. The latter state obeys $\dot{\mathbf{P}}_{\text{stat}} = 0$ and only depends on ratios of transition rates.

A simplification is possible by exploiting spin degeneracy: the population difference $P_{|\uparrow\rangle}(t) - P_{|\downarrow\rangle}(t)$ decouples from $P_{|0\rangle}(t)$ and $P_{|\uparrow\downarrow\rangle}(t)$ and vanishes for $t \to \infty$. For the reduced time-dependent population vector

$$\mathbf{P}_r(t) = \left(P_{|0\rangle}(t), P_{|1\rangle}(t), P_{|\uparrow\downarrow\rangle}(t)\right)^T, \quad P_{|1\rangle}(t) = \left(P_{|\uparrow\rangle}(t) + P_{|\downarrow\rangle}(t)\right)/2, \tag{3.91}$$

we thus obtain a reduced Pauli master equation,

$$\dot{\mathbf{P}}_r(t) = \mathbf{M}_r \mathbf{P}_r(t). \tag{3.92}$$

The normalization condition is here given by

$$P_{|0\rangle}(t) + 2P_{|1\rangle}(t) + P_{|\uparrow\downarrow\rangle}(t) = 1. \tag{3.93}$$

With the above approximations, the matrix $\mathbf{M}_r$ in Eq. (3.92) follows as

$$\mathbf{M}_r = \begin{pmatrix} -2\Gamma^+_{ab} - \Gamma^+_c & 2\Gamma^-_{ab} & \Gamma^-_c \\ \Gamma^+_{ab} & -\Gamma^-_{ab} - \Gamma^+_{ab} & \Gamma^-_{ab} \\ \Gamma^+_c & 2\Gamma^+_{ab} & -2\Gamma^-_{ab} - \Gamma^-_c \end{pmatrix}, \tag{3.94}$$

with $\Gamma^\pm_{ab} = \Gamma^\pm_a + \Gamma^\pm_b$. The stationary solution of Eq. (3.92) reached at asymptotically long times is given by

$$\mathbf{P}_{r,\mathrm{stat}} = \mathcal{N} \begin{pmatrix} 2\Gamma^{-2}_{ab} + \Gamma^-_{ab}\Gamma^-_c + \Gamma^-_c\Gamma^+_{ab} \\ 2\Gamma^-_{ab}\Gamma^+_{ab} + \Gamma^+_{ab}\Gamma^-_c + \Gamma^+_c\Gamma^-_{ab} \\ 2\Gamma^{+2}_{ab} + \Gamma^-_{ab}\Gamma^+_c + \Gamma^+_c\Gamma^+_{ab} \end{pmatrix}, \tag{3.95}$$

where $\mathcal{N}$ follows by normalization, see Eq. (3.93). As expected for a dissipative master equation satisfying detailed balance, the stationary solution does not depend on initial conditions but only on ratios between transition rates. In the following, we focus on how changes of the phase difference ϕ_0 affect the stationary populations in Eq. (3.95). We assume that phase differences are taken from the interval $\phi_0 \in [0, \pi)$ such that the phase quench is uniquely related to a quench of the ABS energy $E_1(\phi_0)$, see Eq. (3.81). As shown below, by analyzing the ϕ_0-dependence of $\mathbf{P}_{r,\mathrm{stat}}$, one can identify parameter regions where a QME is possible when ϕ_0 is quenched. We also discuss the corresponding steady-state current-phase relation (CPR), which for the present case follows in the simple form [37]

$$I(\phi_0) = 2\frac{dE_1}{d\phi_0}\left(P_{|\uparrow\downarrow\rangle,\mathrm{stat}}(\phi_0) - P_{|0\rangle,\mathrm{stat}}(\phi_0)\right). \tag{3.96}$$

In order to check the robustness of the QME in our setup, we consider two particular choices for the environmental spectral density $J(\omega)$. For a microwave-circuit environment with resonance frequency Ω, coupling strength κ, and damping constant η, we use the Lorentzian spectral density [35, 46]

$$J(\omega) = \frac{\kappa^2\eta}{\pi}\left(\frac{1}{(\omega-\Omega)^2 + \frac{\eta^2}{2}} - \frac{1}{(\omega+\Omega)^2 + \frac{\eta^2}{2}}\right), \tag{3.97}$$

while for an Ohmic environment with damping coefficient α_0 and high-frequency cutoff ω_c, we employ [35, 56]

$$J(\omega) = \alpha_0 \omega e^{-|\omega|/\omega_c}. \tag{3.98}$$

For the examples shown below, we have chosen specific values for the key parameters in these spectral densities. However, we have checked that changing, e.g., the values of Ω and/or η in Eq. (3.97) by up to one order of magnitude does not significantly affect the QME. Moreover, as discussed above, changing κ or α_0 implies only a uniform rescaling of all transition rates, which does not affect the QME.

Lorentzian spectral density.— Qualitatively different behaviors are observed, as shown in Fig. 3.3 for a high-transparency junction with the Lorentzian spectral density (3.97). For three different quasiparticle temperatures $T_{\mathrm{qp}} \geq T_b$, Fig. 3.3 shows the components of the steady-state population vector $\mathbf{P}_{r,\mathrm{stat}}$ as function of the average phase difference ϕ_0, which in turn is tunable by a magnetic flux [51]:

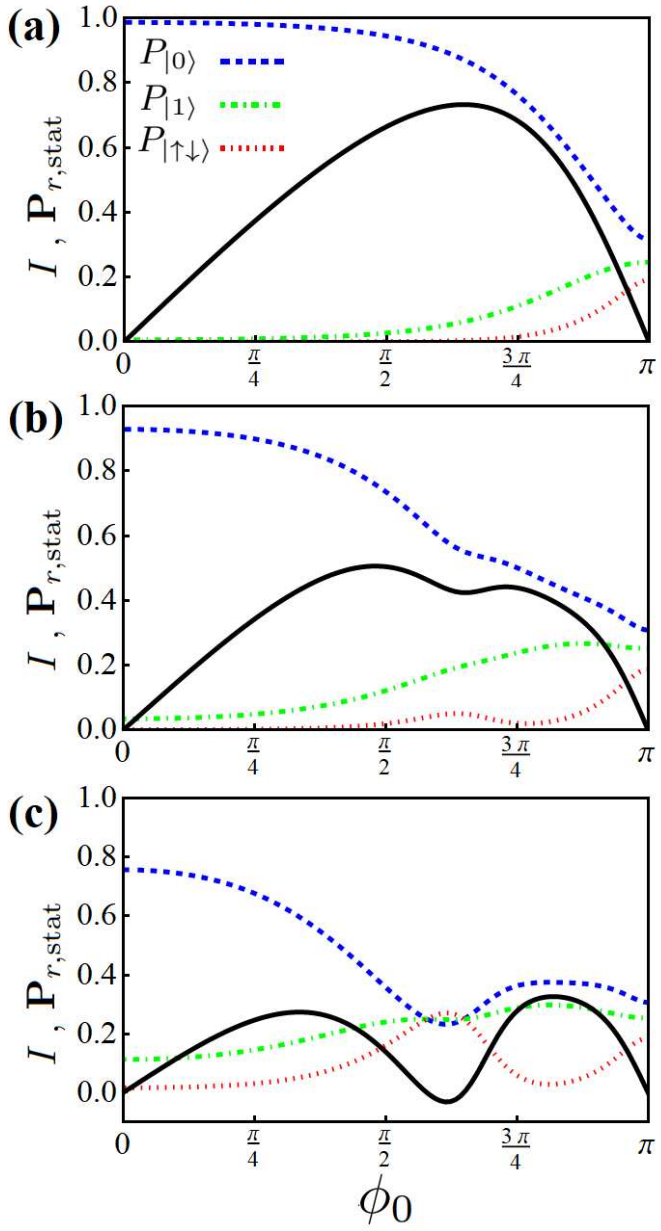

Figure 3.3: Steady-state populations $\mathbf{P}_{r,\mathrm{stat}}$ and CPR vs ϕ_0, see Eqs. (3.91), (3.95) and (3.96), for the many-body Andreev states in a short Josephson junction coupled to a microwave resonator with spectral density (3.97). The current I in the CPR is given in units of $2e\Delta/\hbar$. The elements of $\mathbf{P}_{r,\mathrm{stat}}$ are shown vs ϕ_0, where $P_{|0\rangle}$ is indicated by dashed blue curves, $P_{|1\rangle}$ by dot-dashed green curves, and $P_{|\uparrow\downarrow\rangle}$ by dotted red curves. The CPR is shown as solid black curve. Using units with $\Delta = 1$, we use $T_b = 0.2$, $\epsilon = 0.5$, $\Gamma = 10$, $\Omega = 0.01$, $\eta = 0.1$, and $\kappa = 0.1$. The corresponding junction transparency is $\mathcal{T} = 0.99$ from Eq. (3.82). The panels are for (a) $T_{\mathrm{qp}} = 0.2$, (b) $T_{\mathrm{qp}} = 0.3$, and (c) $T_{\mathrm{qp}} = 0.5$.

a) For $T_{\rm qp} = T_b$, see Fig. 3.3(a), all components of $\mathbf{P}_{r,\rm stat}$ are monotonic functions of ϕ_0;

b) Upon raising $T_{\rm qp}$ to an intermediate value, see Fig. 3.3(b), some components exhibit non-monotonic behavior. In particular, $P_{|1\rangle}$ peaks around $\phi_0 \simeq 0.85\pi$, while $P_{|\uparrow\downarrow\rangle}$ has a maximum at $\phi_0 \simeq 0.65\pi$;

c) for the highest studied value of $T_{\rm qp}$, see Fig. 3.3(c), all population components have nearly simultaneous extrema around $\phi_0 \simeq 0.6\pi$ and around $\phi_0 \simeq 0.8\pi$.

In Fig. 3.3, we also show the steady-state CPR $I(\phi_0)$ for $0 \leq \phi_0 \leq \pi$ in the respective panels, see Eq. (3.96). We observe that upon increasing the ratio $T_{\rm qp}/T_b$, the CPR can feature pronounced minima near those phase values where one has extremal points in the population components $P_{|\uparrow\downarrow\rangle,\rm stat}(\phi_0)$ and/or $P_{|0\rangle,\rm stat}(\phi_0)$. Experimentally, this observation could help to identify the interesting regime $T_{\rm qp} > T_b$. As discussed below, in this regime, the QME is expected to be realizable.

Ohmic spectral density.— In Fig. 3.4, we show that qualitatively the same behavior as in Fig. 3.3 is also encountered for an Ohmic environment described by Eq. (3.98). A high transparence junction is studies again.

a) For a rather low temperature $T_{\rm qp}$, see Fig. 3.4(a), all components of $\mathbf{P}_{r,\rm stat}$ remain monotonic functions of ϕ_0;

b) For an intermediate value of $T_{\rm qp}$, see Fig. 3.4(b), the components of $\mathbf{P}_{r,\rm stat}$ exhibit non-monotonic behavior in some ϕ_0 regions. In particular, $P_{|0\rangle}$ and $P_{|\uparrow\downarrow\rangle}$ share extremal points at $\phi_0 \simeq 0.5\pi$ and $\phi_0 \simeq 0.9\pi$, while $P_{|1\rangle}$ has a maximum for $\phi_0 \simeq 0.75\pi$;

c) for the highest studied value of $T_{\rm qp}$, see Fig. 3.4(c), all populations share extremal points around $\phi_0 \simeq 0.45\pi$ and $\phi_0 \simeq 0.85\pi$.

It is worth stressing that the stationary populations illustrated in Figs. 3.3 and 3.4 depend on which of the six transition rates $\Gamma^{\pm}_{\lambda}$ with $\lambda \in (a, b, c)$ in Eq. (3.80) are dominant. For instance, if at least one of the three rates Γ^{-}_{λ} is much larger than all rates $\Gamma^{+}_{\lambda'}$, ABS quasiparticles tend to be depleted either by hopping into the continuum sector (for $\lambda = a$) or by pair creation processes (for $\lambda = b, c$). One then finds $P_{|0\rangle} \gg P_{|1\rangle}, P_{|\uparrow\downarrow\rangle}$, see, e.g., Fig. 3.3(a) and Fig. 3.4(a) with $\phi_0 \approx 0$. On the other hand, if at least one of the rates Γ^{+}_{λ} exceeds the rates $\Gamma^{-}_{\lambda'}$, excess quasiparticles will be injected into the ABS sector by hopping from the continuum or by processes involving Cooper pair splitting. In this case, $P_{|0\rangle}$ becomes small. The relative magnitude of $P_{|1\rangle}$ vs $P_{|\uparrow\downarrow\rangle}$ is then decided by the parity-preserving rate Γ^{+}_{c} which describes the injection of two ABS quasiparticles, and by the rates $\Gamma^{+}_{a,b}$ which increase the ABS population by one unit. In such cases, as shown in Fig. 3.3(b,c) and Fig. 3.4(b,c) for specific values of ϕ_0, the stationary populations may exhibit an extremum. Experimentally, the ratio between transition rates corresponding to different processes can be tuned, for example, via the temperatures T_b and $T_{\rm qp}$, or by changing ϕ_0.

For the QME protocol, we assume that ϕ_0 is subject to a rapid quench at time $t = 0$. As we show below, the case in Fig. 3.3(a) corresponds to the absence of a QME. However, for the parameters in Fig. 3.3(b,c), two different types of QME as defined in Ref. [24] can take place for suitable initial conditions. The same conclusions apply for the corresponding panels in Fig. 3.4. Since the overall behavior in Figs. 3.3 and 3.4 is similar, we expect that the QME is robust against changes in the electromagnetic environment. In what follows, we then focus on the Lorentzian spectral density (3.97).

QME protocol

Following Ref. [24], see also Sec. 3.1, the protocol for detecting the QME consists of comparing two copies of the system for which the following steps are carried out:

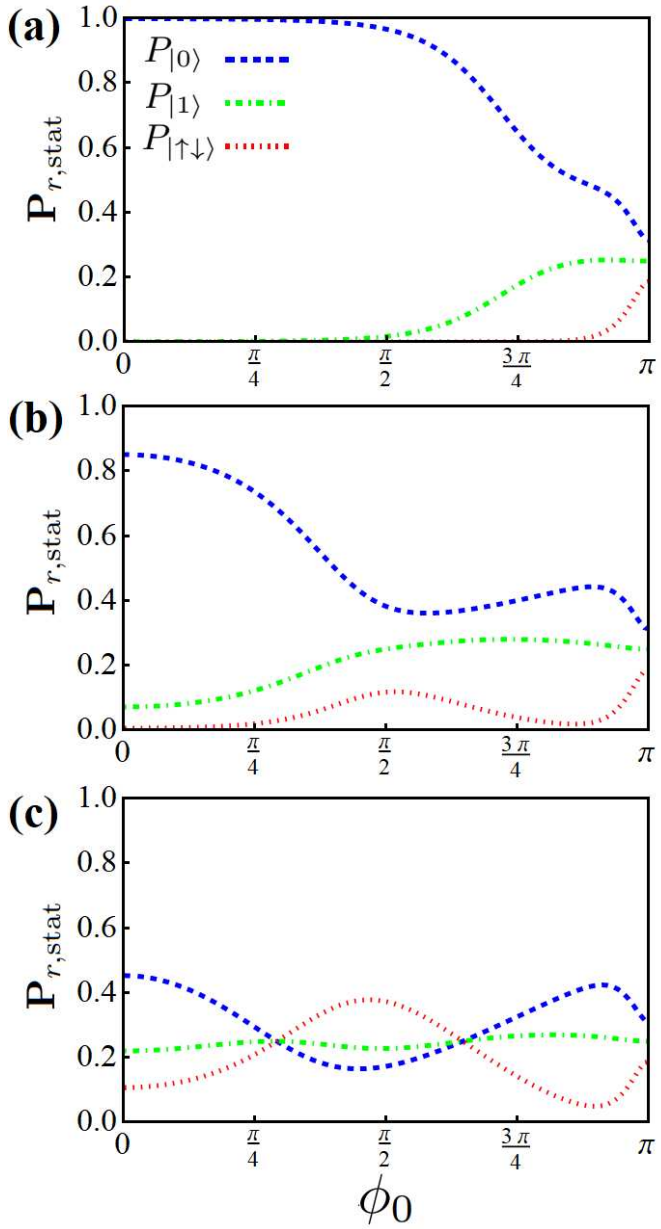

Figure 3.4: Steady-state populations $\mathbf{P}_{r,\mathrm{stat}}$ vs ϕ_0 for the many-body Andreev states in a short Josephson junction as in Fig. 3.3 but for the case of an Ohmic environment, see Eq. (3.98). Again, $P_{|0\rangle}$ is indicated by dashed blue curves, $P_{|1\rangle}$ by dot-dashed green curves, and $P_{|\uparrow\downarrow\rangle}$ by dotted red curves. Putting $\Delta = 1$, we use $T_b = 0.1$, $\epsilon = 0.25$, $\Gamma = 10$, $\omega_c = 1$, and $\alpha_d = 0.1$, such that $\mathcal{T} = 0.99$, see Eq. (3.82). The panels are for (a) $T_{\mathrm{qp}} = 0.14$, (b) $T_{\mathrm{qp}} = 0.3$, and (c) $T_{\mathrm{qp}} = 0.5$.

1. At time $t < 0$, both copies are prepared in the pre-quench stationary states $\mathbf{P}_{\text{stat}}^{(c)}$ and $\mathbf{P}_{\text{stat}}^{(f)}$ corresponding to the phase differences $\phi_0^{(c)}$ and $\phi_0^{(f)}$, respectively, with all other model parameters kept identical;

2. At time $t = 0$, for each of these two system copies, the phase is suddenly quenched to the same post-quench value $\phi_0^{(\text{eq})}$, where we demand

$$|\phi_0^{(\text{eq})} - \phi_0^{(c)}| < |\phi_0^{(\text{eq})} - \phi_0^{(f)}|.$$

   The superscripts (f) vs (c) thus refer to pre-quench values which are "far" vs "close" to the post-quench value, respectively. Since the ABS dispersion (3.81) is symmetric around $\phi_0 = \pi$, i.e., $E_1(2\pi - \phi_0) = E_1(\phi_0)$, we take all phases from the interval $[0, \pi)$. Moreover, since $E_1(\phi_0)$ is a monotonic function in this interval, pre- and post-quench ABS energies obey the same ordering;

3. The corresponding relaxation times $\tau^{(f,c)}$ for reaching the stationary state $\mathbf{P}_{\text{stat}}^{(\text{eq})}$ at $t \to \infty$ are then determined by solving the Pauli master equation (3.92) for $E_1 = E_1(\phi_0^{(\text{eq})})$ under the initial conditions

$$\mathbf{P}(t = 0) = \mathbf{P}_{\text{stat}}^{(f,c)}.$$

4. The QME occurs if $\tau^{(f)} < \tau^{(c)}$.

For the cases shown in Fig. 3.3(a) and Fig. 3.4(a), the QME is ruled out by the monotonicity of the populations. Indeed, with increasing quench amplitude, $\delta\phi_0^{(i\in\{c,f\})} = |\phi_0^{(\text{eq})} - \phi_0^{(i)}|$, the distance between the initial $(t = 0)$ and final $(t \to \infty)$ populations also increases. As a consequence, we always find $\tau^{(f)} > \tau^{(c)}$, and thus no QME can occur. On the other hand, for the cases shown in Fig. 3.3(c) and Fig. 3.4(c), increases in $\delta\phi_0^{(i)}$ may cause a reduction of the effective distance between initial and final populations, resulting in a shorter relaxation time τ. Indeed, for certain values of $\delta\phi_0^{(i)}$, we find $\mathbf{P}_{r,\text{stat}}(\phi_0) \approx \mathbf{P}_{r,\text{stat}}(\phi_0 + \delta\phi_0^{(i)})$. Finally, Fig. 3.3(b) and Fig. 3.4(b) represent a special intermediate situation discussed below.

Quantutative characterization of QME

In order to monitor the time evolution of the system and quantitatively detect the QME and its type, a proper distance function in Hilbert space must be introduced. As discussed in Ref. [24], the trace distance between the time-dependent density matrix $\rho_A(t)$ for $t > 0$ and the final steady-state density matrix $\rho_{A,\text{stat}}^{(\text{eq})}$ is an admissible choice. Since in our case $\rho_A(t)$ is effectively diagonal, the trace distance reduces to a norm-1 (*aka* Manhattan) distance [57] between the respective population vectors,

$$\mathcal{D}_M\left(\mathbf{P}(t)\right) = \frac{1}{2}\sum_n \left| P_{|n\rangle}(t) - P_{|n\rangle,\text{stat}}^{(\text{eq})} \right|. \tag{3.99}$$

This distance function can be obtained experimentally by measuring ABS populations, which in turn can be achieved, e.g., by microwave spectroscopy, see Refs. [58–60] and references therein. We note that $\mathcal{D}_M\left(\mathbf{P}(t)\right) \neq \mathcal{D}_M\left(\mathbf{P}_r(t)\right)$, since the second component of $\mathbf{P}_r$ needs to be counted twice in Eq. (3.99), see Eq. (3.91). We can then define the relaxation time τ by the condition $\mathcal{D}_M\left(\mathbf{P}(t)\right) < \epsilon_c$, where $\epsilon_c \ll 1$ is a small but finite accuracy cutoff value. The cutoff value is reached for $t = \tau$. This procedure is necessary since for the relaxation dynamics described by Eq. (3.77), there is no phase transition and the true stationary solution is reached only in the asymptotic limit $t \to \infty$ [3, 24]. In the following, we set $\epsilon_c = 10^{-4}$. However, we

have checked that the presence or absence of the QME is robust under variations of the value of ϵ_c.

We next note that Eq. (3.92) admits the solution

$$\mathbf{P}_r(t) = \mathbf{P}_{r,\text{stat}}^{(\text{eq})} + \sum_{k=1,2} c_k \mathbf{P}_k e^{\lambda_k t}, \tag{3.100}$$

where λ_k and $\mathbf{P}_k$ denote the two real-valued negative eigenvalues (we assume $\lambda_2 < \lambda_1 < 0$) and the corresponding right eigenvectors of the matrix $\mathbf{M}_r$ in Eq. (3.94), respectively. The coefficients c_k are determined by the initial condition at $t = 0$, and $\mathbf{P}_{r,\text{stat}}^{(\text{eq})}$ is given by Eq. (3.95) with $\phi_0 = \phi_0^{(\text{eq})}$. In the asymptotic long-time limit, Eq. (3.99) reduces to

$$\mathcal{D}_M\left(\mathbf{P}(t)\right) = \frac{1}{2}\mathcal{A}_1 e^{\lambda_1 t}, \quad \mathcal{A}_1 = |c_1| \sum_n \left|P_{1,|n\rangle}\right|. \tag{3.101}$$

Here, the $P_{1,|n\rangle}$ are the components of the vector $\mathbf{P}_k$ in Eq. (3.100) with $|\uparrow\rangle = |\downarrow\rangle \equiv |1\rangle$, where we consider only initial conditions with $P_{|\uparrow\rangle}(0) = P_{|\downarrow\rangle}(0)$. The system therefore relaxes to the final stationary state according to an exponential law with the rate $|\lambda_1|$. In our quench protocol, this rate only depends on $\phi_0^{(\text{eq})}$. The onset of the QME is thus fully determined by the value of $\mathcal{A}_1$, which in turn depends on the initial condition $\mathbf{P}_r(0)$. Indeed, for given accuracy cutoff ϵ_c, the relaxation times $\tau^{(c,f)}$ follow in the form

$$\tau^{(c,f)} \simeq |\lambda_1|^{-1} \ln\left(\frac{\mathcal{A}_1^{(c,f)}}{2\epsilon_c}\right). \tag{3.102}$$

For $\mathcal{A}_1 = 0$, see Eq. (3.101), the relaxation dynamics becomes exponentially accelerated with the larger rate $|\lambda_2|$ [61]. The corresponding relaxation time is computed as in Eq. (3.102) but with $\mathcal{A}_1 \to \mathcal{A}_2$ and $\lambda_1 \to \lambda_2$.

The QME is realized if $\mathcal{A}_1^{(f)} < \mathcal{A}_1^{(c)}$ such that the condition

$$\mathcal{D}_M\left(\mathbf{P}^{(f)}(t)\right) < \mathcal{D}_M\left(\mathbf{P}^{(c)}(t)\right) \tag{3.103}$$

is satisfied at long times. One can then distinguish type-I and type-II QMEs [24]:

1. For the type-I QME, Eq. (3.103) must hold for all $t > 0$. The condition for the trace distance:
$$\mathcal{D}_M\left(\mathbf{P}^{(f)}(0)\right) < \mathcal{D}_M\left(\mathbf{P}^{(c)}(0)\right). \tag{3.104}$$
2. for the type-II QME, Eq. (3.103) holds only for $t > t^*$, where t^* denotes a critical time where $\mathcal{D}_M\left(\mathbf{P}^{(f)}(t)\right)$ and $\mathcal{D}_M\left(\mathbf{P}^{(c)}(t)\right)$ intersect. The condition for the trace distance:
$$\mathcal{D}_M\left(\mathbf{P}^{(f)}(0)\right) > \mathcal{D}_M\left(\mathbf{P}^{(c)}(0)\right), \tag{3.105}$$
together with the existence of a critical time t^*

The monotonic ϕ_0-dependence of the stationary populations for the parameters in Fig. 3.3(a) or Fig. 3.4(a) implies that Eq. (3.103) cannot be satisfied for any choice of $(\phi_0^{(c)}, \phi_0^{(f)}, \phi_0^{(\text{eq})})$. Hence the QME is ruled out in these cases. However, if all components of $\mathbf{P}_r(t)$ have extrema at nearly the same values of ϕ_0, as observed in Fig. 3.3(c) and Fig. 3.4(c), it is possible to choose $\phi_0^{(c)}$ and $\phi_0^{(f)}$ such that for all n,

$$\left|P_{|n\rangle}^{(f)}(t) - P_{|n\rangle,\text{stat}}^{(\text{eq})}\right| < \left|P_{|n\rangle}^{(c)}(t) - P_{|n\rangle,\text{stat}}^{(\text{eq})}\right|. \tag{3.106}$$

As a consequence, Eqs. (3.103) and (3.104) are both satisfied, and a type-I QME takes place. The onset of the more elusive type-II QME requires an intermediate scenario such as the one shown in Fig. 3.3(b) or Fig. 3.4(b). In this case, for some interval of ϕ_0, a subset of the populations have a monotonic dependence while others exhibit an extremal point. Due to this feature, Eq. (3.105) can hold. In particular, if the monotonic populations reach equilibrium faster than the non-monotonic ones, Eq. (3.103) can be restored at some time $t = t^*$. To conclude, both types of QMEs allowed in open quantum systems [24] could be realized in a highly transparent phase-quenched short Josephson junction.

Arbitrary Γ/Δ

If the condition $\Gamma \gg \Delta$ is not satisfied, instead of Eq. (3.81), one needs to employ the numerically exact ABS dispersion obtained by solving Eq. (3.36). Similarly, one then has to numerically evaluate the transition rates in Eq. (3.80) from the corresponding general expressions in Sec. 3.2.3. We have determined the relaxation times $\tau^{(i=c,f)}$ by computing the respective time-dependent distance functions $\mathcal{D}_M(\mathbf{P}(t))$ in Eq. (3.99) from the Pauli equation, using again the quench protocol for ϕ_0 described above. Below, we also address what happens upon lowering the junction transparency $\mathcal{T}$.

Condition for existence of QME.— In Fig. 3.5, we show color-scale plots for relaxation time τ and initial trace distance $\mathcal{D}_M(\mathbf{P}(0))$ in the plane spanned by pre-quench ($\phi_0^{(i=c,f)}$) and post-quench ($\phi_0^{(\mathrm{eq})}$) phases, using three different values for $\mathcal{T}$. In each panel, along the diagonal line $\phi_0^{(i)} = \phi_0^{(\mathrm{eq})}$, no quench takes place, and therefore $\tau = \mathcal{D}_M(\mathbf{P}(0)) = 0$. In the absence of a QME, the relaxation time τ is then expected to monotonically increase when moving away from this diagonal line at fixed $\phi_0^{(\mathrm{eq})}$. However, from panels (a), (c), and (e) of Fig. 3.5, we find that τ suddenly decreases again near special phase values $\phi_0^{(i)} = \phi_0^{(i,*)} \neq \phi_0^{(\mathrm{eq})}$. At those values,

$$\mathbf{P}_{r,\mathrm{stat}}(\phi_0^{(i,*)}) \approx \mathbf{P}_{r,\mathrm{stat}}(\phi_0^{(\mathrm{eq})}),$$

for the stationary occupation probabilities, see Eq. (3.91). The resulting functions $\phi_0^{(i,*)}(\phi_0^{(\mathrm{eq})})$ define *open* curves in the $\phi_0^{(i)}$ - $\phi_0^{(\mathrm{eq})}$ plane which cross the main diagonal. Further, we refer to such curves as **Mpemba arcs**.

In fact, the existence of at least one Mpemba arc is a necessary and sufficient condition for the QME to occur in this system. Indeed, for any value of $\phi_0^{(\mathrm{eq})}$ such that $\phi_0^{(i,*)}$ exists, a non-monotonic function $\tau(\phi_0^{(i)})$ is defined by the relaxation time which has a maximum at some value $\phi_0^{(M)} \in \left(\phi_0^{(\mathrm{eq})}, \phi_0^{(i,*)}\right)$. It is then always possible to prepare two system copies in initial stationary states corresponding to pre-quench values $\phi_0^{(c)}$ and $\phi_0^{(f)}$ such that Eq. (3.103) is satisfied. For example, one can choose

$$\phi_0^{(\mathrm{eq})} \lesseqgtr \phi_0^{(M)} \lesseqgtr \phi_0^{(c)} \lesseqgtr \phi_0^{(f)} \lesseqgtr \phi_0^{(i,*)}.$$

Determining the type of QME.— While analyzing the relaxation time τ in the $\phi_0^{(i)}$ - $\phi_0^{(\mathrm{eq})}$ plane is sufficient for establishing the QME, it is necessary to study $\mathcal{D}_M(\mathbf{P}(0))$ in order to distinguish type-I and type-II QMEs. A useful property for identifying the two types of QME follows from Eqs. (3.99) and (3.100). Indeed, $\mathcal{D}_M(\mathbf{P}(0))$ is symmetric with respect to an exchange of the pre- and post-quench stationary states, and hence panels (b), (d), and (f) of Fig. 3.5 exhibit a mirror symmetry with respect to the main diagonal. However, since the decay rates $|\lambda_k|$ only depend on $\phi_0^{(\mathrm{eq})}$, the relaxation times τ extracted from Eq. (3.100), see panels (a), (c), and (e) of Fig. 3.5, evidently do not display this mirror symmetry. As a consequence, a mismatch between the

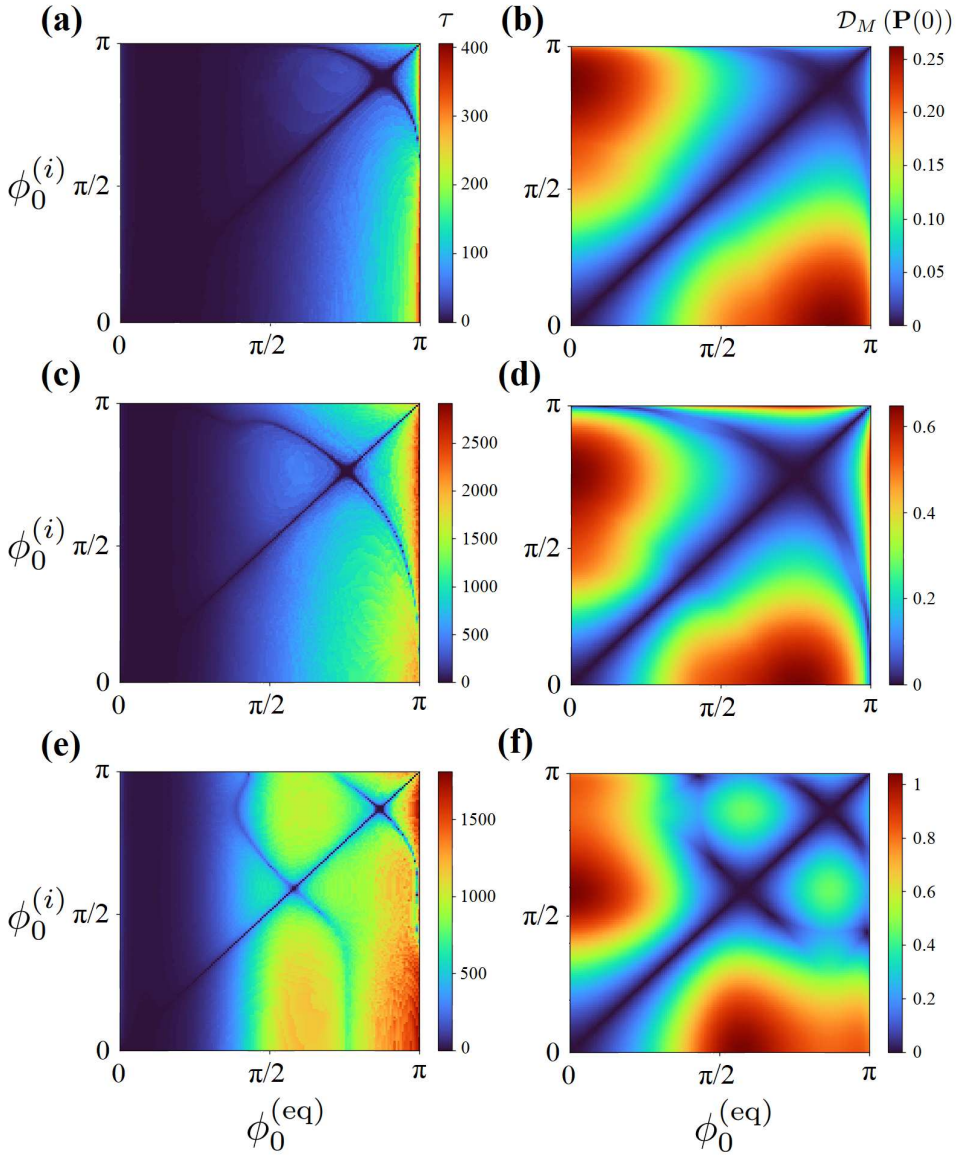

Figure 3.5: QME in Josephson dots of short length, $L = 0.6\xi_0$. Results follow by numerical calculations for the model in Sec. 3.2 by computing $\mathcal{D}_M\,(\mathbf{P}(t))$ in Eq. (3.99) from the Pauli equation. Color-scale plots show the relaxation time τ or $\mathcal{D}_M\,(\mathbf{P}(t=0))$ in the plane spanned by pre-quench $(\phi_0^{(i=c,f)})$ and post-quench $(\phi_0^{(\mathrm{eq})})$ phase differences. Panels (a), (c), and (e) show τ in units of Δ^{-1}. Panels (b), (d), and (f) show $\mathcal{D}_M\,(\mathbf{P}(0))$. With $\Delta = 1$, we use $T_b = 0.2$, $T_{\mathrm{qp}} = 0.5$, $\Omega = 0.01$, $\eta = 0.1$, $\kappa = 0.1$ and $\Gamma = 6.5$. The junction transparency is $\mathcal{T} = 0.3$ (with $\epsilon = 9.8$) for panels (a) and (b); $\mathcal{T} = 0.85$ (with $\epsilon = 2.74$) in panels (c) and (d); and $\mathcal{T} = 0.99$ (with $\epsilon = 0.46$) in panels (e) and (f).

τ-isolines and the $\mathcal{D}_M(\mathbf{P}(0))$-isolines in the $\phi_0^{(i)}$ - $\phi_0^{(\mathrm{eq})}$ plane can occur. Taken as a function of $\phi_0^{(i)}$ at fixed $\phi_0^{(\mathrm{eq})}$, the minima of τ may therefore be located at different positions than the minima of $\mathcal{D}_M(\mathbf{P}(0))$. In such cases, Eq. (3.105) can be fulfilled, resulting in a type-II QME [24].

Transparency variation.— By varying the bare dot level energy ϵ, e.g., by means of a gate voltage applied on the dot, one may change the junction transparency $\mathcal{T}$, see Eq. (3.82). From panels (a), (c), and (e) of Fig. 3.5, we observe that Mpemba arcs tend to move towards higher values of ϕ_0 with decreasing $\mathcal{T}$, eventually fading away for small transparency. As in the case of large Γ/Δ, see Eq. (3.81), we find that for highly transparent contacts ($\mathcal{T} \approx 1$), the ABS dispersion essentially spans the full subgap energy range. For very small $\mathcal{T}$, on the other hand, the ABS energy dispersion approaches the continuum threshold from below, i.e., $E_1(\phi_0) \approx \Delta$ for all ϕ_0. As shown in Figs. 3.3 and 3.4, extrema in the stationary populations as a function of ϕ_0 are typically obtained for intermediate values of $E_1(\phi_0)$ within the gap. As discussed above, at such extremal points, the competition between all transition rates in Eq. (3.80) becomes crucial. For small transparency, we find that Mpemba arcs tend to disappear or fade away, see Fig. 3.5(a), since now the rate Γ_a^- dominates over all other transition rates for the realizable values of $E_1(\phi_0)$. With increasing $\mathcal{T}$, see Fig. 3.5(c,e), the ABS energy $E_1(\phi_0)$ can reach lower values, and ratios between transition rates can change from < 1 to > 1 as function of ϕ_0. As a consequence, one or several well-defined sharp Mpemba arcs can emerge. Since the mirror reflection asymmetry of the relaxation time is then also more pronounced, a type-II QME is commonly encountered. This conclusion is qualitatively consistent with our results for high transparency in Fig. 3.3 and 3.4.

Examples of time evolution of the distance function.— In Fig. 3.6, we show $\mathcal{D}_M(\mathbf{P}(t))$ for selected values of $\phi_0^{(i)}$ and $\phi_0^{(\mathrm{eq})}$, using the same parameters as in Fig. 3.5(e) for a highly transparent junction with $\mathcal{T} = 0.99$.

a) In Fig. 3.6(a), the blue (red) curve corresponds to the closest (farthest) initial configuration $\phi_0^{(i)}$ with respect to the final state defined by $\phi_0^{(\mathrm{eq})} = 0.7\pi$. The orange curve ($\phi_0^{(i)} = 0.5\pi$) represents an intermediate situation. We first observe that for $\phi_0^{(c)} = 0.6\pi$ with $\phi_0^{(f)} = 0.45\pi$ or $\phi_0^{(f)} = 0.5\pi$, a type-I QME emerges. Second, a type-II QME takes place when choosing $\phi_0^{(c)} = 0.5\pi$ and $\phi_0^{(f)} = 0.45\pi$, since the time evolution of the distance function now exhibits a crossing point at $t^* \approx 180\Delta^{-1}$. It is worth noting that all curves have the same slope at long times since the system relaxes to the stationary state with the same rate $|\lambda_1|$.

b) in Fig. 3.6(b), we investigate the case $\phi_0^{(\mathrm{eq})} = 0.8\pi$. As in Fig. 3.6(a), the color assignment is such that the blue (red) curve corresponds to the closest (farthest) initial condition and the orange curve represents an intermediate case. A type-I QME can be observed by choosing $\phi_0^{(c)} = 0.86\pi$ (blue curve) and $\phi_0^{(f)} = 0.9\pi$ (orange), while no QME take places for $\phi_0^{(c)} = 0.9\pi$ and $\phi_0^{(f)} = 0.95\pi$ (red). We identify the quench dynamics defined by the blue and red curves in Fig. 3.6(b) as an "avoided" QME rather than a type-II QME. Indeed, even though a crossing point exists at time $t^* \approx 15\Delta^{-1}$, the blue curve (corresponding to the "close" initial condition) describes a faster relaxation at long times despite the fact that $\mathcal{D}_M\left(\mathbf{P}^{(f)}(0)\right) < \mathcal{D}_M\left(\mathbf{P}^{(c)}(0)\right)$. However, since Eq. (3.103) does not hold, no QME emerges according to our definitions.

It is worth noting that avoided QMEs have previously been classified as QMEs in the literature due the existence of a crossing point in the monitoring function, see, e.g., Refs. [12, 14, 17].

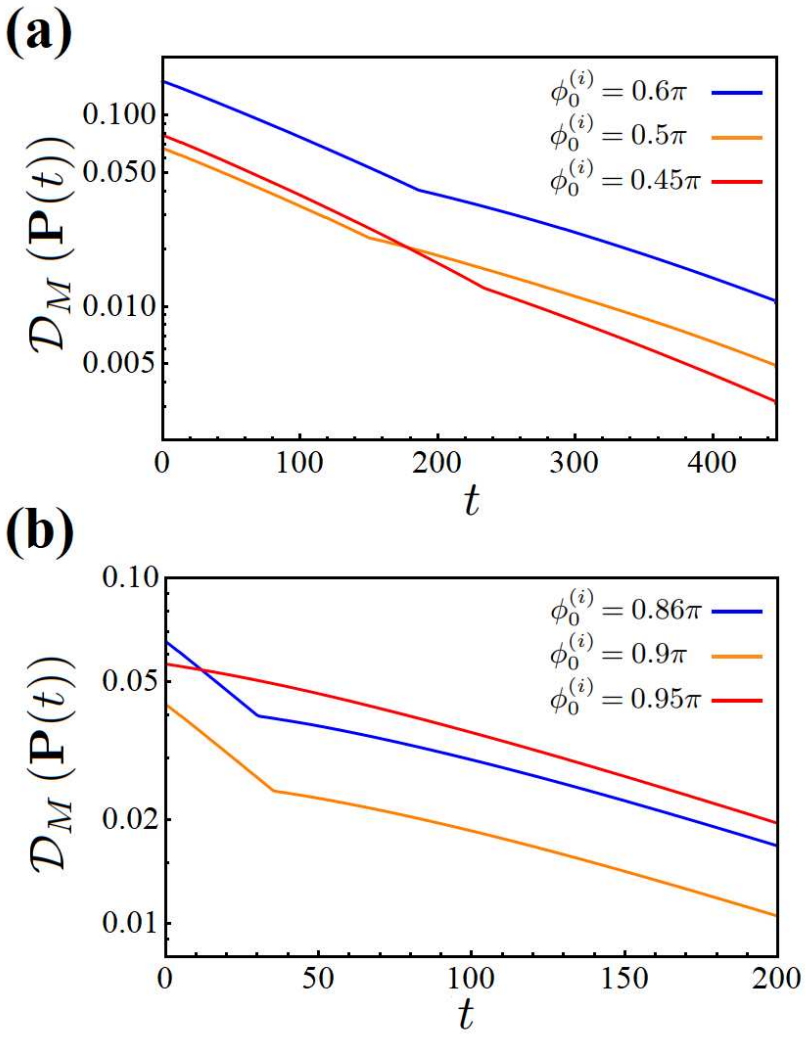

Figure 3.6: Time dependence of the distance function $\mathcal{D}_M(\mathbf{P}(t))$, see Eq. (3.99), for a short Josephson dot with the parameters in Fig. 3.5(e). Time is given in units of Δ^{-1}. Note the semi-logarithmic scales. In panel (a), we consider $\phi_0^{(\mathrm{eq})} = 0.7\pi$ and $\phi_0^{(i)} = 0.6\pi$ (blue curve), $\phi_0^{(i)} = 0.5\pi$ (orange), and $\phi_0^{(i)} = 0.45\pi$ (red). In panel (b), $\phi_0^{(\mathrm{eq})} = 0.8\pi$ with $\phi_0^{(i)} = 0.86\pi$ (blue), $\phi_0^{(i)} = 0.9\pi$ (orange), and $\phi_0^{(i)} = 0.95\pi$ (red).

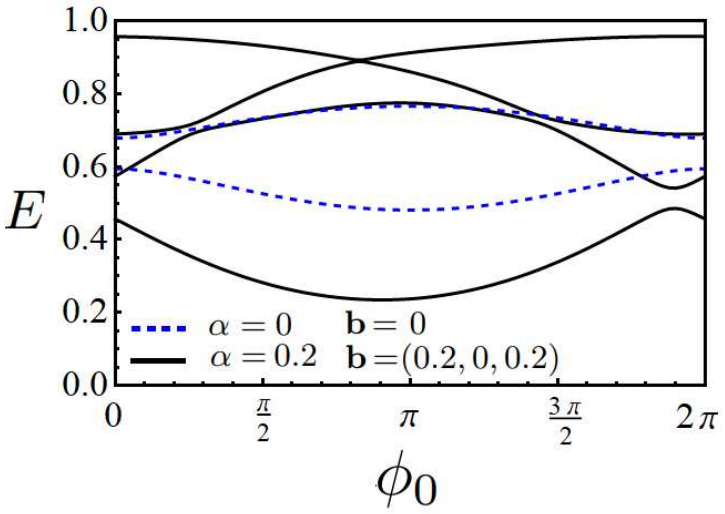

Figure 3.7: The four positive ABS energies vs ϕ_0 for a Josephson dot of intermediate length, $L = 1.7\xi_0$, in a Zeeman field $\mathbf{b} = (0.2, 0, 0.2)$ with SOI coupling $\alpha = 0.2$ (black solid curves), where we set $\Delta = 1$. The presence of both SOI and Zeeman field breaks both the spin symmetry (i.e., each blue curve represents a spin degenerate ABS energy) and the $\phi_0 \to 2\pi - \phi_0$ symmetry so that $E_\lambda(2\pi - \phi_0) \neq E_\lambda(\phi_0)$ [47]. The case $\alpha = 0$ and $\mathbf{b} = 0$ is shown by the blue dashed curves for comparison.

3.3.2 Intermediate-length junction with SOI and Zeeman field

In this section, we investigate the QME for an intermediate-length junction. Increasing the length of the nanowire, the low-energy transport properties are described by more single-particle eigenstates of $H_{\rm dot}$. For instance, for a weak link of intermediate length $L \approx \xi_0 = v_{\rm F}/\Delta$, typically four single-particle ABSs are found [46, 47]. If both SOI and Zeeman are present, orbital and spin angular momenta are no longer conserved, and the (positive) ABS energies split into four distinct levels. Ordering these energies $E_\lambda(\phi_0)$ by increasing energy, $0 < E_1 \leq E_2 \leq E_3 \leq E_4 < \Delta$, see Fig. 3.7 for our numerical results for their energy dispersions, we have 16 many-body Andreev states. We label these many-body states as $|n_1, n_2, n_3, n_4\rangle$ with $n_\lambda \in \{0, 1\}$, where $n_\lambda = 0$ ($n_\lambda = 1$) means that the corresponding ABS level is unoccupied (occupied). The dynamics for the occupation probabilities is still described by the Pauli master equation in Eq. (3.78), where now $\mathbf{M}$ is a 16×16 matrix, see previous chapter for more details.

Even though the system dynamics is now considerably richer, the qualitative effect of the impact of more ABS levels and/or the inclusion of SOI and Zeeman field effects on the QME can be assessed again by starting from a simplified argument as in Sec. 3.3.1. Indeed, for each ABS energy, the same approximation as employed in Sec. 3.3.1 can be applied separately. If E_λ approaches Δ, the transition of an ABS quasiparticle to the continuum or vice versa, see Fig. 3.2(a,d), is the dominant process. On the other hand, Cooper pair processes without contributions of a continuum quasiparticle, see Fig. 3.2(c,f), dominate for $E_\lambda \ll \Delta$. If a continuum quasiparticle is involved in a pair process, see Fig. 3.2(b,c), the corresponding rate is always subleading. However, for longer junctions, additional processes (absent in short junctions) appear since transitions of quasiparticles between different ABS levels become now possible, with the corresponding transition rates in Eq. (3.57). These processes preserve the occupation number of the ABS sector and dominate if both ABS energies are close, $E_\lambda \approx E_{\lambda'}$, regardless of their position within the superconducting gap. Such processes are especially important if both ABS energies are near $\approx \Delta/2$ since the other processes listed above then become ineffective.

After the quantum quench, the occupation probabilities of the many-body Andreev states

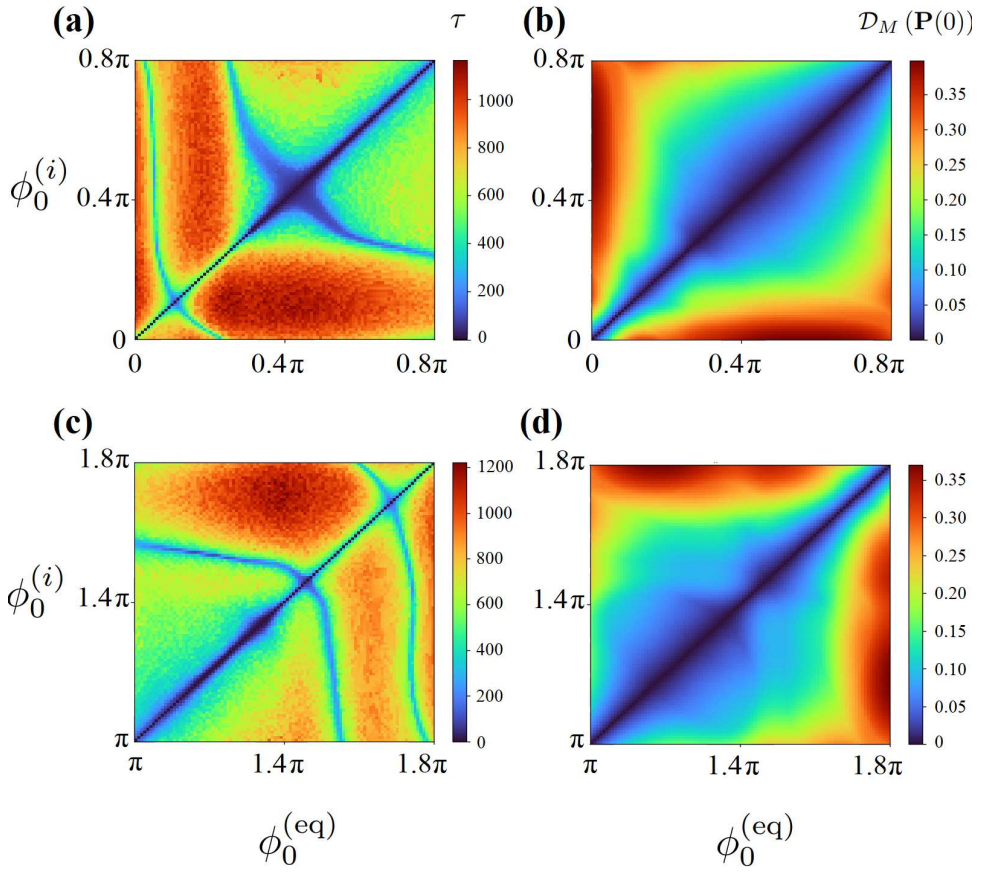

Figure 3.8: QME in a Josephson dot of intermediate length, $L = 1.7\xi_0$, for a Zeeman field $\mathbf{b} = (0.2, 0, 0.2)$ and SOI coupling $\alpha = 0.2$, where we set $\Delta = 1$. Results are obtained from the Pauli equation for the model in Sec. 3.2 by monitoring the distance function $\mathcal{D}_M(\mathbf{P}(t))$ in Eq. (3.99) after the quench. Color-scale plots show the relaxation time τ, see panels (a) and (c), and the distance function at time $t = 0$, see panels (b) and (d), in a plane spanned by the pre-quench phase, $\phi_0^{(i)}$, and the post-quench value $\phi_0^{(\mathrm{eq})}$. The hopping parameters in Eq. (3.7) are $t_1 = t_2 = 0.7$, with $m_x = 9/v_{\mathrm{F}}^2$ in Eq. (3.2), where the four dot energy levels in Eq. (3.9), $\epsilon_\nu \in \{-0.1, 0.41, 0.62, 0.97\}$, correspond to a high-transparency junction. The other parameters are $T_b = 0.2$, $T_{\mathrm{qp}} = 0.5$, $\Omega = 0.01$, $\eta = 0.1$, and $\kappa = 0.1$.

relax to their final steady-state values, which have a characteristic ϕ_0-dependence as shown in Fig. 3.3 for a short junction. With increasing junction length, features like common extremal points of different occupation probabilities as function of ϕ_0, see Fig. 3.3(c), become less and less likely as the number of ABSs increases. Qualitatively, we thus expect that by increasing L, and allowing for finite SOI and Zeeman field, the QME is either washed out or, if it survives, the type-II QME becomes more common than the type-I QME. We next check this prediction using numerical calculations.

In Fig. 3.8, we show color-scale plots of τ and $\mathcal{D}_M(\mathbf{P}(0))$ in a plane spanned by the pre-quench ($\phi_0^{(i)}$) and post-quench ($\phi_0^{(\mathrm{eq})}$) phase differences for an intermediate-length junction with $L = 1.7\xi_0$ in the presence of SOI and a Zeeman field. The remaining parameters are chosen as in Fig. 3.5, i.e., they correspond to a QME regime in the short-junction case. Due the presence of the magnetic field and the SOI, the mirror symmetry of the ABS spectrum is broken, $E_\lambda(2\pi - \phi_0) \neq E_\lambda(\phi_0)$. For this reason, in order to avoid ambiguities in the quench protocol, we restrict the phase differences ϕ_0 studied below to a range in which all ABS energies $E_\lambda(\phi_0)$ are monotonic functions, see Fig. 3.7. In Fig. 3.8(a,b), we show the relaxation time τ and $\mathcal{D}_M(\mathbf{P}(0))$ by assuming that both $\phi_0^{(i)}$ and $\phi_0^{(\mathrm{eq})}$ vary in the interval $[0, 0.8\pi]$. In Fig. 3.8(c,d), these phases instead belong to the interval $[\pi, 1.8\pi]$.

Figure 3.8(a,c) reveals the presence of Mpemba arcs once again. This is a signature that QMEs are still realizable in the longer junction considered here. However, since the mirror symmetry under $\phi_0 \to 2\pi - \phi_0$ is broken by the interplay of SOI and Zeeman field, the Mpemba arcs are not symmetric under point reflections with respect to (π, π). Furthermore, in contrast to the short-junction case in Fig. 3.5, we note that Mpemba arcs are not visible in $\mathcal{D}_M(\mathbf{P}(0))$ anymore, see Fig. 3.8(b,d). As a consequence, if Eq. (3.103) is satisfied, also Eq. (3.105) must be true. We conclude that the more elusive type-II QME is therefore the dominant type of QME realized for a longer Josephson dot in the presence of SOI and Zeeman field.

3.4 Conclusions

In this work, we have introduced a general GF-based framework for studying the dynamics of quasiparticles in multi-level quantum dot systems coupled to multiple reservoirs. The formalism has been described in detail for the case of two superconducting leads, where we allow for SOI and Zeeman fields in the dot region defining the Josephson junction. The general formalism has then been applied to a study of Mpemba effects in this open quantum system context. Following the protocol proposed in Ref. [24] and described in Sec. 3.3.1, we have shown that already the simplest case of a short junction harbors both allowed types of QME which can be observed in phase quench experiments. To that end, one has to monitor the distance function for the occupation probabilities in Eq. (3.99), which in turn are experimentally accessible by microwave spectroscopy [58–60]. The studies setup thus offers a simple platform where quantum generalizations of the Mpemba effect can be systematically studied.

Appendix: Free dot energies and eigenstates

We here provide details concerning the calculation of the wave functions $\chi_\nu(x)$ of an isolated quantum dot in the presence of SOI and Zeeman field, Eq. (3.8), which determine the hybridization matrices (3.27). Without loss of generality, we choose a coordinate system where the wire ends $x_{1,2}$ are located at $x_1 = -x_2 = -L/2$, and we assume $V(x) = 0$ inside the wire region $x \in (x_1, x_2)$. First, we solve the eigenvalue problem Eq. (3.8) in the absence of Zeeman splitting, i.e., for $\mathbf{b} = 0$. In this case, the spin-up and spin-down eigenstates of the

Hamiltonian (3.3) are decoupled, and the spin bands minima are shifted by $q = m_x\alpha$ in opposite directions along the momentum ($\hat{p}$) axis. Applying the Neumann boundary conditions, $\partial_x\chi(-L/2) = \partial_x\chi(L/2) = 0$, the complete set of orthonormal eigenfunctions $\chi_{n\sigma}(x)$ for spin projection σ is given by

$$\chi_{n\sigma}(x) = \frac{e^{-i\sigma qx}}{\sqrt{L}}\left[\cos(\theta_{n\sigma})e^{ik_n(x-L/2)} + \sin(\theta_{n\sigma})e^{-ik_n(x-L/2)}\right], \tag{A1}$$

with the corresponding eigenenergies $\varepsilon_n = k_n^2/(2m_x) - m_x\alpha^2/2 - \mu$, where

$$k_n = \pi n/L, \quad \cos\theta_{n\sigma} = \sin\theta_{n,-\sigma} = \frac{k_n + \sigma q}{\sqrt{2\left(k_n^2 + q^2\right)}}, \tag{A2}$$

and $n \in \{1, 2, ...\}$. Some comments are in order at this point. (i) In the absence of the Zeeman field, we have an infinite set of spin-degenerate dot levels ε_n. (ii) Each state $\chi_{n\sigma}(x)$ is a linear combination of left and right movers. (iii) While spatial inversion symmetry is broken for $\alpha \neq 0$, time-reversal symmetry is present as reflected by the relation $\chi^*_{n\sigma}(x) = \chi_{n,-\sigma}(x)$. (iv) Finally, boundary values of wave functions are connected by the relation $\chi_{n\sigma}(-L/2) = (-1)^n e^{i\sigma qL}\chi_{n\sigma}(L/2)$. We note that the phase shift due to $e^{i\sigma qL}$ in this relation does not affect electronic transport since it can be removed from the total Hamiltonian by a gauge transformation on the lead fermions.

Next, we add the Zeeman field $\mathbf{b} = (b_x, 0, b_z)$ to our consideration and choose the wave functions (A1) as a basis set for constructing the dot-level representation of the full eigenvalue problem. Any solution of Eq. (3.8) that satisfies the Neumann boundary conditions can then be written as

$$\chi_\nu(x) = \sum_{n=1}^{\infty}\begin{pmatrix} u^{(\nu)}_{n\uparrow}\chi_{n\uparrow}(x) \\ u^{(\nu)}_{n\downarrow}\chi_{n\downarrow}(x)\end{pmatrix}, \tag{A3}$$

with complex-valued amplitudes $u^{(\nu)}_{n\sigma}$ corresponding to the energy eigenvalue ϵ_ν. Introducing the multispinor

$$\Psi_\nu = \left(u^{(\nu)}_{1\uparrow}, u^{(\nu)}_{1\downarrow}, u^{(\nu)}_{2\uparrow}, u^{(\nu)}_{2\downarrow}, ...\right)^T, \tag{A4}$$

we can write Eq. (3.8) as

$$\mathcal{H}\Psi_\nu = \epsilon_\nu\Psi_\nu, \tag{A5}$$

with an infinite-size matrix

$$\mathcal{H} = \begin{pmatrix} \varepsilon_1 + b_z & J^-_{11} & 0 & J^-_{12} & ... \\ J^+_{11} & \varepsilon_1 - b_z & J^+_{12} & 0 & \\ 0 & J^-_{21} & \varepsilon_2 + b_z & J^-_{22} & \\ J^+_{21} & 0 & J^+_{22} & \varepsilon_2 - b_z & \\ ... & & & & ... \end{pmatrix}, \tag{A6}$$

where

$$J^\sigma_{mn} = \left(J^{-\sigma}_{nm}\right)^* = b_x\int_{-L/2}^{L/2} dx\,\chi^*_{m,-\sigma}(x)\chi_{n\sigma}(x). \tag{A7}$$

Explicitly, the overlap integrals (A7) are given by

$$J^\sigma_{mn} = -\frac{2b_x}{L}f^\sigma_{mn} \times \begin{cases} \sigma\sin(qL) & \text{for } (-1)^{n+m} = 1 \\ i\cos(qL) & \text{for } (-1)^{n+m} = -1 \end{cases}, \tag{A8}$$

where

$$\begin{aligned} f^{\sigma}_{mn} &= \frac{\cos\theta_{n\sigma}\cos\theta_{m,-\sigma}}{k_n - k_m - 2\sigma q} - \frac{\sin\theta_{n\sigma}\sin\theta_{m,-\sigma}}{k_n - k_m + 2\sigma q} \\ &+ \frac{\cos\theta_{n\sigma}\sin\theta_{m,-\sigma}}{k_n + k_m - 2\sigma q} - \frac{\sin\theta_{n\sigma}\cos\theta_{m,-\sigma}}{k_n + k_m + 2\sigma q}, \end{aligned} \tag{A9}$$

with the symmetry properties

$$f^{\sigma}_{mn} = f^{\sigma}_{nm} = (f^{\sigma}_{nm})^{*}, \quad f^{-\sigma}_{mn} = -f^{\sigma}_{mn}. \tag{A10}$$

In practice, the Hamiltonian matrix (A6) is truncated to the subspace of low-energy eigenstates below some energy cutoff comparable to Δ, and then diagonalized numerically.

References

[1] E B Mpemba and D G Osborne. "Cool?" In: *Physics Education* 4.3 (May 1969), p. 172. DOI: 10.1088/0031-9120/4/3/312. URL: https://dx.doi.org/10.1088/0031-9120/4/3/312.

[2] Monwhea Jeng. "The Mpemba effect: When can hot water freeze faster than cold?" In: *American Journal of Physics* 74.6 (2006), pp. 514–522. ISSN: 0002-9505. DOI: 10.1119/1.2186331. URL: https://doi.org/10.1119/1.2186331.

[3] Zhiyue Lu and Oren Raz. "Nonequilibrium thermodynamics of the Markovian Mpemba effect and its inverse". In: *Proceedings of the National Academy of Sciences* 114.20 (2017), pp. 5083–5088. DOI: 10.1073/pnas.1701264114. URL: https://www.pnas.org/doi/abs/10.1073/pnas.1701264114.

[4] Antonio Lasanta et al. "When the Hotter Cools More Quickly: Mpemba Effect in Granular Fluids". In: *Phys. Rev. Lett.* 119 (14 Oct. 2017), p. 148001. DOI: 10.1103/PhysRevLett.119.148001. URL: https://link.aps.org/doi/10.1103/PhysRevLett.119.148001.

[5] Marco Baity-Jesi et al. "The Mpemba effect in spin glasses is a persistent memory effect". In: *Proc. Natl. Acad. Sci. USA* 116.31 (July 2019), pp. 15350–15355. URL: https://doi.org/10.1073/pnas.1819803116.

[6] Aurora Torrente et al. "Large Mpemba-like effect in a gas of inelastic rough hard spheres". In: *Phys. Rev. E* 99 (6 June 2019), p. 060901. DOI: 10.1103/PhysRevE.99.060901. URL: https://link.aps.org/doi/10.1103/PhysRevE.99.060901.

[7] Andrés Santos and Antonio Prados. "Mpemba effect in molecular gases under nonlinear drag". In: *Physics of Fluids* 32.7 (July 2020), p. 072010. ISSN: 1070-6631. DOI: 10.1063/5.0016243. URL: https://doi.org/10.1063/5.0016243.

[8] Alberto Megías, Andrés Santos, and Antonio Prados. "Thermal versus entropic Mpemba effect in molecular gases with nonlinear drag". In: *Phys. Rev. E* 105 (5 May 2022), p. 054140. DOI: 10.1103/PhysRevE.105.054140. URL: https://link.aps.org/doi/10.1103/PhysRevE.105.054140.

[9] Raphael Chétrite, Avinash Kumar, and John Bechhoefer. "The Metastable Mpemba Effect Corresponds to a Non-monotonic Temperature Dependence of Extractable Work". In: *Frontiers in Physics* 9 (2021), p. 654271. DOI: 10.3389/fphy.2021.654271. URL: https://www.frontiersin.org/journals/physics/articles/10.3389/fphy.2021.654271.

[10] Matthew R. Walker and Marija Vucelja. *Mpemba effect in terms of mean first passage time*. 2023. arXiv: 2212.07496 [cond-mat.stat-mech].

[11] Sara Murciano et al. "Entanglement asymmetry and quantum Mpemba effect in the XY spin chain". In: *Journal of Statistical Mechanics: Theory and Experiment* 2024.1 (Jan. 2024), p. 013103. DOI: 10.1088/1742-5468/ad17b4. URL: https://dx.doi.org/10.1088/1742-5468/ad17b4.

[12] Colin Rylands et al. "Microscopic Origin of the Quantum Mpemba Effect in Integrable Systems". In: *Phys. Rev. Lett.* 133 (1 July 2024), p. 010401. DOI: 10.1103/PhysRevLett.133.010401. URL: https://link.aps.org/doi/10.1103/PhysRevLett.133.010401.

[13] Shahaf Aharony Shapira et al. "Inverse Mpemba Effect Demonstrated on a Single Trapped Ion Qubit". In: *Phys. Rev. Lett.* 133 (1 July 2024), p. 010403. DOI: 10.1103/PhysRevLett.133.010403. URL: https://link.aps.org/doi/10.1103/PhysRevLett.133.010403.

[14] Lata Kh. Joshi et al. "Observing the Quantum Mpemba Effect in Quantum Simulations". In: *Phys. Rev. Lett.* 133 (1 July 2024), p. 010402. DOI: 10.1103/PhysRevLett.133.010402. URL: https://link.aps.org/doi/10.1103/PhysRevLett.133.010402.

[15] Amit Kumar Chatterjee, Satoshi Takada, and Hisao Hayakawa. "Quantum Mpemba Effect in a Quantum Dot with Reservoirs". In: *Phys. Rev. Lett.* 131 (8 Aug. 2023), p. 080402. DOI: 10.1103/PhysRevLett.131.080402. URL: https://link.aps.org/doi/10.1103/PhysRevLett.131.080402.

[16] Amit Kumar Chatterjee, Satoshi Takada, and Hisao Hayakawa. "Multiple quantum Mpemba effect: Exceptional points and oscillations". In: *Phys. Rev. A* 110 (2 Aug. 2024), p. 022213. DOI: 10.1103/PhysRevA.110.022213. URL: https://link.aps.org/doi/10.1103/PhysRevA.110.022213.

[17] Xuanhua Wang and Jin Wang. "Mpemba effects in nonequilibrium open quantum systems". In: *Phys. Rev. Res.* 6 (3 Sept. 2024), p. 033330. DOI: 10.1103/PhysRevResearch.6.033330. URL: https://link.aps.org/doi/10.1103/PhysRevResearch.6.033330.

[18] David J. Strachan, Archak Purkayastha, and Stephen R. Clark. *Non-Markovian Quantum Mpemba effect*. 2024. arXiv: 2402.05756 [quant-ph].

[19] Shuo Liu et al. "Symmetry Restoration and Quantum Mpemba Effect in Symmetric Random Circuits". In: *Phys. Rev. Lett.* 133 (14 Oct. 2024), p. 140405. DOI: 10.1103/PhysRevLett.133.140405. URL: https://link.aps.org/doi/10.1103/PhysRevLett.133.140405.

[20] Xhek Turkeshi, Pasquale Calabrese, and Andrea De Luca. *Quantum Mpemba Effect in Random Circuits*. 2024. arXiv: 2405.14514 [quant-ph].

[21] Simon Kochsiek, Federico Carollo, and Igor Lesanovsky. "Accelerating the approach of dissipative quantum spin systems towards stationarity through global spin rotations". In: *Phys. Rev. A* 106 (1 July 2022), p. 012207. DOI: 10.1103/PhysRevA.106.012207. URL: https://link.aps.org/doi/10.1103/PhysRevA.106.012207.

[22] Israel Klich et al. "Mpemba Index and Anomalous Relaxation". In: *Phys. Rev. X* 9 (2 June 2019), p. 021060. DOI: 10.1103/PhysRevX.9.021060. URL: https://link.aps.org/doi/10.1103/PhysRevX.9.021060.

[23] Filiberto Ares, Vittorio Vitale, and Sara Murciano. *The quantum Mpemba effect in free-fermionic mixed states*. 2024. arXiv: 2405.08913 [cond-mat.stat-mech].

[24] Andrea Nava and Reinhold Egger. "Mpemba Effects in Open Nonequilibrium Quantum Systems". In: *Phys. Rev. Lett.* 133 (13 Sept. 2024), p. 136302. DOI: 10.1103/PhysRevLett.133.136302. URL: https://link.aps.org/doi/10.1103/PhysRevLett.133.136302.

[25] Xuanhua Wang, Jie Su, and Jin Wang. *Mpemba Meets Quantum Chaos: Anomalous Relaxation and Mpemba Crossings in Dissipative Sachdev-Ye-Kitaev Models*. 2024. arXiv: 2410.06669 [quant-ph]. URL: https://arxiv.org/abs/2410.06669.

[26] J. W. Dong et al. *Quantum Mpemba effect of Localization in the dissipative Mosaic model*. 2024. arXiv: 2411.03734 [quant-ph]. URL: https://arxiv.org/abs/2411.03734.

[27] Dongheng Qian, Huan Wang, and Jing Wang. *Intrinsic Quantum Mpemba Effect in Markovian Systems and Quantum Circuits*. 2024. arXiv: 2411.18417 [quant-ph]. URL: https://arxiv.org/abs/2411.18417.

[28] Filiberto Ares, Pasquale Calabrese, and Sara Murciano. *The quantum Mpemba effects*. 2025. arXiv: 2502.08087 [cond-mat.stat-mech]. URL: https://arxiv.org/abs/2502.08087.

[29] Gianluca Teza et al. *Speedups in nonequilibrium thermal relaxation: Mpemba and related effects*. 2025. arXiv: 2502.01758 [cond-mat.stat-mech]. URL: https://arxiv.org/abs/2502.01758.

[30] M. Ibáñez et al. "Heating and cooling are fundamentally asymmetric and evolve along distinct pathways". In: *Nature Physics* 20.1 (Jan. 2024), pp. 135–141. ISSN: 1745-2481. DOI: 10.1038/s41567-023-02269-z. URL: https://doi.org/10.1038/s41567-023-02269-z.

[31] Isidoro González-Adalid Pemartín et al. "Shortcuts of Freely Relaxing Systems Using Equilibrium Physical Observables". In: *Phys. Rev. Lett.* 132 (11 Mar. 2024), p. 117102. DOI: 10.1103/PhysRevLett.132.117102. URL: https://link.aps.org/doi/10.1103/PhysRevLett.132.117102.

[32] Andrea Nava and Michele Fabrizio. "Lindblad dissipative dynamics in the presence of phase coexistence". In: *Phys. Rev. B* 100 (12 Sept. 2019), p. 125102. DOI: 10.1103/PhysRevB.100.125102. URL: https://link.aps.org/doi/10.1103/PhysRevB.100.125102.

[33] Nalina Vadakkayil and Subir K. Das. "Should a hotter paramagnet transform quicker to a ferromagnet? Monte Carlo simulation results for Ising model". In: *Phys. Chem. Chem. Phys.* 23 (19 2021), pp. 11186–11190. DOI: 10.1039/D1CP00879J. URL: http://dx.doi.org/10.1039/D1CP00879J.

[34] Isidoro González-Adalid Pemartín et al. "Slow growth of magnetic domains helps fast evolution routes for out-of-equilibrium dynamics". In: *Phys. Rev. E* 104 (4 Oct. 2021), p. 044114. DOI: 10.1103/PhysRevE.104.044114. URL: https://link.aps.org/doi/10.1103/PhysRevE.104.044114.

[35] Ulrich Weiss. *Quantum Dissipative Systems*. 4th. World Scientific, Singapore, 2012. DOI: 10.1142/8334. eprint: https://www.worldscientific.com/doi/pdf/10.1142/8334. URL: https://www.worldscientific.com/doi/abs/10.1142/8334.

[36] Heinz-Peter Breuer and Francesco Petruccione. *The Theory of Open Quantum Systems*. Oxford: Oxford University Press, 2007, p. 656. DOI: 10.1093/acprof:oso/9780199213900.001.0001.

[37] Yu. V. Nazarov and Ya. M. Blanter. *Quantum transport: Introduction to Nanoscience*. Cambridge University Press, Cambridge, 2009. URL: https://doi.org/10.1017/CBO9780511626906.

[38] M. A. Nielsen and I. L. Chuang. *Quantum Computation and Quantum Information*. Cambridge University Press, Cambridge, UK, 2000. URL: https://doi.org/10.1017/CBO9780511976667.

[39] Xiaoting Wang and S. G. Schirmer. "Contractivity of the Hilbert-Schmidt distance under open-system dynamics". In: *Phys. Rev. A* 79 (5 May 2009), p. 052326. DOI: 10.1103/PhysRevA.79.052326. URL: https://link.aps.org/doi/10.1103/PhysRevA.79.052326.

[40] Domenico Giuliano and Ian Affleck. "The Josephson current through a long quantum wire". In: *Journal of Statistical Mechanics: Theory and Experiment* 2013.02 (Feb. 2013), P02034. DOI: 10.1088/1742-5468/2013/02/P02034. URL: https://dx.doi.org/10.1088/1742-5468/2013/02/P02034.

[41] Domenico Giuliano and Ian Affleck. "dc Josephson current in a long multichannel quantum wire". In: *Phys. Rev. B* 90 (4 July 2014), p. 045133. DOI: 10.1103/PhysRevB.90.045133. URL: https://link.aps.org/doi/10.1103/PhysRevB.90.045133.

[42] A. Zazunov et al. "Quasiparticle trapping, Andreev level population dynamics, and charge imbalance in superconducting weak links". In: *Phys. Rev. B* 90 (10 Sept. 2014), p. 104508. DOI: 10.1103/PhysRevB.90.104508. URL: https://link.aps.org/doi/10.1103/PhysRevB.90.104508.

[43] G Campagnano et al. "Spin-orbit coupling and anomalous Josephson effect in nanowires". In: *Journal of Physics: Condensed Matter* 27 (2015), p. 205301. DOI: 10.1088/0953-8984/27/20/205301. URL: https://iopscience.iop.org/article/10.1088/0953-8984/27/20/205301.

[44] Sunghun Park and A. Levy Yeyati. "Andreev spin qubits in multichannel Rashba nanowires". In: *Phys. Rev. B* 96 (12 Sept. 2017), p. 125416. DOI: 10.1103/PhysRevB.96.125416. URL: https://link.aps.org/doi/10.1103/PhysRevB.96.125416.

[45] M. Minutillo et al. "Anomalous Josephson effect in S/SO/F/S heterostructures". In: *Phys. Rev. B* 98 (14 Oct. 2018), p. 144510. DOI: 10.1103/PhysRevB.98.144510. URL: https://link.aps.org/doi/10.1103/PhysRevB.98.144510.

[46] Nico Ackermann et al. "Dynamical parity selection in superconducting weak links". In: *Phys. Rev. B* 107 (21 June 2023), p. 214515. DOI: 10.1103/PhysRevB.107.214515. URL: https://link.aps.org/doi/10.1103/PhysRevB.107.214515.

[47] Kateryna Zatsarynna et al. "Many-body quantum dynamics of spin-orbit coupled Andreev states in a Zeeman field". In: *Phys. Rev. B* 109 (21 June 2024), p. 214505. DOI: 10.1103/PhysRevB.109.214505. URL: https://link.aps.org/doi/10.1103/PhysRevB.109.214505.

[48] Yoan Fauvel, Julia S. Meyer, and Manuel Houzet. "Opportunities for the direct manipulation of a phase-driven Andreev spin qubit". In: *Phys. Rev. B* 109 (18 May 2024), p. 184515. DOI: 10.1103/PhysRevB.109.184515. URL: https://link.aps.org/doi/10.1103/PhysRevB.109.184515.

[49] Jonas Lidal and Jeroen Danon. *Andreev bound states and supercurrent in disordered spin-orbit-coupled nanowire SNS-junctions*. 2023. arXiv: 2312.13833 [cond-mat.mes-hall].

[50] M. Z. Hasan and C. L. Kane. "Colloquium: Topological insulators". In: *Rev. Mod. Phys.* 82 (4 Nov. 2010), pp. 3045–3067. DOI: 10.1103/RevModPhys.82.3045. URL: https://link.aps.org/doi/10.1103/RevModPhys.82.3045.

[51] A. Martín-Rodero and A. Levy Yeyati. "Josephson and Andreev transport through quantum dots". In: *Advances in Physics* 60.6 (2011), pp. 899–958. DOI: 10.1080/00018732.2011.624266. URL: https://doi.org/10.1080/00018732.2011.624266.

[52] S. B. Kaplan et al. "Quasiparticle and phonon lifetimes in superconductors". In: *Phys. Rev. B* 14 (11 Dec. 1976), pp. 4854–4873. DOI: 10.1103/PhysRevB.14.4854. URL: https://link.aps.org/doi/10.1103/PhysRevB.14.4854.

[53] A. Zazunov et al. "Dynamics and phonon-induced decoherence of Andreev level qubit". In: *Phys. Rev. B* 71 (21 June 2005), p. 214505. DOI: 10.1103/PhysRevB.71.214505. URL: https://link.aps.org/doi/10.1103/PhysRevB.71.214505.

[54] C. W. J. Beenakker and H. van Houten. "Josephson current through a superconducting quantum point contact shorter than the coherence length". In: *Phys. Rev. Lett.* 66 (23 June 1991), pp. 3056–3059. DOI: 10.1103/PhysRevLett.66.3056. URL: https://link.aps.org/doi/10.1103/PhysRevLett.66.3056.

[55] Akira Furusaki and Masaru Tsukada. "Current-carrying states in Josephson junctions". In: *Phys. Rev. B* 43 (13 May 1991), pp. 10164–10169. DOI: 10.1103/PhysRevB.43.10164. URL: https://link.aps.org/doi/10.1103/PhysRevB.43.10164.

[56] J Barr et al. "Spectral density classification for environment spectroscopy". In: *Machine Learning: Science and Technology* 5.1 (Mar. 2024), p. 015043. DOI: 10.1088/2632-2153/ad2cf1. URL: https://dx.doi.org/10.1088/2632-2153/ad2cf1.

[57] Roger A Horn and Charles R Johnson. *Matrix analysis*. Cambridge University Press, Cambridge, UK, 2012. URL: https://www.cambridge.org/de/universitypress/subjects/mathematics/algebra/matrix-analysis-2nd-edition?format=PB&isbn=9780521548236.

[58] C. Janvier et al. "Coherent manipulation of Andreev states in superconducting atomic contacts". In: *Science* 349.6253 (2015), pp. 1199–1202. DOI: 10.1126/science.aab2179. URL: https://www.science.org/doi/abs/10.1126/science.aab2179.

[59] J. J. Wesdorp et al. "Dynamical Polarization of the Fermion Parity in a Nanowire Josephson Junction". In: *Phys. Rev. Lett.* 131 (11 Sept. 2023), p. 117001. DOI: 10.1103/PhysRevLett.131.117001. URL: https://link.aps.org/doi/10.1103/PhysRevLett.131.117001.

[60] J. J. Wesdorp et al. "Microwave spectroscopy of interacting Andreev spins". In: *Phys. Rev. B* 109 (4 Jan. 2024), p. 045302. DOI: 10.1103/PhysRevB.109.045302. URL: https://link.aps.org/doi/10.1103/PhysRevB.109.045302.

[61] Federico Carollo, Antonio Lasanta, and Igor Lesanovsky. "Exponentially Accelerated Approach to Stationarity in Markovian Open Quantum Systems through the Mpemba Effect". In: *Phys. Rev. Lett.* 127 (6 Aug. 2021), p. 060401. DOI: 10.1103/PhysRevLett.127.060401. URL: https://link.aps.org/doi/10.1103/PhysRevLett.127.060401.

4 Conclusion and Outlook

In this chapter, we summarize the main findings of this work and list possible research directions.

Conclusion.— In Chapter 2, we were studying the many-body dynamics and dynamical parity stabilization of the Josephson junctions with broken spin symmetry. The setup of the problem is discussed in Section 1.4. The Josephson junction is modeled as a 1D superconductor-quantum dot-superconductor (SDS) junction, with the intermediate length nanowire. In th nanowire region we include SOI and Zeeman field. We describe the junction by the transfer matrix approach and solve the BdG equations explicitly, in the absence of the microwave environment, to obtain the energies and wave-functions of the single-particle states of the SDS contact - both ABS and continuum states. To avoid double-counting problems when constructing the MBSs, we work in the excitation picture, selecting only the positive-energy single-particle states. Further, in order to describe the dynamics of the ABSs and their interactions with the continuum states in the presence of the electromagnetic environment, we obtain the Lindblad master equation. Here, the e/m environment is treated as a bosonic bath, and continuum states of the junction as a fermionic bath. Due to the vanishing interferences between different many-body ABS, we consider only the Pauli master equation for the occupation probabilities of the many-body ABS. We apply this equation to study the dynamical parity stabilization in Josephson junctions with spin symmetry breaking. First of all, we observe that the dynamical parity stabilization effect is present in our system after an external population inverting pulse. Secondly, we examine the selection rules for this pulse from the transition rates between the MBSs. We study the dependence of the selection rules of the superconducting phase difference and the angle between the SOI and the magnetic field. Lastly, we investigate the properties of the dynamical parity stabilization, such as the maximally achieved polarization and its lifetime, and their dependence on the angle between the SOI and Zeeman field.

In Chapter 3, we consider the same setup. Here,the junction is described in terms of the Green's functions formalism by solving the Heisenberg equation of motion for the quantum dot fermionic states. The derived transition rates are inserted into the previously obtained Pauli master equation for the dynamics of the ABSs in the presence of the fermionic continuum bath and bosonic environment. We apply the developed formalism to study the quantum Mpemba effect in the Josephson junctions with short- and intermediate-length quantum dot with the presence or absence of the spin symmetry. The Mpemba effect is present already in the simplest case (short wire, large-coupling limit), and we examine the effect for more elaborate cases, such as intermediate-length junctions, with or without spin-symmetry breaking.

Overall, our results show that both dynamical parity stabilization and Mpemba effect arise from the interplay between the shape of the ABSs (which is influenced by the parameters of the junction, such as length, transparency, strength of the SOI, and Zeeman field), coupling to the continuum states, and the external microwave field. Theoretical approaches developed in this work provide a framework to analyze time-dependent many-body dynamics in hybrid superconducting systems. Nevertheless, the present analysis focuses on intermediate dot lengths (4 spin-split positive energy ABSs) and Markovian baths, and future work could extend beyond these approximations.

Outlook.— Based on the theoretical frameworks and the effects studied in this work, there are several possible extensions:

- Considering the case of long quantum wires and a large number of ABSs in the junc-

tion. Analyzing how the number of ABSs influences dynamical parity stabilization and Quantum Mpemba effects;

- Regarding Chapter 2, a possible extension may be to consider periodic microwave driving of the Josephson junction. This could be used to achieve stable polarization. More generally, studying the influence of Floquet driving on the ABS spectrum and its dynamics;
- Possibly, studying ABSs to Majorana bound states transition (or its absence), given that all the necessary ingredients are already included in this work (s-wave SC, SOI, Zeeman field). In addition, one could include multiple channels, for a more realistic picture or periodic driving.
- Inclusion of non-Markovian effects in the coupling to the fermionic continuum or electromagnetic environment. This could reveal memory-induced modifications in the dynamics;
- Investigation of the role of interactions on the dot, e.g., Coulomb repulsion, and its interplay with the SOI and external magnetic field.
- Regarding Chapter 3, generalization of the Mpemba-effect analysis to time-dependent protocols, such as quenches of the superconducting phase difference or other parameters: temperature of the bosonic and fermionic environments, magnetic-field direction, to identify optimal control paths for accelerated thermalization;

Selbstständigkeitserklärung

Ich versichere an Eides Statt, dass die Dissertation von mir selbständig und ohne unzulässige fremde Hilfe unter Beachtung der „Grundsätze zur Sicherung guter wissenschaftlicher Praxis an der Heinrich-Heine-Universität Düsseldorf“ erstellt worden ist.

Weiterhin erkläre ich, dass ich die Dissertation keiner anderen Fakultät bereits vorgelegt habe und keinerlei vorherige erfolglose oder erfolgreiche Promotionsversuche vorliegen. Darüber hinaus ist mir bekannt, dass jedweder Betrugsversuch zum Nichtbestehen oder zur Aberkennung der Prüfunsleistung führen kann.

Düsseldorf, ...04.12.2025..... Kateryna Zatsarynna .....